Negative Curvature Fibre optics for delivery of high-peak power light for manufacturing applications

Piotr Jaworski

Submitted for the degree of Doctor of Philosophy

Heriot-Watt University

School of Engineering and Physical Sciences

October 2015

Abstract

This thesis covers investigations into high peak power short (nanosecond) and ultrashort (picosecond and femtosecond) pulse delivery through novel hollow-core microstructured silica fibres - the Negative Curvature Fibre (NCF) and the Free Boundary Anti-Resonant Fibre (FBARF) for manufacturing applications. Both types of fibres provide light guidance in the NIR and green spectral regions via the Anti-Resonant Reflecting Optical Waveguiding (ARROW) mechanism.

NCFs exhibit extremely low attenuations of 0.04 dB/m and 0.15 dB/m at 1030 nm and 532 nm respectively, not achievable with photonic bandap hollow-core fibres. These fibres have been demonstrated to deliver NIR and green picosecond pulses with peak powers at the level of 15 MW and 5 MW respectively, which significantly exceeds the capabilities of commercially available singlemode fibres. Optimised NCFs for transmission in both spectral regimes provide singlemode, high quality output and maintain the spectral and temporal properties of the original laser pulse. Furthermore, these fibres exhibit a low sensitivity to bending with useful bend diameters $\geq$ 5 cm, which is sufficient for most beam delivery applications. This was further improved by developing and introducing a dynamic fibre delivered power stabilisation system which enables efficient compensations of bend-induced power fluctuations.

Practical implementation of NCF delivered pulses in manufacturing applications has been demonstrated in the precision micro-machining of metals, crack-free micro-milling of fused silica and waveguide writing in borosilicate glass.

The FBARF structure is a modification of the NCF design aimed for an improvement in energy handling capacity, light confinement and further reduction of bending loss. However, the fibres reported in this thesis (fabricated for guidance at 1 μm and green wavelengths) are preliminary designs, and so their full potential e.g. their energy handling capacities could not be fully established. Nevertheless, initial tests performed within this work indicated that further development of this fibre design should result in a reduction of the intrinsic attenuation and bend loss to a level comparable with the NCFs while increasing the optical damage threshold.

Acknowledgements

I would like to thank Prof Duncan Hand and Dr Jonathan Shephard for their supervision during this project and giving me the opportunity to become a member of the Applied Optics and Photonics Group. Many thanks also go to Dr Robert Maier and Dr Richard Carter for their support and joint work on this project.

The most special thanks go to my parents for their support.

ACADEMIC REGISTRY
Research Thesis Submission

Name*:*	Piotr Jaworski		
School/PGI:	School of Engineering and Physical Sciences		
Version: *(i.e. First, Resubmission, Final)*	Final	Degree Sought (Award **and** Subject area)	Doctor of Philosophy

Declaration

In accordance with the appropriate regulations I hereby submit my thesis and I declare that:

1) the thesis embodies the results of my own work and has been composed by myself
2) where appropriate, I have made acknowledgement of the work of others and have made reference to work carried out in collaboration with other persons
3) the thesis is the correct version of the thesis for submission and is the same version as any electronic versions submitted*.
4) my thesis for the award referred to, deposited in the Heriot-Watt University Library, should be made available for loan or photocopying and be available via the Institutional Repository, subject to such conditions as the Librarian may require
5) I understand that as a student of the University I am required to abide by the Regulations of the University and to conform to its discipline.

* *Please note that it is the responsibility of the candidate to ensure that the correct version of the thesis is submitted.*

Signature of Candidate*:*		Date:	

Submission

Submitted By *(name in capitals):*	
Signature of Individual Submitting:	
Date Submitted:	

For Completion in the Student Service Centre (SSC)

Received in the SSC by *(name in capitals):*			
Method of Submission *(Handed in to SSC; posted through internal/external mail):*			
*E-thesis Submitted (**mandatory for final theses)***			
Signature:		Date:	

Table of contents

List of publications

Journal articles

1. P. Jaworski, F. Yu, R. M. Carter, J. C. Knight, J. D. Shephard, and D. P. Hand, "High energy green nanosecond and picosecond pulse delivery through a Negative Curvature Fiber for precision micro-machining," Opt. Express **23**, 8498-8506 (2015).
2. J. D. Shephard, A. Urich, R. M. Carter, P. Jaworski, R. R. J. Maier, W. Belardi, F. Yu, W. J. Wadsworth, J. C. Knight and D. P. Hand, "Silica hollow core microstructured fibers for beam delivery in industrial and medical applications," Frontiers: Modern trends in hollow core microstructured optical fibers (2015). Accepted.
3. P. Jaworski, F. Yu, R. R. J. Maier, W. J. Wadsworth, J. C. Knight, J. D. Shephard, and D. P. Hand, "Picosecond and nanosecond pulse delivery through a hollow-core Negative Curvature Fiber for micro-machining applications," Opt. Express **21**(19), 22742-22753 (2013).

Conference publications

4. P. Jaworski, F. Yu, R. M. Carter, J. C. Knight, J. D. Shephard, and D. P. Hand, "Dual-wavelength hollow-core Negative Curvature Fiber for the delivery of high energy short and ultrashort pulsed laser light," Accepted to CLEO Europe 2015.
5. P. Jaworski, F. Yu, R. M. Carter, W. J. Wadsworth, T. A. Birks, J. C. Knight, J. D. Shephard, and D. P. Hand, "High peak power nanosecond and picosecond pulse delivery through a hollow-core Negative Curvature Fiber in the green spectral region for micro-machining," in *Advanced Photonics*, OSA Technical Digest (online) (Optical Society of America, 2014), paper SoM3B.5.
6. P. Jaworski, F. Yu, D. G. MacLachlan, R. R. Maier, R. R. Thomson, W. J. Wadsworth, J. C. Knight, J. D. Shephard, and D. P. Hand, "A hollow-core Negative Curvature Fibre for efficient delivery of NIR picosecond and femtosecond pulses for precision micro-machining," in *Workshop on Specialty Optical Fibers and their Applications*, (Optical Society of America, 2013), paper F3.3.
7. P. Jaworski, F. Yu, R. R. J. Maier, W. J. Wadsworth, T. A. Birks, J. C. Knight, J. D. Shephard, and D. P. Hand, "Delivery of high-power nanosecond and picosecond pulses through a hollow-core Negative Curvature Fibre for micro-machining applications," in *2013 Conference on Lasers and Electro-Optics* -

International Quantum Electronics Conference, (Optical Society of America, 2013), paper CE_4_1.

Conference presentations

8. P. Jaworski, R. M. Carter, F. Yu, W. J. Wadsworth, T. A. Birks, J. C. Knight, J. D. Shephard, and D. P. Hand, "Hollow-core Negative Curvature Fibres for the delivery of high peak power nanosecond and picosecond pulses for micro-machining applications," ILAS 2015, Kenilworth 17-18 March 2015.
9. R. J. Beck, P. Jaworski, N. Weston, D. P. Hand, and J. D. Shephard, "Parallel robot platform for 3D freeform laser manufacturing," poster, ILAS 2015, Kenilworth 17-18 March 2015.
10. R. M. Carter, P. Jaworski, W. Belardi, F. Yu, W. J. Wadsworth, A. Urich, T. Birks, J. D. Shephard, J. C. Knight, and D. P. Hand, "Applications of microstructured “negative curvature” fibre, for high power and mid-IR transmission," Photon 2014 , London 1-4 Sept. 2014.
11. W. Belardi, F. Yu, A. Urich, P. Jaworski, R. R. J. Maier, J. D. Shephard, W. J. Wadsworth, D. P. Hand, and J. C. Knight, "Hollow Core Fibers: An Efficient Way for Handling High Optical Powers and Accessing New Wavelengths," ICP 2013, Melaka 28-30 Oct 2013.

Chapter 1

Introduction

Optical fibres have been used in various applications including ultra low-loss data transmission in telecommunication systems, high power laser sources, industry and many other areas for more than 40 years. However their full potential has not yet been fully realised. One application area where further improvements are possible is flexible beam delivery for high energy pulsed laser sources used in industry, especially in micro-machining. Many applications have a high demand on flexibility, and so a fully flexible beam delivery solution is desirable. This unfortunately cannot be provided by conventional optical elements or even robotic devices such as articulated arms as these suffer from highly complex structures. An articulated arm typically consists of a set of inflexible tubes connected with rotary joints containing mirrors which limits their full range of motion, and therefore fibre optics are required. Different types of fibres that have higher damage threshold than conventional fibre designs such as solid core Large Mode Area and hollow-core photonic crystal fibres have been introduced already into these systems. However their energy handling capabilities are still limited by optical damage, nonlinear effects and fabrication issues, which means that they cannot be used for delivery of high power ultrashort (picosecond and femtosecond) pulses.

The main aim of this work is to develop a flexible beam delivery system using a novel microstructured optical fibre developed by project partners at the University of Bath based on hollow-core designs capable of delivering singlemode high peak power pulsed laser light in the NIR and green spectral regions.

Chapter 2

Literature review

Chapter 2 provides background information with regards to the work presented in this thesis. It includes a brief explanation of the main principles of laser material processing using continuous-wave and pulsed coherent light sources. This is followed by the introduction of currently used beam delivery solutions used in laser manufacturing systems and their limitations. The main types of optical fibres (i.e. conventional solid core and microstructured) currently available for light delivery in the NIR and green wavelength regimes are discussed. This includes a summary of high energy pulse delivery; the limitations of the various fibres arising from nonlinear processes, optical damage threshold, attenuation; and a brief description of the NCF's fabrication process.

2.1 Application of high peak power pulsed lasers for micro-machining

Rapid development of high peak power pulsed laser sources over the last decade has resulted in extensive employment in various industrial applications, especially in precision micro-machining. Current industrial lasers, used for processing of materials, are based on a gain medium formed by rare-earth ion doped (i.e. neodymium or ytterbium) crystals or optical fibres. They typically emit short (nanosecond) and ultrashort (picosecond and femtosecond) pulses in the vicinity of 1 μm, visible (green) and UV spectral regions with peak powers of up to the gigawatt level at repetition rates of up to tens of MHz while maintaining high beam quality. These lasers have provided a significant improvement in precision and quality of components fabricated by laser drilling, cutting, marking and welding of as shown in Fig. 2.1 [1-6].

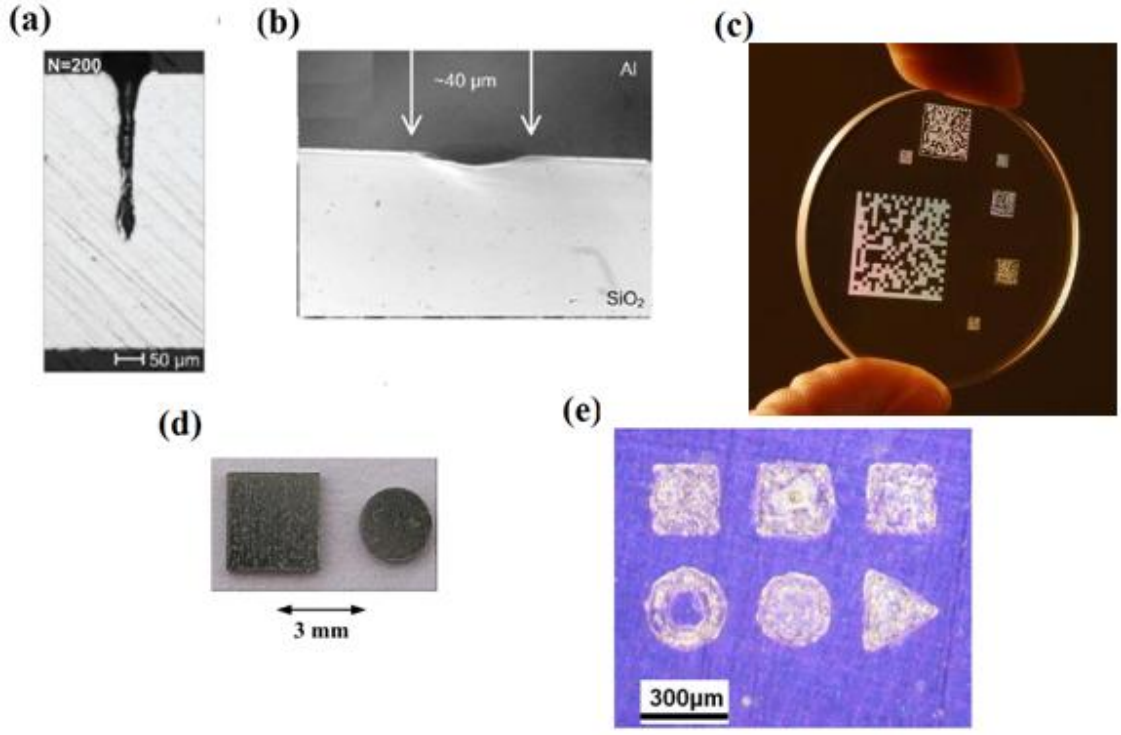

Fig. 2.1. (a) Hole drilled with nanosecond pulses in stainless steel [1]; (b) Al welded to SiO_2 with picosecond pulses [6]; (c) femtosecond marking in sapphire [5]; (d) Features cut in Al sheet with nanosecond pulses; (e) nanosecond marking in polyimide coated metal [2].

The quality of laser-machined features strictly depends on the light-material interaction, hence laser parameters, such as the operation mode (pulsed or continuous-wave CW), power, pulse duration, pulse energy, repetition rate and wavelength have to be carefully chosen with regards to the material type. Pulsed and continuous-wave laser systems modify material via different processes as shown in Fig. 2.2. CW laser light

removes material through melting, which results in the formation of a significant heat affected zone (HAZ), and hence thermal modification of both the processed and surrounding material [7]. Laser pulses with a duration of tens of nanoseconds modify material through melt expulsion forced by generated vapour and recoil pressures [7]. This provides improvement in comparison with CW light (e.g. higher precision of machined features with ns pulses), however it is still not ideal. The melted material is ejected from the laser-treated area, which leads to the formation of a recast layer and spatter or even micro-cracks within the machined and surrounding material. Nevertheless, it is possible to precisely machine some materials e.g. titanium alloys with ns pulses if UV light is used (as the quality depends on the wavelength and material parameters) [8]. This can be improved with the aid of ultrashort laser pulses. Here, the laser beam interacts with the material over an extremely short timescale, and therefore the time during which the energy is transferred to the surrounding material is significantly reduced. As a result the material has less residual energy, which makes the HAZ negligible in comparison with machining with longer laser pulses [9]. In general, the material is modified with direct vaporisation and a melt zone, a recast layer and spatter are not created (however, melting can occur with either ps or fs pulses) [7]. Furthermore, ultrashort laser pulses allow access to nonlinear absorption process, desirable in precision (crack-free) machining of transparent materials i.e. fused silica glass and is not achievable with nanosecond pulses as presented in Fig. 2.3.

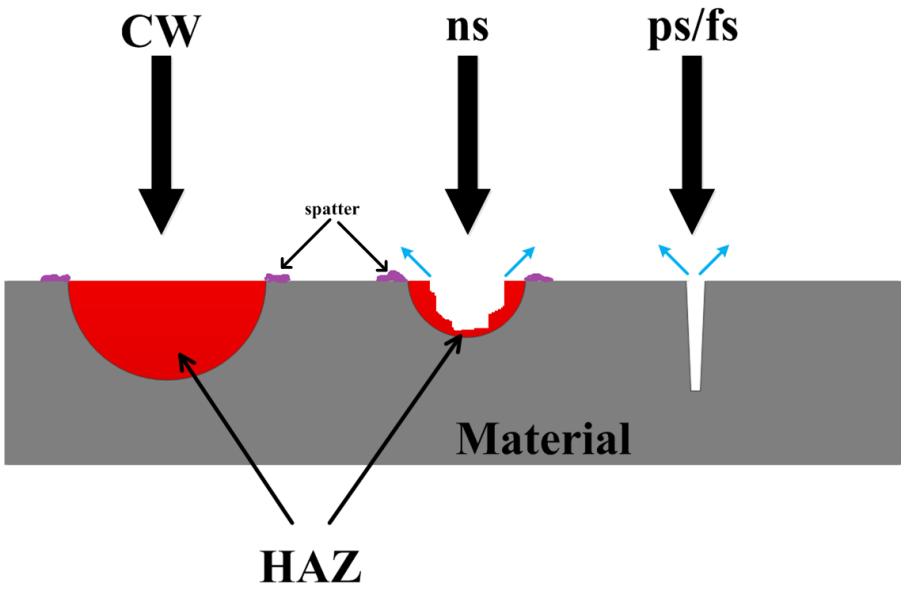

Fig. 2.2. Laser-material interaction with continuous-wave (CW), nanosecond (ns) and pico-/femtosecond (ps/fs) lasers. HAZ - heat affected zone.

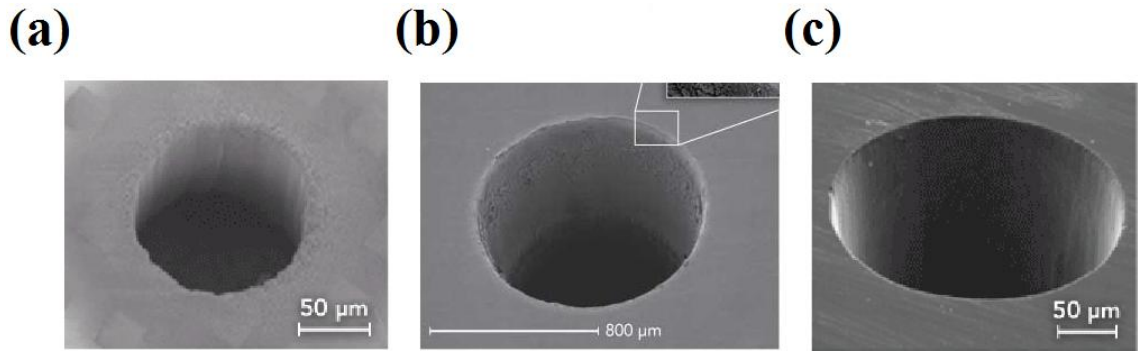

Fig. 2.3. Glass machined with: (a) ns pulses at 266 nm [7]; (b) ps pulses at 1064 nm [10]; (c) fs pulses at 780 nm [7].

2.1.1 Industrial laser beam delivery systems - current solutions

Typical laser-machining industrial systems consist of a high power laser source and a beam delivery assembly. Laser beam delivery is one of the most important parts of the system defining its flexibility, and therefore the ability to process not only planar components but also more complex structures. Currently available laser beam delivery solutions are based on conventional optical elements (lenses, mirrors etc.), or fibre optics connected with a galvo scan head system, or robotic devices.

A galvo scan head consists of a set of two mirrors aligned orthogonally and assembled with galvanometer motors which direct the laser beam onto an f-theta lens. The galvanometer motor provides fast adjustment of the mirrors which are controlled via computer software (used to define component dimensions and machining parameters). The f-theta lens allows focusing of the laser beam over a specified area (it provides a flat focal plane) corresponding to the process feature dimensions (maximum machining area, however is strictly defined by the lens specification). A schematic of a galvo scan head laser-processing system and a commercial scan head (SCANLAB) are shown in Figs. 2.4(a) and 2.4(b) respectively. This solution significantly decreases the machining time in comparison with systems based on motorised translation stages (used to position the sample with respect to the focused laser beam in order to fabricate a desired object). However, due the limitations arising from the dimensions of the machining area a galvo scan head does not provide flexibility at the level achievable with systems based on an optical fibre. Another disadvantage of this solution arises when it has to be used with an ultrashort (ps /fs) laser source. In this case the only method to deliver the laser beam to the scan head is by using a set of conventional optical elements. This can be overcome by the connection of a glavo scan head with a

fibre beam delivery system based on a microstructured fibre capable of delivering high energy ultrashort pulses (as discussed further in this chapter).

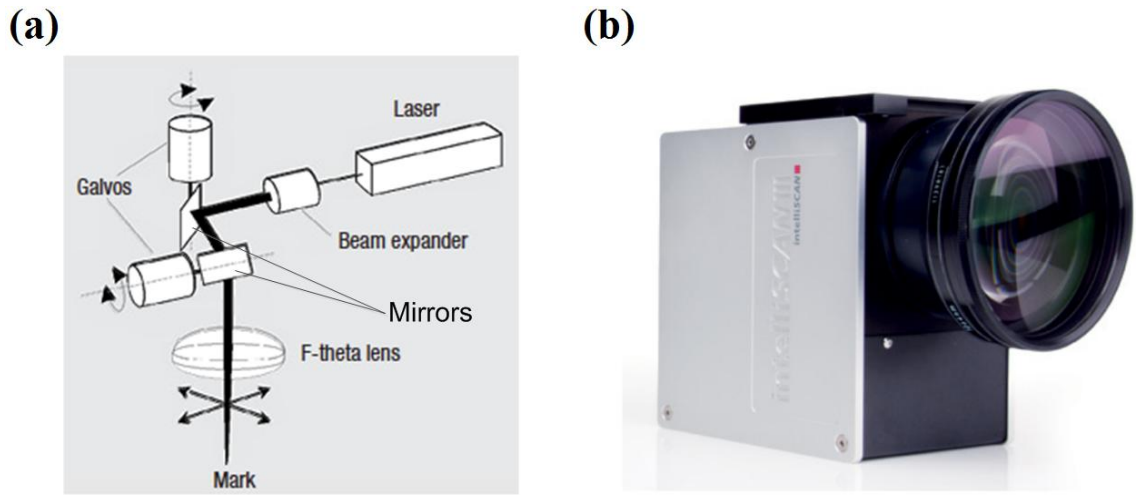

Fig. 2.4. (a) Schematic of a laser-machining system with a galvanometer scan head [11]; (b) SCANLAB galvo scan head [12].

Robot based laser-processing systems are commonly used in many industrial applications e.g. in laser cutting. A schematic of a robotic system and a commercial solution (from Jenoptik) using CO_2 laser light are shown in Figs. 2.5(a) and 2.5(b). The device consists of an articulated arm (equipped with a set of mirrors) delivering the laser beam to the focusing optics. The arm and the optics are joined together and fixed (mechanically) to a robot, which allows positioning of the entire assembly. The system is controlled via computer software and its movement corresponds to the shape of the machined object. The main problem of this solution results from the use of optical elements (mirrors) directing the laser beam onto the focusing optics. These elements require periodical realignment in order to maintain the device accuracy. Furthermore, the mirrors have to be equipped with an additional cooling system to prevent overheating and consequently their misalignment or damage due to high laser power (e.g. 5 kW used in industrial cutting systems) [13,14]. At this moment fibre optic beam delivery is not available for CO_2 laser radiation with powers in the kW regime.

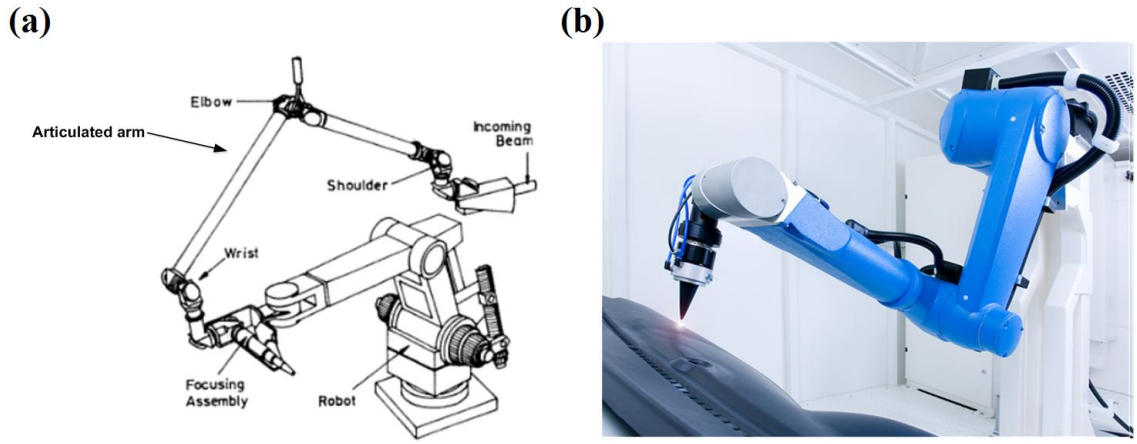

Fig. 2.5. (a) Schematic of a robot-based laser-machining system [13]; (b) Commercial robotic laser-cutting system (mirror-based) from Jenoptik [14].

Optical fibres (both conventional solid core and microstructured) are capable of transmitting laser light almost over the entire spectral bandwidth that is used in micro-machining applications (from the UV to NIR). These fibres provide excellent flexibility, not achievable with laser beam delivery systems currently available on the market, and provide an excellent alternative to conventional optical elements. An optical fibre can be introduced as a beam delivery tool to a system using e.g. flying optics, galvo scan heads or robotic devices, which can extend their versatility. Furthermore, the use of fibre optics does not require the laser to be placed close to the machining optics, which provides a significant improvement in flexibility of the laser-processing system. Unfortunately, currently available fibres provide only a partial solution, mainly for CW lasers and nanosecond lasers with energies not exceeding 1 mJ. Commercially available industrial laser-machining systems typically use solid core silica fibres (singlemode or multimode), which are not capable of delivering high energy ultrashort laser pulses due to limitations arising from the optical damage threshold and the strong influence of nonlinear effects (see section 2.3 for further information). The lack of a truly flexible beam delivery system for high peak power laser sources significantly restricts their application range, however the use of novel microstructured fibres which enable transmission of high energy ps and fs pulsed laser light (discussed further in this chapter) seems to be the perfect solution to this problem. Examples of commercial laser-machining systems using fibre optics are shown in Fig. 2.6.

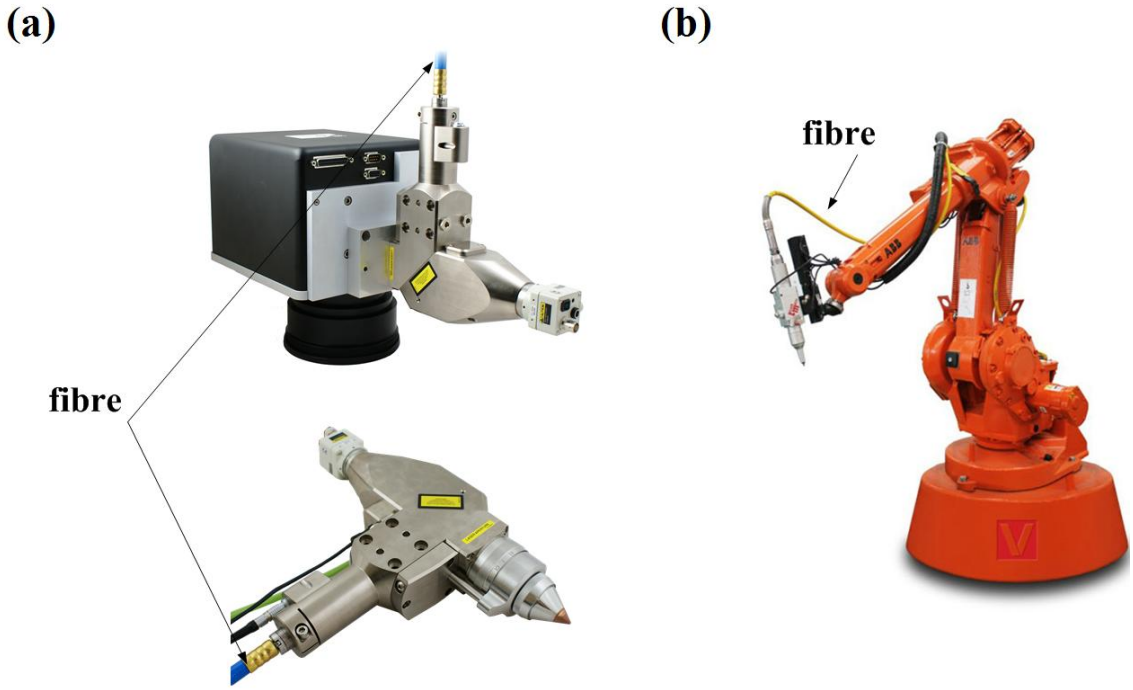

Fig. 2.6. (a) Galvanometer scan head (top) and processing head (bottom) with fibre optics from JK™Lasers [15]; (b) Fibre laser 3D cutting robot arm from Golden Laser [16].

2.2 Optical fibres for short and ultrashort pulse delivery in the NIR and green spectral regions

This section covers a review of different types of optical fibres currently used for the delivery of high energy and high peak power short and ultrashort laser pulses in the near infrared (NIR) and visible (green) part of the spectrum. The discussed fibres, operating in the aforementioned spectral regimes, are based on silica glass and can be divided into two main classes with regards to their structure and light guidance mechanism - solid core fibres and microstructured fibres.

2.2.1 Solid core silica fibres

Solid core silica fibre is a type of optical waveguide which typically consists of two materials with different refractive index values - high-index core and low-index cladding and transmits light via the total internal reflection (TIR) phenomenon as illustrated in Fig. 2.7. When a ray of light is incident on the interface between fibre core and cladding at a specific angle θ (angle of incidence), smaller than the acceptance angle of the fibre θ_c (typically defined by a parameter called Numerical Aperture - see section 4.1 for further details), it can be well confined within the core. Consequently, when the angle of incidence is greater than the θ_c angle the light is refracted and guidance within the fibre core is not possible. The acceptance angle of the fibre strictly

depends on the ratio of the refractive index of the cladding to the refractive index of the core as defined by the following formula

$$\theta_c = \arcsin\left(\frac{n_2}{n_1}\right) \tag{2-1}$$

where n_1 and n_2 define the refractive index of the core and cladding respectively. The refractive index values can be controlled by introducing different dopants to the silica glass e.g. germanium, fluorine etc. [17].

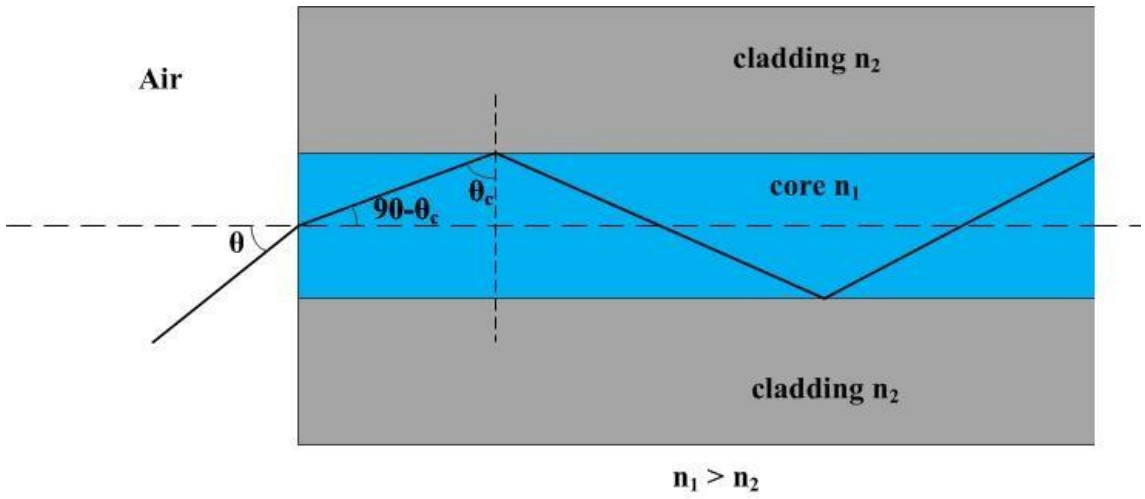

Fig. 2.7. TIR in singlemode step-index fibre. θ - angle of incidence, θ_c - acceptance angle of the fibre, n_1 and n_2 correspond to the refractive index of the fibre core and cladding respectively.

Furthermore, guidance of light in an optical fibre can be described by the propagation constant parameter (wavevector component) - β defined as

$$\beta = kn \tag{2-2}$$

where k is the wavevector and n is the refractive index of the considered region. Therefore, propagation of light in a fibre occurs (via TIR) when the following condition is fulfilled

$$kn_2 < \beta < kn_1 \tag{2-3}$$

where n_1 and n_2 define the refractive index of the fibre core and cladding respectively.

Solid core silica fibres can be classified in terms of their guidance properties as singlemode or multimode fibres with step or graded refractive index profiles as presented in Fig. 2.8. A step-index fibre consists of a core with a constant value of the refractive index while in a graded-index one the refractive index of the core is variable

(the core consists of layers with different dopants, hence with different indexes). Graded refractive index change can be used to compensate for modal dispersion of the fibre [17]. The singlemodeness of an optical fibre is defined by the so called normalised frequency V (the V number) defined by the following formula

$$V = \frac{2\pi a}{\lambda}\sqrt{n_1^2 - n_2^2} \tag{2-4}$$

where a is the fibre core radius, λ is the wavelength, n_1 and n_2 are the refractive indexes of the core and cladding respectively. For singlemode transmission the normalised frequency should typically be lower than 2.405 [18]. Since the type of guidance depends on the fibre core size (the number of supported modes decreases with a decrease in core diameter) a singlemode fibre (SMF) typically has a core with a diameter of ~ 10 μm while in the case of multimode fibres the core size can reach up to 1 mm and beyond (Large Mode Area (LMA) fibres). Furthermore, solid core silica fibres are characterised by very low attenuation down to approximately 0.2 dB/km and 30 dB/km in the NIR and green wavelength regions respectively [19,20].

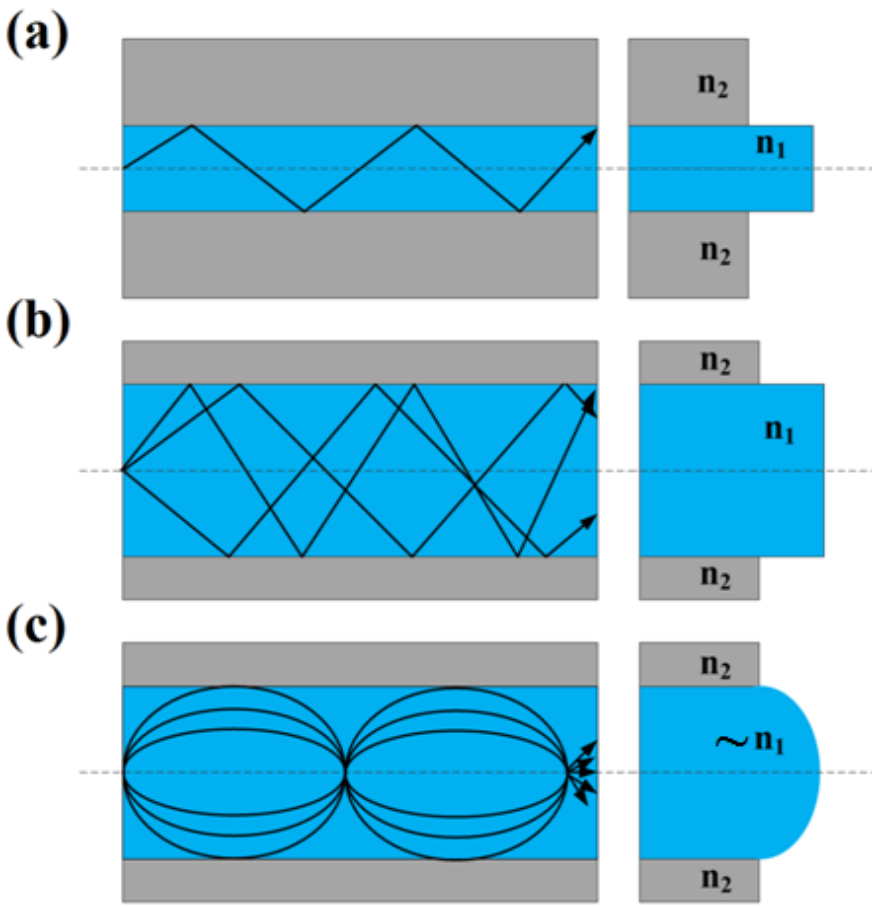

Fig. 2.8. (a) Singlemode step-index fibre; (b) Multimode step-index fibre; (c) Multimode graded-index fibre (~n_1 - variable refractive index of the core due to different dopants used).

Singlemode solid core fibres are capable of delivering a high quality laser beam which is required for precision micro-machining, however their energy handling capability is significantly limited due to their low damage threshold resulting in end-face damage, and transmission of ultrashort pulses is not possible within these fibres due to nonlinear processes originating from light-glass interaction (see section 2.3 for further details). These fibres have shown the capacity to deliver singlemode 1064 nm laser radiation with a single pulse duration of 0.125 ms and a peak power of 250 W [21]. Furthermore, the energy handling capability of singlemode fibres in the nanosecond pulse regime at 532 nm is limited to approximately 5 μJ [22] which makes them unsuitable for manufacturing applications.

Multimode (LMA, see Fig. 2.9) fibres, due to larger core sizes, and therefore a reduced intensity inside the core can withstand much higher pulse energies. Mullett et al. reported delivery of 15 ns pulses with energies of 65 mJ through a step-index LMA fibre (600 μm core, see Fig. 2.9) at 1064 nm without damaging the fibre [23]. A successful transmission of ns pulses with energies of 35 mJ at 532 nm through a multimode silica fibre (1000 μm core diameter) was reported in [24]. In both cases, the fibres provided poor beam quality with an M^2 of approximately 20. Therefore, these types of fibres are typically used in manufacturing applications were the beam quality is not a critical requirement e.g. in welding. Commercially available fibre-based ns laser systems for micro-machining offer maximum pulse energies not exceeding 1 mJ (with $M^2 \sim 1.2$) [25]. Furthermore, efficient transmission of ultrashort laser pulses through LMA fibres has not been reported, even though they reduce the negative influence of nonlinear effects on the propagating light and have significantly higher damage thresholds in comparison with singlemode fibres.

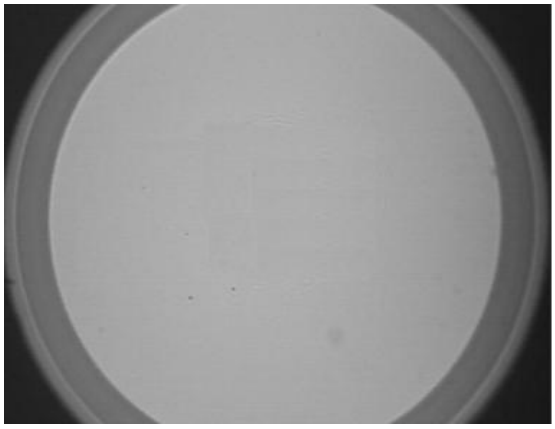

Fig. 2.9. Microscope image of a solid core silica LMA fibre [26].

2.2.2 Microstructured Optical Fibres (MOF)

2.2.2.1 Bragg fibres

Bragg fibres consist of a low refractive index core (either solid or air) surrounded by a specifically designed alternating cladding of high and low refractive index layers which form an array of Bragg mirrors (a 1-D photonic structure) as presented in Fig. 2.10 [27]. The light guidance mechanism in this structure is realised via the Bragg reflection principle. This occurs when the Bragg condition (see ref. [28] for further details) is satisfied, i.e. when the light which is Fresnel reflected from the alternating cladding layers interferes constructively. It is strongest when the interfering wavelengths are in phase [29]. The wavelengths of light which are supported by the fibre depend on the number of layers forming the structure, their dimensions and the refractive index contrast between them. For example, a silica Bragg fibre for guidance at 1064 nm consists of a 26 μm diameter core and a three-layer cladding with the thicknesses of 4 μm to 6 μm and a refractive index contrast of 0.03 (see Fig. 2.10(a)) [30].

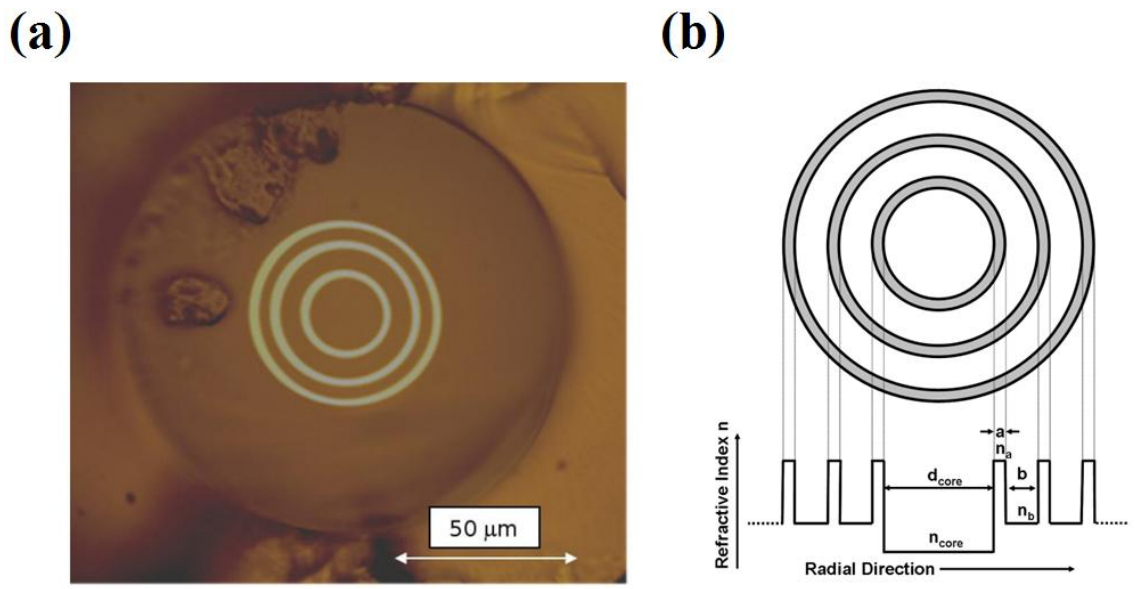

Fig. 2.10. (a) Cross-section of a Bragg fibre for guidance at 1064 nm [30]; (b) Refractive index profile in a Bragg fibre [33]. a and b corresponds to the thickness of the high refractive index and low refractive index layers respectively.

Studies conducted with Bragg fibres have shown that these fibres provide reduction in bending losses (significant sensitivity to bending for bend radii ≤ 4 cm and ≤ 2.5 cm in solid and air core Bragg fibre respectively) in comparison with conventional step-index solid core fibres with similar physical dimensions and are characterised by very low attenuation, down to 10 dB/km at 1064 nm [30-32].

Energy handling capability tests performed with Bragg fibres in the nanosecond pulse regime at 1064 nm have confirmed that these fibres can successfully withstand 9 ns pulses (10 Hz rep. rate) with energies of up to 0.9 mJ (energy density of 130 Jcm^{-2}) and 0.7 mJ (energy density of 780 Jcm^{-2}) for a fibre with an air (72 μm dia.) and solid (26 μm dia.) core respectively [32]. Furthermore, Jelinek et al. reported in [30] delivery of 20 ps pulses (10 Hz rep. rate) with energies of 15 μJ (1064 nm, an energy density of 2 Jcm^{-2}) through a solid core Bragg fibre (26 μm core dia.). The fibre was not damaged, although Stimulated Raman Scattering (SRS) was observed [30]. Experiments performed in the femtosecond pulse range indicated that transmission of 120 fs laser pulses with a peak power of 82 kW (1067 nm, 1 kHz rep. rate, 625 Jcm^{-2} energy density) induced a strong nonlinear response in a Bragg fibre with a 11 μm solid core resulting in spectral broadening [34].

2.2.2.2 Solid core Photonic Crystal Fibres (PCFs)

Solid core Photonic Crystal Fibres (PCFs) can be classified into two types in regard to the light guidance mechanism (depending on the structure): index-guiding and photonic bandgap (PBG) fibres. A PCF consists of a periodic lattice formed by a number of capillaries (in the case of index-guiding fibres these are usually filled with air) typically shaped in a hexagonal pattern and surrounded by silica glass as illustrated in Fig. 2.11(a). The core of a PCF is realised by introducing a "defect" in the periodic lattice in which light is allowed to propagate with low loss (the refractive index profile in an index-guiding PCF structure is shown in Fig. 2.11(b)) by omitting one or several capillaries. The main parameters of a PCF which define its transmission (guided wavelength) are the air hole (capillary) diameter - d, and the distance between the adjacent holes - Λ (interhole spacing or pitch). The ratio of d/Λ is considered as an air-filling fraction of the fibre structure and can reach up to 90% [35]. A PCF's properties can be easily altered by a modification of these parameters which results in changes of the propagation constant of the guided mode [35].

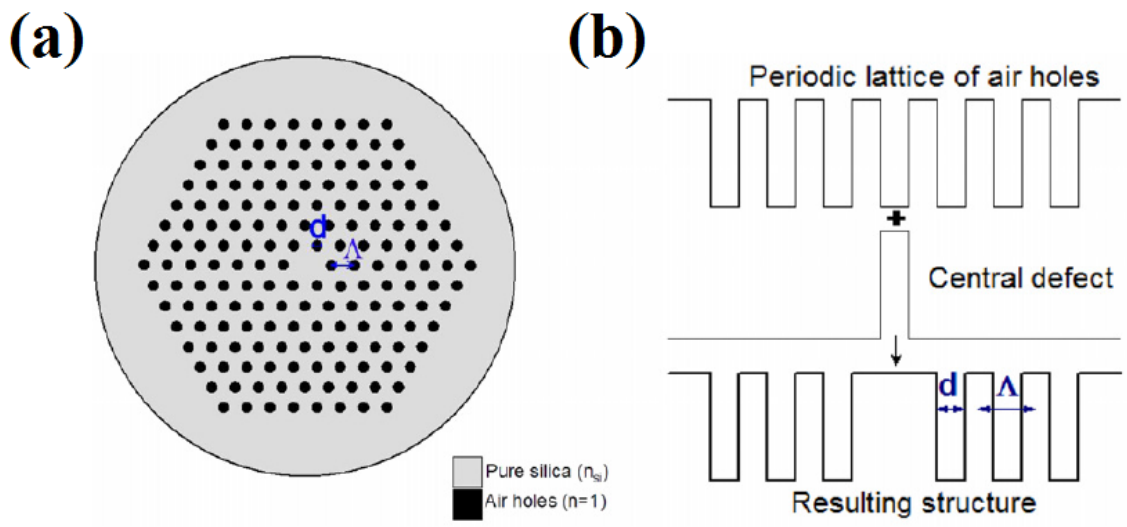

Fig. 2.11. Solid core index- guiding PCF with air filled capillaries: (a) schematic of a hexagonal structure; (b) refractive index profile [35]. d - diameter of a capillary (air hole), Λ - pitch.

Index-guiding PCFs transmit light via the so called modified TIR effect. Since the "defect" is typically formed from the same material as the fill of the fibre it's refractive index is higher than the index of the periodic lattice of air-filled capillaries, which is analogous to the structure of a conventional solid core fibre, hence the V number can be described by the following formula [36]

$$V = k\Lambda\sqrt{n_1^2 - n_2^2} \tag{2-3}$$

where, k is the wavevector, Λ is the pitch, n_1 and n_2 are the refractive index of the core and cladding respectively. The lattice of air holes can be treated as a modal filter in which light is evanescent [35,36]. The guided mode of the fibre is trapped in the "defect" as its mode field diameter (MFD) corresponds to 2Λ, and therefore it cannot leak away to the cladding [35]. Higher order modes, having a smaller MFD in comparison to the fundamental experience leakage to the cladding and strong attenuation. The number of higher order modes evanescent in the cladding increases with an increase in d/Λ ratio [35]. With $d/\Lambda < 0.43$ the fibre cannot support higher order modes, and therefore can be considered as endlessly single mode [37,38]. Modal filtering in a solid core PCF is shown in Fig. 2.12.

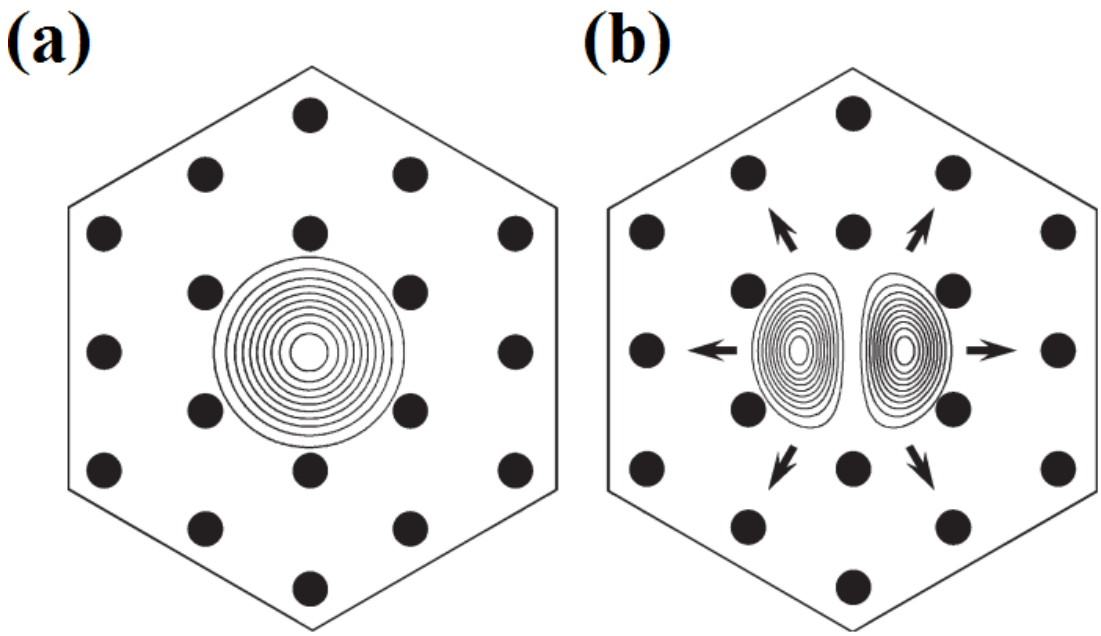

Fig. 2.12. Modal filtering in a solid core PCF (cited from ref. [34]): (a) Fundamental mode is trapped; (b) Higher order modes leak away through the gaps between the air holes [37].

The first fabricated solid core silica index-guiding PCF reported in [39] consisted of a photonic lattice formed by 0.3 μm diameter air holes with a 2.3 μm pitch and a 4.6 μm diameter core as presented in Fig. 2.13.

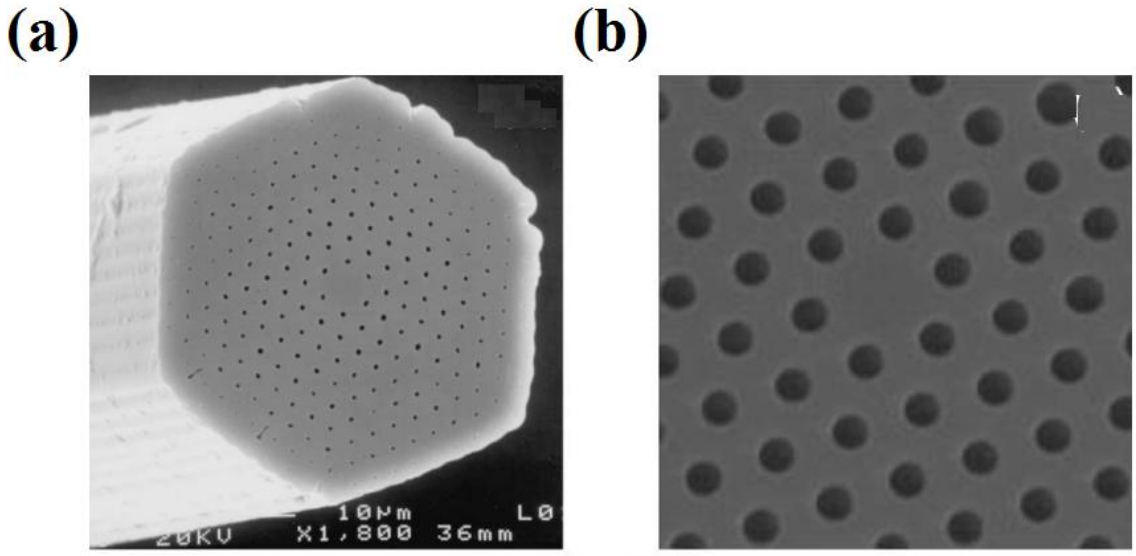

Fig. 2.13. First fabricated solid core (index-guiding) silica PCF: (a) cross-section; (b) photonic lattice [37].

The structure of PCFs guiding via the photonic bandgap (PBG fibres, see Fig. 2.14(a)) principle is entirely different in comparison with index-guiding fibres. Here, the fibre core has a refractive index lower than the refractive index of the cladding, and

therefore light cannot propagate via modified TIR. A low-index core is usually formed by an air (hollow) "defect" in the photonic lattice (discussed further in subsection 2.2.2.3), however it can also be solid e.g. in a fibre consisting of a pure silica core which is surrounded by a periodic lattice of germanium-doped silica rods [40,41]. The guidance behaviour of all-solid PBG fibres can be explained by the means of 1-D ARROW (Anti-Resonant Reflecting Optical Waveguide) structure. Certain wavelengths (frequencies) of light are antiresonant to the cladding structure and are confined within the core propagating with low-loss [37,42]. Guidance of light occurs for wavelength ranges (low-loss transmission bands) which are strictly defined by the position of high-loss frequency windows where the cladding becomes resonant with the guided mode (more detailed discussion of the ARROW mechanism can be found in subsection 2.2.2.4) [37]. Low-loss transmission windows in a PBG PCF cover up to a few hundred nanometres as shown in Fig. 2.14(b). Attenuation of these fibres at 1 μm reaches the level of a few dB/km (dependant on the fibre) [43].

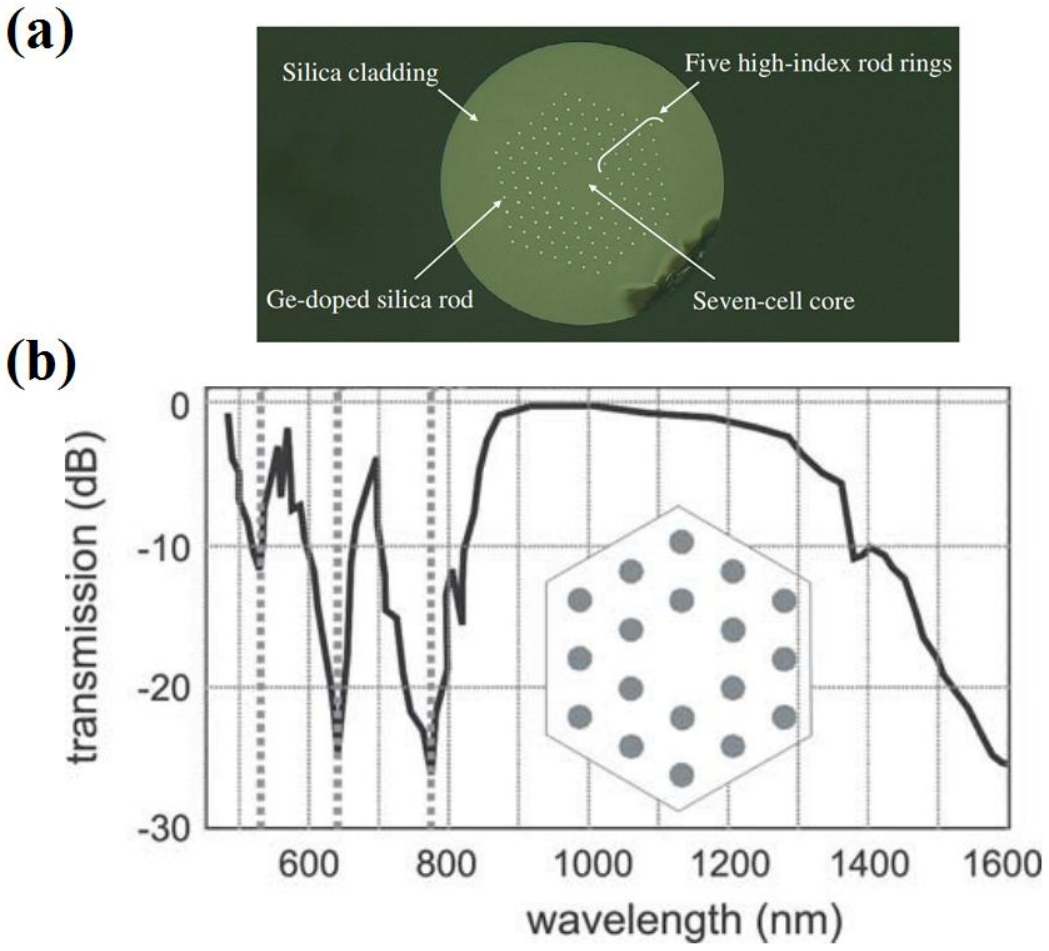

Fig. 2.14. (a) Cross-section of an all-solid photonic bandgap PCF [44]; (b) Example of a transmission spectrum of an all-solid PBG PCF [37].

Photonic Crystal Fibres offer significantly better performance in terms of high energy pulse delivery in the singlemode regime in comparison with conventional solid core fibres. Singlemode operation in a PCF is determined by the fibre geometry i.e. d/Λ value, which makes it independent of the core size, and therefore LMA singlemode PCFs can be fabricated [37]. This is not possible in conventional step-index fibres as these have a significant limit on both the core size and numerical aperture for singlemode guidance. For any wavelength and core diameter there is a maximum NA which allows singlemode operation (as can be seen from equation 2-4) [45]. For instance, a LMA singlemode PCF for guidance at 458 nm can have a core diameter of 22 μm, which is approximately an order of magnitude greater than the maximum core size of a step-index SMF for the same wavelength range [43,46]. A larger core diameter results in lower energy density in the fibre which leads to higher damage threshold of the fibre as well as reducing nonlinear effects e.g. Raman and Brillouin effects or self-focusing. Nevertheless, the laser beam is still transmitted in a solid core, and therefore these fibres are also limited in terms of high energy pulse delivery. All-solid LMA bandgap PCFs are capable of delivering nanosecond pulses (65 ns) at 1064 nm with a pulse energy not exceeding 0.334 mJ and peak power of 9.3 kW [47]. The experiments performed by Petersen et al. in [48] have indicated that a transmission of 40 ps laser pulses (1064 nm) through a solid core LMA PCF (25 μm core diameter) becomes dominated by Raman scattering for peak powers above 35 kW.

2.2.2.3 Hollow-Core Bandgap Photonic Crystal Fibres (HC-PCFs)

The main idea of guiding light via a photonic bandgap mechanism within an air (hollow) core is to reduce transmission losses present in solid core fibres arising from material scattering and absorption issues along with increasing the threshold for damage and nonlinear effects. Since light is confined in air and the TIR effect does not exist, a low loss propagation can occur only in the strictly defined frequency (wavelengths) regimes of the photonic bandgap. These bandgaps exist for a propagation constant $\beta < k$ (k is the vacuum wavevector), and therefore can be used to trap the light in a "cage" formed by an air core via coherent Bragg scattering (see Fig. 2.15) [35,49]. Furthermore, the range of $k > \beta$ for which a bandgap is obtainable is limited, hence low loss guidance can be observed only over a limited wavelength bandwidth [49]. To fulfill these conditions a high air-filling fraction and small interhole spacing is required [37]. If the air-filling fraction is at the level of $\leq 90\%$ the fibre structure exhibits several narrow bandgaps, from which one located at higher frequencies tend to gradually

disappear with an increase of d/Λ [50]. Moreover, the bandwidth of an existing bandgap can be broadened by an increase of d/Λ e.g. an increase from 94% to 96% doubles the bandwidth [50]. The number of (N) supported modes by the hollow core can be approximated by the following equation [37]

$$N \approx \frac{k^2 \rho^2 \left(n_{high}^2 - n_{low}^2\right)}{2} \tag{2-5}$$

where k is the vacuum wavevector, ρ is the core radius, n_{high} and n_{low} define the refractive indexes at the edges of the bandgap at fixed frequency [37]. Therefore, the existence of a guided mode requires a sufficiently large hollow core [37].

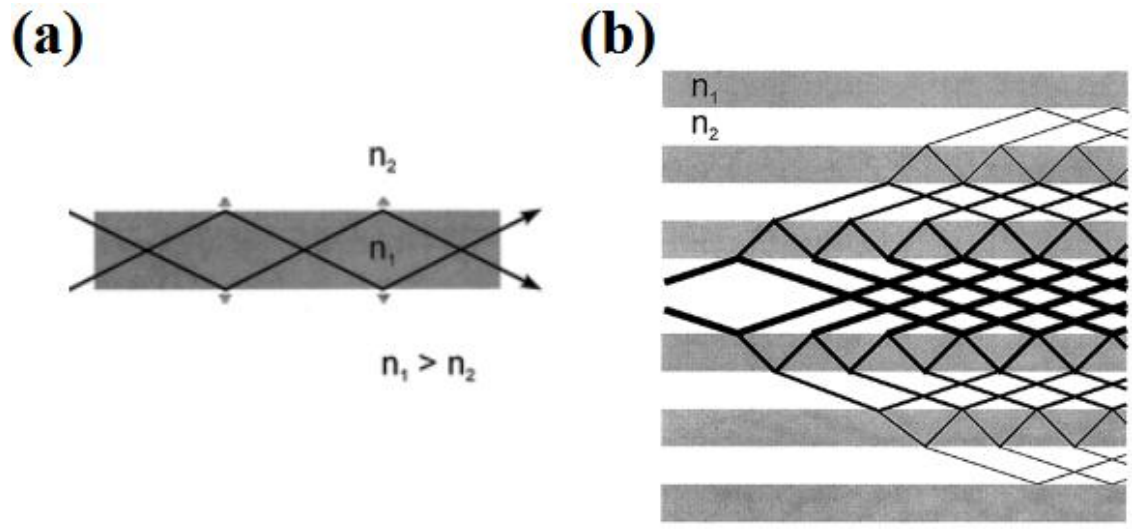

Fig. 2.15. Comparison of guidance mechanisms: (a) conventional TIR guidance; (b) Photonic bandgap guidance via Bragg effect present in HC-PCFs [51].

The first air-core fibre (see Fig. 2.16(a)), the so called Hollow-Core Photonic Crystal Fibre (HC-PCF) was demonstrated by Cregan et al. in 1999 [51]. The hollow air core, with a diameter of 14.8 μm, was formed by removing 7 capillaries (the fibre core can be obtained also by omitting more i.e. 19 capillaries [52]) from the photonic lattice as shown in Fig. 2.16 (b). The pitch was set to 4.9 μm and the air-filling fraction in the cladding was 39%. The experiments performed with a white light source and 40 mm long HC-PCF have shown the presence of three narrow low loss transmission windows in the vicinity of 850 nm, 610 nm and 490 nm as illustrated in Fig. 2.16(c).

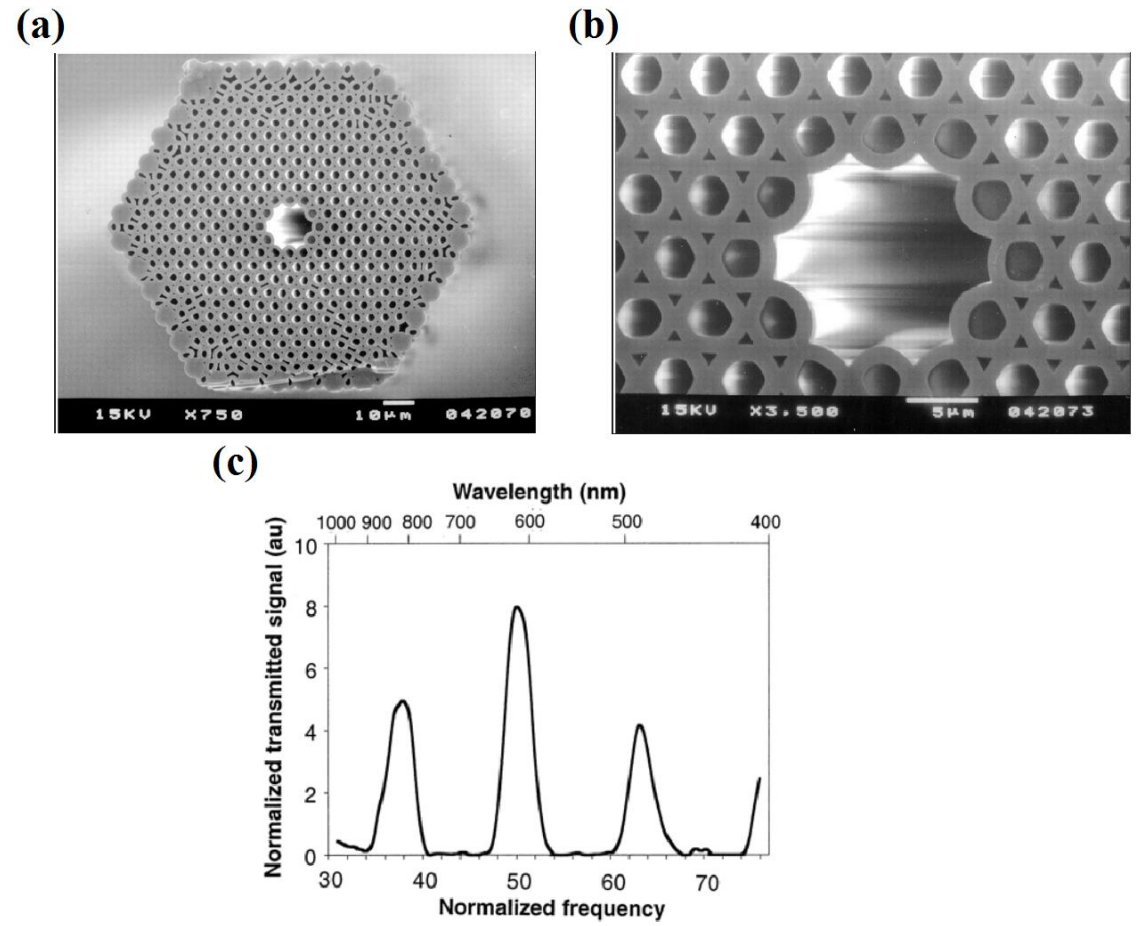

2.16. First fabricated HC-PCF: (a) cross section; (b) hollow air core; (c) Transmission spectrum measured with a white light source plotted against wavelength and normalised frequency kΛ [51].

Efficient transmission of light through the first fabricated fibre was possible only through short fibre lengths as the structure suffered from nonuniformity resulting in fluctuations in the fibre properties and hence loss. Further development of the hollow-core design and optimisation of the fibre drawing process led to a capability to fabricate a HC-PCF with low loss and broadened bandgaps. HC-PCFs for guidance at 1 µm exhibit attenuation at the level of 60 dB/km and 20 dB/km for 7- and 19-cell defect fibres respectively with low loss regions covering ~ 180 nm of the spectral bandwidth [52]. At shorter wavelengths i.e. in the green spectral region these fibres are characterised by higher attenuation of 500 dB/km mainly due to scattering and fabrication issues [53]. Furthermore, HC-PCFs show extremely low sensitivity to bending, which gives a great advantage in terms of flexible beam delivery [37].

As light is propagating in a hollow air core one would expect the HC-PCFs to withstand much higher intensities in comparison with conventional solid core silica fibres and solid core PCFs. Shephard et al. performed energy handling capability tests in the nanosecond pulse regime (65 ns) at 1064 nm with two different types of HC-PCFs:

7- and 19-cell defect fibres (see Figs. 2.17(a) and 2.17(b)) [52,54]. The maximum delivered pulse energy without fibre damage reached 0.38 mJ and 0.53 mJ for 7- and 19-cell fibres accordingly [52]. The delivered energy through a 7-cell fibre was approximately 25 times greater than what can be transmitted through a conventional solid core fibre with a similar core diameter [52,55]. Furthermore, the experiments were also conducted at 532 nm (with the same pulse width) with the 19-cell fibre. In this case, the fibre suffered damage for pulse energies exceeding 0.15 mJ [56]. Konorov et al. reported in [57] a 7-cell HC-PCF exhibiting a damage threshold of 1 mJ for 40 ps laser pulses (rep. rate in the microsecond range) at 1064 nm, which is an order of magnitude higher than the critical value for fused silica. These fibres have also shown a capacity to deliver ultrashort (femtosecond) laser pulses with relatively high pulse energy [53,58,59]. A 5 m long HC-PCF designed to operate at 800 nm was reported to deliver 300 fs pulses with energies of 120 nJ [58]. In 2008 Hensley et al. demonstrated efficient transmission of femtosecond pulses with energies of approximately 1.5 μJ at 790 nm with a similar fibre [58]. Experiments performed in the visible spectral region demonstrated HC-PCF (see Fig. 2.17(d)) for transmission of green (540 nm) femtosecond pulses with a duration and an average power of approximately 100 fs and 500 mW respectively [60].

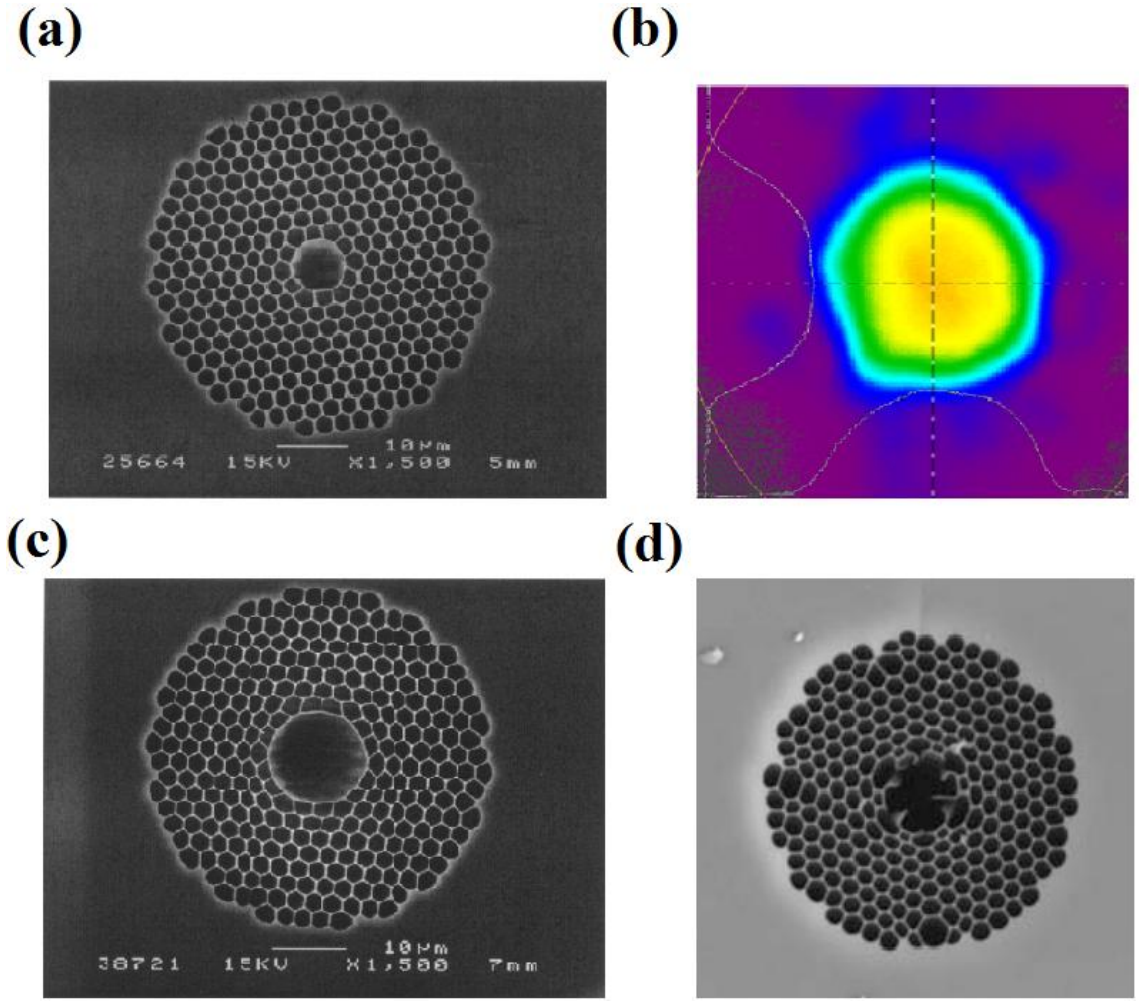

Fig. 2.17. (a) 7-cell HC-PCF for 1064 nm [52]; (b) Near-field delivered beam profile through 7-cell HC-PCF at 1064 nm [54]; (c) 19-cell HC-PCF for 1064 nm [52]; (d) HC-PCF for guidance at 540 nm [60].

2.2.2.4 ARROW-guiding HC-PCFs

Light guidance mechanism of HC-PCFs which do not use the photonic bandgap effect can be described by the means of the 2-D Anti-Resonant Reflecting Optical Waveguiding mechanism [61]. An example of an ARROW structure and its transmission spectrum is shown in Fig. 2.18. The structure consists of a low refractive index core surrounded by a cladding formed by high- and low-index layers. According to this model, each layer can be considered as a Fabry-Perot (F-P) resonant cavity [61]. Therefore all wavelengths of light which do not match a resonant wavelength of the Fabry-Perot resonator are reflected back into the core and propagate with low loss as a result of destructive interference in the F-P cavity. The resonance wavelengths, meanwhile, cannot be confined in the core and leak away to the cladding region where they are highly attenuated. The anti-resonant wavelength is characterised by the following formula [62]

$$\lambda_{anti-res} = \frac{4d}{(2m+1)}\sqrt{n_2^2 - n_1^2},\ m = 0,1,2,\ldots \quad (2\text{-}6)$$

where d is the thickness of the first (high-index) cladding layer, n_1 and n_2 are the refractive indexes of the core and cladding respectively. The resonant wavelength, therefore are defined as [63]

$$\lambda_{res} \sim \frac{2d}{m}\sqrt{n_2^2 - n_1^2},\ m = 0,1,2,\ldots \quad (2\text{-}7)$$

As can be noted from the above equations the position of low loss transmission windows depends mainly on the thickness of the cladding layer (core wall thickness).

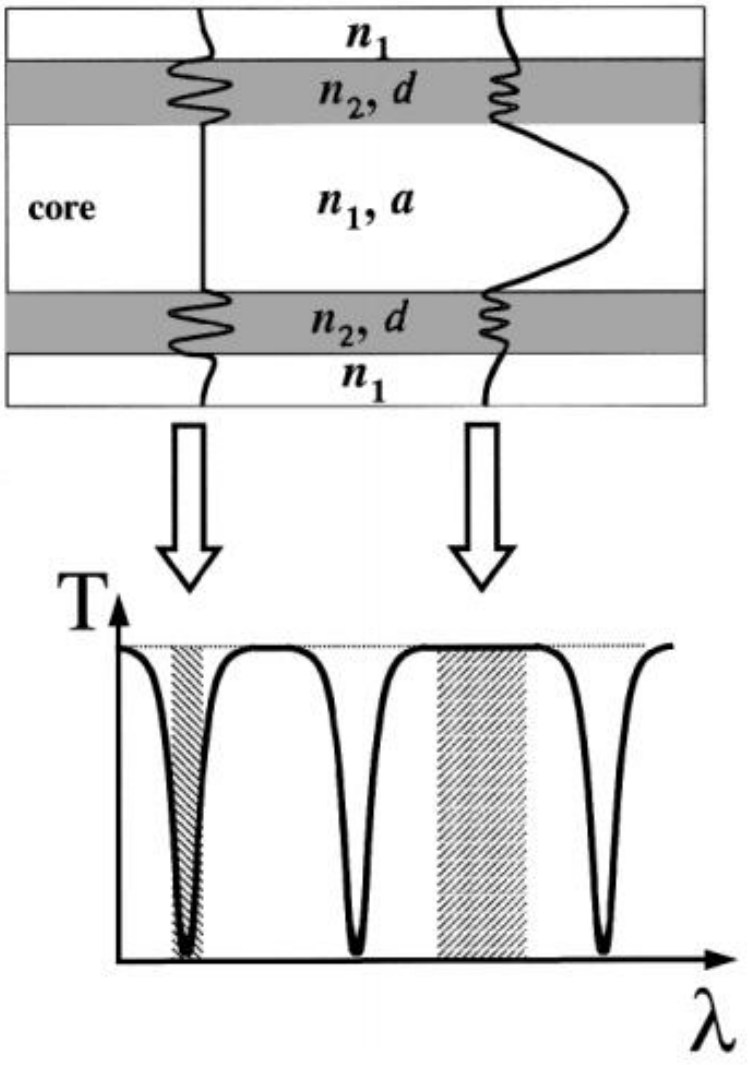

Fig. 2.18. Example of ARROW structure (top) and corresponding transmission spectrum (bottom) [61]. Spectral windows with the maximum transmission correspond to anti-resonant wavelengths, while minima represent wavelengths matching the resonant wavelengths of the Fabry-Perot cavity. n_1 is the refractive index of the core and low-index cladding layer, n_2 is the refractive index of the high-index cladding layer, a is the core diameter and d defines the thickness of the high-index layer.

HC-PCFs guiding via the ARROW principle have been a subject of extensive researches over the last couple of years, which have resulted in fabrication of various structures of these fibres covering the optical spectrum from the UV to 10.6 μm wavelength range [63-71]. These fibres are discussed in more details in the following subsections.

2.2.2.4.1 Negative Curvature Fibre (NCF)

The influence of curvature in the core wall of an anti-resonant guiding HC-PCF on transmission properties was firstly investigated by Weng et al. in [72]. The experiments have shown that by introducing negative curvature in the core boundary (hypocycloid shape) in a Kagome fibre (see subsection 2.2.2.5 for further information about these fibres) the fibre loss can be significantly reduced [72,73].

An alternative approach to Kagome fibres a hollow-core Negative Curvature Fibre (NCF) was fabricated and reported for the first time by Pryamikov et al. in 2011 (see Fig. 2.19(a)) [74]. The fibre consisted of only one cladding layer (single ring, all silica) formed by 8 circular capillaries and exhibited low loss transmission windows in the mid-infrared (MID-IR) spectral range as shown in Fig. 2.19(b).

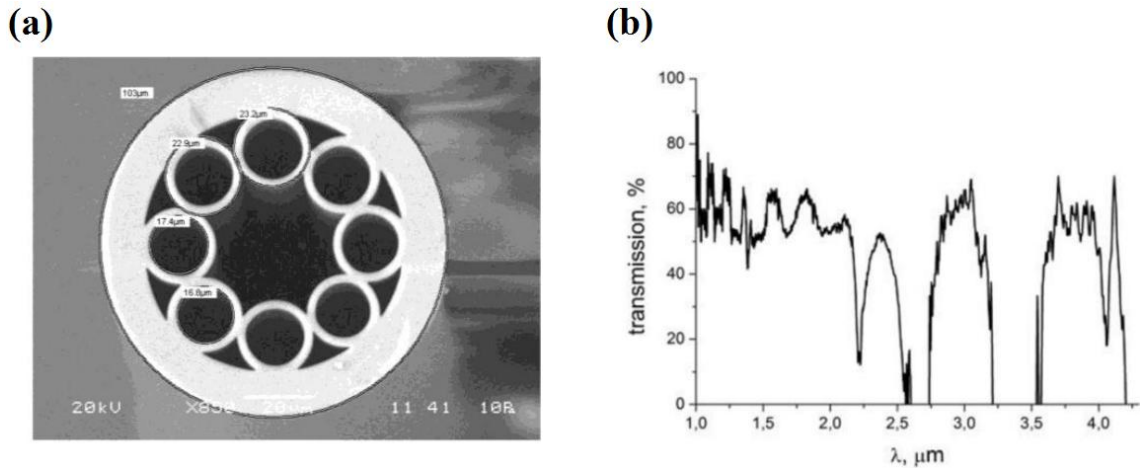

Fig. 2.19. First fabricated NCF: (a) cross-section; (b) measured transmission spectrum [74].

Further development and optimisation of the NCFs for guidance in the MID-IR carried out particularly by the research groups at the University of Bath and Heriot-Watt University allowing a fibre to be fabricated (see Fig. 2.20) with extremely low attenuation, 34 dB/km at 3050 nm, capable of delivering high energy Er:YAG laser radiation (2.94 μm) for medical applications (see ref. [63] and [75] for further details). The cladding also consisted of a single ring of 8 capillaries, however shaped into an ice

cream cone like shape. The most crucial points of the NCF fibre structure are the so called cladding nodes, which represent the meeting points between the adjacent capillaries forming the cladding. These introduce high loss (marked with red circles in Fig. 2.20). These nodes behave as independent waveguides supporting their own lossy modes. Therefore, the curvature of the core boundary (core wall) is directed in the opposite direction (in comparison with a typical cylindrical core such as in the HC-PCF structure) in order to physically separate the fibre guided mode from the cladding nodes, significantly reducing coupling between them.

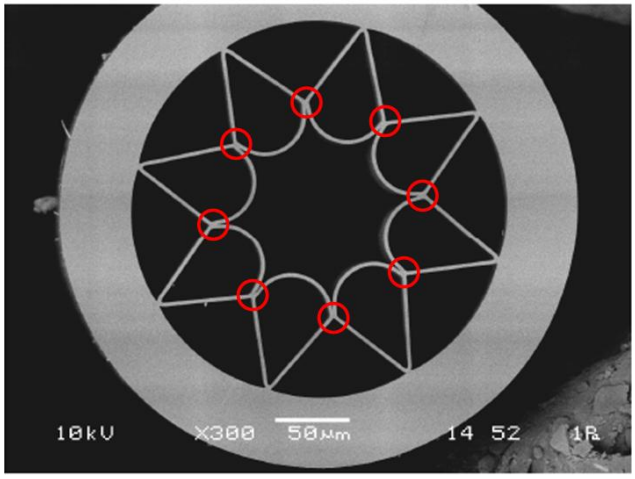

Fig. 2.20. SEM image of low loss NCF for guidance in the MID-IR. Red circles show the cladding nodes [63].

The results obtained with MID-IR NCFs indicated the excellent energy handling capacity of these fibres, and therefore their operation range was extended towards shorter wavelength ranges (1 µm and green); more desirable from the micro-machining point of view. The first NCF designed to operate at 1 µm wavelength (see Fig. 2.21(a)) was fabricated by Dr. Fei Yu at the University of Bath in 2012 and its properties were characterised by myself and reported in [65] (the NCFs are discussed in more detail in chapters 3 and 4 of this thesis). The fibre had a 43 µm diameter hollow core (approximately 4 times larger in comparison with standard HC-PCFs for the same wavelength), which enabled the delivery of 6 ps pulses with energies of 92 µJ corresponding to a peak power density of the delivered beam of 1.5 $TWcm^{-2}$, which is not possible to achieve with conventional step-index fibres and HC-PCFs and comparable with the capabilities of hypocycloid Kagome fibres [76]. Furthermore, the fibre provided efficient delivery of nanosecond and femtosecond pulses with energies at the level required for various precision micro-machining applications [65,77]. However, due to un-optimised structure the fibre suffered from few-moded behaviour resulting in

significant sensitivity to bending, pulse broadening (ps and fs) and also relatively high attenuation of 160 dB/km at 1064 nm. The latest NCF for 1 μm (however, not yet reported) also fabricated by Dr. Fei Yu at the University of Bath has a minimum attenuation of 4 dB/km at 1030 nm and a lower sensitivity to bending. Moreover, it has been demonstrated to have the capacity to deliver singlemode picosecond laser pulses (maintaining spectral and temporal properties of the laser pulse) with energies of approximately 75 μJ and nanosecond radiation with the same power as delivered through the previous fibre (see chapter 4 for further details). In 2014 the NCF structure was scaled down to operate in the visible - green spectral region. The first green-guiding NCF was reported in [78] (also fabricated by Dr. Fei Yu and characterised by myself). The fibre had an attenuation of 210 dB/km at 532 nm (more than two times lower than for a HC-PCF) and allowed nanosecond and picosecond pulses with peak powers at the level of 10 kW and 4.7 MW respectively to be delivered, although the issue with output stability was still observed. Shortly after that, another green NCF was drawn (presented in Fig. 2.21(b)) and shown to provide better performance in comparison with the initial version [71]. Attenuation was reduced to 150 dB/km at 532 nm (almost an order of magnitude lower in comparison with commercially available HC-PCFs [79]) and bending loss together with output stability were significantly improved. Moreover, maximum delivered pulse energies in the nanosecond and picosecond pulse regimes were increased. The delivered average power of ps pulses (12 W) is the highest reported value in the green spectral and ultrashort pulse regimes. Spectral and temporal properties of the original laser pulse were well preserved even after propagation through a few meters length of this fibre, which indicates its low dispersion.

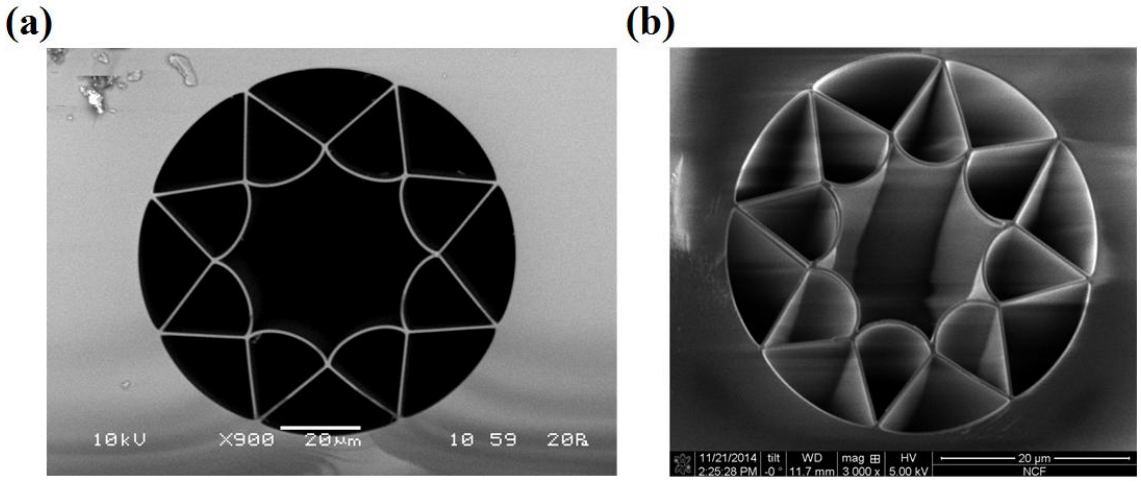

Fig. 2.21. Examples of NCF fibres for guidance in: (a) 1 μm spectral range [64]; (b) green spectral bandwidth [71].

NCFs operating in the 1 μm and green spectral regions were the main subject of the work discussed within this thesis, and therefore more detailed characterisation of their spectral and temporal properties as well as energy handling capability can be found in chapters 3 and 4.

2.2.2.4.2 Free Boundary and Nodeless Anti-Resonant Fibres (FBARF and HC-NANF)

As it was mentioned in the previous subsection the touching points between the capillaries forming the cladding of anti-resonant fibres act as additional waveguides causing an increase in optical loss in the transmission windows (see Fig. 2.22(a)). To address this issue Kolyadin et al. proposed in [80] a modified structure of NCF fibre in which the cladding nodes were removed as shown in Fig. 2.22(b). Numerical simulations have shown that the absence of the cladding nodes leads to a significant reduction in the loss of the fundamental mode as plotted in Fig. 2.22(c). Furthermore, Belardi and Knight reported in [81] that the lack of touching points in the cladding results in low bending loss of an anti-resonant fibre (the fabricated fibre was called Free Boundary Anti-Resonant Fibre and guided in the MID-IR).

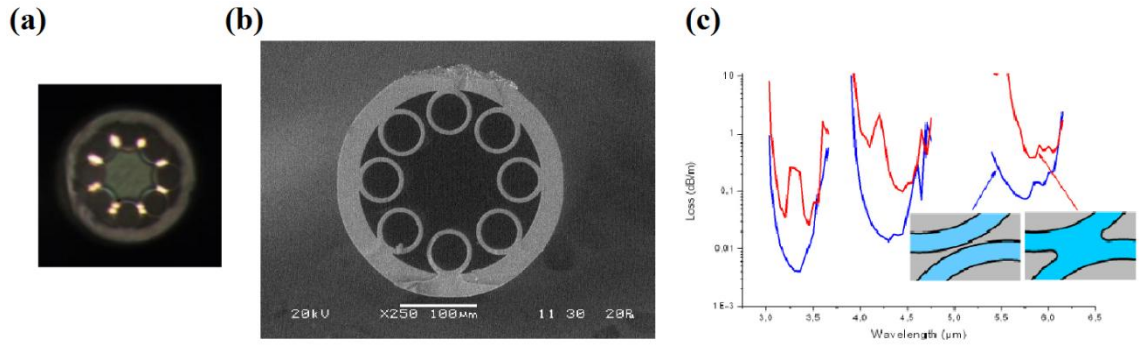

Fig. 2.22. (a) Output end-facet of a NCF fibre with touch capillaries excited with a white light source. Strong guidance in the cladding nodes can be observed [80]; (b) SEM image of the first reported NCF with non-touching capillaries for guidance in the MID-IR [80]; (c) Calculated loss for the fundamental mode of a NCF with touching (red line) and non-touching (blue line) capillaries [80].

Based on the promising results in the MID-IR a Free Boundary Anti-Resonant Fibre (FBARF acronym will be used in the thesis while discussing these fibres) for transmission in the green spectral region was designed and fabricated by Dr. Walter Belardi and characterised within the work discussed in this thesis (see chapters 3 and 4). The fibre being a preliminary design does not provide a performance comparable with other anti-resonant fibres. It exhibits very high loss in the range of 1200 dB/km at 532

nm, delivers few-moded and unstable output and its power handling capabilities are worse than reported with NCF fibres (more details can be found in chapters 3 and 4).

In 2014 Poletti proposed a further modification of a free boundary fibre (however, based on the work reported by Belardi and Knight in [82]), the so called Nested Antiresonant Nodeless Hollow Core fibre (HC-NANF) consisting of an additional set of capillaries (second anti-resonant layer) nested inside the first cladding layer as shown in Fig. 2.23(a) [69]. The additional anti-resonant structure allows lower confinement loss and bending sensitivity to be obtained [69,82]. The first fabricated FBARF with second cladding layer was reported by Belardi in [70] and is presented in Fig. 2.23(b). The transmission measurements performed with a broadband light source have indicated a presence of several low loss transmission windows from the visible to NIR with the lowest loss of 175 dB/km at 480 nm [70]. Further characterisation of this particular fibre with coherent light sources at 1030 nm and 1064 nm (conducted by myself) has shown significantly higher loss at these wavelengths in comparison with NCF fibres and confirmed the few-moded guidance. Furthermore, the fibre did not enable efficient delivery of ns and ps laser pulses. For more details please see chapters 3 and 4 of this thesis.

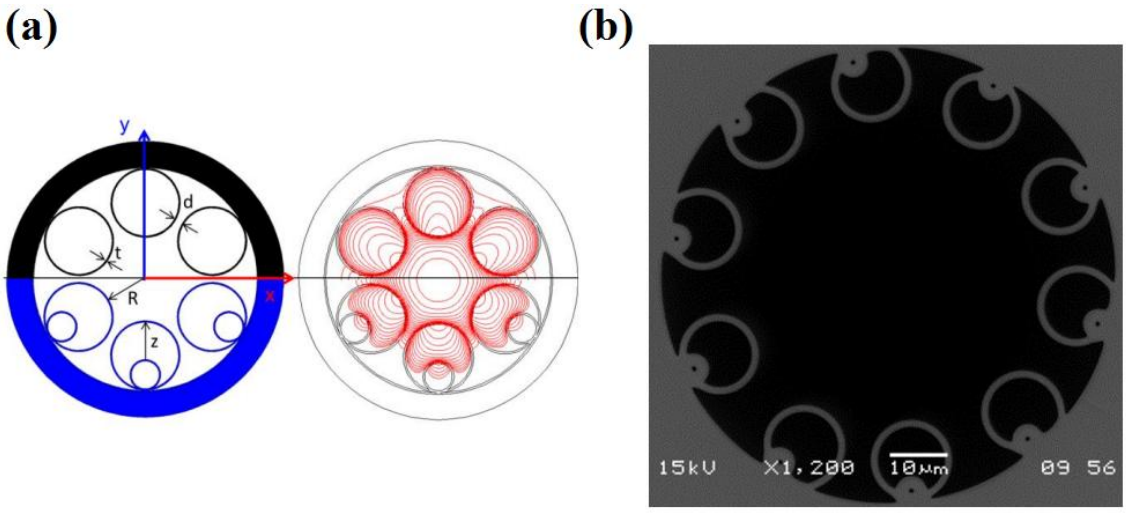

Fig. 2.23. (a) Comparison of free boundary fibres without (black) and with additional anti-resonant structure (blue) and corresponding light confinement (left) [69]; (b) Fabricated FBARF for guidance in the NIR [70].

2.2.2.4.3 Other ARROW-guiding HC-PCFs

Poletti et al. reported in [68] a simplified design of an ARROW-guiding fibre consisting of a single cladding layer formed by six capillaries arranged in a Star of David or

hexagram like shape and a hollow core with a diameter of ~ 50 µm as shown in Fig. 2.24(a). The fibre has a low loss transmission window covering approximately 200 nm of the NIR spectral region with average loss of 0.2 dB/m and provides singlemode output as plotted in Fig. 2.24(b) [68]. However, the fibre was shown to support higher order modes when the coupling conditions were not perfectly chosen [68]. Furthermore, the fibre is characterised by relatively high sensitivity to bending in the vicinity of 1 µm wavelength as can be seen from Fig. 2.24(c). It was investigated that overall loss of this structure depends mainly on the strut thickness and orientation of the cladding nodes [68].

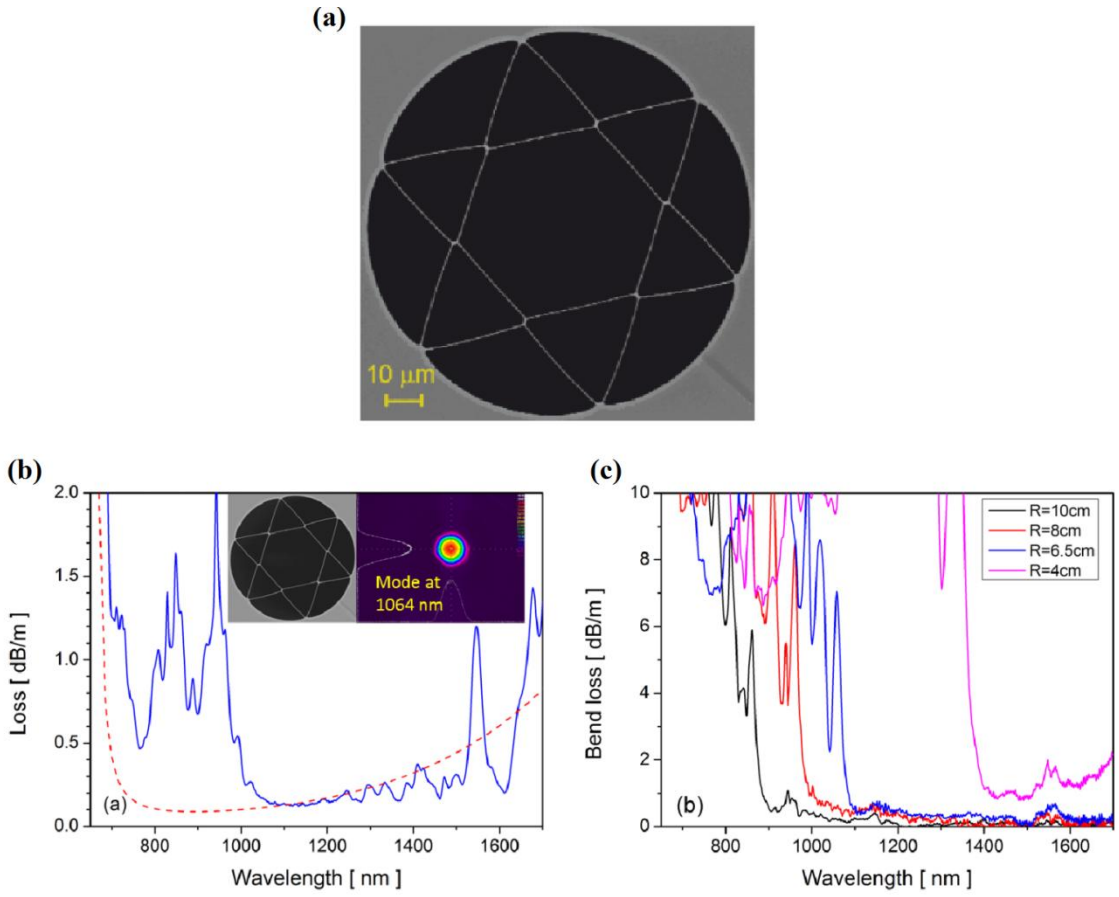

Fig. 2.24. Hexagram antiresonant fibre: (a) SEM image of fibre cross-section; (b) Loss spectrum with mode profile at 1064 nm; (c) Bending loss [68].

Another interesting silica anti-resonant fibre, operating in the UV was recently proposed by Hartung et al. in [64]. The fibre shown in Fig. 2.25(a) has a square-shape hollow core with a diameter of 16.6 µm surrounded by four capillaries with an average strand (core wall) thickness of 560 nm. The fibre exhibits several transmission windows from 1 µm down to deep UV as illustrated in Fig. 2.25(c). The minimum attenuation of the fibre in the ultraviolet spectral range is approximately 200 dB/km at 350 nm. The

loss of this particular fibre structure in the UV spectral range depends mainly on the variation of strand thickness and are not related to the surface scattering (which for solid core silica fibres becomes dominant in this wavelength regime) [64].

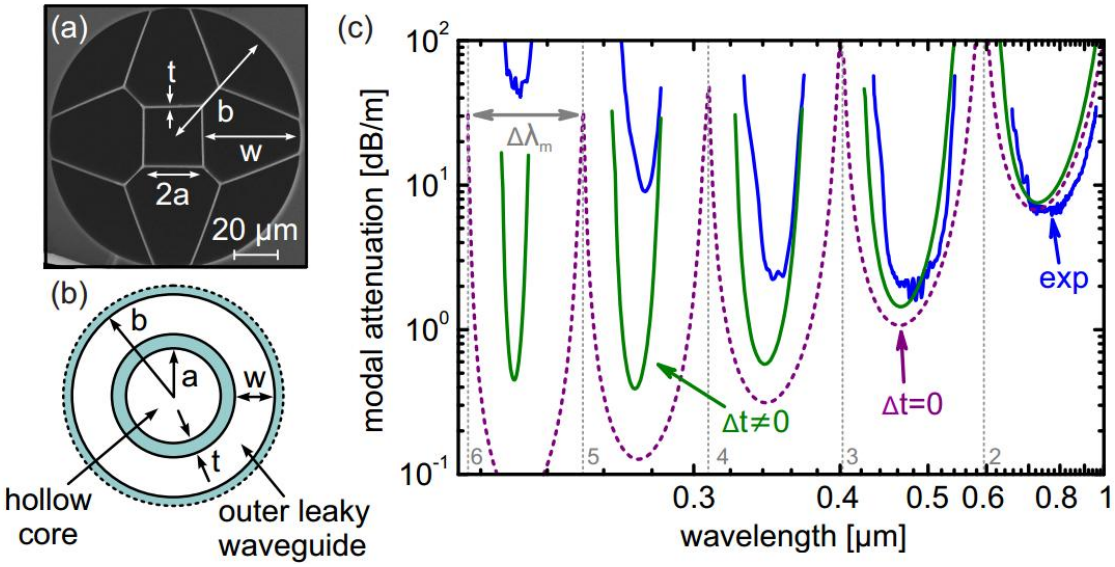

Fig. 2.25. (a) Scanning electron microscope image of the fibre cross section (2a: core extension, t: strand thickness, b: radius of microstructured part, w: extension of outer waveguide). Dark area is air and bright are is silica. (b) Extended ring model (ERM) used for calculations shown in (c) including a high index ring and an infinite high index cladding (white is air, cyan is silica). Dashed line indicates extension to infinity. (c) Measured attenuation of the fundamental mode (blue line) and corresponding calculated leakage loss using the ERM (depicted in (b)) for a single wall thickness t = 560 nm (purple dashed line) and of a thickness variation Δt = 70 nm (solid green line) is included. The grey vertical dotted lines refer to the order of strand resonance. Band are labeled by the respective short-wavelength strand resonance (e.g. the band located with a minimum loss at 230 nm is named 6). Cited from ref. [64].

2.2.2.5 Kagome HC-PCFs

A Kagome HC-PCF was reported for the first time in 2002 by Benabid et al. [83]. The fibre structure (see Fig. 2.26(a)) consisted of a hollow air core surrounded by a cladding formed by silica capillaries arranged in a Star of David shape. The Kagome structure does not exhibit a photonic bandgap effect and light guidance is based on the inhibited coupling principle [84]. The cladding supports only modes which are strongly mismatched in phase with the core modes, hence preventing the guided modes from leaking away from the core [85]. This phenomenon can be observed when the cladding modes exhibit a strong confinement within the Kagome lattice and very fast transverse oscillations, which result in the absence of phase-matched cladding modes to remove light from the fibre core [85]. Kagome HC-PCFs have been shown to guide light over much wider low loss transmission windows (covering up to a few hundred of

nanometers of the optical spectrum) in comparison with conventional hollow-core PCFs as shown in Fig. 2.26(b) [86].

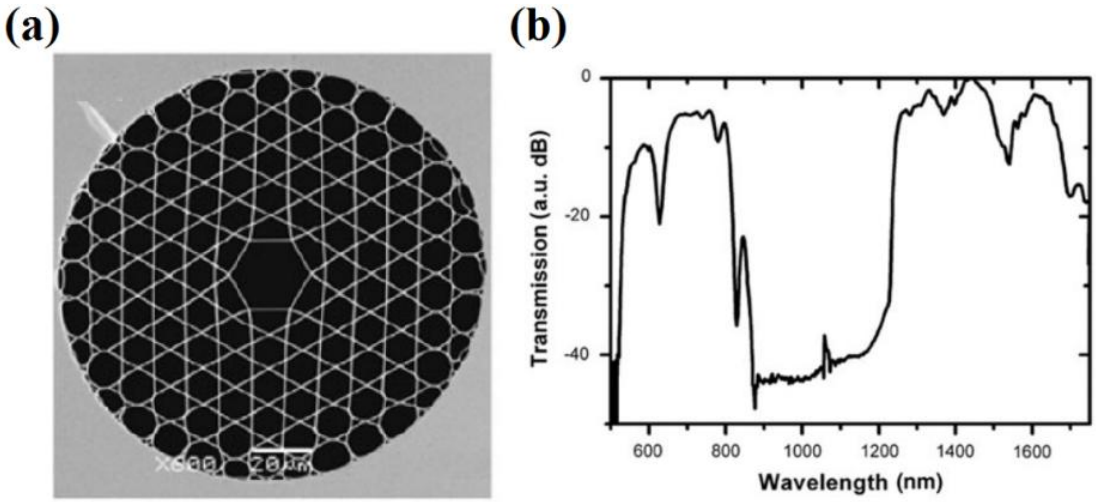

Fig. 2.26. Kagome HC-PCF: (a) SEM image of fibre cross-section; (b) transmission spectrum [86].

Further development and optimisation of the Kagome structure have resulted in introducing the so called hypocycloid shape of the core wall (similar to the negative curvature of the core boundary in NCF fibres) as shown in Fig. 2.27 [72]. The hypocycloid contour of the core boundary provides an enhancement of inhibited coupling by decreasing the overlap between the guided mode and oscillating cladding modes [85]. Furthermore, the inverted curvature of the core wall physically pushes away the cladding nodes (similarly to the NCFs), which results in further reduction of confinement loss [85]. Wang et al. reported in [73] that the hypocycloid shape of the core wall can provide a 1 dB decrease in fibre loss in comparison with an unmodified Kagome structure as plotted in Fig. 2.27. Benabid et al. demonstrated in [87,88] that confinement loss as well as bending loss of these fibres strongly depend on the number of cladding layers (rings) and curvature radius of the core wall and reported a fibre with an attenuation of 17 dB/km at ~ 1064 nm.

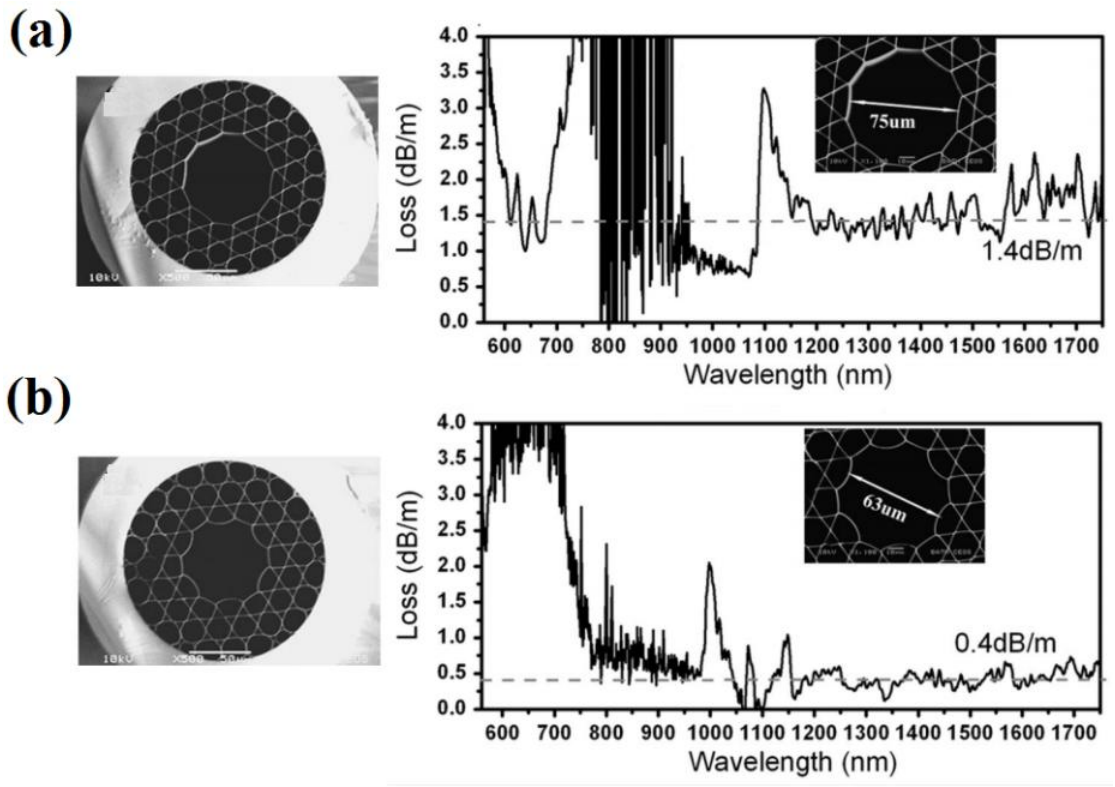

Fig. 2.27. (a) SEM image of Kagome fibre with a circular core (right) and loss spectrum (left); (b) SEM image of hypocycloid Kagome HC-PCF (right) and corresponding loss spectrum (left) [73].

Over the last couple of years hypocycloid Kagome HC-PCF have proven their excellent suitability for the delivery of high energy short and ultrashort pulsed laser light in the 1 μm and green spectral regions. Beaudou et al. demonstrated in [89] efficient transmission of nanosecond pulses (9 ns) at 1064 nm for an Nd:YAG laser system through a hypocycloid fibre with energies of up to 10 mJ. One year later Emaury et al. showed a capacity of these fibres to deliver 10.5 ps pulses with energies of 97 μJ and a peak power two times greater than the critical value for self-focusing in silica [90]. Furthermore hypocycloid Kagome HC-PCFs due to their dispersion properties have been reported in applications aimed for femtosecond pulse compression [90-93]. Guichard et al. reported in [94] efficient compression of 330 fs pulses with energies of 70 μJ to 34 fs with a single pulse energy of 50 μJ through a 1.2 m air filled hypocycloid fibre. In 2014 Debord et al. reported a hypocycloid fibre exhibiting low loss guidance in the green spectral region (lowest loss of 130 dB/km at 532 nm) capable of transmitting 27 ps pulses with an average power of 10 W [95]. Furthermore delivery of CW light (15 mW average power) in the deep UV (280 nm) via a standard Kagome fibre (with ~ 1 dB/m loss in this spectral range) was demonstrated in [96].

2.3 Fibre limitations for high peak power pulse delivery

Transmission of high energy laser pulses in optical fibres can be significantly limited by the presence of nonlinear processes altering spectral and temporal properties of a pulse, the optical damage threshold and scattering issues which become especially dominant towards shorter wavelength range. However, nonlinear effects i.e. Raman and Brillouin scattering strongly depend on the fibre length, and therefore are less of an issue for most beam delivery applications due to short lengths of fibre used (~ 1 m).

2.3.1 Nonlinear effects

2.3.1.1 Self phase modulation (SPM)

Self phase modulation is a nonlinear process which originates from nonlinear modification of the refractive index of a medium. As a result of this effect a laser pulse travelling through a medium experiences a nonlinear phase shift which leads to spectral broadening [97]. The refractive index n of a medium e.g. an optical fibre at a certain wavelength of propagating light can be described as [97,98]:

$$n = n_0 + \Delta n \tag{2-8}$$

where

$$\Delta n = n_2' I \tag{2-9}$$

with

$$n_2' = \frac{2n_2}{\varepsilon_0 c n_0}; \tag{2-10}$$

$$I = \frac{P}{A_{eff}} \tag{2-11}$$

where n_0 is the refractive index at the minimum intensity of light, n_2 is the nonlinear refractive index (also known as Kerr nonlinearity coefficient), ε_0 is vacuum permittivity, c is the speed of light, P is the optical power transmitted within the fibre guided mode and A_{eff} is the effective area of the fibre.

An optical pulse (Gaussian) with a duration of $2t_0$ propagating in an optical fibre with an intensity represented by

$I = I_0 \exp\left(-\frac{2t^2}{t_0^2}\right)$, I_0 is the peak intensity (2-12)

produces the aforementioned modulation of the fibre refractive index, which causes changes in its phase as [97,98]

$$\Delta\Phi = \Delta n k_0 L \quad (2\text{-}13)$$

and finally

$$\Delta\Phi = n_2' k_0 L I_0 \exp\left(-\frac{2t^2}{t_0^2}\right) \quad (2\text{-}14)$$

where k_0 is the propagation constant in vacuum and L is the fibre length. Since the nonlinear phase shift is time dependent, spectral broadening of a travelling pulse can be observed [97]. The pulse intensity (energy) for which SPM becomes significant scales with a second power of pulse duration [97].

2.3.1.2 Self-focusing

Self-focusing is another nonlinear phenomenon that occurs in an optical medium e.g. a fibre which experiences changes in its refractive index induced by a high optical power of propagating light. When the optical power of the laser beam coupled into a fibre is greater than the critical value for self-focusing, the modified refractive index of the fibre acts like a focusing lens which can lead to a premature fibre failure. The critical power determining a threshold for this effect can be calculated as [99]

$$P = \frac{0.148\lambda^2}{n_0 n_2} \quad (2\text{-}15)$$

where λ is the wavelength of light, n_0 is the refractive index at low intensity (linear) and n_2 is the nonlinear refractive index, which is typically positive and leads to self-focusing at higher optical powers. Solid core silica fibres suffer from self-focusing for peak powers in the range of 4 MW (at 1 μm wavelength range) [100].

2.3.1.3 Stimulated Raman Scattering (SRS)

The Raman effect is a nonlinear response in a medium resulting from its interaction with high intensity light. This interaction leads to an energy transfer between the light travelling in a medium and the optical phonons of the medium. The incident light therefore behaves like a pump for generating a wave with shifted frequency the so

called Stokes wave [97]. The Stokes wave arises at a wavelength longer than the wavelength of the pump signal as the energy is transferred to an optical phonon with lower frequency. However, when the intensity of the incident light is increased generation can also be observed at wavelengths shorter than the pump wavelength (Anti-Stokes wave). An example of Stimulated Raman Scattering (SRS) generated in a hydrogen filled HC-PCF is shown in Fig. 2.28.

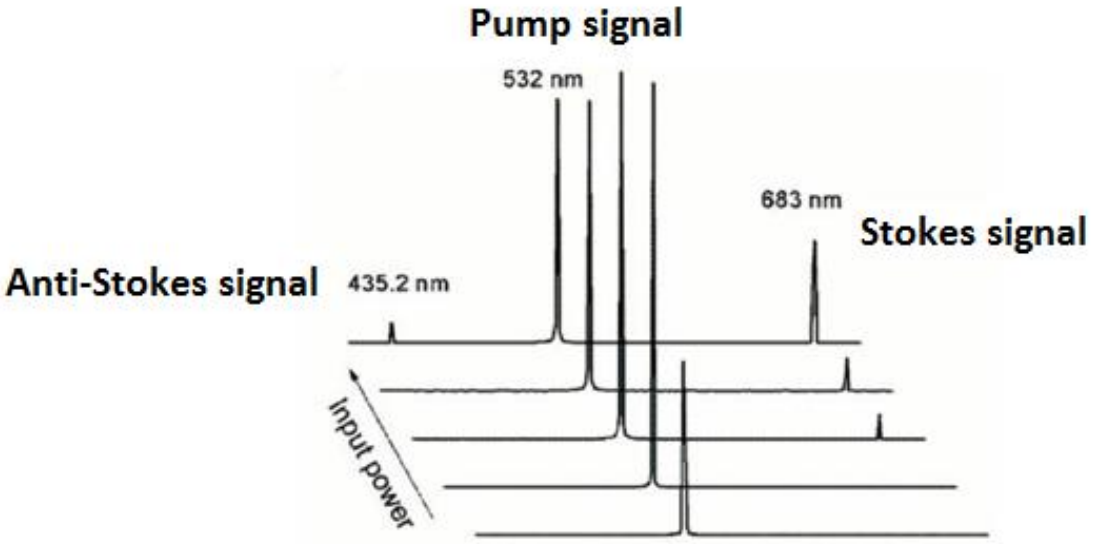

Fig. 2.28. Generation of SRS in a hydrogen filled HC-PCF for a pump signal at 532 nm [101].

SRS can also lead to a spectral broadening of an ultrashort laser pulse propagating through a fibre (the spectrum of an ultrashort pulse can be shifted towards a longer wavelength range) when the critical power is achieved. The SRS threshold is defined by the following formula [97]

$$P_{SRS} \approx 16 \frac{A_{eff}}{L_{eff} g_R} \tag{2-16}$$

where P_{SRS} is the critical power, A_{eff} is the effective fibre area, L_{eff} defines the effective interaction length and g_R is the Raman coefficient gain. The SRS threshold strongly depends on the fibre length and is also proportional to pulse duration [97]. The SRS threshold dependence on the fibre length in solid core silica single mode fibre is shown in Fig. 2.29. The curves confirm significant reduction in the SRS threshold with an increase of fibre length.

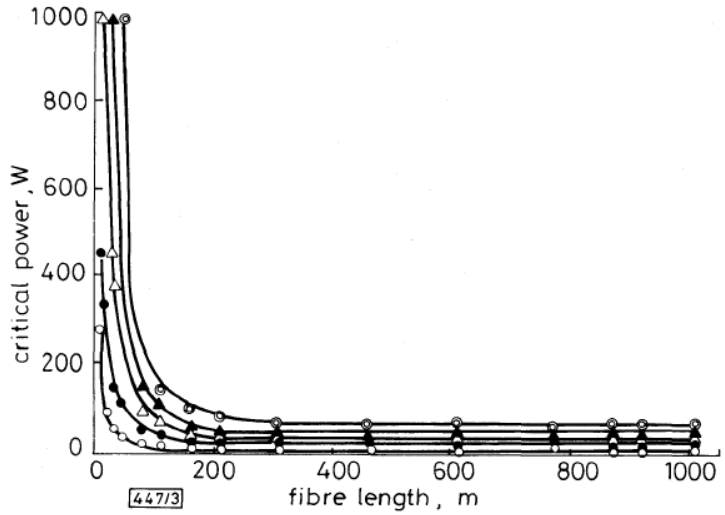

Fig. 2.29. SRS threshold dependence on fibre length in solid core silica single mode fibre [102].

2.3.1.4 Stimulated Brillouin Scattering (SBS)

Brillouin scattering is a similar nonlinear effect to Raman scattering, however here the interaction between light and matter occurs between the acoustic phonons instead of optical. Furthermore, the effect is a mono-directional process, which means that the generated Stokes wave propagates in the opposite direction (towards shorter wavelengths) to the pump signal when the Stimulated Brillouin scattering (SBS) occurs in an optical fibre as illustrated in Fig. 2.30 [97]. In this process the pump light generates an acoustic wave via the electrostriction phenomenon. This induces changes in the refractive index of the fibre (or other medium) that result in the formation of a grating which scatters light through Bragg diffraction [97]. The scattered pump signal has a downshifted frequency due to the Doppler shift associated with the grating moving at the acoustic velocity [97]. The SBS is dominant for longer laser pulses as it exhibits a strong dependence on the laser linewidth (> 1 μs, longer pulses have a narrow spectral bandwidth as the spectral width (FWHM) of a pulse can be defined as $\Delta\lambda \approx \Delta\lambda_0^2/(c\tau)$, where λ_0 is the central wavelength, c is the speed of light and τ is the pulse duration) [97]. The critical power P_{SBS} for generation of SBS can be approximated as [97]

$$P_{SBS} \approx 21 \frac{A_{eff}}{L_{eff} g_B} \tag{2-17}$$

where g_B is the peak value for the Brillouin gain, A_{eff} is the effective area and L_{eff} is the effective interaction length. Similar to the Raman effect, the Brillouin threshold strongly depends on the fibre length.

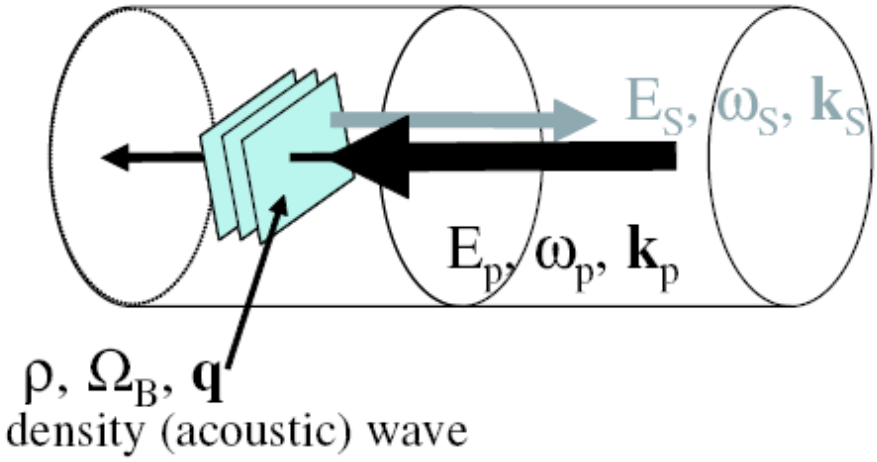

Fig. 2.30. Brillouin scattering. E_S, E_p are the Stokes and pump waves, ω_p – optical frequency of the pump wave, ω_s – optical frequency of Stokes wave, k_p – pump wave vector, k_s – Stokes wave vector [103].

2.3.2 Damage threshold dependence on wavelength and pulse duration

Efficient delivery of high energy pulsed laser light at wavelengths below 1 μm through solid core fibres is limited not only due to increased fibre loss (from scattering) but also from the damage threshold which is wavelength dependent. It was reported in [104 and 105] that the damage threshold (for pulsed laser light) varies roughly linearly with wavelength. Furthermore, the MFD of the fibre also exhibits dependence on the wavelength, hence a singlemode fibre at a short wavelength has a core diameter (thus MFD) smaller than one at a longer wavelength, which results in different light intensities in the core. This eliminates conventional solid core singlemode fibres from being used as a high power laser beam delivery tool in the UV spectral region (these fibres were reported to transmit CW UV light with an average power of only 2 mW [96]).

Furthermore, the damage threshold strongly depends on pulse duration. According to ref. [97 and 99] the laser induced damage threshold (LIDT) scales with a square root of pulse length, i.e. $\tau^{0.5}$. The influence of pulse duration on LIDT of fused silica at two different wavelengths is shown in Fig. 2.31.

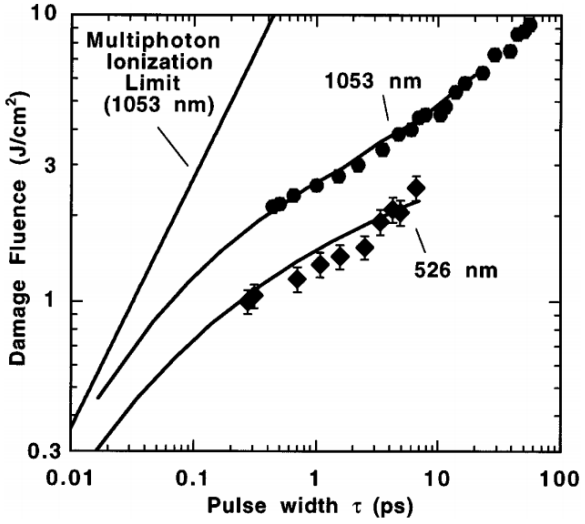

Fig. 2.31. LIDT for fused silica at 1053 nm and 526 nm for different pulse durations [104].

2.3.3 Group Velocity Dispersion (GVD)

GVD is caused by the dependence of the group velocity of light propagating in e.g. an optical fibre on frequency (wavelength) and is crucial in the delivery of pulsed laser light. In principal, spectral components of the laser pulse cover a certain range of wavelengths (frequencies) which travel with different velocities due to the fact that the refractive index of a transparent medium depends non-linearly on the optical frequency. This is especially significant for femtosecond pulses which necessarily cover a broad spectral bandwidth due to the short pulse duration (discussed in the previous subsection). Therefore, the difference in velocity between these components alter the temporal properties of the laser pulse, which typically leads to pulse broadening (see Fig. 2.32).

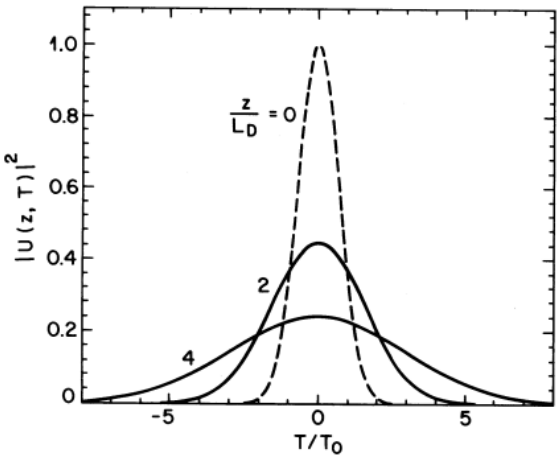

Fig. 2.32. Pulse broadening induced by dispersion. T_0 is the pulse width (FWHM), L_D is the dispersion length. Dashed line defines the original pulse [97].

Photonic bandgap HC-PCFs do indeed exhibit lower GVD than solid core fibres (GVD of 2500 ps/nm/km [106]), however at 1 μm it is still high at the level of ~ 120 ps/nm/km [79]. The level of dispersion at this particular wavelength can be significantly reduced in hypocycloid Kagome fibres, which have been reported to have a GVD as low as + 0.8 and -16 ps/nm/km for a 7-cell and 19-cell fibre respectively (see Fig. 2.33), which is desirable for efficient compression of ultrashort laser pulses [92]. Based on the data reported in [62] NCF fibres operating at 1 μm can be expected to exhibit similar dispersion properties.

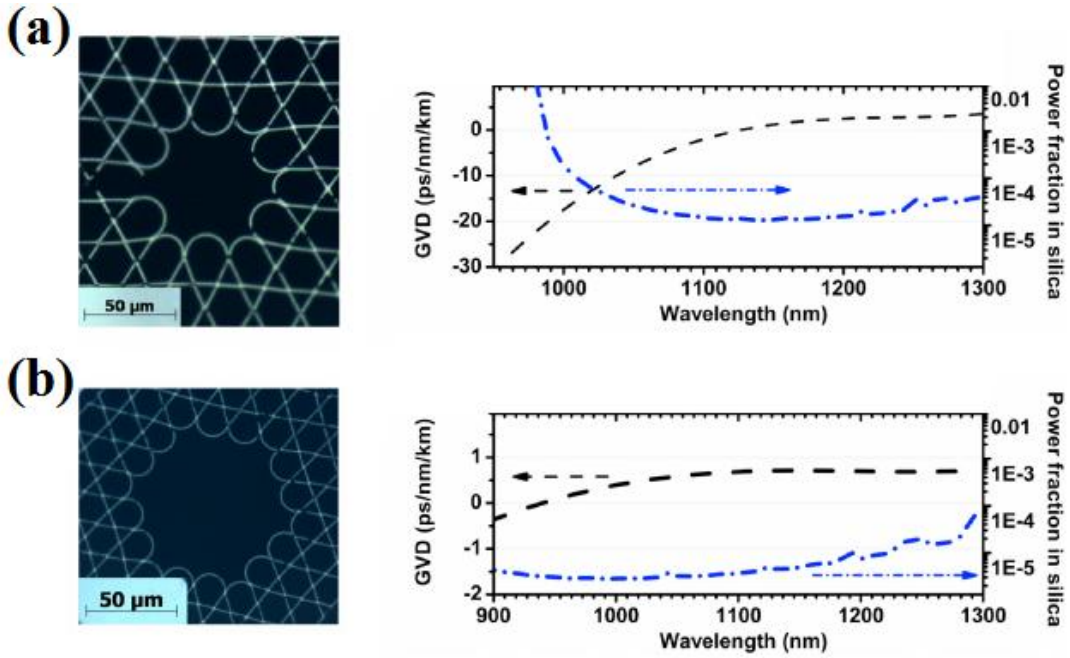

Fig. 2.33. GVD (black dashed curve) for: (a) 7-cell hypocycloid Kagome HC-PCF; (b) 19-cell hypocycloid Kagome HC-PCF [92].

2.3.4 Rayleigh scattering - fibre loss at shorter wavelengths

Conventional solid core silica fibres suffer from significantly increased attenuation at shorter wavelengths (especially below 1 μm) due to Rayleigh scattering. Light propagating within the fibre encounters random local changes of the refractive index originating from the physical properties of the fibre (resulting from fabrication process) e.g. defects, material composition fluctuations and various inhomogeneities, and therefore experiences scattering [107]. Rayleigh scattering is proportional to the fourth root of wavelength - $\sqrt[4]{\lambda}$, hence it becomes a dominant source of loss in an optical fibre at shorter wavelengths and its influence is reduced for wavelengths above 1600 nm as shown in Fig. 2.34.

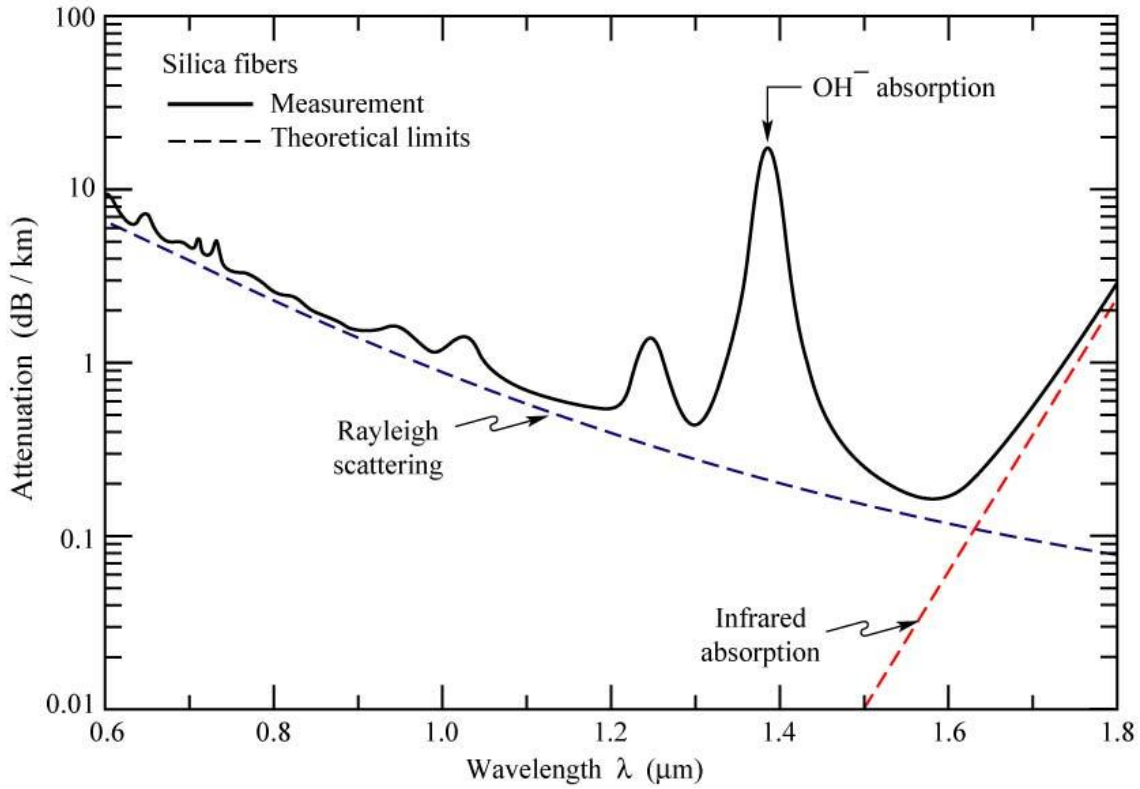

Fig. 2.34. Measured attenuation in silica fibres (solid line) and theoretical limits (dashed lines) given by Rayleigh scattering in the short-wavelength region, and by molecular vibrations (infrared absorption) in the infrared spectral region. Cited from ref. [108].

2.4 Fabrication of NCF

Negative Curvature Fibres are fabricated with the commonly used stack and draw method as illustrated in Fig. 2.35. The technique is a three stage process consisting of stacking, cane drawing and fibre drawing.

Stacking is used to form a desired contour of the fibre with eight silica capillaries (Suprasil F300), which at this stage are additionally supported by two rods (which are removed later) in order to maintain the shape. The final stack has a typical diameter of 25 cm [62]. In the next step, the stack is drawn down to a cane with a diameter of 3 cm to 4 cm. The final cane is an initial representative of the final fibre, and therefore a high precision drawing process is essential. The final fibre is then drawn down directly from the earlier fabricated cane. In order to obtain the negative curvature of the core wall and an ice-cream cone like shape of the cladding different pressures are applied to the fibre core and cladding regions. The cane is mounted into a drawing tower which is equipped with an assembly allowing the core and cladding regions to be pressurised (typically with pure nitrogen [62]) during drawing. The core walls of the capillaries forming the cladding are pushed towards the fibre core when the cladding

pressure is greater than the pressure applied to the core [62]. Other crucial parameters of the fibre drawing process are the drawing speed and temperature, which are required to be at the level of 11 m/min and 1920ºC respectively in order to obtain a desired and uniform fibre structure. The final fibre has an outer diameter typically in the range of 120 µm to 400 µm (depends on the guided wavelength) and a protection coating made of polymer [62]. For further details regarding the NCF drawing process see reference [62].

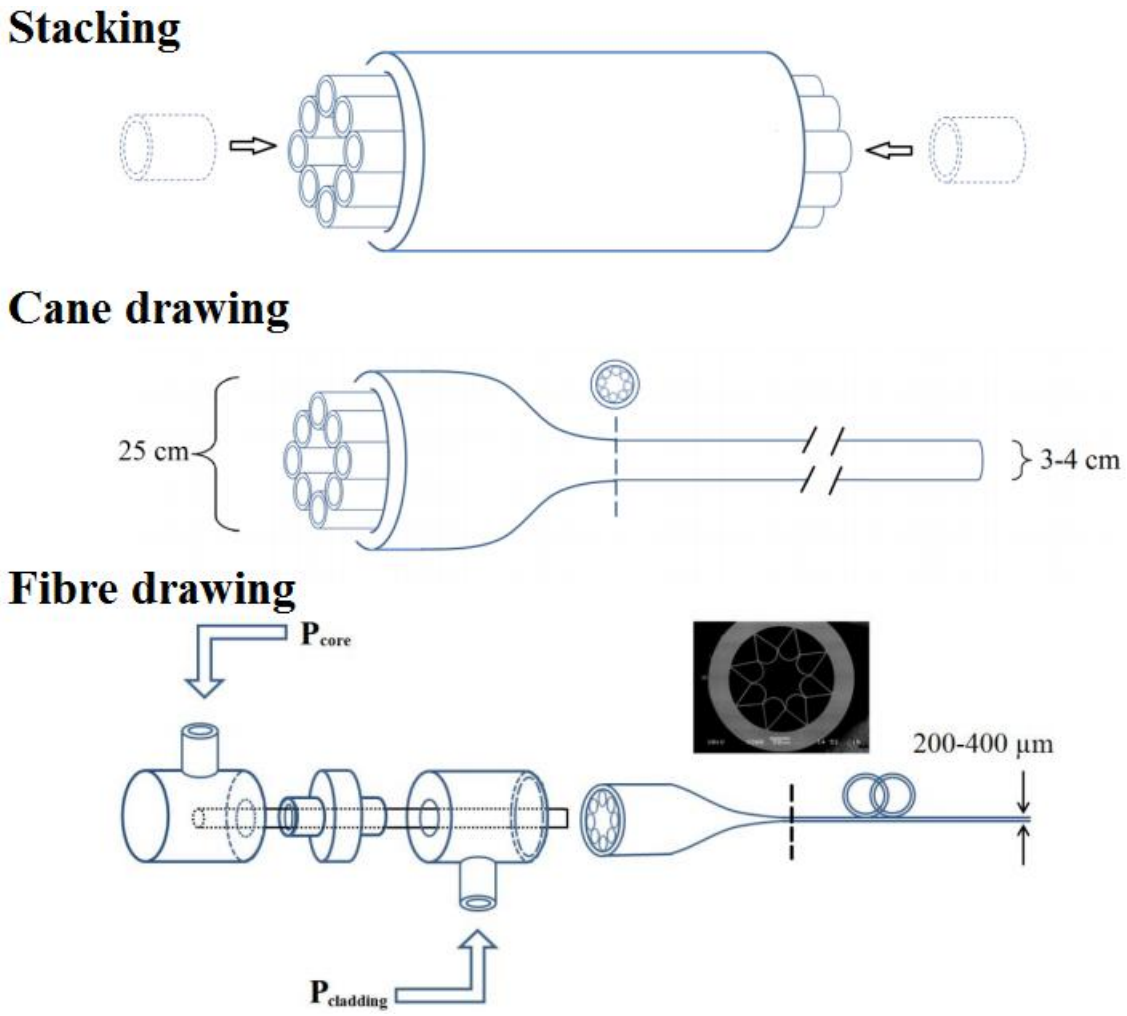

Fig. 2.35. Fabrication of NCFs with stack and draw method [62].

2.5 Summary

This chapter briefly explained main issues of the currently available beam delivery systems for high energy pulsed laser sources used in industrial applications and introduced various types of optical fibres as potential solutions to this problem.

Optical fibres have been experiencing a continuous and intensive development especially over the last decade, which enabled the fabrication of microstructured fibres guiding light in an air core (ARROW and inhibited coupling guiding HC-PCFs) with a capacity to deliver short and ultrashort high energy laser pulses from visible to MID-IR spectral regions. These fibres are characterised by significantly greater damage threshold and lower nonlinearities in comparison with conventional solid core silica fibres. Furthermore, they have been recently shown to guide light with a low loss in the deep UV, which opens a new application window.

References

1. KH. Leitz, B. Redlingshofer, Y. Reg, A. Otto, and M. Schmidt, "Metal ablation with short and ultrashort laser pulses," Phys. Proc. **12**, 230-238 (2011).
2. R. J. Beck, J. P. Parry, W. N. MacPherson, A. Waddie, N. J. Weston, J. D. Shephard, and D. P. Hand, "Application of cooled spatial light modulator for high power nanosecond laser micromachining," Opt. Express, **18**, 17059-17065 (2010).
3. R. Negarestani, L. Li, H. K. Sezer, D. Whitehead, J. Methven, "Nano-second pulsed DPSS Nd:YAG laser cutting of CFRP composites with mixed reactive and inert gases," Int. J. Adv. Manuf. Technol. **49**, 553-566 (2010).
4. K. L. Wlodarczyk and D. P. Hand, "Shaping the surface of Borofloat 33 glass with ultrashort laser pulses and a spatial light modulator," Appl. Opt. **53**, 1759-1756 (2014).
5. http://www.wophotonics.com
6. R. M. Carter, J. Chen, J. D. Shephard, R. R. Thomson, and D. P. Hand, "Picosecond laser welding of similar and dissimilar materials," Appl. Opt. **53**, 4233-4238 (2014).
7. L. Lucas and J. Zhang, "Femtosecond laser micromachining: A back-to-basics primer," Industrial Lasers Solutions for Manufacturing (2012).
8. A. Y. Fasasi, S. Mwenifumbo, N. Rahbar, J. Chen, M. Li, A. C. Beye, C. B. Arnold, and W. O. Soboyejo, "Nano-second UV laser processed micro-grooves on Ti6Al4V for biomedical applications," Materials Science and Engineering **29**, 5-13 (2009).
9. M. S. Brown and C. B. Arnold, "Fundamentals of laser-material interaction and application to multiscale surface modification," Laser Precision Microfabrication - Springer Series in Materials Science **135**, 91-120 (2010).
10. C. Moorhouse, "Picosecond laser enables new high-tech devices," Industrial Lasers Solutions For Manufacturing (2012).
11. G. Shannon, "Increased use of fiber lasers for microwelding," Micro Manufacturing **6** (2013).
12. www.scanlab.de
13. J. A. Marszalec and E. A. Marszalec, "Integration of lasers and fiber optics into robotic systems," publ. by SPIE, ISBN: 0-8194-1313-5.
14. www.jenoptik.com
15. www.jklasers.com
16. www.goldenlaser.org

17. C. E. Webb and J. D. C. Jones, "Handbook of laser technology and applications," publ. by Institute of Physics Publishing, ISBN: 0-7503-0607-6.
18. M. Bass, "Handbook of Optics - Volume V: Atmospheric optics, Modulators, Fiber optics, X-Ray and Neutron optics," publ. by The McGraw-Hill Companies, ISBN: 978-0-07-163314-7.
19. www.corning.com
20. www.thorlabs.com
21. D. P. Hand and J. D. C. Jones, "Single-mode delivery of Nd:YAG for precision machining applications," Appl. Opt. **37**, 1602-1606 (1998).
22. T. J. Stephens, "Fibre-optic delivery of high peak power laser pulses for flow measurement," PhD Thesis, Heriot-Watt University, UK (2003).
23. J. D. Mullett, G. Dearden, R. Dodd, A. T. Shenton, G. Triantos, and K. G. Watkins, "A comparative study of optical fiber types for application in a laser-induced ignition system," J. Opt. A: Pure Appl. Opt. **11**, 054007 (2009).
24. M. Biruduganti, S. Gupta, B. Bihari, G. Klett, and R. Sekar, "Performance analysis of a natural gas generator using laser ignition," ICEF2004–983, ASME ICE Fall Technical Conference, Long Beach, California, 2004.
25. www.rofin.com
26. A. Kuhn, I. J. Blewett, D. P. Hand, P. French, M. Richmond, J. D. C. Jones, "Optical fibre beam delivery of high-energy laser pulses: beam quality preservation and fibre end-preparation," Opt. and Las. in Eng. **34**, 273-288 (2000).
27. P. Yeh, A. Yariv, and E. Marom, "Theory of Bragg fiber," J. Opt. Soc. Am. **68**, 1196-1201 (1978).
28. M. Born and E. Wolf, "Principles of Optics: Electromagnetic theory of propagation, interference and diffraction of light," Publ. by Pergamon Press Ltd., ISBN: 0-521-642221.
29. C. Martijn de Sterke, I. M. Bassett, and A. G. Street, "Differential losses in Bragg fibers," J. of Appl. Phys. **76**, 680-688 (1998).
30. M. Jelinek, V. Kubecek, H. Jelinkova, V. Matejec, I. Kasik, O. Podrazky, "Experimental investigation of high power picosecond 1.06 μm pulse propagation in Bragg fibers," Proc. of SPIE **87772** (2013).
31. M. E. Lichachev, S. L. Semjonov, M. M. Bubnov, E. M. Dianov, M. Y. Salganskii, M. A. Gurjanov, A. N. Gurjanov, R. Jamier, P. Viale, S. Fevrier, and J. -M. Blondy, "Development and study of Bragg fibres with a large mode field and low optical losses," Quant. Electr. **36**, 581-586 (2006).

32. V. Matejec, I. Kasik, O. Podrazky, J. Aubrecht, M. Frank, M. Jelinek, V. Kubecek, "Preperation and characterization of Bragg fibers with air cores for transfer of laser radiation," Proc. of SPIE **8775** (2013).
33. M. M. Vogel, M. Abdou-Ahmed, A. Voß, D. Kauffmann, and T. Graf, "Full vectorial finite-element simulations of Bragg fibers for single-mode bam delivery system," Proc. of SPIE **6998** (2008).
34. H. T. Bookey, S. Dasgupta, N. Bezawada, B. P. Pal, A. Sysoliatin, J. E. McCarthy, M. Salaganskii, V. Khopkin, and A. K. Kar, "Experimental demonstration of spectral broadening in an all-silica Bragg fiber," Opt. Express **17**, 17130-17135 (2009).
35. S. Arismar Cerqueira Jr, "Recent progress and novel applications of photonic crystal fibers," Rep. Prog. Phys. **73** (2010).
36. P. St. J. Russell, "Review: Photonic Crystal Fiber," Science **229**, 358-62 (2003).
37. P. St. J. Russell, "Photonic-Crystal Fibers," J. Lightwave Technol. **24**, 4729-4749 (2006).
38. T. A. Birks, J. C. Knight, and P. St.J. Russell, "Endlessly single-mode photonic crystal fiber," Opt. Lett. **22**, 961-963 (1997).
39. J. C. Knight, T. A. Birks, P. St. J. Russell, and D. M. Atkin, "All-silica single-mode fiber with photonic crystal cladding," Opt. Lett. **21** (19), 1547-1549 (1996).
40. F. Luan, A. K. George, T. D. Hedley, G. J. Pearce, D. M. Bird, J. C. Knight, and P. St. J. Russell, "All-solid photonic bandgap fiber," Opt. Lett **12**, 69-74 (2004).
41. A. Argyros, T. A. Birks, S. G. Leon-Saval, C. M. B. Cordeiro, F. Luan, P. St. J. Russell, "Photonic bandgap with an index step of one percent," Opt. Express **13**, 1540-1550 (2004).
42. N. M. Litchinitser, S. C. Dunn, B. Usner, B. J. Eggleton, T. P. White, R. C. McPhedran, and C. M. de Sterke, "Resonances in microstructured optical waveguides," Opt. Express **11**, 1243-1251 (2003).
43. www.thorlabs.com
44. M. Kashiwagi, K. Saitoh, K. Takenaga, S. Tanigawa, S. Matsuo, and M. Fujimaki, "Effectively single-mode all-solid photonic bandgap fiber with large effective area and low bending loss for compact high-power all-fiber lasers," Opt. Express **20**, 15061-15070 (2012).
45. R. Buczyski, "Photonic Crystal Fibers," Acta Physcia Polonica A **106** (2004).

46. J. C. Knight, T. A. Birks, R. F. Cregan, P. St.J. Russell, and J.-P. de Sandro, "Large mode area photonic crystal fiber," Electron. Lett. **34**, 1347–1348 (1998).
47. S. Fevrier, D. Gruppi, P. Viale, C. Humbert, R. Jamier, B. Beaudou, A. Hirth, S. L. Semjonov, M. E. Likhachev, M. M. Bubnov, E. M. Dianov, V. F. Khopin, M. Y. Salganskii, and A. N. Guryanov, "High-energy nanosecond pulse delivery through singlemode Large Mode Area all-solid bandgap fibres," in Proc. of ECOC 2006 (2006).
48. S. R. Petersen, Thomas T. Alkeskjold, and Jesper Lægsgaard, "Degenerate four wave mixing in large mode area hybrid photonic crystal fibers," Opt. Express **21**, 18111-18124 (2013).
49. G. Bouwmans, F. Luan, Jonathan Knight, P. St. J. Russell, L. Farr, B. Mangan, and H. Sabert, "Properties of a hollow-core photonic bandgap fiber at 850 nm wavelength," Opt. Express **11**, 1613-1620 (2003).
50. F. Benabid, "Hollow-core photonic bandgap fibre: new light guidance for new science and technology," Phil. Trans. R. Soc. A. **364**, 3439-3462 (2006).
51. R. F. Cregan, B. J. Mangan, J. C. Knight, T. A. Birks, P. St. J. Russell, P. J. Roberts, and D. C. Allan, "Single-mode photonic band gap guidance of light in air," Science **285**, 1537-1539 (1999).
52. J. D. Shephard, F. Couny, P. St. J. Russell, J. D. C. Jones, J. C. Knight, and D. P. Hand, "Improved hollow-core photonic crystal fiber design for delivery of nanosecond pulses in laser micromachining applications," Appl. Opt. **44**, 4582-4588 (2005).
53. P. J. Mosley, W. C. Huang, M. G. Welch, B. J. Mangan, W. J. Wadsworth, and J. C. Knight, "Ultrashort pulse compression and delivery in a hollow-core photonic crystal fiber at 540 nm wavelength," Opt. Lett. **35**, 3589-3591 (2010).
54. J. D. Shephard, J. D. C. Jones, D. P. Hand, G. Bouwmans, J. C. Knight, P. St. J. Russell, and B. J. Mangan, "High energy nanosecond laser pulses delivered single-mode through hollow-core PBG fibers," Opt. Express **12**, 717-723 (2004).
55. T. J. Stephens, "Fibre-optic Delivery of High Peak Power Laser Pulses for Flow Measurement," PhD Thesis, HeriotWatt University, UK (2003).
56. J. D. Shephard, J. D. C. Jones, D. P. Hand, and J. C. Knight, "Delivery of nanosecond pulses through hollow core photonic crystal fibres and the associated damage limitations," Proc. of SPIE 5991 (2005).

57. S. O. Konorov, A. B. Fedotov, V. I. Beloglazov, N. B. Skibina, A. V. Shcherbakov, E. Wintner, and A. M. Zheltikov, "Laser breakdown with millijoule trains of picosecond pulses transmitted through a Hollow-Core Photonic-Crystal Fiber," Las. Phys. **13**, 652-656 (2003).

58. F. Luan, J. C. Knight, P. St. J. Russell, S. Campbell, D. Xiao, D. T. Reid, B. J. Mangan, D. P. Williams, P. J. Roberts, "Femtosecond soliton pulse delivery at 800 nm wavelength in hollow-core photonic bandgap fibers", Opt. Express **12**, 835-840 (2004).

59. C. J. Hensley, M. A. Foster, B. Shim, and A. L. Gaeta, "Extremely high coupling and transmission of high-powered-femtosecond pulses in Hollow-Core Photonic Band-Gap Fiber," in *Conference on Lasers and Electro-Optics/Quantum Electronics and Laser Science Conference and Photonic Applications Systems Technologies*, OSA Technical Digest (CD) (Optical Society of America, 2008), paper JFG1.

60. P. J. Mosley, W. C. Huang, M. G. Welch, B. J. Mangan, W. J. Wadsworth, and J. C. Knight, "Ultrashort pulse compression and delivery in a hollow-core photonic crystal fiber at 540 nm wavelength," Opt. Lett. **35**, 3589-3591 (2010).

61. N. M. Litchinitser, A. K. Abeeluck, C. Headley, and B. J. Eggleton, "Antiresonant reflecting photonic crystal optical waveguides," Opt. Lett. **27**, 1592-1594 (2002).

62. F. Yu, "Hollow core negative curvature optical fibres," PhD thesis, University of Bath, UK (2014).

63. F. Yu, W. J. Wadsworth, and J. C. Knight, "Low loss silica hollow core fibers for 3–4 μm spectral region," Opt. Express **20**, 11153-11158 (2012).

64. A. Hartung, J. Kobelke, A. Schwuchow, K. Wondraczek, J. Bierlich, J. Popp, T. Frosch, and M. A. Schmidt, "Origins of modal loss of antiresonant hollow-core optical fibers in the ultraviolet," Opt. Express **23**, 2557-2565 (2015).

65. P. Jaworski, F. Yu, R. R. J. Maier, W. J. Wadsworth, J. C. Knight, J. D. Shephard, and D. P. Hand, "Picosecond and nanosecond pulse delivery through a hollow-core Negative Curvature Fiber for micro-machining applications," Opt. Express **21**, 22742-22753 (2013).

66. A. D. Pryamikov, A. S. Biriukov, A. F. Kosolapov, V. G. Plotnichenko, S. L. Semjonov, and E. M. Dianov, "Demonstration of a waveguide regime for a silica hollow-core microstructured optical fiber with a negative curvature of the core boundary in the spectral region > 3.5 μm," Opt. Express **19**, 1441–1448 (2011).

67. A. F. Kosolapov, A. D. Pryamikov, A. S. Biriukov, V. S. Shiryaev, M. S. Astapovich, G. E. Snopatin, V. G. Plotnichenko, M. F. Churbanov, and E. M. Dianov, "Demonstration of CO_2-laser power delivery through chalcogenide-glass fiber with negative-curvature hollow core," Opt. Express **19**, 25723-25728 (2011).
68. J. R. Hayes, F. Poletti, M. S. Abokhamis, N. V. Wheeler, N. K. Baddela, and D. J. Richardson, "Anti-resonant hexagram hollow core fibers," Opt. Express **23**, 1289-1299 (2015).
69. F. Poletti, "Nested antiresonant nodeless hollow core fiber," Opt. Express **22**, 23807-23828 (2014).
70. W. Belardi, "New possibilities with hollow core antiresonant fibers," arXiv:1501.00586 [physics.optics] (2015).
71. P. Jaworski, F. Yu, R. M. Carter, J. C. Knight, J. D. Shephard, and D. P. Hand, "High energy green nanosecond and picosecond pulse delivery through a Negative Curvature Fiber for precision micro-machining," Opt. Express **23**, 8498-8506 (2015).
72. Y. Wang, F. Couny, P. J. Roberts, and F. Benabid, "Low Loss Broadband Transmission In Optimized Core-shape Kagome Hollow-core PCF," in *Conference on Lasers and Electro-Optics 2010*, OSA Technical Digest (CD) (Optical Society of America, 2010), paper CPDB4.
73. Y. Y. Wang, N. V. Wheeler, F. Couny, P. J. Roberts, and F. Benabid, "Low loss broadband transmission in hypocycloid-core Kagome hollow-core photonic crystal fiber," Opt. Lett. **36**, 669-671 (2011).
74. A. D. Pryamikov, A. S. Biriukov, A. F. Kosolapov, V. G. Plotnichenko, S. L. Semjonov, and E. M. Dianov, "Demonstration of a waveguide regime for a silica hollow - core microstructured optical fiber with a negative curvature of the core boundary in the spectral region > 3.5 μm," Opt. Express **19**, 1441-1448 (2011).
75. A. Urich, R. R. J. Maier, Fei Yu, J. C. Knight, D. P. Hand, and J. D. Shephard, "Flexible delivery of Er:YAG radiation at 2.94 μm with negative curvature silica glass fibers: a new solution for minimally invasive surgical procedures," Biomed. Opt. Express **4**, 193-205 (2013).
76. F. Emaury, , C. F. Dutin, C. J. Saraceno, M. Trant, O. H. Heckl, Y. Y. Wang, C. Schriber, F. Gerome, T. Südmeyer, F. Benabid, and U. Keller, "Beam delivery and pulse compression to sub-50 fs of a modelocked thin-disk laser in a gas-filled Kagome-type HC-PCF fiber," Opt. Express **21**, 4986-4994 (2013).

77. P. Jaworski, F. Yu, D. G. MacLachlan, R. R. Maier, R. R. Thomson, W. J. Wadsworth, J. C. Knight, J. D. Shephard, and D. P. Hand, “A hollow-core Negative Curvature Fibre for efficient delivery of NIR picosecond and femtosecond pulses for precision micro-machining, ” in *Workshop on Specialty Optical Fibers and their Applications*, (Optical Society of America, 2013), paper F3.3.
78. P. Jaworski, F. Yu, R. M. Carter, W. J. Wadsworth, T. A. Birks, J. C. Knight, J. D. Shephard, and D. P. Hand, “High peak power nanosecond and picosecond pulse delivery through a hollow-core Negative Curvature Fiber in the green spectral region for micro-machining,” in *Advanced Photonics*, OSA Technical Digest (online) (Optical Society of America, 2014), paper SoM3B.5.
79. www.nktphotonics.com
80. A. N. Kolyadin, A. F. Kosolapov, A. D. Pryamikov, A. S. Biriukov, V. G. Plotnichenko, and E. M. Dianov, " Light transmission in negative curvature hollow core fiber in extremely high material loss region," Opt. Express **21**, 9514-9519 (2013).
81. W. Belardi and J. C. Knight, "Hollow antiresonant fibers with low bending loss," Opt. Express **22**, 10091-10096 (2014).
82. W. Belardi and J. C. Knight, "Hollow antiresonant fibers with reduced attenuation," Opt. Lett. **39**, 1853-1856 (2014).
83. F. Benabid, J. C. Knight, G. Antonopoulos, and P. St. J. Russell, "Stimulated Raman Scattering in Hydrogen-Filled Hollow-Core Photonic Crystal Fiber," Science **298**, 399-402(2002).
84. F. Couny, F. Benabid, P. J. Roberts, P. S. Light, and M. G. Raymer, "Generation and Photonic Guidance of Multi-Octave Optical-Frequency Combs," Science **318**, 1118-1121 (2007).
85. F. Benabid, F. Gerome, B. Debord, and M. Alharbi, "Fiber For Fiber Lasers: Kagome PC fiber goes to extremes for ultrashort-pulse lasers," Laser Focus World (2014).
86. Y. Wang, M. Alharbi, T. D. Bradley, C. Fourcade-Dutin, B. Debord, B. Beaudou, F. Gerome, and F. Benabid, "Hollow-core photonic crystal fibre for high power laser beam delivery," High Power Laser Science and Engineering **1**, 17-28(2013).
87. B. Debord, M. Alharbi, T. Bradley, C. Fourcade-Dutin, Y.Y. Wang, L. Vincetti, F. Gérôme, and F. Benabid, "Hypocycloid-shaped hollow-core photonic crystal

fiber Part I: Arc curvature effect on confinement loss," Opt. Express **21**, 28597-28608 (2013).

88. M. Alharbi, T. Bradley, B. Debord, C. Fourcade-Dutin, D. Ghosh, L. Vincetti, F. Gérôme, and F. Benabid, "Hypocycloid-shaped hollow-core photonic crystal fiber Part II: Cladding effect on confinement and bend loss," Opt. Express **21**, 28609-28616 (2013).
89. B. Beaudou, F. Gerome, Y. Y Wang, M. Alharbri, T. D. Bradley, G. Humbert, J. –L. Auguste, J. –M. Blondy, and F. Benabid, "Milijoule laser pulse delivery for spark ignition through kagome hollow-core fiber," Opt. Lett. **37**, 1430-1432 (2012).
90. F. Emaury, C. F. Dutin, C. J. Saraceno, M. Trant, O. H. Heckl, Y. Y. Wang, C. Schriber, F. Gerome, T. Südmeyer, F. Benabid, and U. Keller, "Beam delivery and pulse compression to sub-50 fs of a modelocked thin-disk laser in a gas-filled Kagome-type HC-PCF fiber," Opt. Express **21**, 4986-4994 (2013).
91. O. H. Heckl, C. J. Saraceno, C. R. E. Baer, T. Südmeyer, Y. Y. Wang, Y. Cheng, F. Benabid, and U. Keller, "Temporal pulse compression in a xenon-filled Kagome-type hollow-core photonic crystal fiber at high average power," Opt. Express **19**, 19142-19149 (2011).
92. B. Debord, M. Alharbi, L. Vincetti, A. Husakou, C. Fourcade-Dutin, C. Hoenninger, E. Mottay, F. Gérôme, and F. Benabid, "Multi-meter fiber-delivery and pulse self-compression of milli-Joule femtosecond laser and fiber-aided laser-micromachining," Opt. Express **22**, 10735-10746 (2014).
93. F. Emaury, C. J. Saraceno, B. Debord, D. Ghosh, A. Diebold, F. Gèrôme, T. Südmeyer, F. Benabid, and U. Keller, "Efficient spectral broadening in the 100-W average power regime using gas-filled kagome HC-PCF and pulse compression," Opt. Lett. **39**, 6843-6846 (2014).
94. F. Guichard, A. Giree, Y. Zaouter, M. Hanna, G. Machinet, B. Debord, F. Gérôme, P. Dupriez, F. Druon, C. Hönninger, E. Mottay, F. Benabid, and P. Georges, "Nonlinear compression of high energy fiber amplifier pulses in air-filled hypocycloid-core Kagome fiber," Opt. Express **23**, 7416-7423 (2015).
95. B. Debord, M. Alharbi, A. Benoi, D. Gosh, M. Dontabactouny, L. Vincetti, J. -M. Blondy, F. Gerome, and F. Benabid, "Ultra low-loss hypocycloid-core Kagome hollow-core photonic crystal fiber for green spectral-range applications," Opt. Lett. **39**, 6245-6248 (2014).

96. F. Gebert, M. H. Frosz, T. Weiss, Y. Wan, A. Ermolov, N. Y. Joly, P. O. Schmidt, and P. St. J. Russell, "Damage-free single-mode transmission of deep-UV light in hollow-core PCF," Opt. Express **22**, 15388-15396 (2014).
97. G. P. Agrawal, "Nonlinear Fiber Optics - third edition," publ. by A Harcourt Science and Technology Company, ISBN: 0-12-045143-3.
98. W. Belardi, "Holey optical fibres for high nonlinearity devices," PhD thesis, University of Southampton, UK (2003).
99. A. V. Smith, B. T. Do, G. R. Hadley, and R. L. Farrow, "Optical damage limits to pulse energy from fibers," IEEE Journal of Selected Topics in Quantum Electronics **15**, 153-158 (2009).
100. A. V. Smith and B. T. Do, "Bulk and surface laser damage of silica by picosecond and nanosecond pulses at 1064 nm," Appl. Opt. **47**, 4812-4832 (2008).
101. A. R. Bhagwat and A. L. Gaeta, "Nonlinear optics in hollow-core photonic bandgap fibers", Optics Express **16**, 5035-5047 (2008).
102. Y. Ohmori, Y. Sasaki, T. Edahiro, "Fibre-length dependence of critical power for stimulated Raman scattering", Electronics Letters **17**, 593-594 (1981).
103. A. B. Ruffin, "Stimulated Brillouin Scattering: An Overview of Measurements, System Impairments, and Applications", NIST Symposium on Optical Fiber Measurements, Technical Digest, 23-28 (2004).
104. B. C. Stuart, M. D. Feit, A. M. Rubenchik, B. W. Shore, and M. D. Perry, "Laser-Induced Damage in Dielectrics with Nanosecond to Subpicosecond Pulses," Physical Review Letters **74**, 2248-2251 (1995).
105. G. Mann, J. Vogel, R. Preuss, P. Vaziri, M. Zoheidi, M. Eberstein, and J. Kruger, "Nanosecond laser-induced surface damage of optical multimode fibers and their preforms," Appl. Phys. A **92**, 853-857 (2008).
106. M. Wahle, H. Kitzerow, "Measurement of group velocity dispersion i a solid-core photonic crystal fiber filled with a nematic liquid crystal," Opt. Lett. **39**, 4816-4819 (2014).
107. M. Azadeh, "Fiber Optics Engineering," publ. by Springer Dordrecht Heidelberg London New York, e-ISBN: 978-1-4419-0304-4.
108. http://www.ecse.rpi.edu/~schubert

Chapter 3

Fibre characterisation

Chapter 3 covers characterisation of main properties of NCFs and FBARFs which determines their suitability for efficient transmission and flexible delivery of pulsed laser light in the NIR and green spectral regions. Attenuation, bending losses, polarisation properties, quality of the delivered beam and light guidance (single- or few-moded) have been experimentally established using cutback method and the M^2 measurement technique.

3.1 Negative Curvature Fibre

The following subsections cover the characterisation of physical and optical properties of Negative Curvature Fibres designed for the guidance in the near infrared (NIR) and green spectral regions. All the NCFs presented in this work were fabricated at the University of Bath by Dr. Fei Yu.

3.1.1 Guidance in the NIR

Three different Negative Curvature Fibres: NCF-01, NCF-140414 and NCF-150414-G were investigated in the vicinity of 1 μm wavelength range. The SEM images and physical parameters of the fibres are shown in Fig. 3.1 and Table 3.1 respectively.

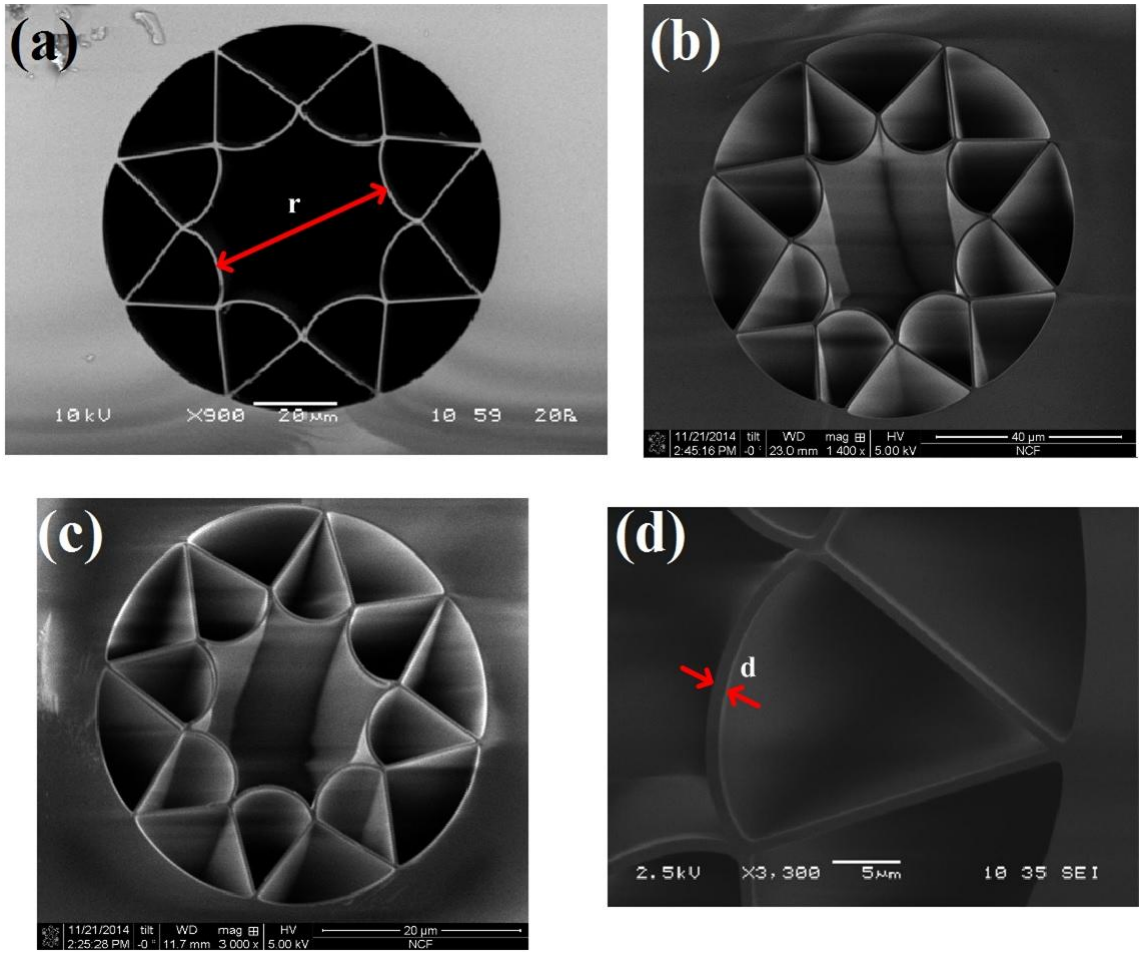

Fig. 3.1. SEM images of NCFs for the guidance at 1 μm: (a) NCF-01 (r defines fibre core diameter); (b) NCF-140414; (c) NCF-150414-G; (d) Capillary forming NCF-01 cladding (d is the core wall thickness). Images (a) and (d) were provided by Dr. Fei Yu.

Table 3.1. Physical parameters of the NCFs.

Fibre	Core wall thickness - d [nm]	Core diameter - r [µm]
NCF-01	910 ± 50	43 ± 1
NCF-140414	840 ± 50	36 ± 1
NCF-150414-G	550 ± 30	15 ± 1

The NCF-01 and NCF-140414 were designed and fabricated for transmission at 1 µm, and therefore the core wall thickness of these fibres (defining the position of antiresonant bandwidth) was set to 910 ± 50 nm and 830 ± 50 nm respectively. This provided low loss bandwidths spanning 1010 nm - 1320 nm and 870 nm - 1240 nm for NCF-01 and NCF-140414 respectively as shown in Fig. 3.2. According to the ARROW model [1] (described in more details in subsection 2.2.2.4) the aforementioned wavelength ranges correspond to the second antiresonant band of these fibres. The NCF-150414-G, on the other hand, was originally developed for low loss guidance in the visible (green) spectral range, and therefore the thickness of the capillaries forming the cladding was adjusted to provide low loss guidance in the range of 550 ± 30 nm. However, the results of transmission measurements and consequently the calculated attenuation of this fibre (performed by Dr. Fei Yu at the University of Bath) indicated the presence of a second low loss region covering 940 nm - 1170 nm as presented in Fig. 3.2 and reported in [2]. This observed transmission window corresponds to the first antiresonant band of this particular fibre, with NIR losses comparable to the two other fibres, hence its properties were investigated in both NIR and green.

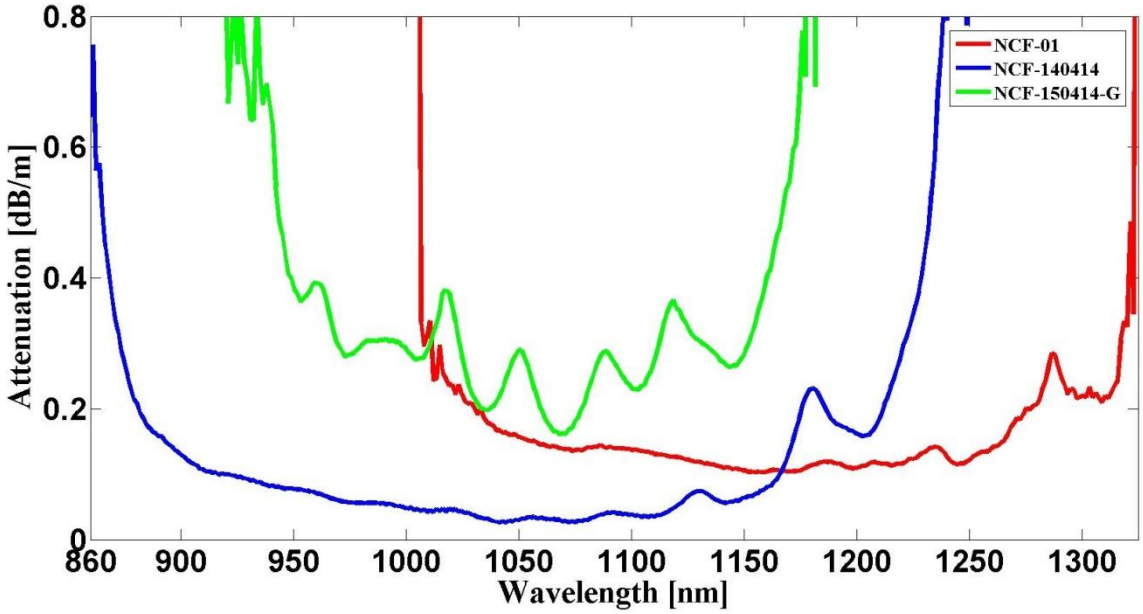

Fig. 3.2. Attenuation spectra of: NCF-01 (solid red); NCF-140414 (solid blue); NCF-150414-G (solid green). Data provided by Dr. Fei Yu.

Two main wavelengths of interest in the NIR spectral regime were 1030 nm and 1064 nm, which correspond to the fundamental wavelengths of the ps, ns and fs laser systems used within this work. Hence, to establish the attenuation of each NCF at these particular wavelengths, additional experiments were performed, based on the commonly used cutback technique. This method consists of a two step measurement. Firstly, light from a coherent or a broadband source is coupled into a long piece of fibre and the delivered (output) power is measured. The next step is to cut back the fibre to a shorter length while maintaining the same coupling conditions and consequently measure the optical power at its end. Then, the fibre attenuation can be calculated by

$$\alpha = \frac{10}{L}\log_{10}\left(\frac{P_{short}}{P_{long}}\right) \tag{3-1}$$

where α is the attenuation of the fibre, L corresponds to the length of removed fibre, P_{short} and P_{long} define the optical powers delivered through short and long fibres respectively.

The preliminary experiments carried out with the described NCFs indicated their bending sensitivity, especially significant with NCF-01 (further investigation of the bending properties can be found in subsection 3.1.1.2). Therefore, to measure attenuation independently of bend loss, 1 m long, straight pieces of each fibre were used. Furthermore, any additional micro-bends which could potentially affect the results were eliminated by maintaining the fibres within the same horizontal position during the

measurements [3]. The light sources used were a TRUMPF Tru Micro thin disk ps laser (6 ps, M^2 = 1.3, 1030 nm), a JDS Uniphase microchip ns laser (100 ns, M^2 = 1.2, 1064 nm) and a Spectra Physics Q-switched Nd:YVO_4 laser (60 ns, M^2 < 1.3, 1064 nm), and the fibres were cut from 1 m to 10 cm. The measurements and calculations were repeated five times for each fibre in order to obtain reliable results and estimate the measurement uncertainty. The measurement uncertainty was calculated using standard deviation method defined by the following formula [4]

$$\sigma = \sqrt{\frac{1}{n}\sum_{i=1}^{n}(x_i - \bar{x})^2} \tag{3-2}$$

where σ is the standard deviation, n is the number of measurements, x_i is the result of a measurement and $\bar{x}$ is the arithmetic mean of the set of measurement results. An example of the calculation procedure can be found below (for the results for NCF-01 at 1030 nm, please see Table 3.2).

The first step was to calculate the arithmetic mean of the set of measured attenuations defined as

$$\bar{x} = \frac{0.23+0.23+0.25+0.22+0.24}{5}\,\mathrm{dB/m} \approx 0.23\ \mathrm{dB/m} \tag{3-3}$$

then the standard deviation value was calculated as

$$\sigma = \sqrt{\frac{(0.23-0.23)^2+(0.23-0.23)^2+(0.25-0.23)^2+(0.22-0.23)^2+(0.24-0.23)^2}{5}}\,\mathrm{dB/m} \approx 0.01\ \mathrm{dB/m} \tag{3-4}$$

The final value of the attenuation of the NCF-01 at 1030 nm was defined as

$$\alpha = \bar{x} \pm \sigma = 0.23 \pm 0.01\ \mathrm{dB/m} \tag{3-5}$$

The experimental setup is shown in Fig. 3.3, and the measurement and calculation results are presented in Table 3.2.

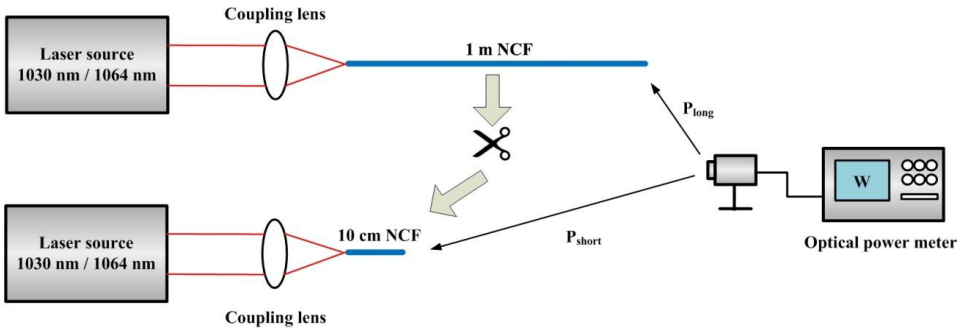

Fig. 3.3. Experimental setup for cutback measurements.

Table 3.2. Attenuation of NCFs at 1030 nm and 1064 nm.

	1030 nm				1064 nm			
Fibre	**Measured Attenuation [dB/m]**	**$\bar{x}$ [dB/m]**	**σ [dB/m]**	**α [dB/m]**	**Measured Attenuation [dB/m]**	**$\bar{x}$ [dB/m]**	**σ [dB/m]**	**α [dB/m]**
NCF-01	0.23	0.23	0.01	0.23±0.01	0.16	0.16	0.01	0.16±0.01
	0.23				0.17			
	0.25				0.16			
	0.22				0.14			
	0.24				0.16			
NCF-140414	0.04	0.04	0.01	0.04±0.01	0.03	0.05	0.01	0.05±0.01
	0.06				0.06			
	0.04				0.07			
	0.04				0.04			
	0.03				0.06			
NCF-150414-G	0.20	0.20	0.01	0.20±0.01	0.22	0.24	0.01	0.24±0.01
	0.19				0.25			
	0.22				0.26			
	0.20				0.24			
	0.18				0.24			

The lowest attenuation at 1030 nm and 1064 nm was observed with the NCF-140414 which is comparable with the values reported with more complex hypocycloid Kagome HC-PCF [5] and half that of commercially available HC-PCFs [6]. The relatively high (in comparison with the NCF-140414) attenuation of the NCF-01 was caused by the position of two wavelengths of interest in the transmission band (on the edge of the bandwidth where a high loss region begins) as a result of non-optimised structure of this fibre (the first fabricated NCF for 1 μm). To obtain lower attenuation the core wall thickness of the fibre has to be reduced as reported in [7]. A decrease in the thickness of the core wall in the NCF-140414 resulted in shifting the low loss transmission band towards shorter wavelength range, and consequently positioned these wavelengths into the middle (flat part) of the bandwidth, which significantly reduced the attenuation at these wavelengths. The NCF-150414-G, however, whilst not designed

to operate at these wavelengths exhibits an attenuation at the level required for efficient delivery of pulsed laser light (see sections 4.2.1 and 4.3.1 for further details) [2,8].

3.1.1.1 Characterisation of fibre delivered beam

The quality of delivered beam through an optical fibre is one of the crucial parameters to determine fibre suitability for many applications, especially for precision laser micro-machining. Therefore, to characterise the output of a fibre the near-field profile of the delivered beam has to be captured. This provides information regarding light confinement, the Mode Field Diameter (MFD) and indicates single or few-moded behaviour of the fibre. Observation of the delivered beam should not be performed in the far-field since it is not possible to distinguish whether the delivered beam is entirely transmitted within the core or a part of it is confined within the cladding.

The near-field beam profiles of the NCFs were recorded by directly imaging the end-facet of each fibre onto a CCD camera (PULNIX TM-6CN) connected with Spiricon LBA-PC beam profiling software in the experimental setup shown in Fig. 3.4. MFDs of each negative curvature fibre were defined by measuring $1/e^2$ diameter of the delivered beam. False-color near-field beam profiles delivered through the NCFs and measured MFDs are shown in Fig 3.5 and Table 3.3 respectively. The results obtained with the NCF-01 clearly indicates its few-moded guidance, however it is possible to excite only the fundamental mode (see Fig. 3.7) under specific circumstances (very careful alignment of the coupling optics with respect to the input end-facet of the fibre and the most crucial, the fibre itself must not be bent). Furthermore, it is important to mention that the transmitted light was entirely confined within the fibre core (regardless of the number of excited modes) and no light was observed in either the cladding nodes or cladding itself. The difference in the beam profiles at 1030 nm and 1064 nm are related not only to the few-moded nature of the fibre but also to a combination of wavelength difference, the fibre structure and source lasers (more specifically to their pumping systems) [9]. The two other NCFs, meanwhile, delivered singlemode beams at both wavelengths and no higher order modes were observed. The improved properties of the NCF-140414 are due to its optimised structure, smaller core size (decrease in core size reduces number of supported modes) and the position of low loss band in comparison with the NCF-01. 1064 nm and 1030 nm wavelengths are in the middle of the transmission windows of the optimised NCFs instead of being shifted towards the shorter wavelength edge of the bandwidth (in the case of the NCF-01). The NCF-

150414-G, meanwhile, provides singlemode guidance mainly due to its small core size. Furthermore, no difference between MFDs measured at 1030 nm and 1064 nm for each fibre was observed.

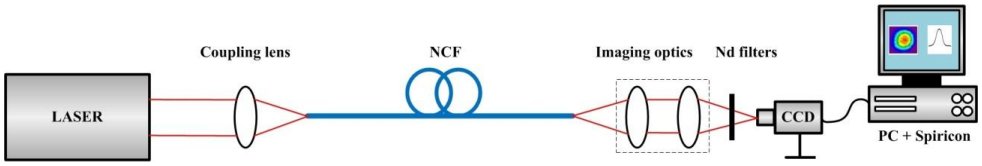

Fig. 3.4. Experimental setup for fibre delivered beam characterisation.

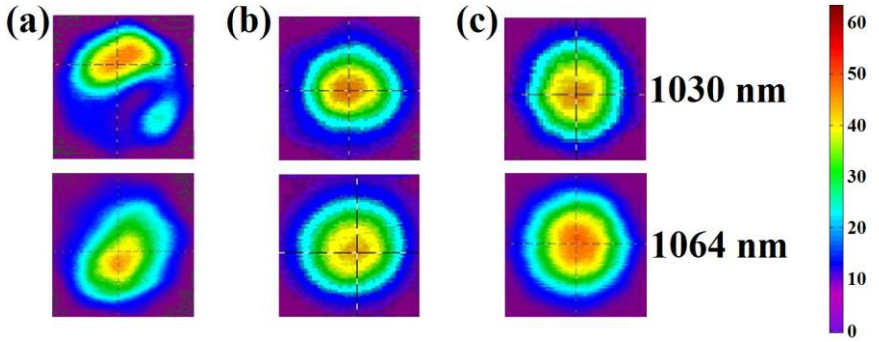

Fig. 3.5. False-color near-field beam profiles delivered through: (a) NCF-01; (b) NCF-140414; (c) NCF-150414-G.

Table 3.3. MFDs of investigated NCFs measured in the NIR.

	MFD ($1/e^2$) [µm]	
Fibre	**1030 nm**	**1064 nm**
NCF-01	36 ± 1	
NCF-140414	24 ± 1	
NCF-150414-G	9 ± 1	

The quality of a laser beam (fundamental Gaussian) is determined by the commonly used M^2 factor (beam propagation ratio) defined by ISO Standard 11146 [10]. According to the aforementioned standard, the following measurements and calculations have to be performed in order to establish the M^2 of the beam:

1) The width of the beam has to be measured at least at five positions within the distance of one Rayleigh length of the beam waist and another five measurements of the same parameter has to be taken at the distance outside of two Rayleigh lengths. The Rayleigh length for a Gaussian beam is defined as

$$Z_R = \frac{\pi\omega_0^2}{\lambda} \qquad (3\text{-}6)$$

where Z_R is the Rayleigh length, ω_0 is the beam width (radius) at the beam waist, λ is the wavelength.

2) Then, the M^2 factor can be determined by fitting to the following equation

$$\omega(z) = \omega_0 \sqrt{1 + \left(\frac{z\lambda M^2}{\pi \omega_0^2}\right)^2} \tag{3-7}$$

where $\omega(z)$ corresponds to the beam width (radius) at the distance z from the beam waist.

The $\omega(z)$ values of fibre delivered beam were determined by capturing spatial profiles at a number of positions with the CCD camera and consequently measuring beam radii (with $1/e^2$ criteria) with Spiricon software in the arrangement shown in Fig. 3.6. The CCD camera was mounted on a translation stage in order to provide its precise position (± 0.01 mm given by a micrometer driving screw) from the focusing lens. A PBS (Polarising Beam Splitter cube) with a HWP (Half-Wave Plate) were used to control the optical power of the laser beam coupled into the NCF, and therefore to adjust the intensity of the captured beam profile to maintain maximum signal-to-noise ratio on the camera regardless of camera position. This way of controlling the laser power provided stable and unchanged coupling conditions throughout the entire experiment. Changing the optical power of the laser directly via its control software usually results in a slight change in divergence of the emitted light which could significantly alter the coupling conditions and finally cause an excitation of the higher order modes and/or partially incident the beam onto the fibre cladding instead of its core (which dramatically increases the M^2). Furthermore, it is necessary to mention that the ND filter supplied with the camera did not have any influence (e.g. due to interference features) on the measurements. Again, as light sources the ps (1030 nm) and ns (1064 nm) lasers were used. The M^2 factor for each NCF delivered beam was established by fitting the measured beam radii to the formula 3-7 using Matlab software. The measurements were repeated five times for each fibre in order to get accurate results. The results uncertainty was calculated using the standard deviation as described earlier in this subsection. The results are presented in Fig. 3.7.

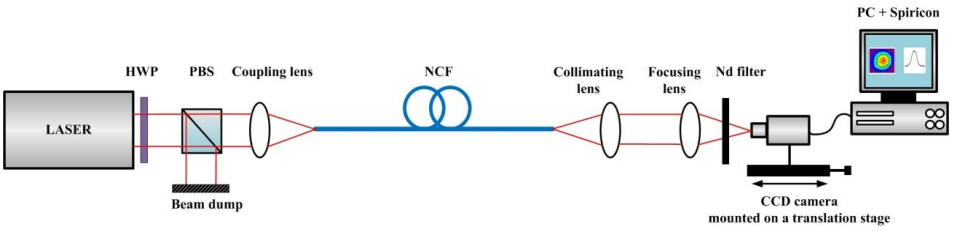

Fig. 3.6. Setup for the M^2 measurements. HWP - Half-Wave Plate, PBS - Polarising Beam Splitter cube.

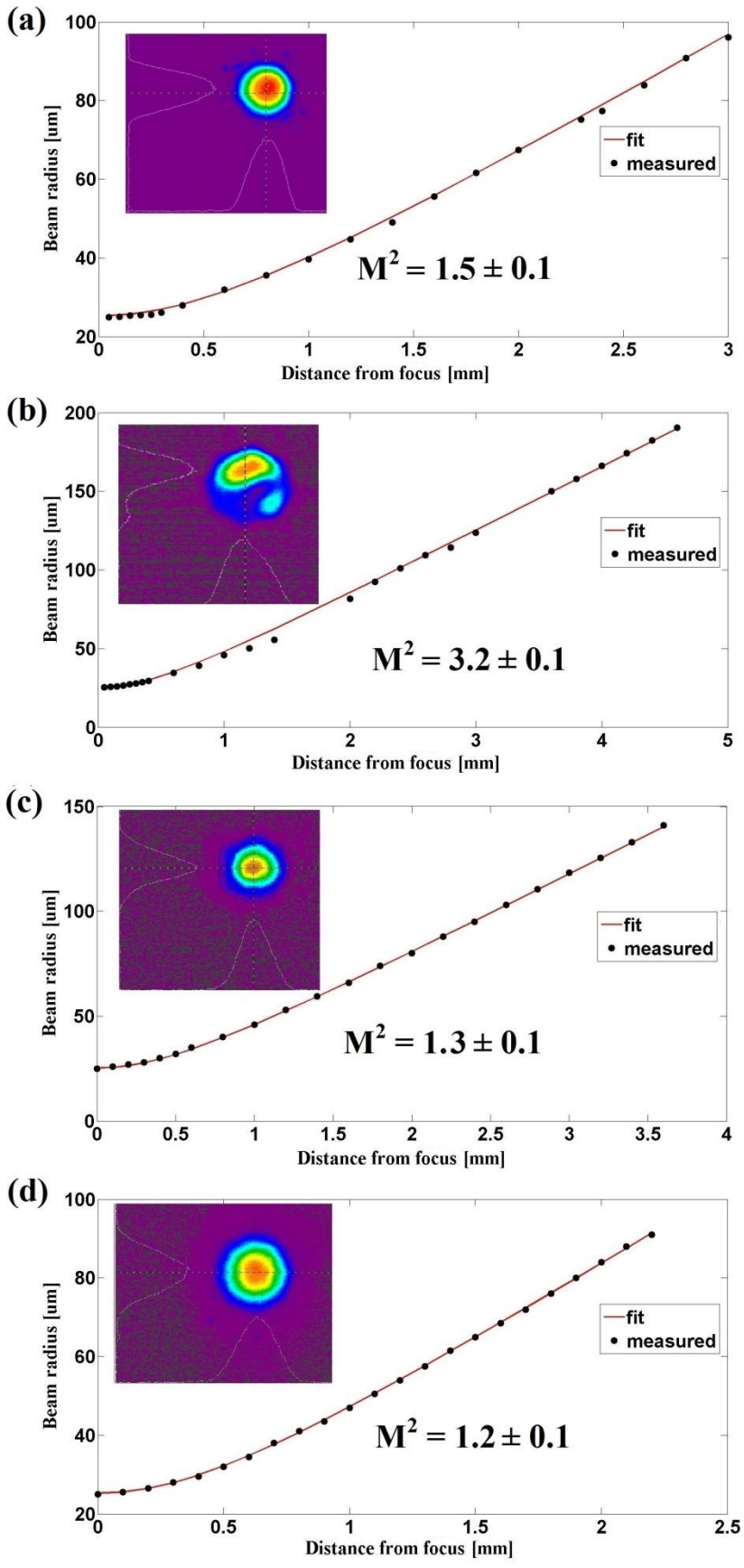

Fig. 3.7. Results of M^2 measurements of the NCF delivered beam in the NIR for: (a) highest beam quality that can be delivered through NCF-01 when exciting only the fundamental mode; (b) typical beam profile delivered with NCF-01; (c) NCF-140414; (d) NCF-150414-G.

The highest quality of the delivered beam was provided by the NCF-150414-G and NCF-140414 with M^2 values of 1.2 ± 0.1 and 1.3 ± 0.1 respectively due to pure singlemode guidance. Furthermore, no difference in the quality of the output of each fibre at 1030 nm and 1064 nm was observed and delivered modes are close to Gaussian, which is comparable with the results obtained with more complex Kagome hypocycloid HC-PCFs [11] . This shows an excellent suitability of these NCFs as a tool for flexible laser beam delivery for precision micro-machining applications (as described in more details in chapter 5). The NCF-01, on the other hand, typically delivered a beam with an M^2 of 3.2 ± 0.1 as a result of its few-moded guidance. However, a better M^2 value (1.5 ± 0.1) of the transmitted beam is achievable with this fibre when some specific requirements are fulfilled (as mentioned earlier in this subsection), although because of them it is unlikely to be present in the applications such as investigated within this work. Furthermore, the mode profile delivered through a negative curvature fibre is circularly symmetric, in contrast to the hexagonal symmetry usually seen with typical hollow-core photonic crystal fibres, and therefore makes it orientation independent [12], potentially providing improvement e.g. to micro-machining processes.

3.1.1.2 Impact of fibre bending

The impact of bending on the light transmitted through the NCFs was investigated at 1030 nm and 1064 nm. In this case, the same high power ps and ns laser systems and the microchip ns laser (used only for the measurements with the NCF-01) were used as coherent light sources.

The bending losses of the NCF-01 at 1064 nm were measured for both a coiled fibre (4.1 m long) and a bent fibre by 180º (3.1 m long) in the experimental setup shown in Fig. 3.8(a). To define the bend diameter of a coil a plastic tube was used as shown in Fig. 3.8(b). This solution provided good control of the bend diameter. A similar approach was used while bending the fibre by 180º. The bend loss at 1030 nm was investigated only for the 180º bend NCF (1 m long) due to limited working space with this laser. In each case, to obtain reliable and accurate results the entire fibre was kept in the same horizontal plane during the entire experiment (to avoid any micro-bends) and the coupling conditions were unchanged (the input end-facet of the fibre was not readjusted).

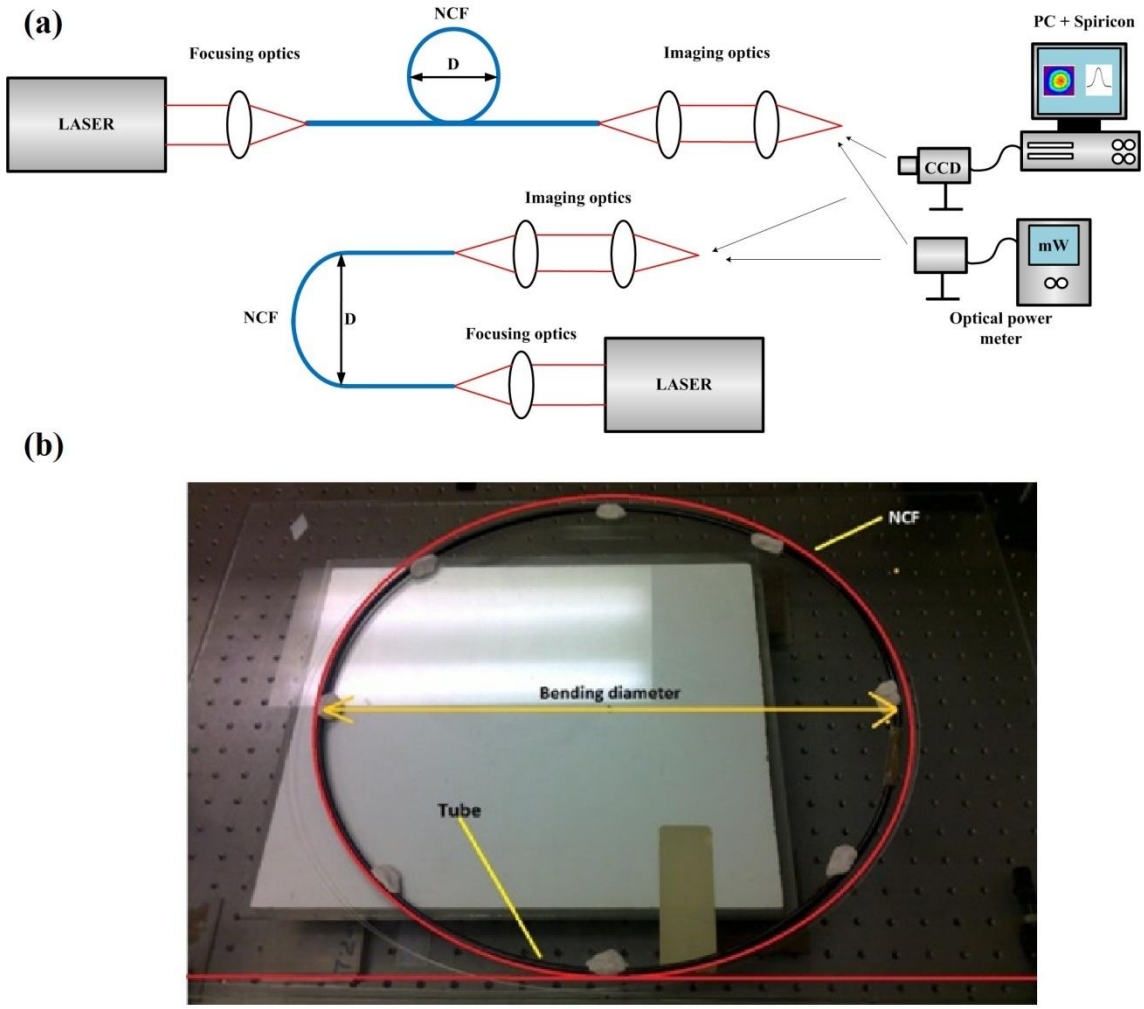

Fig. 3.8. (a) Experimental setups for bending tests. D defines the bending diameter; (b) Plastic tube used to define coil diameter.

The measurements were performed for different bend diameters ranging from 45 cm to 15 cm and 24 cm to 4 cm for coiled and half-turn bent fibre respectively at 1064 nm, while at 1030 nm bend diameters varied from 30 cm to 1 cm. The bend loss was established by comparing the delivered optical power through a bent fibre with the value transmitted through a straight piece. Fibre bending leads to a physical deformation of the fibre structure resulting in changes in the refractive index distribution in the cladding, and therefore enhances coupling between the core and cladding modes and consequently significantly increases losses [13,14]. This phenomenon was confirmed by observation (using an infrared viewer) of a significant amount of light leaking from the bent part of the fibre. The results presented in Fig. 3.9 clearly show that fiber bending introduces significant loss for bend diameters below 40 cm and 25 cm for coiled and 180º bent fibre respectively (at both wavelengths). Furthermore, for bend diameters below 5 cm (for a half-turn bend) the bend loss increases rapidly up to approximately 8 dB making the NCF-01 unsuitable for laser light delivery in this bending regime. For

larger bend radii, no bend-induced loss was observed. Additionally, the output of the fibre was analysed during bending with the CCD camera and Spiricon software. The examples of delivered beam profile changes due to fibre bending are shown in Fig. 3.10. In the case of coiling the fibre the delivered beam patterns are more singlemode like in comparison with a single 180º bend, which indicates significant attenuation of the higher order modes along the longer bending lengths. Furthermore, the observed fiber output beam profiles are not specific to a particular bend diameter but are representative of various profiles which can be visible at any bend radius at both considered wavelengths. It is likely that the observed excitation of the different modes during fibre bending is easy to induce mainly due to very similar propagation constant of the higher order modes and the fundamental mode which results in coupling between them. Moreover, coupling between guided modes can be induced by applying a point force to either a straight or bent fibre (i.e. touching or moving it). As a result the delivered power can vary by up to ± 10%. However, when the fibre is stationary no changes in the delivered beam profile and transmitted power are observed [3].

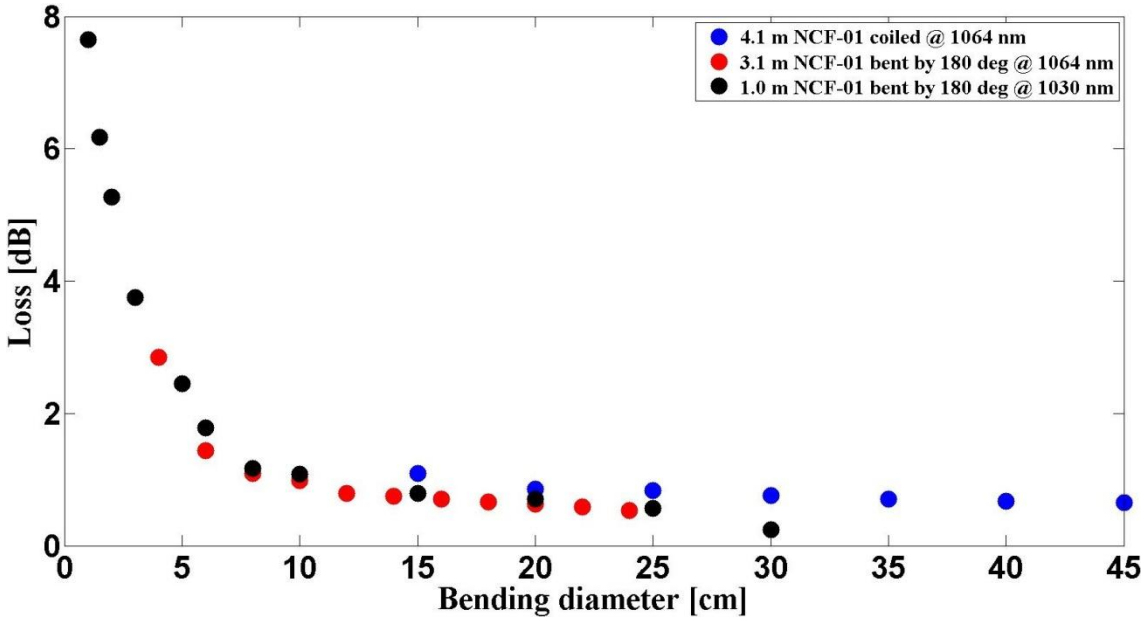

Fig. 3.9. Bending loss in NCF-01 introduced by coiling and bending the fibre by 180º with different bend diameters at 1064 nm and 1030 nm.

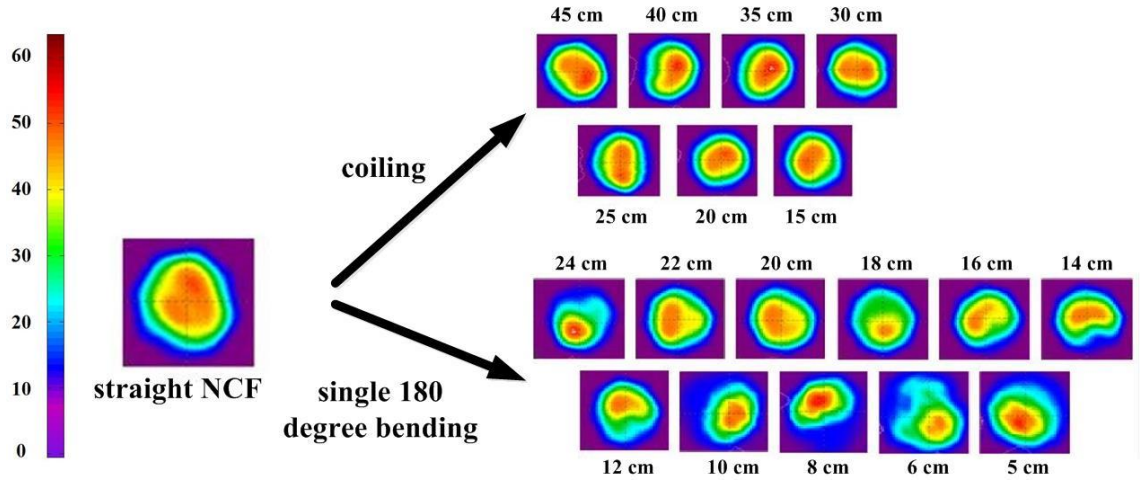

Fig. 3.10. Changes in the fibre delivered beam profiles observed while coiling or bending by 180º (for different bend diameters) NCF-01.

The impact of bending on the performance of NCF-140414 and NCF-150414-G was investigated by bending a 1 m length of fibre in each case through 180º, with bend diameters ranging from 25 cm to 1 cm. The measurements were carried out at both 1030 nm and 1064 nm. The experimental arrangement, measurement steps and procedures were the same as described with the NCF-01. The results are presented in Figs. 3.11 and 3.12 for NCF-140414 and NCF-150414-G respectively, and show an excellent improvement in bending loss and stability of the delivered beam in comparison with the NCF-01. Significant sensitivity to bending was observed only for very tight bends (diameter $\leq$ 3 cm) for both fibers, however with lower loss in the case of the NCF-140414. Bending the NCFs with greater bend diameters had negligible effect on the transmitted light. Furthermore, no influence on the delivered beam profiles (stable outputs of the NCFs) due to bending or applied point force was observed with either fibre. This improved performance is likely to be connected with the position of two considered wavelengths in their low loss regions as discussed in subsection 3.1.1. Furthermore, the absence of higher order modes (singlemode guidance in both fibres) which are associated with higher losses [7] eliminated coupling with the fundamental mode (as observed with the NCF-01), and therefore could have a positive impact on the bending sensitivity of both NCFs. A slight difference between the results obtained at 1030 nm and 1064 nm with all NCFs is again most likely associated with the position and shape of their transmission windows. The bending loss of a NCF with a single-layer cladding is similar to that observed with multiple-layer Kagome hypocycloid HC-PCF[15]. However, the discussed NCFs exhibit stable and singlemode output for bend diameters below 10 cm, which shows an excellent improvement in comparison with the

behaviour of Kagome hypocycloid structure reported in [16]. Benabid et. al discussed in [16] the influence of the number of cladding layers (in the fibres with negative curvature of the core wall) on bending loss. It was postulated that a multiple-layer cladding in a hypocycloid fibre leads to significant reduction of bend loss and improvement in modal content in comparison with a single-layer structure [16]. However, the SEM images of the investigated fibres [16] clearly indicate lack of symmetry of the structures (especially in the case of single- and dual-layer cladding) and most important deformations of core wall curvature, which could unintentionally resulted in few-moded output and increased loss. The studies reported in [14] show that the negative curvature of the core wall has a strong impact on the confinement loss and coupling between the core mode and cladding modes in a fibre that could alter its bending properties.

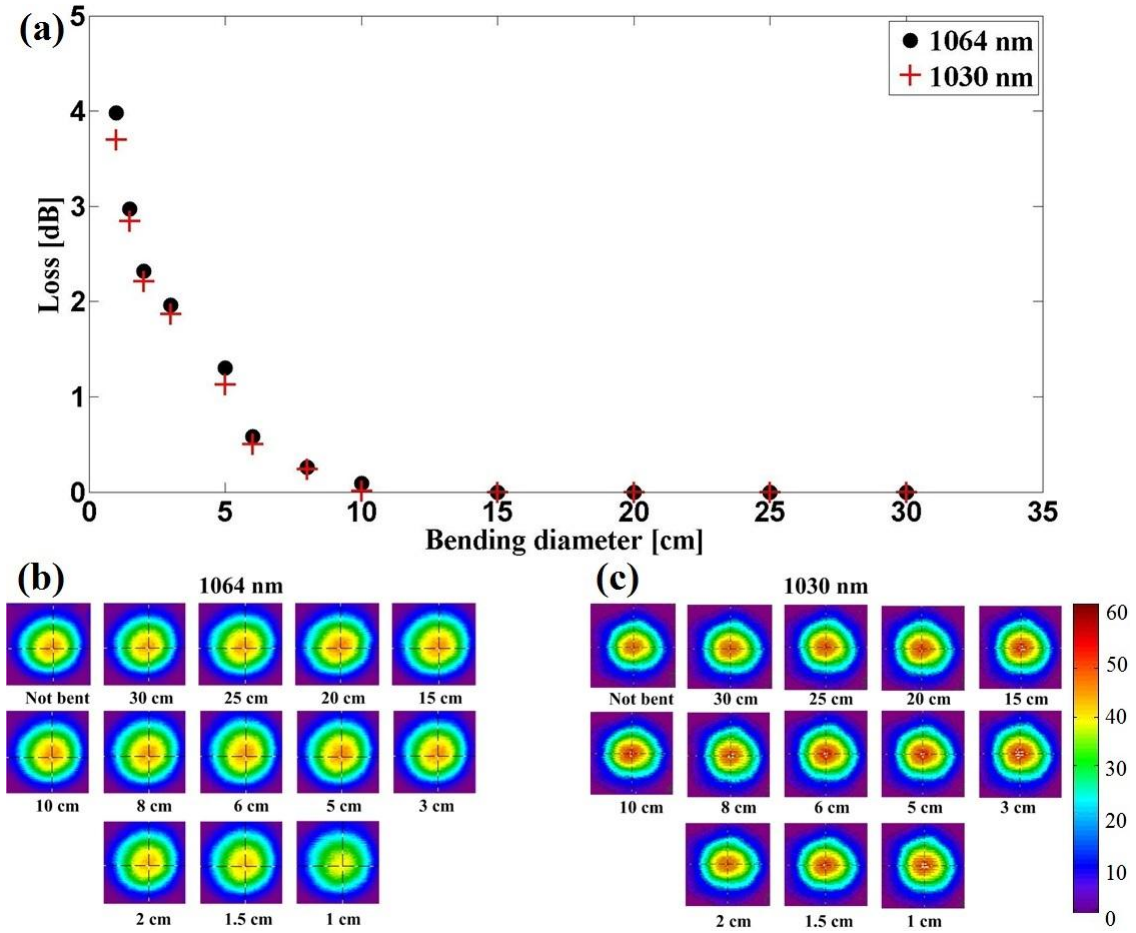

Fig. 3.11. (a) Bending loss present in 1 m NCF-140414 due to bending by 180º at 1030 nm and 1064 nm. Delivered near-field beam profiles for different bend diameters at: (b) 1064 nm; (c) 1030 nm.

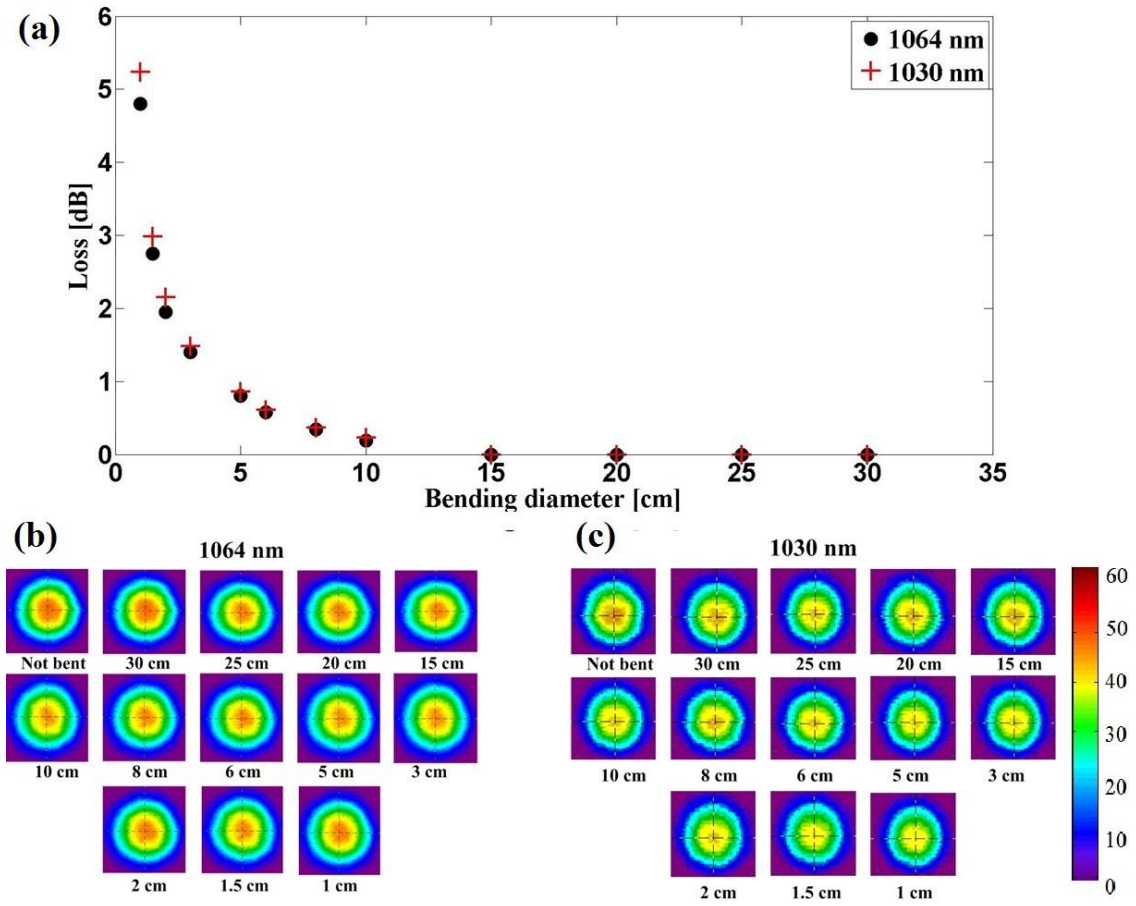

Fig. 3.12. (a) Loss due to bending 1 m NCF-150414-G by 180º for different bend diameters at 1030 nm and 1064 nm. Delivered beam profiles associated with each bending diameter at: (b) 1064 nm; (c) 1030 nm.

3.1.1.3 Polarisation properties

A singlemode fibre (conventional solid core or microstructured) is not entirely singlemode since it can support two degenerate modes which are orthogonally polarised [17]. If we consider an ideal circumstances where a fibre lacks of any imperfections in its structure i.e. has a perfect cylindrical symmetry a coupling between these two modes will not occur [17]. However, in reality all fibres suffer from a lack of uniformity in the structure formed during fabrication process or some deformations due to induced stress, which results in a mixing of the two polarisation states by breaking the mode degeneracy, and therefore the propagation constant becomes different for each mode and a fibre exhibits modal birefringence [17]. Modal birefringence in standard fibres is not constant and changes randomly along the fibre (i.e. due to the aforementioned structural imperfections) and leads to a difference in velocity of the two orthogonally polarised modes travelling through the fibre, which in the case of ultrashort pulse transmission results in pulse broadening due to polarisation mode dispersion (PMD)

[17]. This effect can be controlled by introducing some specific modifications to the fibre structure i.e. by adding stress elements (polarisation maintaining /hi-bi fibres i.e. PANDA or BOW-TIE) or a fibre twist (spun fibres, fabricated by spinning the fibre during fabrication process). The stress inducing elements in polarisation maintaining fibres define two birefringent axis of the fibre (fast and slow), hence when a polarisation orientation of light coupled into such fibre is perfectly aligned with respect to one of this axes, the original polarisation state will be well-preserved after propagation through the fibre. Spinning the fibre introduces a modification to intrinsic birefringence of the fibre, which results in controlled polarisation-mode coupling that reduces PMD [18,19].

It can be assumed that the NCFs presented in this work due to their structure could exhibit some level of birefringence, hence their polarisation properties were investigated by performing a set of experiments. The measurements were conducted with the NCF-01 fibre at 1030 nm using the linearly polarised Trumpf TruMicro ps system which provides a linearly polarised beam in the arrangements shown in Figs. 3.13(a) and 3.13(b). In the experimental setup the first half-wave plate HWP1 controls the polarisation orientation of the input laser beam, whilst the HWP2 in combination with polarising beam splitter forms a polarisation analyser. HWP2 is used to set the angle of PBS, and therefore the orientation (position) of analyser. The polarisation orientation of the input beam was changed from 0º to 90º with a 10º step during the experiment and changes in transmitted power after the analyser (set at fixed position) were measured with an optical power meter. The experiment was repeated for several analyser positions set at: 0º, 15º, 30º, 45º, 60º, 75º and 90º. Furthermore, the results obtained with the NCF-01 were compared with the polarisation properties of a commercial HC-PCF HC-1060 from NKT Photonics (details of the fibre can be found in [6]) characterised using the same method.

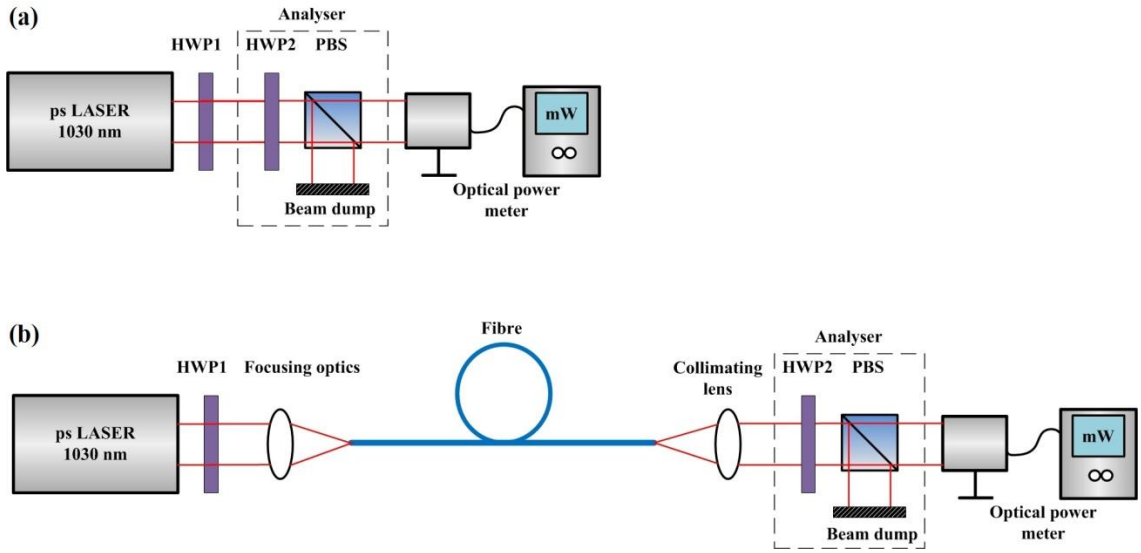

Fig. 3.13. Experimental setups used in polarisation tests: (a) without the fibre in the alignment and (b) with a fibre. HWP - Half Wave Plate, PBS - Polarising Beam Splitter cube.

Firstly, the measurements were performed without a fibre in the setup in order to obtain the reference data presented in Fig. 3.14(a) and then repeated with a fibre. The results plotted in Fig. 3.14(b) confirm that linear polarisation of the laser beam was maintained after propagation through a 1 m, straight NCF-01. A 34 m coiled (30 cm coil diameter) NCF-01 altered the state of polarisation and the transmitted light was no longer linearly polarised, as shown in Fig. 3.14(c). An additional measurement was taken with the 34 m NCF but twisted by 90º along its axis (both ends of the fibre were fixed and not twisted). Fig. 3.14(d) shows that twisted fibre changed the polarisation state of the transmitted beam by π as a result of induced birefringence (a twist in the fibre introduces circular birefringence). In comparison, a 1 m, straight HC-PCF introduced changes to the polarisation of the coupled light, although it is still close to being linearly polarised (see Fig. 3.15(a)). Furthermore, an 8 m coiled (with 15 cm coil dia.) HC-PCF did not maintain the polarisation state of the incident light as shown in Fig. 3.15(b), which is similar to the behaviour observed with the long NCF. A twist of the 8 m fibre by 90º resulted in a rotation of the polarisation by the same amount as presented in Fig. 3.15(c).

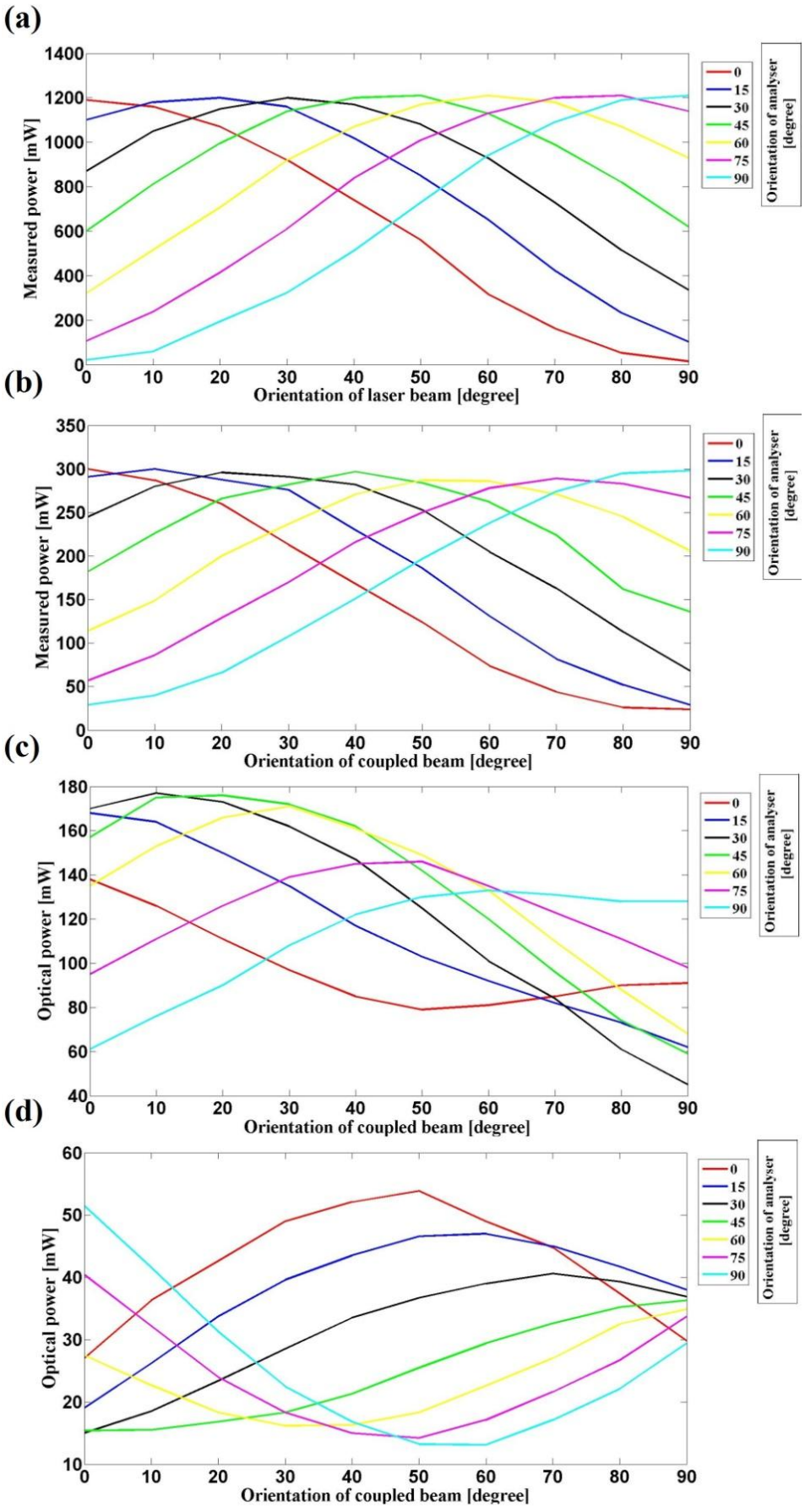

Fig. 3.14. Results of polarisation tests: (a) without a fibre; (b) 1 m, not bent NCF-01; (c) 34 m, coiled NCF-01; (d) 34 m, coiled, twisted by 90º NCF-01.

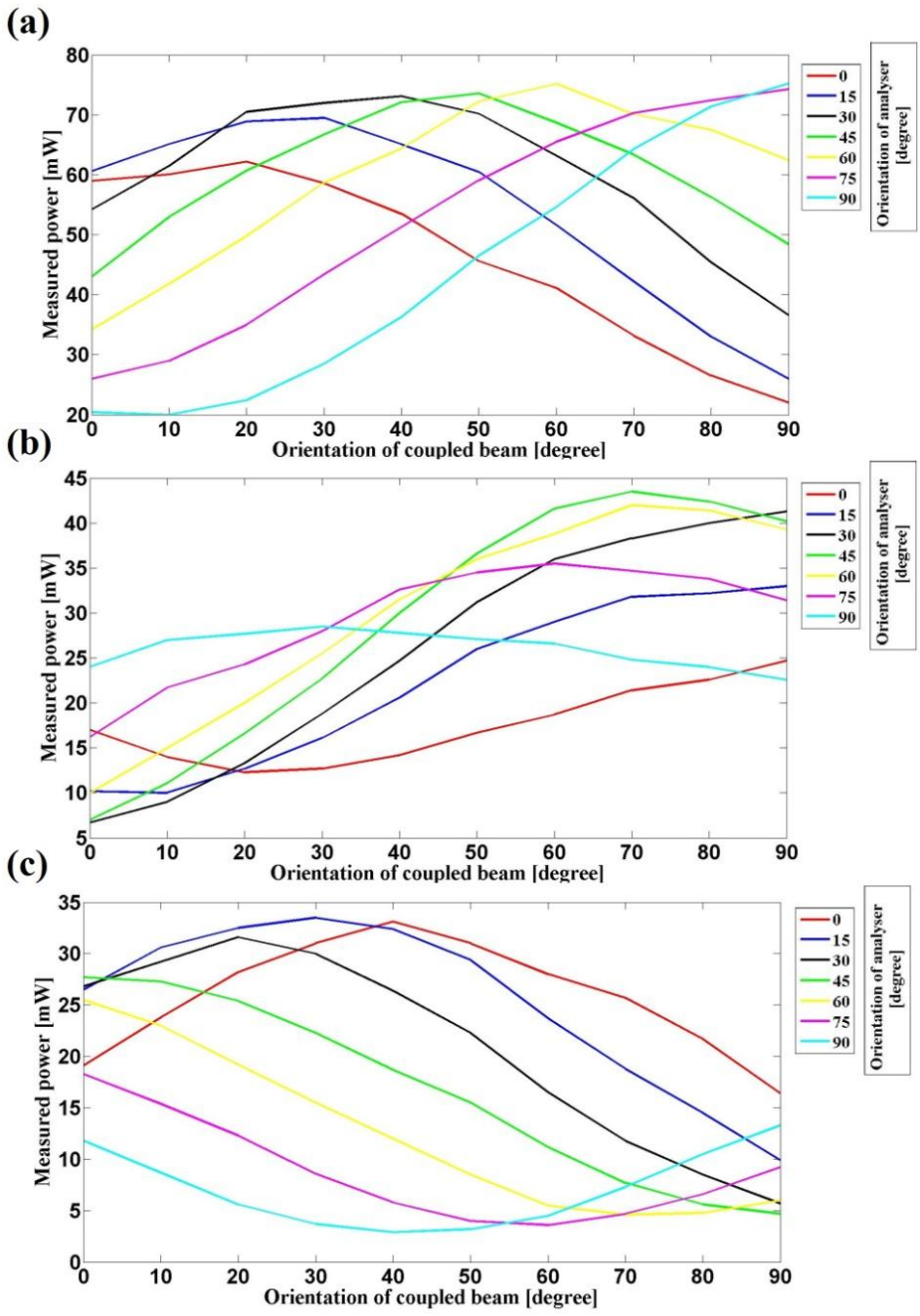

Fig. 3.15. Results of polarisation experiments for: (a) 1 m , not bent HC-PCF; (b) 8 m, coiled HC-PCF; (c) 8 m, coiled, twisted by 90º HC-PCF.

The portion of light which is polarised can be quantitively described by the parameter called the degree of polarisation - DOP (or polarisation ratio) [20]. The DOP is defined by the following formula

$$\mathrm{DOP} = \frac{P_{max} - P_{min}}{P_{max} + P_{min}} \tag{3-5}$$

where P_{max} and P_{min} correspond to the maximum and minimum transmitted through the analyser. The measured DOP of the ps laser beam was 98 ± 1%, which indicates almost

ideal linear polarisation (DOP = 100% corresponds to perfectly polarised light and DOP = 0% characterises an unpolarised beam, while 0% < DOP < 100% indicates a presence of polarised and unpolarised components in the beam). The DOPs of delivered beam through NCF-01 and HC-PCF were calculted for different orientations of the coupled (laser) beam. The results plotted in Fig. 3.16(a) show a decrease in the DOPs for 1 m and 34 m fibres in comparision with the value for the incident beam, and therefore indicate a presence of unpolarised component in the transmitted light. The data for 34 m NCF (both twisted and not) shows that approximately 50% of the delivered beam was unpolarised, while after 1 m fibre the polarisation ratio dropped only by 15% in comparision with the ps laser. Furthermore, a dependence of the DOP on the orientation of coupled beam was observed with each NCF. The fluctuations of the DOP observed in the 1 m fibre had similar trend as for the laser itself. Additional measurements conducted for the HC-PCF show similiar changes in the polarisation ratio and dependence of the DOP on the orientation of incident beam as presented in Fig. 3.16(b). However, a more significant increase of the DOP was noticed for the twisted HC-PCF in comparision with NCF-01, which can be expected due to the difference in structure of both fibres, and therefore various birefringence.

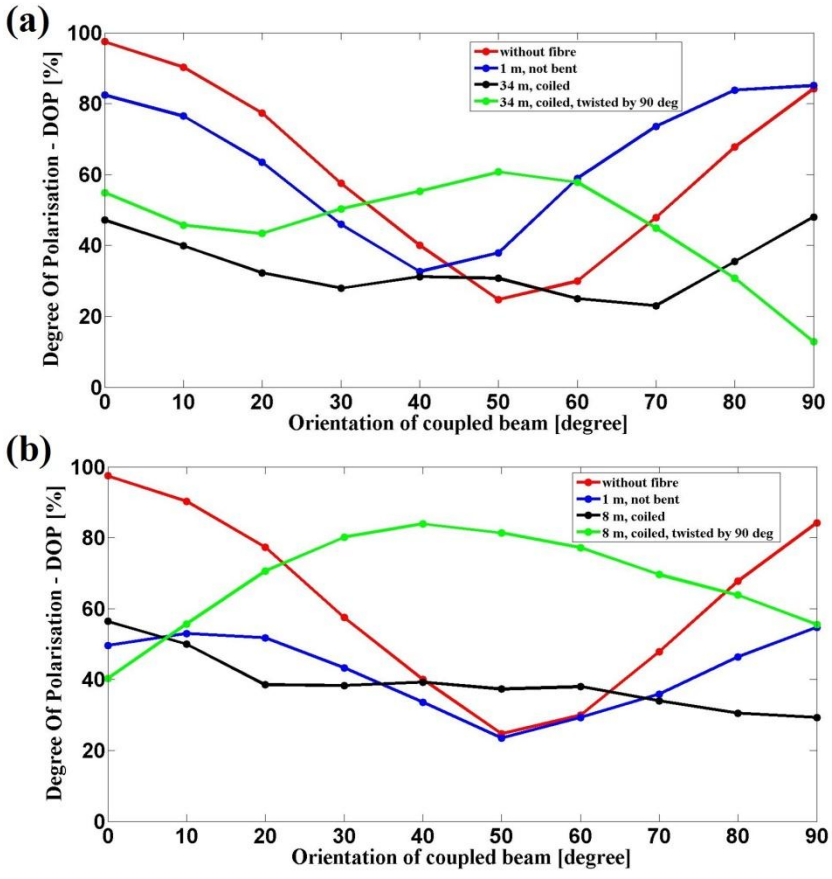

Fig. 3.16. DOP dependence on the orientation of coupled beam in: (a) NCF-01 and (b) HC-PCF.

The experiments showed that a fibre based on the negative curvature design exhibits low birefringence and polarisation properties similiar to the typical hollow-core photonic crystal fibre. The results obtained with the 1 m fibre, however proved that the polarisation state of the coupled beam was maintained, but it was more likely due to the short length of the fibre, and therefore had insignificant influence on the propagating light, nevertheless, it still indicates that the fibre has low birefringence.

3.1.2 Guidance in the green spectral range

The flexible delivery of high energy laser pulses in the green spectral range is especially desirable for micro-machining applications (in comparison with the NIR) mainly due to the focused spot size, enabling greater precision and the more readily accessed nonlinear absorption. Furthermore, the damage threshold of conventional fibres decreases with a decrease in the wavelength, and therefore the energy handling capability of these fibres becomes significantly lower e.g. in the green, which eliminates them from being used as an efficient high power beam delivery tool (see subsection 2.3.2 for further details). Therefore, three Negative Curvature Fibres: NCF-240314-G, NCF-080414-G and NCF-150414-G (discussed in subsection 3.1.1 due to its dual-band transmission) were designed and fabricated for guidance in particular around 515 nm - 540 nm where the neodymium and ytterbium based short and ultrashort pulsed lasers operate at their second harmonic wavelength are discussed within this subsection. The most crucial parameters of these fibres were characterised, including attenuation, bending properties and quality of the delivered beam. SEM images of the investigated fibres and their physical properties are presented in Fig. 3.17 and Table 3.4 respectively.

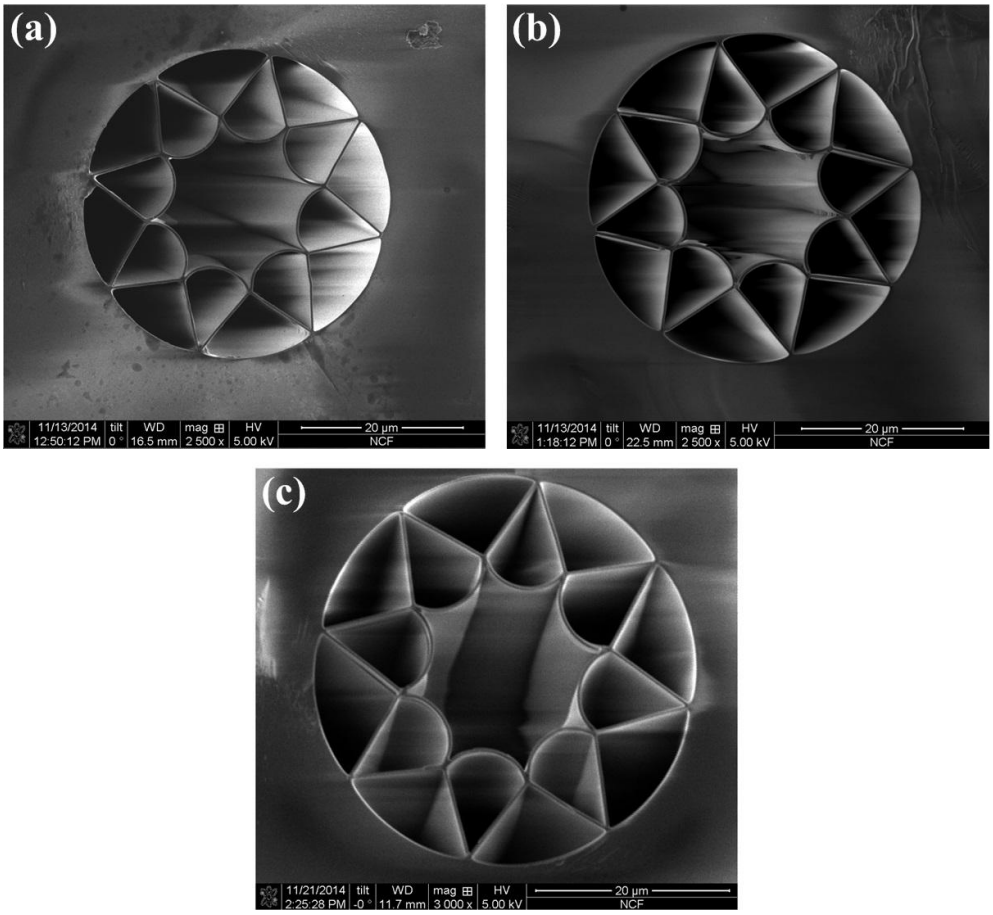

Fig. 3.17. SEM images of: (a) NCF-240314-G; (b) NCF-080414-G; (c) NCF-150414-G. Note different magnification used in the SEM.

Table 3.4. Physical parameters of the green NCFs.

Fibre	Core wall thickness* [nm]	Core diameter** [µm]
NCF-240314-G	520 ± 30	16 ± 1
NCF-080414-G	550 ± 30	15 ± 1
NCF-150414-G	550 ± 30	15 ± 1

*,** Core wall thickness and core diameter are defined as shown in Fig. 3.1.

To position the low loss guidance bandwidth of the fibres in the green spectral range the thickness of their core wall was set to 520 ± 30 nm and 550 ± 30 nm for the NCF-240314-G and both NCF-080414-G and NCF-150414-G respectively, which corresponds to the second antiresonant bands of these structures. The measured (by Dr. Fei Yu at the University of Bath with cutback method and a broadband light source) low attenuation transmission windows of the considered fibres are shown in Fig. 3.18. The width of the low loss regions in the visible is approximately 45 nm, 130 nm and 140 nm the NCF-240314-G, NCF-080414-G and NCF-150414-G respectively. NCF-080414-G

and NCF-150414-G were better optimised for the transmission at this wavelength range, therefore both exhibit a more uniform bandwidths in comparison with the NCF-240314-G (first fabricated NCF for green) where higher loss peaks are visible along its bandwidth. Furthermore, the attenuation spectrum of NCF-080414-G is flatter for wavelengths below 510 nm in comparison with the data from NCF-150414-G, which could result from some differences in structures along both fibres formed during the fabrication process. The NCF-150414-G, however, exhibits lowest loss in the spectral region where high energy pulsed lasers operate. The width of low loss band of the optimised fibres is comparable with the results reported with a Kagome hypocycloid HC-PCF [20].

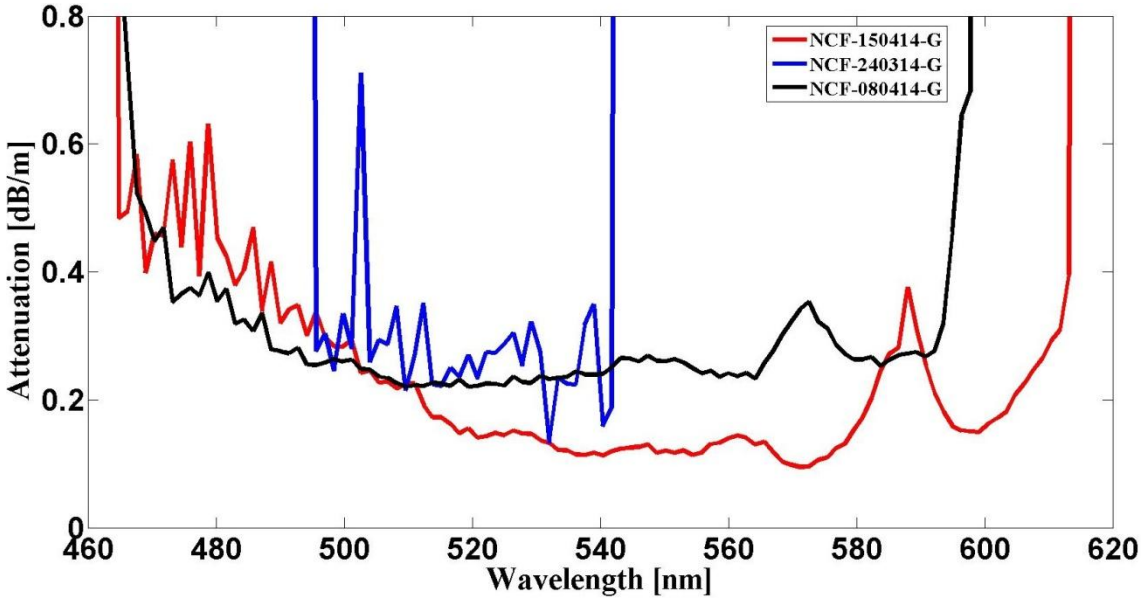

Fig. 3.18. Attenuation spectra of NCF-240314-G (blue line), NCF-080414-G (black line) and NCF-150414-G (red line). Results provided by Dr. Fei Yu (University of Bath).

In addition to results presented above, the attenuation of each NCF was measured and calculated at 515 nm and 532 nm. Here, the Trumpf TruMicro ps laser and the Spectra Physics ns laser operating at their second harmonic wavelengths were used as light sources. The measurements and calculations were conducted in the same manner as described in subsection 3.1.1. Similar to the approach used in the NIR 1 m straight fibres were cut to 10 cm in order to prevent potential micro-bends having a negative impact on the measured values. The measurements and calculations were repeated five times for each fibre and the results uncertainty was estimated using the standard deviation method as discussed in subsection 3.1.1. The results are included in Table 3.5. The higher attenuation of the NCF-240314-G at both wavelengths in comparison with the other fibres is likely to be linked to surface scattering due to the

non-uniform structure of this fibre [7]. The attenuation of NCF-080414-G and NCF-150414-G was calculated to be at the similar level. The results obtained with all fibres show significant improvement in comparison with typical HC-PCFs where the lowest reported attenuation reached 0.5 dB/m at 540 nm [22]. Furthermore, the attenuation of the NCF-150414-G is at level comparable with what is achievable with the Kagome hypocycloid HC-PCF [21].

Table 3.5. Attenuation of the NCFs at 515 nm and 532 nm.

	515 nm				532 nm			
Fibre	**Measured Attenuation [dB/m]**	**$\bar{x}$ [dB/m]**	**σ [dB/m]**	**α [dB/m]**	**Measured Attenuation [dB/m]**	**$\bar{x}$ [dB/m]**	**σ [dB/m]**	**α [dB/m]**
NCF-240314-G	0.22	0.22	0.01	0.22±0.01	0.19	0.21	0.01	0.21±0.01
	0.21				0.21			
	0.22				0.23			
	0.22				0.21			
	0.24				0.22			
NCF-080414-G	0.18	0.19	0.01	0.19±0.01	0.15	0.15	0.01	0.15±0.01
	0.20				0.15			
	0.19				0.18			
	0.19				0.15			
	0.21				0.14			
NCF-150414-G	0.19	0.18	0.01	0.18±0.01	0.16	0.15	0.01	0.15±0.01
	0.18				0.14			
	0.18				0.15			
	0.17				0.17			
	0.20				0.15			

3.1.2.1 Characterisation of fibre delivered beam

In order to determine the guidance behaviour of NCFs (single- or multimodeness) their outputs were characterised by capturing near-field delivered beam profiles with the CCD camera and Spiricon software using the method described in more detail in subsection 3.1.1.1. The MFDs of the fibres were measured by using $1/e^2$ criteria directly

from the recorded spatial profiles. Near-field NCF delivered beam profiles at 515 nm and 532 nm and corresponding mode field diameters are presented in Fig. 3.19 and Table 3.6 respectively. The beam profiles delivered through NCF-230414-G and NCF-080414-G indicate that they are somewhat few-moded (discussed further in subsection 3.1.2.2). The NCF-150414-G provides stable and singlemode output at both wavelengths (the distortions present in the images are due to interference features from the filters used in the imaging system, rather than the excitation of the higher order modes). Similar to the NIR results, the difference in delivered beam profiles at 515 nm and 532 nm relates to the position of these wavelengths in the transmission window, the shape of the bandwidth and the beam profile of the lasers used. Furthermore, the beam profile (especially at 515 nm) provided by the NCF-150414-G is more Gaussian like in comparison with the output of hypocycloid Kagome fibre [21]. No difference in the MFDs at both wavelengths was observed with each fibre.

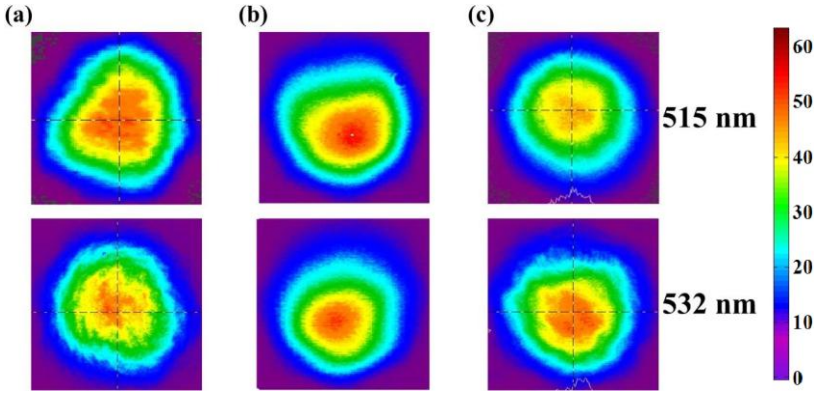

Fig. 3.19. Near-field beam profiles delivered at 515 nm and 532 nm through: (a) NCF-240314-G; (b) NCF-080414-G; (c) NCF-150414-G.

Table 3.6. MFDs of the NCFs in the green spectral region.

	MFD ($1/e^2$) [µm]	
Fibre	**515 nm**	**532 nm**
NCF-240314-G	9 ± 1	
NCF-080414-G	8 ± 1	
NCF-150414-G	8 ± 1	

The quality of delivered beams at both investigated wavelengths was determined by M^2 measurements. The experiments and calculations were conducted using the same method and optical arrangement as discussed in subsection 3.1.1.1. Similar to the

experiments performed with NIR NCFs the measurements and calculations were repeated five times for all fibres and the measurement uncertainty was calculated using the standard deviation. The results are presented in Figs. 3.20(a), 3.20(b) and 3.21 for the NCF-230414-G, NCF-080414-G and NCF-150414-G respectively. No significant difference between the M^2 values calculated at 515 nm and 532 nm was observed for each fibre. However, the results obtained with the NCF-150414-G at both wavelengths were additionally included as this particular fibre (due to the best performance) was used as a beam delivery tool for micro-machining with ns and ps systems (see chapter 5 for further details). All the NCFs delivered a high quality beam (M^2 in the range of 1.3 - 1.4 ± 0.1) at both wavelengths. Furthermore, the results obtained with NCF-230414-G and NCF-080414-G (low M^2 values) can indicate that the majority of the delivered light was guided within the fundamental mode without coupling to higher order modes (despite the few-moded behaviour observed with both fibres). The measurements confirmed that the fibre delivered light is well-suited to precision micro-machining. Further details can be found in chapter 5 and reference [23].

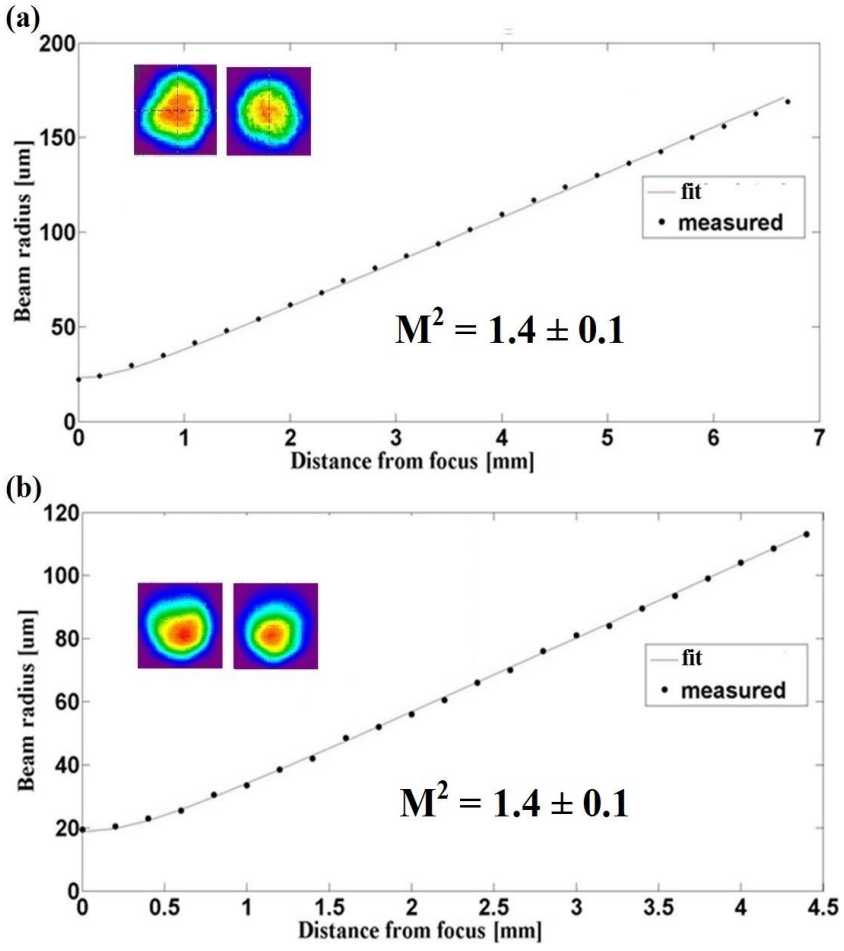

Fig. 3.20. M^2 of the beams delivered at 515 nm and 532 nm through: (a) NCF-230414-G and (b) NCF-080414-G.

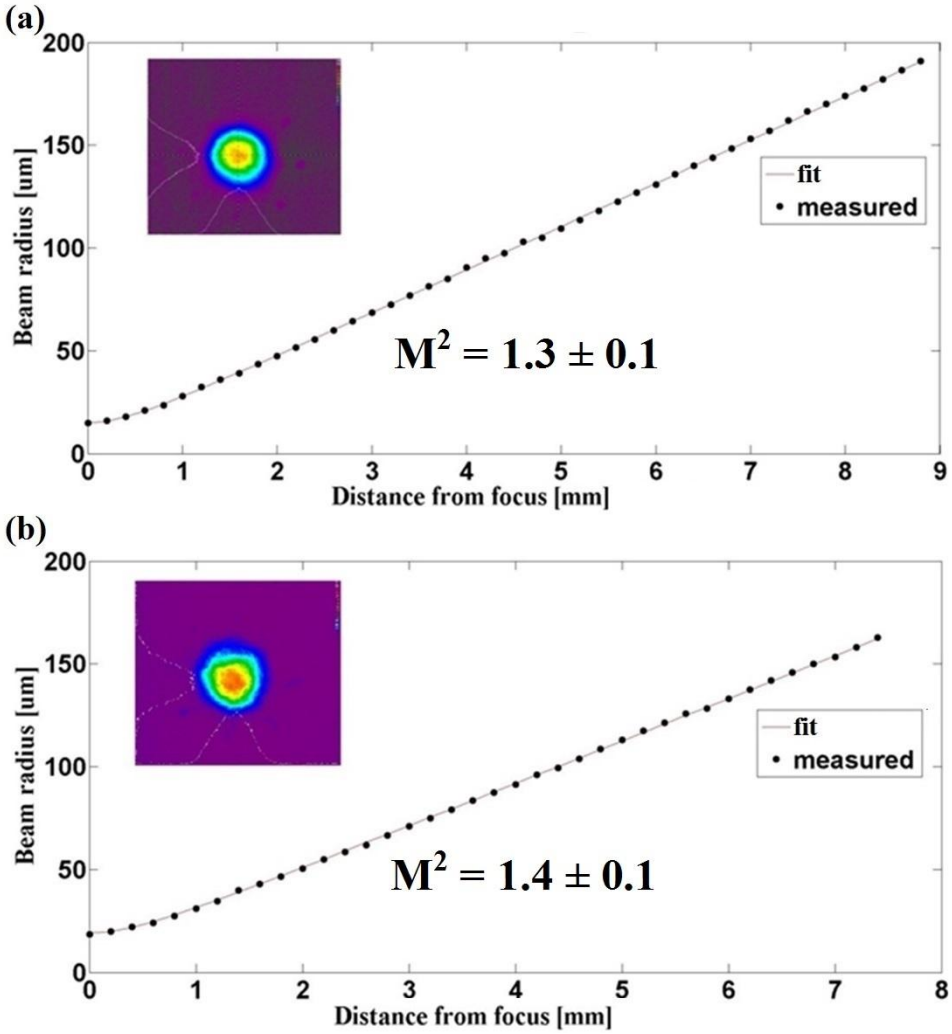

Fig. 3.21. Measured M^2 of the beam after propagation through NCF-150414-G at: (a) 515 nm and (b) 532 nm.

3.1.2.2 Impact of fibre bending

The bending properties of NCFs in the green spectral range were investigated by bending each fibre (1.2 m long) into semi circle (180º bend) with different bending diameters. The measurements were conducted for bend diameters from 25 cm to 1 cm in the case of NCF-150414-G and NCF-080414-G and down to 1.5 cm with the NCF-230414-G (for smaller bend dia. this particular fibre broke due to the tension introduced).

The experiments used the setup previously shown in Fig. 3.8. Similar to the measurements in the NIR the output of each fibre was monitored during bending and delivered beam profiles for each bending diameter were captured with the CCD camera and Spiricon software. The results plotted in Figs. 3.22(a), 3.23(a) and 3.24(a) show overall low sensitivity to bending of all fibres, provided the bend diameter > 5 cm. The

better performance of the NCF-150414-G gives a lower bend loss, especially for the very tight bends in comparison with other fibres. Furthermore, no bend-induced loss was observed for bend diameters above 8 cm with the NCF-150414-G. The captured beam profiles delivered through the NCF-150414-G shown in Figs. 3.22(b) and 3.22(c) confirm singlemode operation and great stability of this fibre with both lasers, however with the mode closer to Gaussian at 515 nm (similar phenomenon was observed with the fibres operating in the NIR and its origin is discussed in subsection 3.1.1.2). Few-moded NCF-230414-G exhibits a significant instability of its output induced by bending as shown in Figs. 3.23(b) and 3.23(c). This instability can be associated with a change in the interference pattern at the fibre output resulting from path length changes of the excited modes whilst bending the fibre. The NCF-080414-G, also supporting multiple modes, has better output stability (see Figs. 3.24(b) and 3.24(c)) as well as lower bend loss in comparison with NCF-230414-G mainly resulting from optimised shape and the position of low loss region. Furthermore, the delivered beam profile images presented for both few-moded NCFs were not associated with particular bend diameter but are rather an example of fluctuations induced by bending. Moreover, a significant leakage of transmitted light was observed from the bent part of each fibre (a similar effect was noticed with the NIR NCFs) as shown in Fig. 3.25.

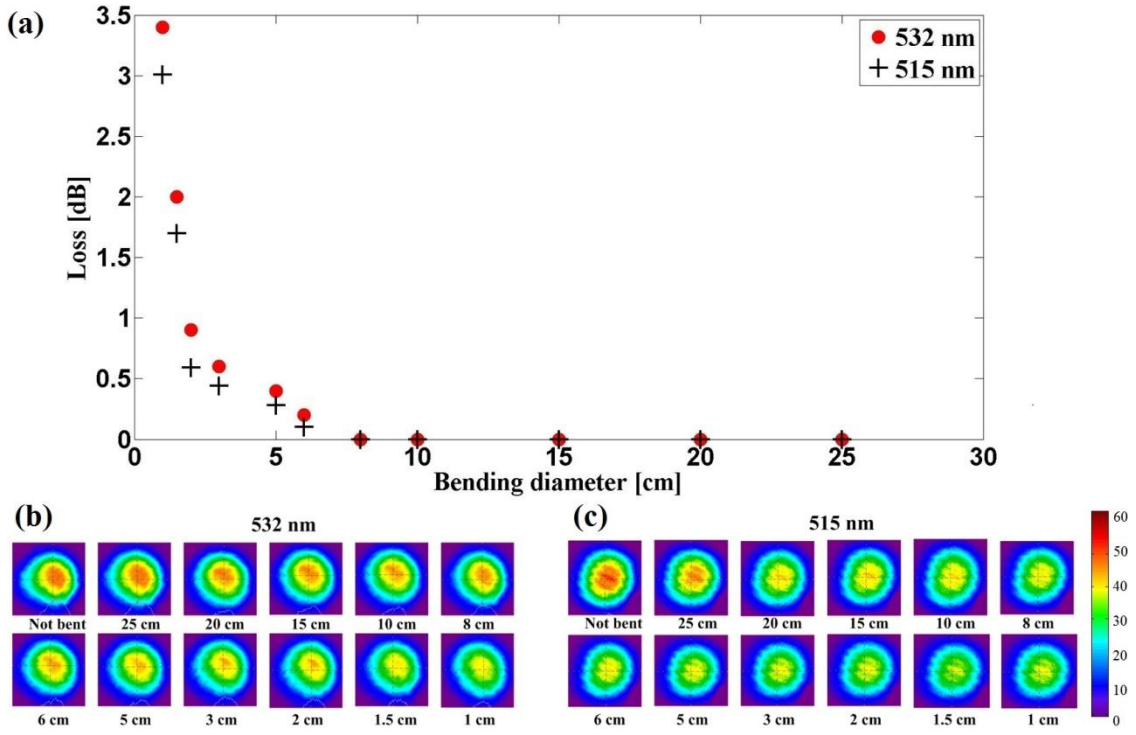

Fig. 3.22. Results of bending tests with 1.2 m NCF-150414-G in the green: (a) loss introduced by bending the fibre through 180º with different bend diameters; (b) Delivered beam pattern changes due to bending at 532 nm; (c) Transmitted spatial beam profiles captured for different bending diameters at 515 nm.

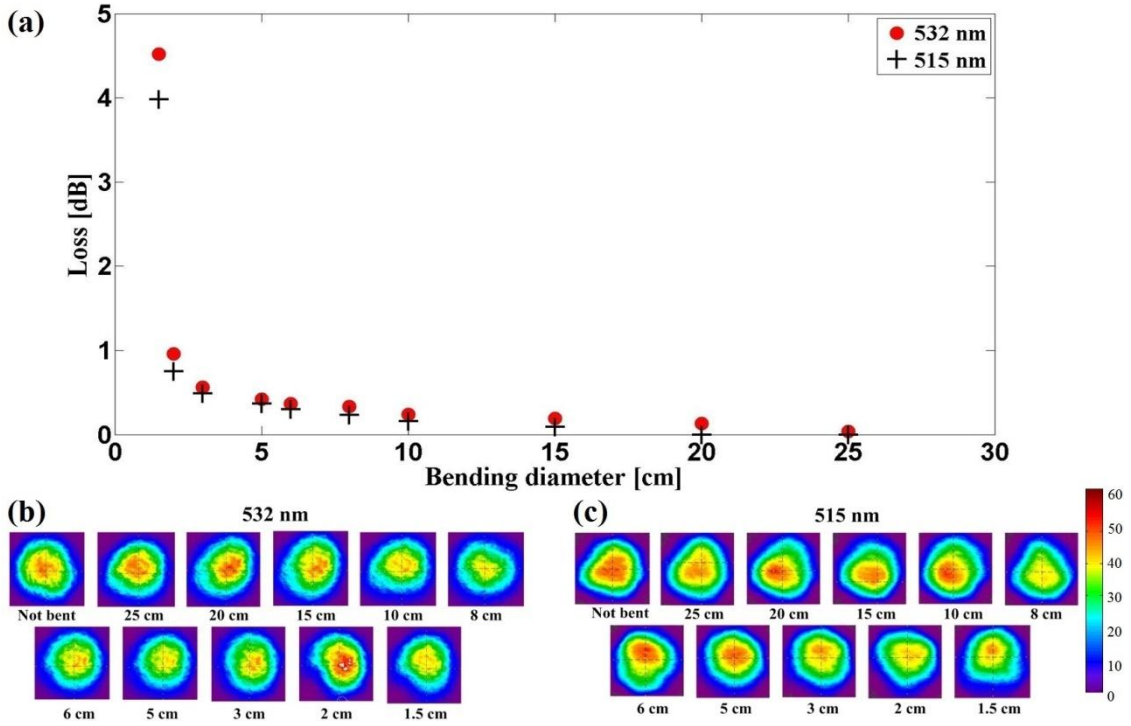

Fig. 3.23. (a) Loss introduced by bending 1.2 m long NCF-240314-G through 180º in the green spectral range. Delivered beam profile changes due to fibre bending at: (b) 532 nm and (c) 515 nm.

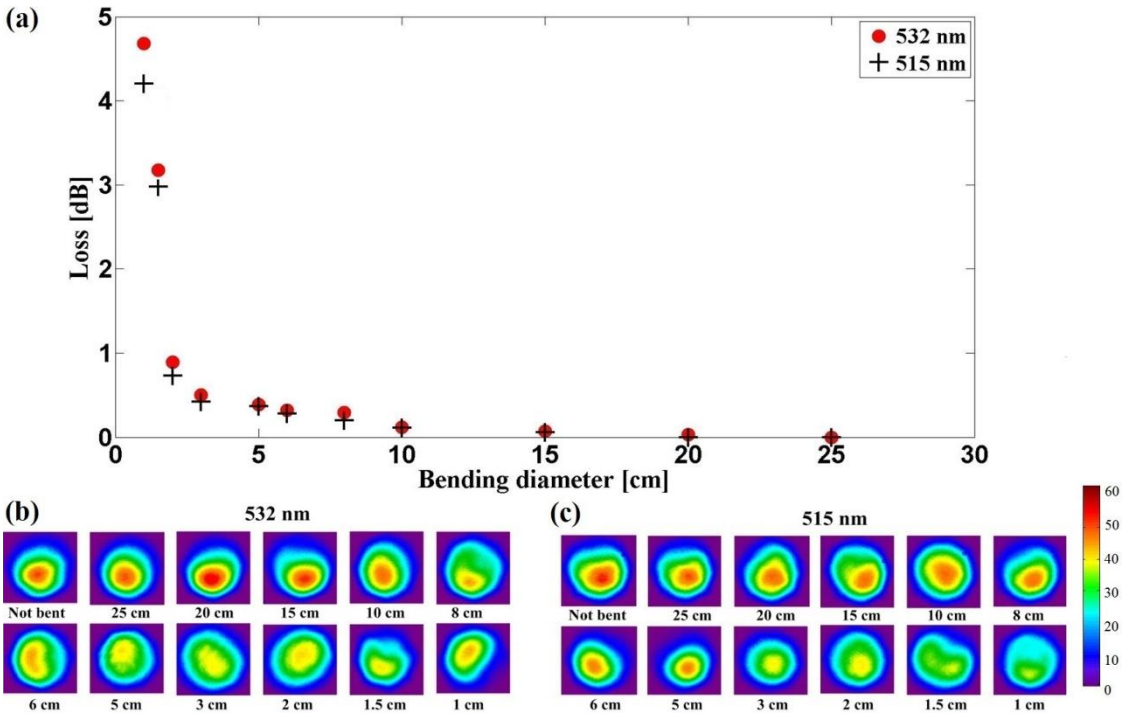

Fig. 3.24. Bending properties of NCF-080414-G: (a) Loss introduced by bending 1.2 m fibre by 180º for different bend diameters; (b) Changes in delivered beam profiles induced by bending at 532 nm; (c) Different delivered beam profiles as a results of fibre bending at 515 nm.

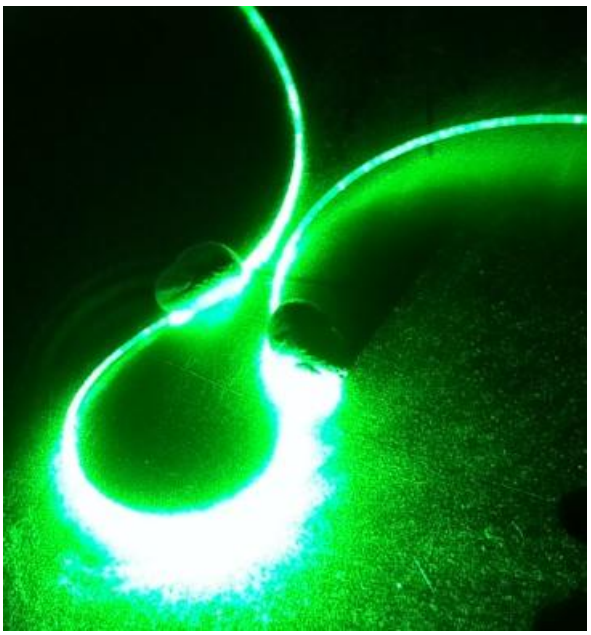

Fig. 3.25. Leakage of transmitted light from the bent part of the reviewed NCFs.

The impact of bending with the negative curvature fibres operating in the green spectral region could not be compared with other hollow-core fibres (hypocycloid Kagome and typical HC-PCFs) at the time of writing this thesis due to the lack of publicly available comparative data.

3.2 Free Boundary Anti-Resonant Fibre (FBARF)

This section is focused on the characterisation of a novel type of hollow-core fibre with negative curvature of the core wall, the so called Free Boundary Anti-Resonant Fibres (FBARFs) designed for guidance in the NIR and green spectral regions. Two types of these fibres with double (NIR) and single (green) antiresonant structures were investigated within this work. The most important parameters of these fibres such as attenuation, quality of the delivered beam and bending sensitivity were established. The fibres were designed and fabricated by Dr. Walter Belardi at the University of Bath.

The concept of the free boundary cladding with single and double antiresonant structures is discussed in more details in subsection 2.2.2.4.2.

3.2.1 Double-layer FBARF for guidance in the NIR

The FBARF with a double-layer cladding forming its anti-resonant structure is shown in Fig. 3.26 together with its physical parameters included in Table 3.7.

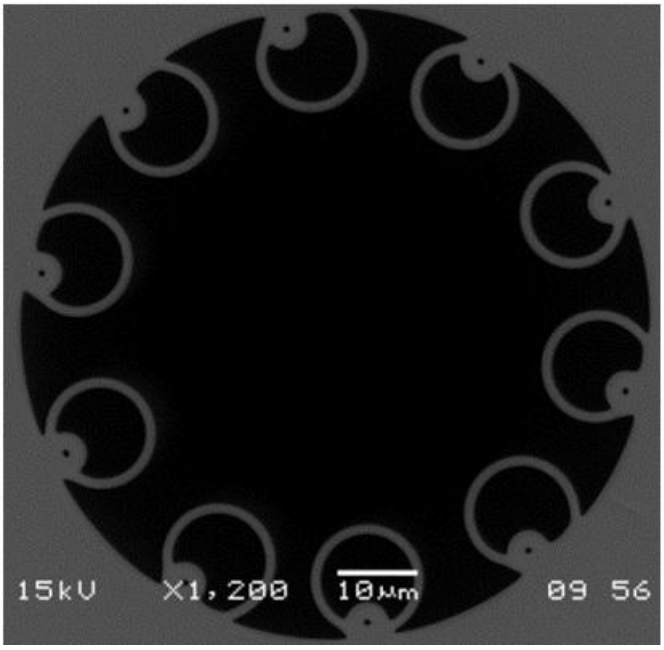

Fig. 3.26. SEM image of double-layer FBARF. Image provided by Dr. Walter Belardi [24].

Table 3.7. Physical parameters of double-layer FBARF.

Fibre	**Core wall thickness*** **[µm]**	**Core diameter** [µm]**
double-layer FBARF	1.33 ± 0.05	51 ± 1

*Thickness of the outer capillaries forming the cladding. **Defined as a distance between the diagonal capillaries.

The guidance properties of this modified structure of the negative curvature fibre are still described by the ARROW model, and therefore the thickness of the cladding strut defines the position of low loss region in the optical spectrum. The double-layer fibre was designed to guide in the NIR spectral regime, in particular around 1 µm wavelength, hence the core wall thickness was set to approximately 1.33 ± 0.05 µm. The fibre has a hollow air-core with a diameter of 51 ± 1 µm (larger in comparison with the NCFs). The cutback measurements performed by Dr. Walter Belardi at the University of Bath indicated a low loss region spanning 975 nm to 1125 nm as presented in Fig. 3.27. The results show no improvement in the attenuation level in comparison with the NCFs discussed in subsection 3.1.1 and Kagome hypocycloid fibres [5]. Furthermore, additional low loss transmission windows (with centre wavelengths of 480 nm, 600 nm and 1600 nm) corresponding to the higher antiresonant bands were observed. The guidance properties of the fibre within these other low loss windows are not investigated in this thesis.

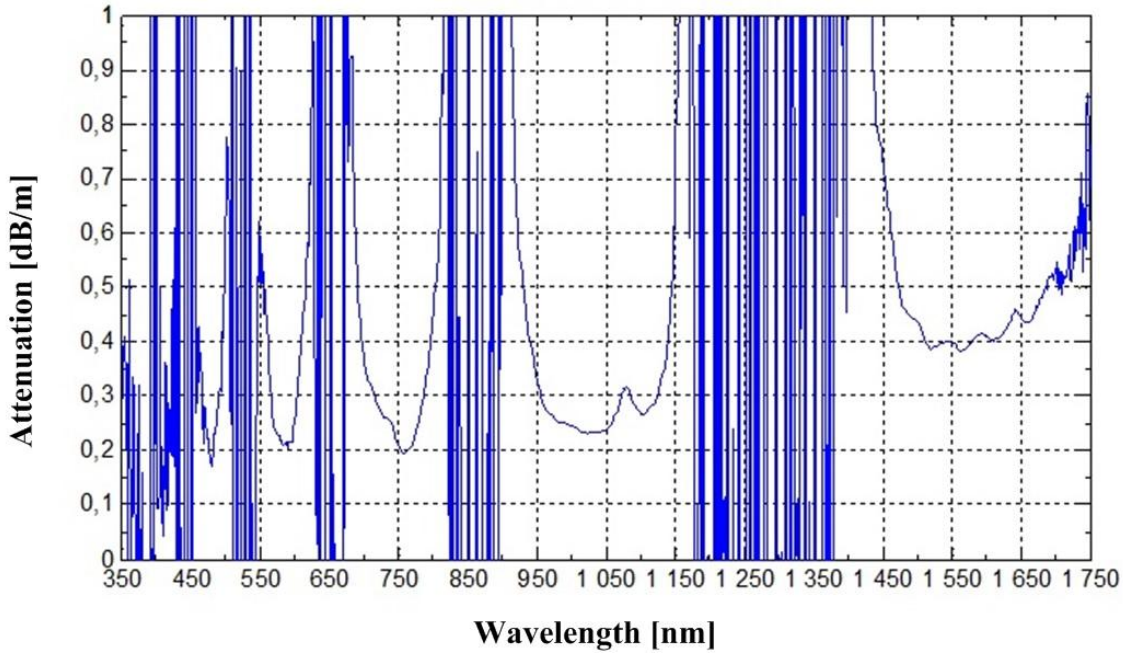

Fig. 3.27. Attenuation spectrum of double-layer FBARF. Data provided by Dr. Walter Belardi [21].

The attenuation of double-layer FBARF at 1030 nm and 1064 nm (the same ps and ns lasers described in previous subsections of this chapter were used as light sources) were measured by performing additional cutback measurements using the same approach as described in subsection 3.1.1. The fibre was cut from 1 m to 10 cm at both wavelengths. The measurements and calculations were performed five times and the uncertainty of the results was estimated using the standard deviation as discussed in subsection 3.1.1. The calculated attenuations were 0.33 ± 0.01 dB/m and 0.45 ± 0.01 dB/m at 1064 nm and 1030 nm respectively as included in Table 3.8. The difference in the attenuation between two wavelengths is mainly caused by few-moded behaviour of the fibre at 1030 nm (more details can be found in subsection 3.2.1.1). Furthermore, the higher level of attenuation in comparison with other antiresonant fibres is most likely to be related to imperfections of the fibre structure, i.e. a significant lack of symmetry in the alignment between each pair of diagonal inner (nested) capillaries (forming the second layer of the cladding) which has a strong impact on the leakage loss [24]. The level of leakage loss in this particular structure depends on the angle between two diagonal nested tubes, and therefore increases with the size of the angle [24].

Table 3.8. Attenuation of double-layer FBARF at 1030 nm and 1064 nm.

	1064 nm				1030 nm			
Fibre	**Measured Attenuation [dB/m]**	**$\bar{x}$ [dB/m]**	**σ [dB/m]**	**α [dB/m]**	**Measured Attenuation [dB/m]**	**$\bar{x}$ [dB/m]**	**σ [dB/m]**	**α [dB/m]**
double-layer FBARF	0.32	0.33	0.01	0.33±0.01	0.45	0.45	0.01	0.45±0.01
	0.33				0.45			
	0.33				0.42			
	0.31				0.45			
	0.34				0.46			

3.2.1.1 Characterisation of fibre delivered beam

The fibre output was characterised by directly imaging on the CCD camera connected with Spiricon beam profiling software using the experimental setup shown in Fig. 3.4. The delivered near-field spatial beam profiles recorded at 1030 nm and 1064 nm are shown in Fig. 3.28. The pattern of the mode at 1064 nm is closer to being singlemode than that at 1030 nm, however with an insignificant amount of light in higher order modes, which gives a relatively week inference pattern. The difference between the two wavelengths is likely to result from the non-optimised structure and parameters of this fibre (the first fabricated FBARF for the NIR).

The mode field diameters at both considered wavelengths were calculated (using the $1/e^2$ criteria) from captured near-field beam profiles and results were included in Table 3.9. No significant difference in MFDs at both wavelengths was noticed.

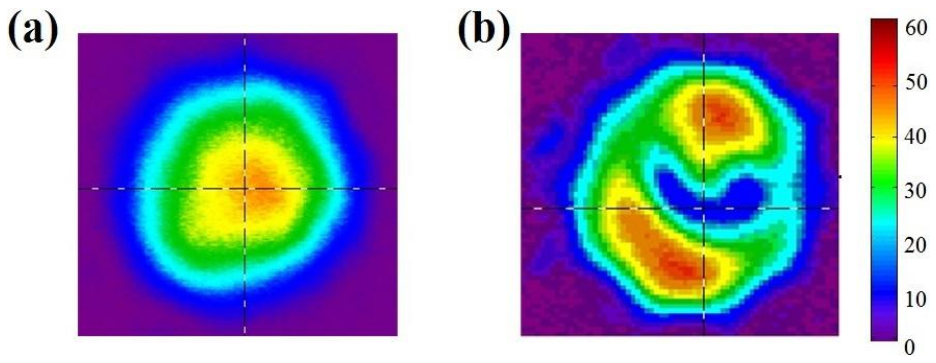

Fig. 3.28. Near-field beam profiles delivered through double-layer FBARF at: (a) 1064 nm and (b) 1030 nm.

Table 3.9. MFDs of double-layer FBARF in the NIR.

	MFD ($1/e^2$) [µm]	
Fibre	**1030 nm**	**1064 nm**
double-layer FBARF	41 ± 1	

To determine the quality of beams delivered at both wavelengths through the double-layer FBARF M^2 measurements were carried out. The same method and calculations (for calculation of both M^2 values and the results uncertainty) were applied as discussed in subsection 3.1.1.1. The results are plotted in Fig. 3.29. The M^2 of 1.6 ± 0.1 and 3.3 ± 0.1 obtained at 1064 nm and 1030 nm respectively are at the level comparable with the beam quality provided by few-moded NCF-01, still acceptable for many micro-machining applications.

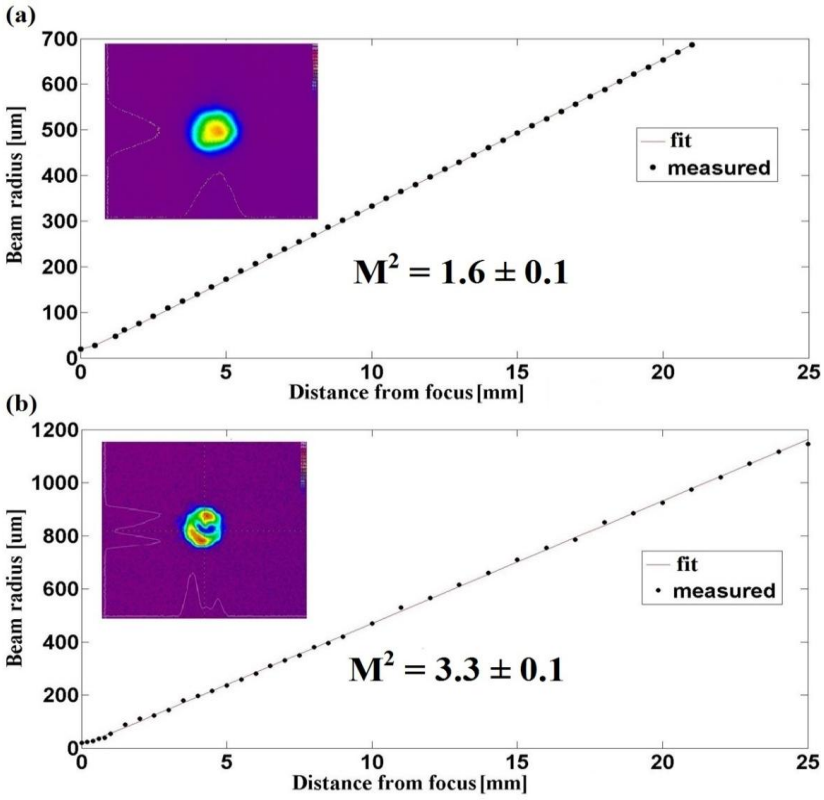

Fig. 3.29. M^2 of the beam delivered through double-layer FBARF at: (a) 1064 nm and (b) 1030 nm.

3.2.1.2 Impact of fibre bending

Sensitivity to bending of the double-layer FBARF was established by calculating the loss introduced by bending a 1 m long fibre through 180º (with different bend diameters) using the same methods as described earlier in this chapter. Again, the response of fibre to bending in terms of the delivered beam stability was characterised

by capturing near-field beam patterns for each bend diameter using a similar approach as with the NCFs. The calculated loss plotted in Fig. 3.30(a) shows significant sensitivity to bending for the bend diameters below 5 cm, a similar trend to the results obtained with the NCFs. However, the level of bend-induced loss in this bending regime is significantly higher (by up to 5 dB) in comparison with that measured in NCF-140414 and NCF-150414-G. This higher sensitivity to bending for very tight bends is due to few-moded guidance of the fibre, and a similar phenomena was observed with NCF-01 (also few-moded at 1 μm). Nevertheless, for the larger bend diameters the bend losses are comparable with the values for the NCFs. The lower loss observed at 1064 nm in comparison with 1030 nm is mainly due to the few-moded guidance of the fibre at 1030 nm, and stronger coupling between the higher order modes and cladding modes. Examples of the delivered beam profile changes (not specific to a particular bend diameter) induced by bending demonstrate significant intermodal inference, hence an unstable beam profile (as earlier observed with the NCFs) as shown in Figs. 3.30(b) and 3.30(c).

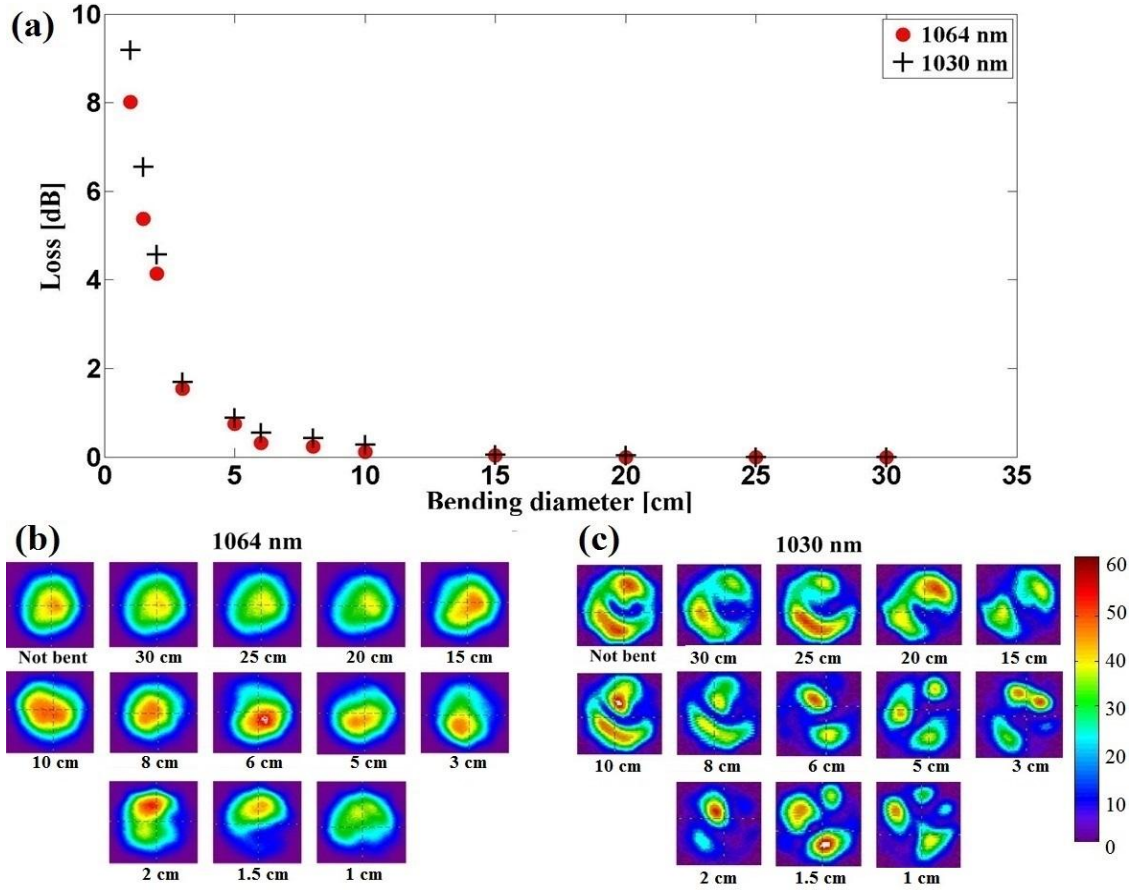

Fig. 3.30. (a) Loss resulted from bending 1 m double-layer FBARF by 180º with different bend diameters. Examples of the bending influence on the delivered beam profiles at: (b) 1064 nm and (c) 1030 nm.

3.2.2 Single-layer FBARF for transmission in the green spectral region

The FBARF designed and fabricated for guidance in the green spectral region has an antiresonant structure without the additional capillaries stacked inside the first cladding layer. An SEM image of the investigated fibre is shown in Fig. 3.31. The physical parameters of the fibre are presented in Table 3.10.

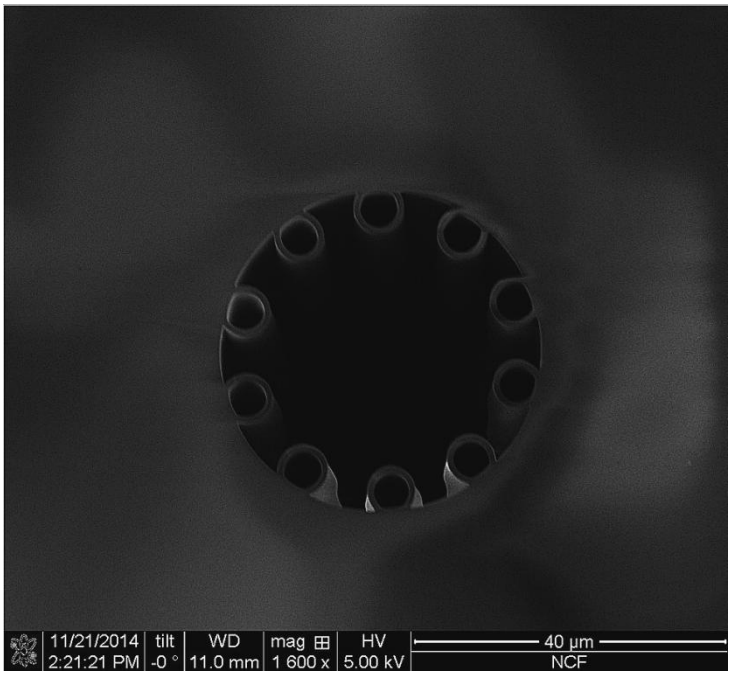

Fig. 3.31. SEM image of single-layer FBARF.

Table 3.10. Physical parameters of single-layer FBARF.

Fibre	**Core wall thickness*** **[nm]**	**Core diameter**** **[µm]**
single-layer FBARF	800 ± 50	34 ± 1

*Thickness of the capillaries forming the cladding. **Defined as a distance between the diagonal capillaries.

The FBARF core diameter of 34 ± 1 µm is approximately 3 and 1.5 times larger than that of the NCF and Kagome hypocycloid fibres [21] respectively designed to operate in the same spectral window. This could potentially provide an increase in damage threshold a larger guided mode, and hence a lower energy density present on the fibre input end-facet (this issue is further investigated in chapter 4). The core wall thickness was approximately 800 ± 50 nm, which resulted in several low loss transmission bands in the attenuation spectrum shown in Fig. 3.32, measured using a cutback method and a broadband light source (a tungsten halogen lamp) by Dr. Walter Belardi at the University of Bath. The transmission band of particular interest to the

work presented in this thesis covers approximately 80 nm of the green spectral region (500 - 580 nm). The attenuation in this low loss region is however higher than that of the NCFs designed for the same wavelength range and it lacks of uniformity.

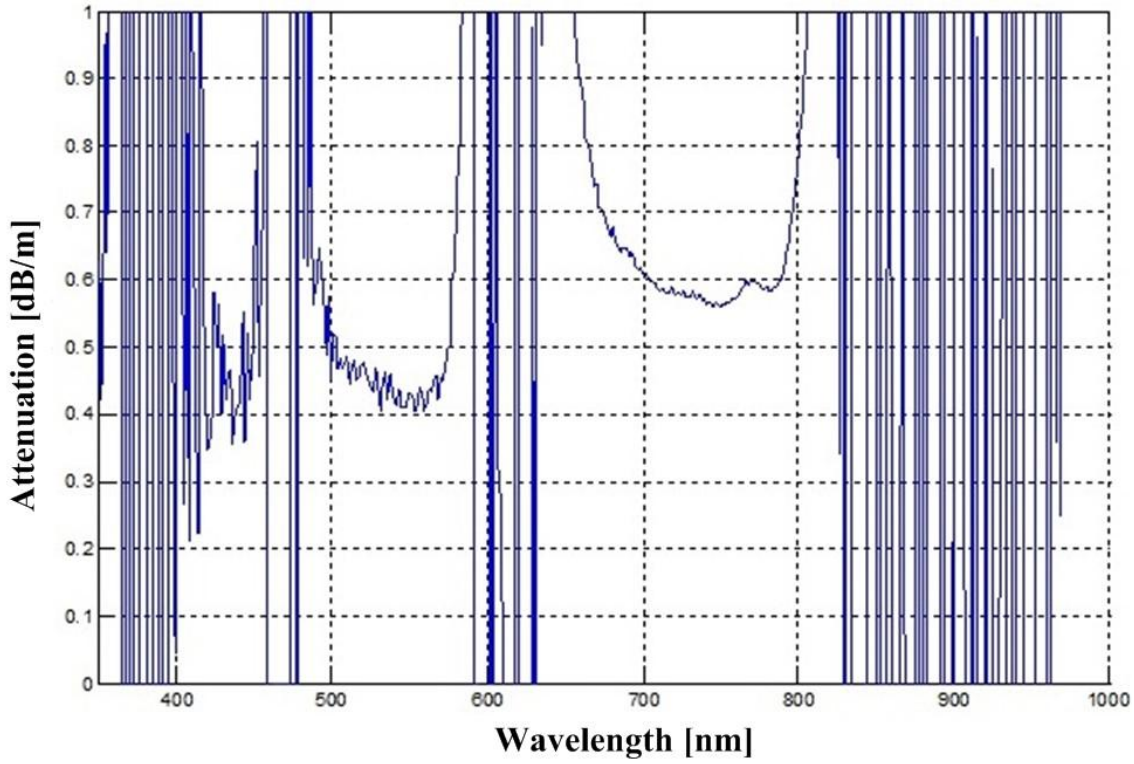

Fig. 3.32. Attenuation spectrum of single-layer FBARF. Data provided by Dr. Walter Belardi.

The attenuation of this fibre at the wavelengths of interest in the green spectral region (532 nm and 515 nm) was measured by the cutback method (discussed in subsection 3.1.1) where a 1 m, straight fibre was cut to 10 cm. The measurement and calculation procedures were the same as discussed in subsection 3.1.1. The calculated values of attenuations at 532 nm and 515 nm are shown in Table 3.11. The fibre exhibits very high loss at both wavelengths most likely due to its few-moded nature as shown in Fig. 3.33. Furthermore, the attenuation is an order of magnitude higher than that of the 'green' NCFs and hypocycloid Kagome fibre [21], which disqualifies this fibre from use as a practical beam delivery tool. However, as this particular fibre is an initial attempt to fabricate such a fibre, optimisation of its properties (dependent on fabrication process and the shape of low loss region) is likely to result in performance improvements.

Table 3.11. Attenuation of single-layer FBARF at 532 nm and 515 nm.

	532 nm				515 nm			
Fibre	**Measured Attenuation [dB/m]**	**$\bar{x}$ [dB/m]**	**σ [dB/m]**	**α [dB/m]**	**Measured Attenuation [dB/m]**	**$\bar{x}$ [dB/m]**	**σ [dB/m]**	**α [dB/m]**
single-layer FBARF	1.21	1.20	0.01	1.20±0.01	1.10	1.08	0.01	1.08±0.01
	1.18				1.08			
	1.20				1.09			
	1.20				1.06			
	1.22				1.0			

3.2.2.1 Characterisation of fibre delivered beam

The delivered beam was again characterised by directly imaging the fibre output on the CCD camera and capturing near-field beam profiles (in the setup from Fig. 3.4). The profiles at 532 nm and 515 nm were analysed with Spiricon software and examples are shown in Figs. 3.33(a) and 3.33(b) respectively. The results clearly indicate few-moded guidance of the fibre. Furthermore, it was not possible to excite only the fundamental mode at either wavelength. Even after propagation through approximately 7 m (the longest available fibre) higher order modes were not attenuated and the few-moded behaviour was maintained.

The MFDs at both wavelengths were defined by $1/e^2$ criteria with no difference observed between two wavelengths. The MFDs are included in Table 3.12.

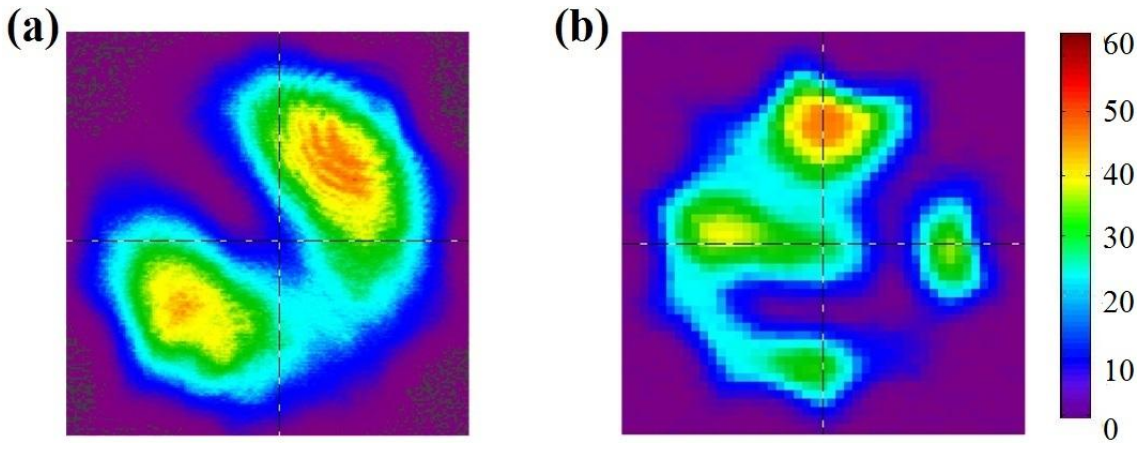

Fig. 3.33. Near-field beam profiles delivered through single-layer FBARF at: (a) 532 nm and (b) 515 nm.

Table 3.12. MFDs of single-layer FBARF at 532 nm and 515 nm.

	MFD ($1/e^2$) [µm]	
Fibre	**532 nm**	**515 nm**
single-layer FBARF	26 ± 1	

The quality of fibre delivered beam was determined by M^2 measurements and calculations conducted using the approach described in subsection 3.1.1.1. The measured M^2 at both wavelengths was 3.5 ± 0.1 as shown in Fig. 3.34. This is expected as a result of few-moded nature of the fibre.

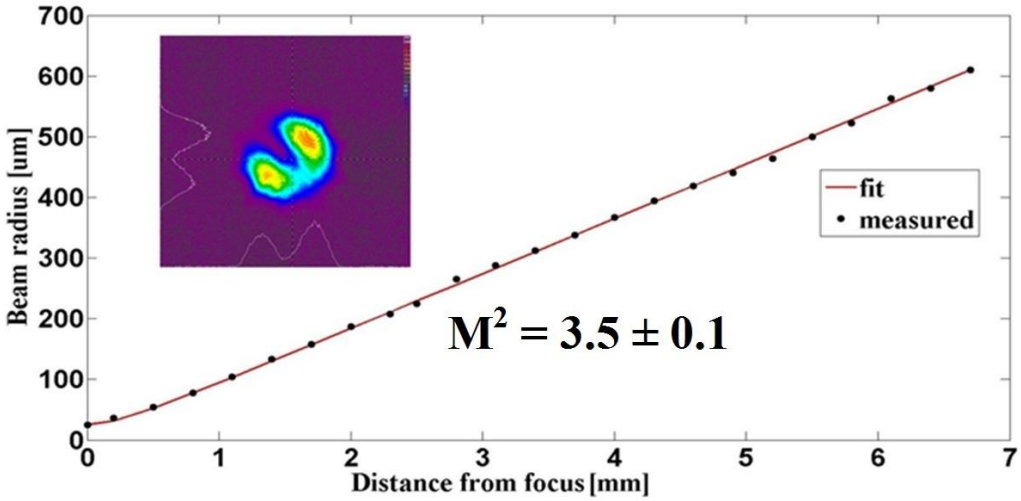

Fig. 3.34. Typical beam quality delivered through single-layer FBARF at 532 nm and 515 nm.

3.2.2.2 Impact of fibre bending

Similar to the measurements conducted with 'green' NCFs the bending properties of single-layer FBARF were established with a 1 m fibre bent through 180º with different bend diameters at both investigated wavelengths. The experimental setup and measurement procedure were the same as described in subsection 3.1.1.2. The results plotted in Fig. 3.35(a) show that bending significantly influences the fibre performance for bend diameters below 20 cm. Furthermore, the difference in bend loss is close to 7 dB for the tightest bend diameter in comparison to NCF-150414-G. The changes in the delivered beam profiles (modal interference patterns) shown in Figs. 3.35(b) and 3.35(c) for 532 nm and 515 nm respectively indicate coupling between the higher order modes guided within the fibre or a change in the relative phases of the modes altering the interference pattern. The different beam profiles are not specific to a particular bend diameter and represent fluctuations of fibre output at any bend radius. Furthermore, a

presence of light in the cladding was observed at 532 nm which resulted from coupling between the core modes and the cladding modes due changes in the fibre structure induced by bending (and therefore increased bend loss). It can be assumed that poor bending properties of this fibre are mainly due to its few-moded nature. The properties of single- and double-layer FBARFs despite of the same structural principle cannot be directly compared due to the guidance in different spectral regions.

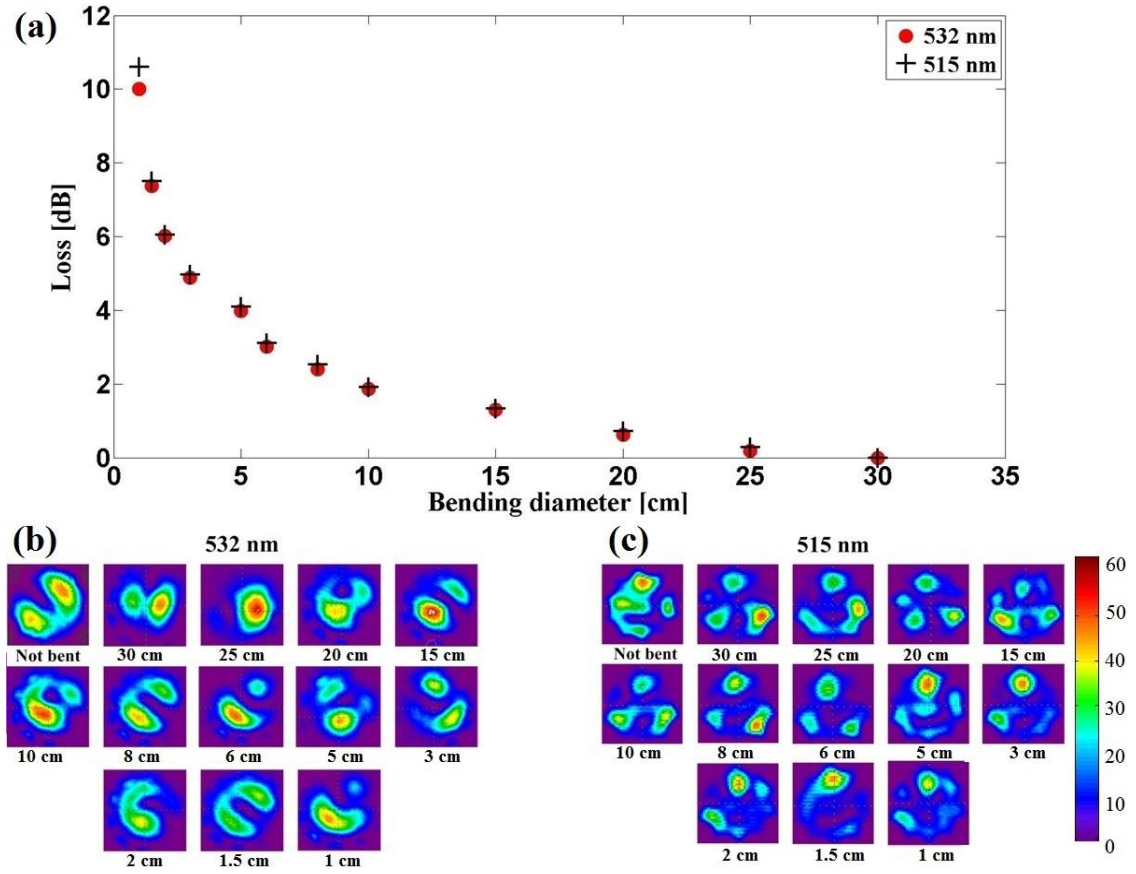

Fig. 3.35. (a) Bending loss present in 1 m single-layer FBARF due to bending by 180º with different bend diameters at 532 nm and 515 nm. Delivered beam profile changes induced by fibre bending captured at: (b) 532 nm and (c) 515 nm.

3.3 Summary

Chapter 3 presents the study of physical and optical properties of Negative Curvature Fibres and Free Boundary ARFs for guidance in the NIR and green spectral regimes.

The development of the NCF fibres discussed within this thesis is a result of close collaboration between Heriot-Watt University (myself in major together with Dr Richard Carter, Dr Robert Maier, Dr Jonathan Shephard and Prof Duncan Hand) and University of Bath (Prof Jonathan Knight's research group). The NCF-01 was the first fibre (for guidance in the NIR) fabricated in order to establish the performance and

weak points of this particular fibre concept. The entire characterisation of the NCF, which included transmission measurements, bending sensitivity tests and characterisation of fibre output was performed by myself and have indicated the main issues of the structure i.e. sensitivity to bending and few-moded guidance resulting in unstable output and poor quality of the fibre-delivered beam. Based on these results and discussion between the collaborators during the project meetings we have established that the main reason of the aforementioned problems was the position of the guided wavelength in the low loss transmission window (the guided wavelength must be positioned in the middle, flat part of the transmission window instead of being placed towards the edges of the bandwidth were the high loss regions begin). This meant that the thickness of the core wall (which defines the guided wavelength range) needed to be precisely adjusted in order to shift the low loss bandwidth so that the guided wavelength was no longer positioned on the edges of the transmission window. The next fabricated 1 μm fibre - NCF-140414 has been shown to exhibit a flat low loss bandwidth in which the wavelengths of interest (1030 nm and 1064 nm) were positioned away from the bandwidth edges. Further experiments performed by myself have proved that the modifications introduced into the fibre structure resulted in stable, singlemode fibre output and significantly lower attenuation and sensitivity to bending. Based on these results we decided to scale down the NCF structure to operate in the visible - green spectral range, more desirable from the micro-machining applications point of view. The initial experiments carried out by myself with the green NCFs have indicated similar problems as observed with the NIR fibres i.e. output instability due to few-moded behavior and bending sensitivity. This was especially significant in the case of the first green NCF - NCF-240314-G which exhibited some asymmetry of the structure. We indicated that the aforementioned asymmetry could have some impact on the light confinement, and therefore could lead to few-moded behavior of the fibre and increased loss. The next green fibres fabricated in Bath have their structure and parameters modified with regards to the results obtained during the experiments I performed (adjusted core wall thickness and improved symmetry). This resulted in significant improvement of the fibre performance i.e. lower sensitivity to bending, lower attenuation and most important singlemode output which led to obtain the best results in terms of ps pulse delivery achieved with silica fibres (see chapter 5 for further details). Based on the obtained results in the green and NIR spectral regions it was stated that the performance limit of the NCF structure was reached and further development of these fibres in these wavelength regimes is not planned for the future.

The NCFs operating at 1 μm wavelength, especially NCF-140414 and NCF-150415-G exhibit excellent performance in terms of attenuation, singlemodeness and delivered beam quality comparable with the parameters of more complex hypocycloid Kagome fibres. The fibres are characterised by low sensitivity to bending, and therefore provide stable output, which is especially desirable in the flexible laser beam delivery systems.

The double-layer FBARF, which is a novel type of ARROW fibre with the inverted curvature of the core wall has not yet shown any improvement in comparison with the NCFs and hypocycloid Kagome fibres. The investigated fibre exhibits a high attenuation, bending sensitivity and few-moded guidance. Nevertheless, further optimisation and studies of this structure will be performed in the future. A comparison of the antiresonant fibres guiding in the NIR investigated within this work is included in Table 3.13.

Table 3.13. Comparison of antiresonant fibres for guidance in the NIR.

Fibre	**NCF-01**	**NCF-140414**	**NCF-150414-G**	**double-layer FBARF**
Core dia. [μm]	43 ± 1	36 ± 1	15 ± 1	51 ± 1
Core wall thickness [nm]	910 ± 50	840 ± 50	550 ± 30	1330 ± 50
MFD [μm]	36 ± 1	24 ± 1	9 ± 1	41 ± 1
Attenuation [dB/m]				
1030 nm	0.23 ± 0.01	0.04 ± 0.01	0.20 ± 0.01	0.45 ± 0.01
1064 nm	0.16 ± 0.01	0.05 ± 0.01	0.24 ± 0.01	0.33 ± 0.01
Guidance	few-moded	singlemode	singlemode	few-moded
M^2	1.5 - 3.2 ± 0.1	1.3 ± 0.1	1.2 ± 0.1	1.6 - 3.3 ± 0.1
Bending sensitivity	high	very low	very low	very high

Three different NCFs for guidance at 515 nm and 532 nm were investigated within this work. The optimisation of fibre structure led to a NCF with parameters significantly better than offered up to date by typical HC-PCFs. The optimised NCF-150414-G exhibits singlemode guidance with very low attenuation at the level compared with hypocycloid Kagome fibres. Furthermore, this fibre exhibits very low bending sensitivity and provides stable output with high quality of the delivered beam extremely important for precision micro-machining applications. The green NCFs open new possibilities for efficient and low loss transmission at the wavelengths in the visible spectral range.

The single-layer FBARF has shown poor performance resulting in a few-moded guidance, very high attenuation and significant sensitivity to bending, which prevents its use in industrial applications. However, further investigation of this structure is planned for the future. A comparison of the physical and optical parameters of the green fibres discussed within this thesis is shown in Table 3.14.

Table 3.14. Comparison of antiresonant fibres for guidance in the green spectral region.

Fibre	**NCF-240314-G**	**NCF-080414-G**	**NCF-150414-G**	**single-layer FBARF**
Core dia. [µm]	16 ± 1	15 ± 1	15 ± 1	34 ± 1
Core wall thickness [nm]	520 ± 30	550 ± 30	550 ± 30	800 ± 50
MFD [µm]	9 ± 1	8 ± 1	8 ± 1	26 ± 1
Attenuation [dB/m]				
515 nm	0.22 ± 0.01	0.19 ± 0.01	0.18 ± 0.01	1.08 ± 0.01
532 nm	0.21 ± 0.01	0.15 ± 0.01	0.15 ± 0.01	1.20 ± 0.01
Guidance	few-moded	few-moded	singlemode	few-moded
M^2	1.4 ± 0.1	1.4 ± 0.1	1.3 - 1.4 ± 0.1	3.5 ± 0.1
Bending sensitivity	low	low	very low	very high

References

1. N. M. Litchinitser, A. K. Abeeluck, C. Headley, and B. J. Eggleton, "Antiresonant reflecting photonic crystal optical waveguides," Opt. Lett. **27**, 1592-1594 (2002).
2. P. Jaworski, F. Yu, R. M. Carter, J. C. Knight, J. D. Shephard, D. P. Hand, "Dual-wavelength hollow-core Negative Curvature Fibre for the delivery of high energy short and ultrashort pulsed laser light," submitted to CLEO Europe 2015.
3. P. Jaworski, F. Yu, R. R. J. Maier, W. J. Wadsworth, J. C. Knight, J. D. Shephard, and D. P. Hand, "Picosecond and nanosecond pulse delivery through a hollow-core Negative Curvature Fiber for micro-machining applications," Opt. Express **21**, 22742-22753 (2013).
4. https://en.wikipedia.org/wiki/Standard_deviation
5. B. Debord, M. Alharbi, L. Vincetti, A. Husakou, C. Fourcade-Dutin, C. Hoenninger, E. Mottay, F. Gérôme, and F. Benabid, "Multi-meter fiber-delivery and pulse self-compression of milli-Joule femtosecond laser and fiber-aided laser-micromachining," Opt. Express **22**, 10735-10746 (2014).
6. www.nktphotonics.com
7. F. Yu and J. C. Knight, "Spectral attenuation limits of silica hollow core negative curvature fiber," Opt. Express **21**, 21466-21471 (2013).
8. P. Jaworski, F. Yu, R. M. Carter, W. J. Wadsworth, T. A. Birks, J. C. Knight, J. D. Shephard, and D. P. Hand, "High peak power nanosecond and picosecond pulse delivery through a hollow-core Negative Curvature Fiber in the green spectral region for micro-machining," in *Advanced Photonics*, OSA Technical Digest (online) (Optical Society of America, 2014), paper SoM3B.5.
9. P. Roy, A. Benoit, D. Darwich, R. Jamier, R. Dauliat, K. Schuster, S. Grimm, J. Saby, D. Sangla, and F. Salin, "High Energy Pulsed Sources from Infrared to UV with Yb Rod Type fibers: current limits and prospects," in *Advanced Photonics*, OSA Technical Digest (online) (Optical Society of America, 2014), paper SoM3B.1.
10. "EN ISO 11146", Laser and Laser-Related Equipment—Test Methods for Laser Beam Parameters - Beam Width, Divergence Angle and Beam Propagation Factor, 1999.
11. F. Emaury, C. Fourcade Dutin, C. J. Saraceno, M. Trant, O. H. Heckl, Ya. Y. Wang, C. Schriber, F. Gerome, T. Südmeyer, F. Benabid, and U. Keller, "Beam

delivery and pulse compression to sub-50 fs of a modelocked thin-disk laser in a gas-filled Kagome-type HC-PCF fiber," Opt. Express **21**, 4986-4994 (2013).

12. J. D. Shephard, P. J. Roberts, J. D. C. Jones, J. C. Knight, and D. P. Hand, "Measuring Beam Quality of Hollow Core Photonic Crystal Fibers," J. Lightwave Technol. **24**, 3761-3769 (2006).
13. F. Yu, "Hollow core negative curvature optical fibres," PhD thesis, University of Bath, UK (2014).
14. W. Belardi and J. C. Knight, "Effect of core boundary curvature on the confinement losses of hollow antiresonant fibers," Opt. Express **21**, 21912-21917 (2013).
15. B. Beaudou, A. Bhardwaj, T. D. Bradley, M. Alharbi, B. Debord, F. Gerome, and F. Benabid, "Macro Bending Losses in Single-Cell Kagome-Lattice Hollow-Core Photonic Crystal Fibers," J. Lightwave Technol. **32**, 1370-1373 (2014).
16. M. Alharbi, T. Bradley, B. Debord, C. Fourcade-Dutin, D. Ghosh, L. Vincetti, F. Gérôme, and F. Benabid, "Hypocycloid-shaped hollow-core photonic crystal fiber Part II: Cladding effect on confinement and bend loss," Opt. Express **21**, 28609-28616 (2013).
17. G. P. Agrawal, "Nonlinear Fiber Optics - third edition," publ. by A Harcourt Science and Technology Company, ISBN: 0-12-045143-3.
18. D. A. Nolan, X. Chen, and M. -J. Li, "Fibers with low polarization-mode dispersion," J. Lightwave Technol. **22**, 1066-1077 (2004).
19. A. J. Barlow, J. J. Ramskov-Hansen, and D. N. Payne, "Birefringence and polarization mode-dispersion in spun single-mode fibers," Appl. Opt. **20**, 2962-2968 (1981).
20. A. Al-Qasimi, O. Korotkova, D. James, and E. Wolf, "Definitions of the degree of polarization of a light beam," Opt. Lett. **32**, 1015-1016 (2007).
21. B. Debord, M. Alharbi, A. Benoît, D. Ghosh, M. Dontabactouny, L. Vincetti, J.-M. Blondy, F. Gérôme, and F. Benabid, "Ultra low-loss hypocycloid-core Kagome hollow-core photonic crystal fiber for green spectral-range applications," Opt. Lett. **39**, 6245-6248 (2014).
22. P. J. Mosley, W. C. Huang, M. G. Welch, B. J. Mangan, W. J. Wadsworth, and J. C. Knight, "Ultrashort pulse compression and delivery in a hollow-core photonic crystal fiber at 540 nm wavelength," Opt. Lett. **35**, 3589-3591 (2010).
23. P. Jaworski, F. Yu, R. M. Carter, J. C. Knight, J. D. Shephard, and D. P. Hand, "High energy green nanosecond and picosecond pulse delivery through a Negative

Curvature Fiber for precision micro-machining," Opt. Express **23**, 8498-8506 (2015).

24. W. Belardi, "New possibilities with hollow core antiresonant fibers," arXiv:1501.00586 [physics.optics] (2015).

Chapter 4

High-average power pulse delivery in the green and NIR spectral regions

Chapter 4 presents the results of high-peak power nanosecond, picosecond and femtosecond pulse delivery through NCFs and FBARFs in the green and NIR spectral regions of interest in this thesis. This includes the measurement of the fibre's numerical aperture, optical damage threshold as well as experimental characterisation of the spectral and temporal properties of fibre delivered ultrashort pulses.

4.1 Numerical Aperture (NA)

Efficient delivery of a laser beam through an optical fibre is only possible when the laser mode is well-matched with the fibre guided mode. In order to achieve this the laser beam needs to be characterised by an M^2 similar to that supported by the fibre, which allows the beam to be focused to a diameter comparable with the MFD of the fibre and provide a focus cone angle matching the acceptance angle of the fibre. When these requirements are fulfilled the majority of incident light is coupled directly into the fibre core (exciting the core mode) instead of being partially incident on its cladding (which leads to high loss and increased possibility of fibre damage), hence a high coupling (launch) efficiency is obtained.

The acceptance angle of a fibre with negative curvature structure (and other optical fibres) (see Fig. 4.1) defines its ability to collect light, which is then guided within the core and is characterised by the so called Numerical Aperture (NA). The NA can be described by the following formula

$$NA = n\sin\theta \tag{4-1}$$

where n is the refractive index of the medium outside the fibre, usually air and θ is the acceptance angle.

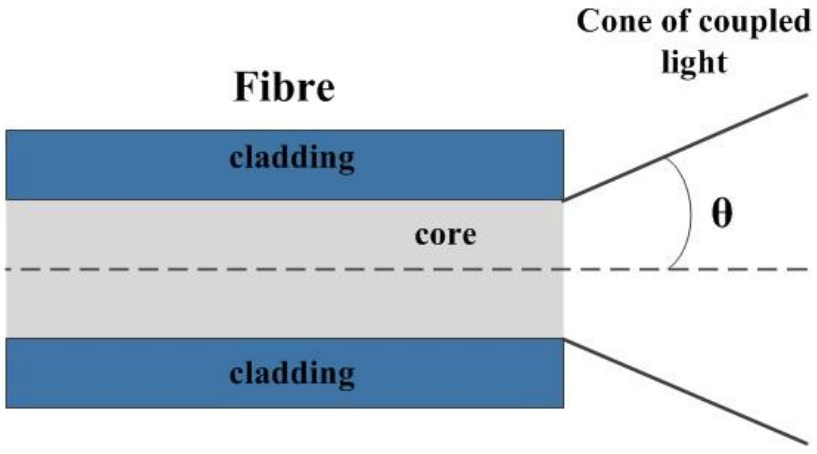

Fig. 4.1. Acceptance angle θ of an optical fibre.

The NA of each fibre presented in this work was determined experimentally, using the optical setup consisting of the coupling optics and the CCD camera (same as in chapter 3) with the Spiricon beam profiling software as shown in Fig. 4.2. The NA of a fibre can be determined from its delivered beam profile observed in the far-field. However, firstly the fibre output has to be analysed by directly imaging it onto a CCD

sensor (measurement in the near-field as previously described in subsection 3.1.1.1) in order to confirm that the delivered light is confined within the core and is not propagating within the cladding, which could significantly alter the results.

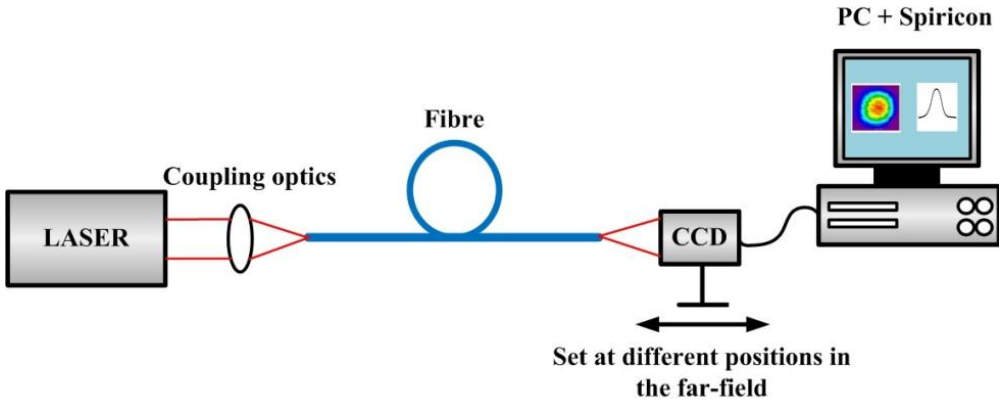

Fig. 4.2. Experimental setup for NA measurements.

The far-field delivered beam profiles of each fibre were captured for several different positions of the CCD camera (to obtain reliable results) and their $1/e^2$ diameters were measured. As shown in Fig. 4.3 the acceptance angle of the fibre can be calculated by using the inverse trigonometric function arctan as

$$\theta = \arctan\left(\frac{d}{2z}\right) \tag{4-2}$$

where d corresponds to the $1/e^2$ diameter of the delivered beam measured in the far-field and z defines the distance between the fibre end-facet and the position of the CCD camera in the far field. Consequently, the Numerical Apertures of the investigated fibres were calculated from the formula 4-1. The results are presented in Table 4.1.

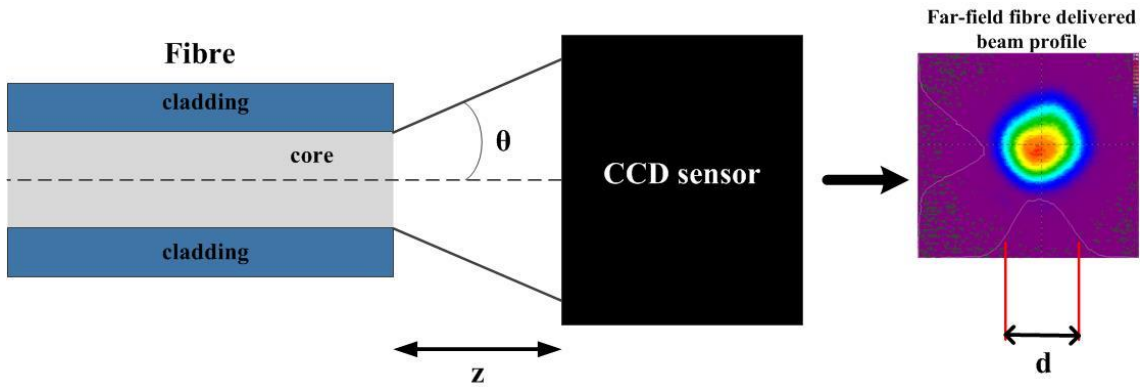

Fig. 4.3. Measurement procedure for calculation of fibre NA.

Table 4.1. Numerical Apertures of investigated fibres.

Fibre	Numerical Aperture
NCF-01	0.030 ± 0.02
NCF-140414	0.032 ± 0.02
NCF-150414-G	0.038 ± 0.02
NCF-240314-G	0.037 ± 0.02
NCF-080414-G	0.038 ± 0.02
Double-layer FBARF	0.028 ± 0.02
Single-layer FBARF	0.032 ± 0.02

The Negative Curvature Fibres and Free Boundary Anti-Resonant Fibres discussed within this thesis are characterised by a very small NA in comparison with conventional silica single- and multi-mode fibres [1,2]. Comparable NAs can be observed with the similar fibres guiding in the mid-infrared [3]. On the other hand, the hypocycloid Kagome fibres reported in [4] exhibit even lower NA.

4.2 Nanosecond pulse delivery at 1064 nm and 532 nm

Nanosecond pulses with a duration in the range of 60 ns with energies of 0.5 mJ to 1 mJ are especially desired for micro-machining processes such as marking or cutting of metals. Solid core silica fibres and typical HC-PCFs allow such pulse energies to be delivered, however only in the NIR. Efficient transmission of high energy light in the green spectral range with these fibres is impossible due to a low damage threshold and high attenuation (in HC-PCFs) resulting from fabrication issues. Furthermore, nanosecond pulses with energies in the range of a few mJ are required in applications such as spark ignition, and cannot be delivered through the conventional fibres.

This section will cover the results of high-average power, high-energy nanosecond (short) pulse delivery at 1064 nm and 532 nm through NCFs and FBARFs discussed in chapter 3. The experiments conducted within this part of work were aimed at establishing energy handling capacity and ultimate damage limitations of the fibres with the negative curvature of the core boundary in the short pulse regime.

Two ns lasers: the Spectra Physics Q-switched Nd:YVO_4 (Neodymium-doped Yttrium OrthoVanadate) operating at 1064 nm and 532 nm and a Quanta-Ray Q-switched Nd:YAG (Neodymium-doped Yttrium Aluminum Garnet) emitting radiation

at 1064 nm with specifications included in Table 4.2 were used in the measurements. The Quanta-Ray system was used only during the damage limitation tests with the NCF-01 due to its poor beam quality, and hence low coupling efficiency.

Table 4.2. Specification of nanosecond lasers.

Spectra Physics Q-switched Nd:YVO_4 laser						
Wavelength [nm]	**Pulse duration [ns]**	**Repetition rate [Hz]**	**Pulse energy [mJ]**	**Average power [W]**	**Peak power [kW]**	**M^2**
1064	60	15000	1.20	18.2	20.0	< 1.3 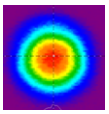
532	55		0.65	9.8	11.8	
Quanta-Ray Q-switched Nd:YAG laser						
1064	9	10	300	3	3333.0	~ 5-6

The tests performed with each fibre were carried out in the experimental setup shown in Fig. 4.4. The optical power of the laser beam coupled into a fibre was controlled via a combination of a half-wave plate and a PBS (as discussed in subsection 3.1.1.1). The coupling optics used was different for each fibre and depended on the wavelength (as discussed in the following subsections). The input end of the fibre was held with magnetic clamps (the part of the magnet that touches the fibre is covered with soft rubber, and therefore does not introduce any additional loss) on a v-groove fixed to a translation stage which provided its precision alignment (in three axes) with respect the focusing lens. An optical power meter was used to monitor the level of fibre delivered power. Furthermore, both ends of each fibre were carefully cleaved with a sharp ceramic blade and the quality of a cleave was examined under an optical microscope before the beginning of an experiment. The structure of a hollow-core photonic crystal fibre is significantly more fragile due to its complexity in comparision with the solid core fibres, and therefore cannot be cleaved with the use of a commercial fibre cleaver (it causes cracking of the fibre structure).

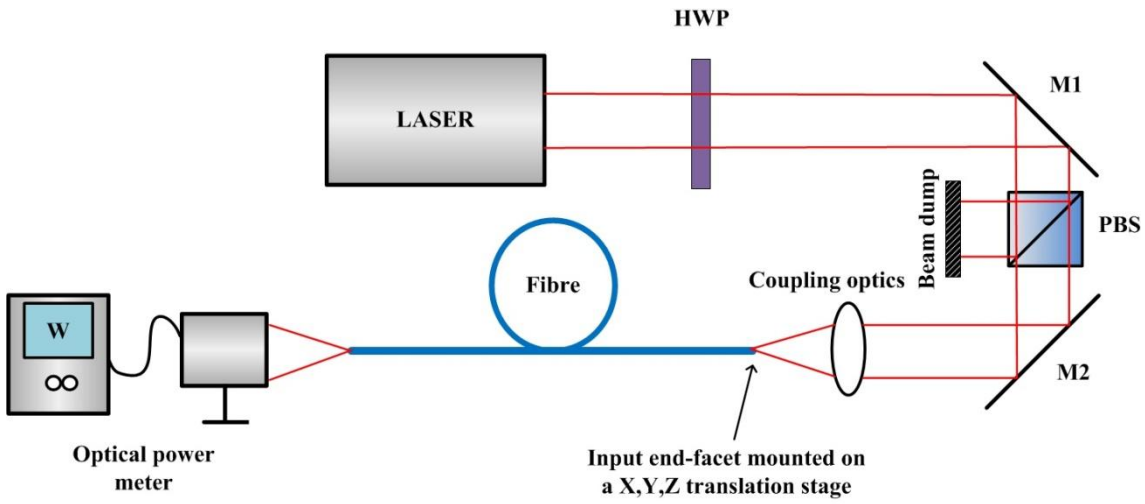

Fig. 4.4. Experimental setup for fibre pulse delivery. HWP - half wave plate; PBS - Polarising Beam Splitter, M1,M2 - mirrors.

4.2.1 Negative Curvature Fibres

4.2.1.1 Results at 1064 nm

The delivery of 60 ns pulses at 1064 nm was tested with three negative curvature fibres: NCF-01, NCF-140414 and NCF-150414-G.

NCF-01

The pulse delivery tests with the NCF-01 were performed for both a 0.7 m straight and a 10.5 m coiled fibre to a diameter of 60 cm (a coil diameter of 60 cm did not introduce additional loss due to bending). The laser beam from the Spectra Physics system was coupled directly into the fibre core using a plano-convex lens giving a focused spot diameter of 36 µm ($1/e^2$) with a focus cone angle of 60 mrad (equivalent NA = 0.03) matching the acceptance angle of the fibre. The alignment procedure was conducted with minimal laser power (in order to protect the fibre end-facet from being damaged due to misalignment) until the highest possible coupling efficiency was obtained. The high quality of the laser beam and well optimised coupling parameters allowed a coupling efficiency of 92% to be obtained. Then the power of the incident beam was increased to the maximum level available from the laser and the fibre delivered power was measured. The maximum pulse energy from the laser of 1.2 mJ at 15 kHz rep. rate (18.2 W average power) was coupled into the NCF-01 (energy and peak power densities at the fibre input end-facet of 120 Jcm^{-2} and 2 $GWcm^{-2}$ respectively) without damage, providing fibre delivered pulses of energy 1.1 mJ (ideal for precision micro-machining applications as shown in chapter 5) with an average

power of 16.3 W and a peak power of 18.3 kW. The delivered energy and peak power densities reached 110 Jcm^{-2} and 1.8 $kWcm^{-2}$ respectively. As described in [5,6], the fibre damage threshold normally scales with $\tau^{0.5}$, where τ is the pulse duration. Thus, given the damage threshold measured for the 9 ns pulses (reported in [7] and discussed further below) it is expected that the NCF-01 is capable of delivering at least 8 mJ in a 60 ns pulse before damage occurs. This is approximately 25 and 15 times greater than previously obtained with a conventional 7-cell and 19 cell defect HC-PCFs respectively [8,9]. After propagation through 10.5 m NCF-01, the delivered energy was reduced to 0.8 mJ with an average power of 12 W as a result of the fibre attenuation, which is still sufficient for micro-machining (see chapter 5).

Due to the lack of a nanosecond system with higher pulse energy in the 60 ns pulse regime, the damage threshold of the NCF-01 was tested with the Quanta-Ray ns laser, that provided 9 ns pulses with a 10 Hz repetition rate. The M^2 of the laser beam meant that in order to focus to a 36 μm spot, it was necessary to have a focus cone angle of 180 mrad (NA = 0.09, not matching the acceptance angle of the NCF-01). If a larger spot is used in order to provide a focus cone angle comparable with the fibre NA, the damage threshold is reduced (as more light is incident on the cladding). The coupling efficiency, however was maintained at a relatively high level of 78%, mainly due to the few-moded guidance of the fibre. Fibre failure was observed at pulse energies exceeding 3.2 mJ with a peak power of 0.35 MW, corresponding to an energy density at the input fibre end-face of 310 Jcm^{-2} and a peak power density of 34.3 $GWcm^{-2}$, which is approximately three times greater than previously achieved for standard HC-PCF and conventional solid core silica fibres within the same pulse regime [9]. The input end of the NCF-01 was destroyed and light guidance was no longer observed. The main reason for fibre failure at this particular pulse energy is a high M^2 value of the laser beam introducing a poorer coupling efficiency (in comparison with the Spectra Physics laser) and mismatch with the fibre guided mode, which results in light being partially incident on the microstructured fibre cladding, hence damaging the structure. Therefore, the damage limitations discussed should be considered as an approximation of the energy handling capabilities of this particular fibre rather than a precise value determining its ultimate damage threshold. Furthermore, Benabid et. al reported in [10] that an anti-resonant hypocycloid Kagome fibre can withstand approximately 10 mJ in the 9 ns pulse regime at 1064 nm. In this case, the high damage threshold most likely resulted

from a better quality of the laser beam used, hence a direct comparison with the results presented here for the NCF-01 is not appropriate.

NCF-140414

A train of 60 ns pulses for the Spectra Physics system was coupled into 0.8 m straight and 9 m coiled NCF-140414 (with 15 cm coil diameter, for which there is negligible bending loss) using a plano-convex lens providing a focus spot diameter of 26 μm ($1/e^2$) and a focus cone angle of 68 mrad (NA = 0.034). The coupling efficiency reached 89.7%. The decrease in coupling efficiency in comparison with NCF-01 is mainly due to a slight mismatch with the acceptance angle of the fibre. Nevertheless, the chosen parameters allowed excitation of only the fundamental mode (as discussed in chapter 3). The energy and peak power densities (for the maximum values available from the source laser, shown in Table 4.2) at the input end-facet of the fibre reached 230 Jcm^{-2} and 3.8 $GWcm^{-2}$ respectively, which approximately doubles the values presented with the NCF-01. The maximum delivered power through 0.8 m NCF-140414 was 16 W with a pulse energy of 1.07 mJ and a peak power of 17.8 kW, which is comparable with the results for the previous fibre. However, due to the smaller MFD (see Table 3.3 in subsection 3.1.1) of the NCF-140414 the delivered energy and peak power densities were at the level of 240 Jcm^{-2} and 3.9 $GWcm^{-2}$ respectively, which are more than two times greater than that observed with the NCF-01. 9 m coiled NCF provided fibre delivered pulses with energies of 0.94 mJ and an average power of 14.1 W. Furthermore, the fibre did not fail even with the maximum available power launched into the fibre, and therefore it was impossible to establish damage limitations of the NCF-140414 in the short pulse regime.

NCF-150414-G

Identical experiments were carried out with the NCF-150414-G. Here, a NBK7 plano-convex lens was used to focus the laser beam to a 11 μm ($1/e^2$ diameter) spot with a 150 mrad (NA = 0.075) focus cone angle. The coupling efficiency was reduced to 73% as a result of significant mismatch between the focus cone angle and the NA of the fibre, as a result of a fibre structure that was not designed for this particular wavelength (small core with low NA). It was impossible to focus the laser beam to a spot matching the MFD of the fibre and provide the focus cone angle close to the acceptance angle of the fibre at the same time. This means that the focus cone angle given by the focusing lens matching the NA of the NCF resulted in a larger focused spot size at the fibre input

end-facet (due to the 1 μm wavelength), which led to premature fibre failure (as in this case a significant amount of light was incident on the cladding). Despite the relatively low coupling efficiency (in comparison with other NCFs), the established coupling parameters (11 μm spot and 150 mrad focus cone angle) were at the optimum level required for delivering a singlemode, stable beam with a pulse energy sufficient for micro-machining. The maximum pulse energy launched into the fibre without introducing any damage to its structure was 1 mJ with an average power of 15 W (16.6 kW peak), which corresponds to energy and peak power densities at the fibre input end-facet of 1050 Jcm^{-2} and 17.5 $GWcm^{-2}$ respectively, which are approximately 5 times higher than values for the NCF-140414 (optimised fibre for the guidance in the NIR). The fibre (0.8 m straight) proved its capacity to deliver 60 ns pulses with a single pulse energy of 0.7 mJ (10.5 W average power and 11.6 kW peak power). Here, the delivered energy and peak power densities reached 1100 Jcm^{-2} and 18.2 $kWcm^{-2}$ respectively. Fibre failure occured when the energy of the incident beam was increased to 1.07 mJ, corresponding to a Laser Induced Damage Threshold (LIDT) of 1130 Jcm^{-2}, which is approximately 1.5 times higher than the estimated LIDT for the NCF-01 (here for 60 ns pulses with an energy of 8 mJ and a focused spot diameter of 36 μm the LIDT is at the level of 790 Jcm^{-2}). 9 m coiled NCF-150414-G has successfully transmitted nanosecond pulses with an energy of 0.46 mJ and an average power of 6.9 W.

The investigated negative curvature fibres have been shown to be highly suitable for efficient delivery of nanosecond pulses at 1064 nm with energies higher than achievable with conventional HC-PCFs. Furthermore, the established LIDT in the 60 ns pulse regime is an order of magnitude greater than previously reported with HC-PCFs [9]. The results of ns pulse delivery through the NCFs at 1064 nm are included in Table 4.3.

Table 4.3. Results of ns pulse delivery through NCFs at 1064 nm.

Fibre	**Avg. power [W]**	**Pulse energy [mJ]**	**Peak power [kW]**	**Energy density [Jcm^{-2}]**	**Peak power density [$GWcm^{-2}$]**	**LIDT [Jcm^{-2}]**
NCF-01	16.3	1.10	18.3	110	1.8	790*
NCF-140414	16.0	1.07	17.8	240	3.9	-
NCF-150414-G	10.5	0.70	11.6	1100	18.2	1130

*estimated value

4.2.1.2 Results at 532 nm

Fibre power handling experiments in the ns regime at 532 nm were investigated with three NCFs (see section 3.1.2) designed for the guidance in this spectral region, using the Spectra Physics ns system operating at its second harmonic (55 ns, 0.65 mJ). Two lengths of each fibre, short, 1.2 m (straight), and long, 8.8 m (coiled on a drum with 15 cm coil diameter, which eliminated any potential bend induced loss) were tested. The experiments were conducted using the optical arrangement shown in Fig. 4.4, using a plano-convex lens to couple into the fibre, providing a focused spot diameter of 8.5 μm ($1/e^2$) and a focus cone angle of 76 mrad (NA = 0.038). The chosen coupling conditions were the same for each NCF due to similar MFDs and NAs. The energy and peak power densities at the input end-facets of each fibre investigated reached 1150 Jcm^{-2} and 20.8 $GWcm^{-2}$ at the maximum pulse energy and peak power provided by the Spectra Physics laser (see Table 4.2).

NCF-240314-G

The first negative curvature fibre that was fabricated at the University of Bath for guidance in the green, the NCF-240314-G (1.2 m), delivered 55 ns pulses with energies of 0.55 mJ, an average power of 8.3 W and a peak power of 10 kW for the maximum available pulse energy from the laser coupled with a 90.3% launch efficiency. The energy and peak power densities of the delivered beam were 870 Jcm^{-2} and 15.7 $GWcm^{-2}$ respectively. After transmission through the 8.8 m length of NCF-240314-G, the pulse energy was reduced to 0.37 mJ due to fibre attenuation only. In both cases the NCF structure was not damaged.

NCF-080414-G

With the 1.2 m straight NCF-080414-G the coupling efficiency exceeded 89%, which enabled the delivery of pulses with energies of 0.56 mJ and peak and average power of 10.2 kW and 8.4 W respectively without fibre damage (for the maximum output from the laser launched into the fibre). Here, the energy and peak power densities of the fibre delivered beam were at the level of 1270 Jcm^{-2} and 23.1 $GWcm^{-2}$ accordingly. These values are approximately 1.5 times greater than that delivered through the NCF-240314-G due to smaller MFD. The pulse delivery through a 8.8 m NCF-080414-G resulted in a decrease in transmitted pulse energy to 0.32 mJ with an average power of 4.8 W.

NCF-150414-G

With the NCF-150414-G fibre, the coupling efficiency was 91.5%. This resulted in the delivery of the laser beam (through 1.2 m NCF) of 8.6 W average power, pulse energy of 0.57 mJ and 10.4 kW peak power without introducing any damage to the fibre launching end-facet. Furthermore, as a result of the improved coupling efficiency in comparison with two other NCFs, the peak power and energy densities of the delivered light reached 23.6 $GWcm^{-2}$ and 1290 Jcm^{-2} respectively, which are the highest values reported in the green ns pulse regime with an optical fibre [11]. The pulse energy delivered through the 8.8 m fibre was reduced (in comparison with the shorter length) to 0.44 mJ, similar to that observed with NCF-240314-G and NCF-080414-G. Furthermore, the delivered pulse energy is significantly higher than previously reported with a 19-cell HC-PCF (0.09 mJ delivered) [12].

In this subsection the capacity of NCFs for the efficient and robust delivery of high energy nanosecond pulses in the green spectral region has been confirmed. Furthermore, the optimised NCF-150414-G provides a stable and singlemode output that is not disturbed by the presence of higher order modes in comparison with two other fibres (as discussed in subsection 3.1.2.2). Hence, the parameters of the laser beam delivered through this particular fibre are ideal for precision micro-machining processes (see chapter 5). Due to the lack of a ns laser system providing higher power and pulse energy it was impossible to establish damage limitations of the NCFs in the investigated pulse and spectral regimes. A comparison of the results of ns pulse delivery at 532 nm is shown in Table 4.4.

Table 4.4. Results of ns pulse delivery through NCFs at 532 nm.

Fibre	**Avg. power [W]**	**Pulse energy [mJ]**	**Peak power [kW]**	**Energy density [Jcm^{-2}]**	**Peak power density [$GWcm^{-2}$]**	**LIDT [Jcm^{-2}]**
NCF-240314-G	8.3	0.55	10.0	870	15.7	-
NCF-080414-G	8.4	0.56	10.2	1270	23.1	
NCF-150414-G	8.6	0.57	10.4	1290	23.6	

4.2.2 Free Boundary Anti-Resonant Fibres

4.2.2.1 Double-layer FBARF at 1064 nm

The energy handling tests in the ns pulse regime were also performed with two lengths of the double-layer FBARF, a 0.7 m straight and a 14 m coiled with a 15 cm diameter of a single coil using the experimental setup shown in Fig. 4.4. The maximum output of the Spectra Physics ns laser was coupled into the fibre with a launch efficiency of 75% using a focusing lens providing a spot diameter of 36 μm ($1/e^2$) and a focus cone angle of 60 mrad (NA = 0.03). This relatively low (in comparison with the values obtained with NCFs) coupling efficiency mainly resulted from a slight mismatch between the focus cone angle and the fibre NA and the non-optimised structure of the fibre (resulting in its few-moded nature). Furthermore, different coupling conditions were tested during the experiments, but did not provide any improvement in launch efficiency. Despite the poor coupling efficiency and non-ideal performance of the fibre (high loss and unstable output), the double-layer FBARF allowed 60 ns pulses with energies of 0.73 mJ (11 W average power and 12.2 kW peak power) to be delivered without damage. The energy and peak power densities of the fibre delivered beam were 55 Jcm^{-2} and 0.9 $GWcm^{-2}$ respectively. High attenuation meant that with the 14 m fibre, only 0.23 mJ was delivered. This loss was a combination of intrinsic attenuation (resulting from fibre structural imperfections formed during fibre drawing process) and additional bend-induced loss (random bending of the fibre forced by limited working space). In both cases, the pulse delivery was limited only by the laser parameters.

4.2.2.2 Single-layer FBARF at 532 nm

Frequency-doubled light from the Spectra Physics system was coupled into a 1 m straight and approximately 6 m coiled (15 cm coil diameter) single-layer FBARF with a coupling efficiency of 87.6% without damage. The high launch efficiency was provided by a plano-convex lens giving a focused spot diameter of 16 μm ($1/e^2$) and a focus cone angle of 60 mrad (NA = 0.03), matching the acceptance angle of the fibre. Even though the focused spot diameter was significantly smaller than the MFD of the fibre, this did not have any influence on the coupling conditions and mode excitation (few-moded output, discussed in subsection 3.2.2). The delivered pulse energy through a short length of fibre reached 0.4 mJ with average and peak powers of 6 W and 7.3 kW respectively, corresponding to an energy density of 75 Jcm^{-2} and a peak power density of 1.4 $GWcm^{-2}$ at the output end-facet of the fibre. After propagation through 6 m single-layer

FBARF the delivered power was significantly attenuated to a level of a few milliwatts. Extremely high decrease of the delivered power resulted from few-moded nature of the fibre and its sensitivity to bending, and consequently increased loss.

4.2.3 Summary

The experiments conducted within this part of work have proven that NCFs are highly suitable for efficient and robust delivery of high energy nanosecond pulsed laser light at 1064 nm and 532 nm.

The optimised near-infrared NCF-140414 allowed 60 ns laser pulses with energies above 1 mJ to be delivered (limited only by the laser parameters), which shows an improvement in comparison with conventional HC-PCFs [9]. The damage threshold of this particular fibre has not been established, however based on the results obtained with the NCF-01 (first, not optimised fibre for guidance at 1 μm) it can be estimated that it should deliver pulses with energies exceeding 10 mJ in the 60 ns pulse regime. Furthermore, Dumitrache et al. reported in [13] damage-free delivery of 30 ns pulses at 1064 nm with energies of 30 mJ through a hypocycloid Kagome HC-PCF which is approximately three times greater than the pulse energies transmitted through a solid core LMA fibre (with a 400 μm dia. core) [13]. Based on the similar energy handling capabilities of NCFs and hypocycloid Kagome HC-PCFs it can be assumed that the NCFs should provide similar performance in this pulse regime.

The NCF-150414-G, (specifically designed for ~500 nm wavelength rather than 1 μm) delivered a singlemode beam with pulse energy of 0.7 mJ (sufficient for various micro-machining purposes). This fibre has been shown to fail at pulse energies above 1 mJ as a result of high energy flux at its input end-facet (5 times greater in comparison with the NCF-140414). At 532 nm this fibre delivered pulses (55 ns, singlemode) of energy around 0.6 mJ without damage (limited only by the laser parameters), which significantly exceeds performance of the typical HC-PCFs [12,14]. Furthermore, the transmitted energy is the highest delivered value reported with an optical fibre in this regime.

The free boundary fibres did not perform as well as the NCFs as a consequence of their high attenuation and poor guidance properties (however both are preliminary designs of this kind of fibre structure). Nevertheless, the single- and double-layer FBARFs were not damaged with the maximum available power from the ns laser.

Hence, it can be assumed that both fibres should withstand higher pulse energies in comparison with the NCFs due to their greater MFDs, and therefore lower energy densities inside the core. It is expected that further modifications of these fibres should result in an improvement of their laser beam delivery capabilities (increased transmission efficiency due to lower attenuation and bending sensitivity).

A comparison of ns pulse delivery results (the highest values obtained with the investigated fibres) in the NIR and green spectral region with NCFs and FBARFs is shown in Table 4.5.

Table 4.5. Comparison of ns pulse delivery results at 1064 nm and 532 nm with NCFs and FBARFs.

1064 nm, 60 ns						
Fibre	**Avg. power [W]**	**Pulse energy [mJ]**	**Peak power [kW]**	**Energy density [Jcm^{-2}]**	**Peak power density [GWcm^{-2}]**	**LIDT [Jcm^{-2}]**
NCF-140414	16.0	1.07	17.8	240	3.9	-
NCF-150414-G	10.5	0.70	11.6	1100	18.2	1130
double-layer FBARF	11.0	0.73	12.2	55	0.9	-
532 nm, 55 ns						
NCF-150414-G	8.6	0.57	10.4	1290	23.6	-
single-layer FBARF	6.0	0.40	7.3	75	1.4	-

4.3 Picosecond pulse delivery at 1030 nm and 515 nm

Flexible delivery of ultrashort high peak power pulsed laser light in the NIR and green spectral regions through silica singlemode solid core fibres is restricted by the strong influence of nonlinear effects i.e. Stimulated Raman Scattering and self-focusing, which significantly alter spatial and temporal properties of a laser pulse and by the relatively low damage threshold (see section 2.3 for further details). The impact of these effects is indeed reduced in LMA fibres due to larger core size and conventional HC-PCFs due to guidance in air, however the nonlinear and damage thresholds are still too low for transmission of high peak power ps pulses. Furthermore, attenuation of these fibres

becomes greater at shorter wavelengths due to a strong impact of Rayleigh scattering and fabrication issues (HC-PCF), hence an efficient transmission of a laser beam is not possible (discussed in more details in section 2.3).

This section is focused on the delivery of high energy, high peak power picosecond pulses at 1030 nm and 515 nm through the NCFs and FBARFs investigated within this thesis. The experiments were conducted in a similar optical arrangement as shown in Fig. 4.4. However, the fibre holding elements were modified due to an observed issue with the magnetic clamps resulting from a high power density of the laser beam launched into a fibre. A magnetic clamp has to be placed as close as possible to the fibre coupling end-facet in order to eliminate a potential deflection of a fibre held in a v-groove holder (as the v-groove dimensions are larger than the fibre outer diameter). The ps laser beam was coupled into a fibre with an efficiency not exceeding 90% during the tests, and therefore the remaining energy (not launched into the core) caused sufficient heating of the magnetic clamp (its rubber part) to induce its movement. This issue resulted in a misalignment of a fibre against the focusing lens, which led to a fibre failure (see Fig. 4.5). The entire fibre holding element of the experimental setup was modified by introducing a standard FC-connector (with a stainless steel ferrule) as shown in Fig. 4.6. The launching end of a fibre was placed inside the FC ferrule (bore diameters used were close to an outer diameter of each fibre), which allowed the magnetic clamps to be separated from the incident laser beam, hence the aforementioned issue was eliminated. The fibre end-face preparation was carried out using the same method as described in subsection 4.2. The laser used was the TRUMPF TruMicro industrial thin disk ps laser with the specification included in Table 4.6.

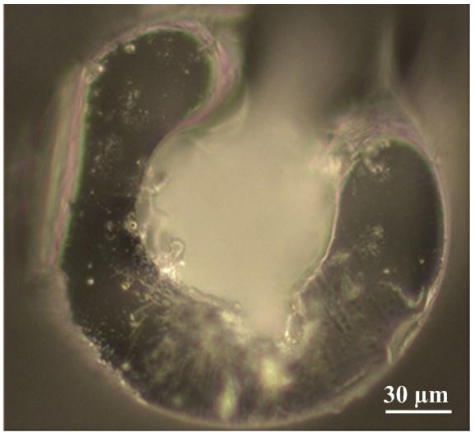

Fig. 4.5. Microscope image of a damaged fibre end-facet as a result of its misalignment due to magnetic clamp issue.

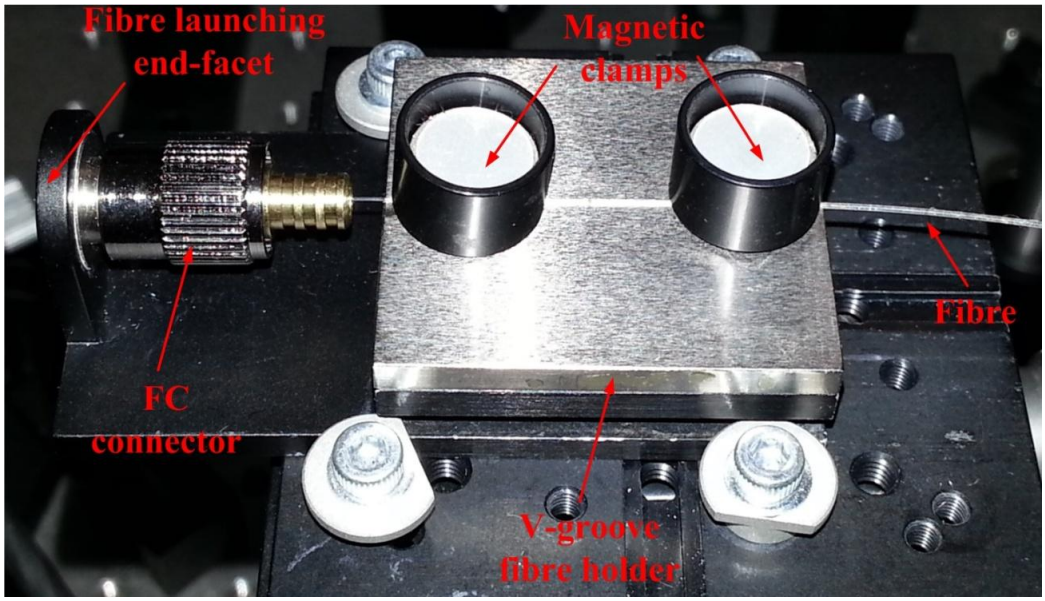

Fig. 4.6. Fibre holder with a standard FC-connector used in the experiments.

Table 4.6. Parameters of TRUMPF TruMicro ps system used in the experiments.

Wavelength [nm]	Pulse duration [ps]	Repetition rate [kHz]	Pulse energy [µJ]	Average power [W]	Peak power [MW]	M^2
1030	6	400	116	46.3	19.3	~ 1.3
515			58	23.0	9.7	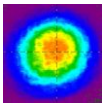

4.3.1 Negative Curvature Fibre

4.3.1.1 Results at 1030 nm

The energy handling tests in the picosecond pulse regime at 1030 nm were conducted with three near-infrared NCFs - NCF-01; NCF-140414 and NCF-150414-G.

NCF-01

6 picosecond pulses from the TRUMPF TruMicro laser system with energies of 116 µJ and average and peak powers of 46.3 W and 19.3 MW respectively (maximum available from the laser) were coupled into a 1 m straight length of NCF-01 and 8 m coiled length (with a 23 cm coil diameter). The tight bending of the fibre was essential due to limited working space. To launch the laser beam directly into the NCF-01 core a singlet NBK-7 lens providing a focused spot diameter of ~36 µm ($1/e^2$) with a focus

cone angle of 58 mrad (NA = 0.029) was used. The obtained coupling efficiency, ~ 84%, allowed pulse delivery without fibre damage. The launch efficiency is decreased in comparison with the ns laser mainly due to lower ps laser beam quality and a slight mismatch between the focused cone angle and the fibre acceptance angle. The maximum delivered pulse energy through the 1 m length was 92 μJ with an average power of 36.7 W corresponding to peak power of 15.3 MW. The energy and peak power densities of the fibre delivered beam were at the level of 9 Jcm^{-2} and 1.5 $TWcm^{-2}$ accordingly. The transmitted average and peak powers are 7 and 2 times greater respectively than previously reported with a 10 cm hypocycloid Kagome HC-PCF in [15]. The delivered energy density was approximately three times higher than the LIDT of fused silica as can be seen in Fig. 2.31. The additional high bending loss with the 8 m length reduced the transmitted energy to 49 μJ with an average power of 19.6 W and a peak power of 5.6 MW [7]. Even at the maximum energy density of 11.4 Jcm^{-2} and peak power density of 1.75 $TWcm^{-2}$ at the fibre launch, the NCF-01 did not suffer any damage, hence it was impossible to establish its damage limitation. However, the coupled peak power was two times greater than the critical value reported for a more complex hypocycloid Kagome hollow-core fibre [15] and approximately 5 times larger than the self-focusing threshold for solid core silica fibres [16].

NCF-140414

The power handling capability in the 6 ps pulse regime of the NCF-140414 was tested with two lengths of this fibre, a 1 m straight piece and a 7 m coil of diameter 20 cm. The smaller MFD of the fibre and slightly larger acceptance angle in comparison with the NCF-01 required a different focusing lens to be used in the setup. Here, the plano-convex lens used provided a focused spot diameter of 23 μm ($1/e^2$) with a focused cone angle of 72 mrad (NA = 0.036). The chosen coupling parameters allowed 89.6% coupling efficiency to be achieved. 6 ps pulses with an average power of 33.6 W and energy of 84 μJ (14 MW peak power) coupled into the 1 m fibre without destroying its structure resulted in a fibre delivered beam with single pulse energy of 75 μJ and an average power of 29.8 W corresponding to 12.4 MW peak power. The energy and peak power fluxes of the delivered beam reached 17 Jcm^{-2} and 2.9 $TWcm^{-2}$ respectively, double the results obtained with the NCF-01. Coiling the 7 m fibre did not introduce any additional loss to the delivered power, although its level was reduced to 27.5 W with pulse energy of 69 μJ due to fibre attenuation at 1030 nm. The launching end-facet of the fibre (either 1 m or 7 m) was completely destroyed when the power of the

coupled laser beam was increased to 35 W (88 μJ pulse energy). Hence, the LIDT of the NCF-140414 is 21 Jcm^{-2} (peak power density of 3.5 $TWcm^{-2}$). According to Fig. 2.31 the established LIDT is 6 times greater than the damage fluence of fused silica.

NCF-150414-G

The third negative curvature fibre operating at 1030 nm that was investigated is the NCF-150414-G. The optimum launching conditions for this particular fibre were provided by a plano-convex lens focusing the laser beam to approximately 8 μm $1/e^2$ diameter with 180 mrad focused cone angle (NA = 0.09). Similar to the situation observed with this particular fibre during ns pulse delivery, a focus cone angle close to the acceptance angle of the fibre (therefore a much larger spot due to the wavelength) resulted in fibre failure at low pulse energies (~20 μJ). Despite significant mismatch with the fibre NA, a relatively high coupling efficiency of 80% was achieved. A 1 m straight length of NCF-150414-G successfully transmitted singlemode 6 ps laser pulses with energies of 25 μJ and an average power of 10 W corresponding to a peak power of 4.2 MW, when the laser beam with an average power of 13.2 W (33 μJ pulse energy) was coupled into its hollow core without introducing any damage to the silica cladding. As a result of the small MFD of the fibre in comparison with two previously discussed NCFs the energy and peak power densities of the fibre delivered beam were significantly higher, at the level of 39 Jcm^{-2} and 6.6 $TWcm^{-2}$ respectively. The same experiment was performed with a 7 m fibre coiled with a 10 cm radius. Here, the delivered power was decreased to 7.5 W (19 μJ pulse energy) due to fibre attenuation only. The fibre input end-facet suffered damage when the average power and pulse energy of the incident laser beam were increased to 14 W and 35 μJ (5.8 MW peak power) accordingly. The established LIDT for this fibre at 1030 nm in the ultrashort pulse regime is 59 Jcm^{-2} (9.8 $TWcm^{-2}$ critical peak power density), which based on the data from Fig. 2.31 is almost 17 times higher than the critical value for fused silica (approximately 3.5 Jcm^{-2} for 6 ps pulses at 1053 nm).

All of the NIR-guiding NCFs presented in this chapter have shown excellent suitability for the delivery of ultrashort high peak power laser pulses. They overcome limitations present in conventional solid core singlemode silica fibres resulting from significantly lower damage threshold (as critical energy density for fused silica is ~9 Jcm^{-2}). Konorov et al. have shown in [17] that HC-PCFs can withstand ps pulses (40 ps) with energies of 0.8 mJ, corresponding to a peak power of 20 MW. The peak power is

indeed at the level comparable with the NCF-01 results, however poor performance of the HC-PCF used meant that the maximum transmission efficiency over a 20 mm length of this fibre was only ~9%, which eliminates the fibre from practical use. Furthermore, the power handling capability is significantly greater in comparison with more complex hypocycloid Kagome hollow-core PCFs. Indeed, the maximum power delivered through the NCF-01 is the highest reported value in the ps pulse regime at 1 μm wavelength. The results of ps pulse delivery through the discussed fibres are presented in Table 4.7.

Table 4.7. Results of ps pulse delivery through NCFs at 1030 nm.

Fibre	**Avg. power [W]**	**Pulse energy [μJ]**	**Peak power [MW]**	**Energy density [Jcm^{-2}]**	**Peak power density [$TWcm^{-2}$]**	**LIDT [Jcm^{-2}]**
NCF-01	36.7	92.0	15.3	9.0	1.5	-
NCF-140414	29.8	74.5	12.4	17	2.9	21
NCF-150414-G	10.0	25.0	4.2	39	6.6	59

4.3.1.2 Results at 515 nm

Ultrashort pulse delivery tests in the green spectral region were carried out using the Trumpf TruMicro ps laser system emitting 515 nm, 6 ps pulses at a 400 kHz repetition rate (see Table 4.6). Three negative curvature fibres: NCF-240314-G, NCF-080414-G and NCF-150414-G designed to operate in the vicinity of this particular wavelength were tested. The experiments were carried out using the same methods and approach as previously discussed in section 4.2. The coupling conditions used in the measurements were the same for the NCF-080414-G and NCF-150414-G due to the similarity between their physical and optical parameters (mode field diameter and numerical aperture). Here, light from the ps laser was coupled into the core of each NCF using a standard plano-convex lens to generate an 8.0 μm diameter ($1/e^2$) spot and a focus cone angle of 84 mrad (NA = 0.042). In the case of the NCF-240314-G a focusing lens provided focused spot with a $1/e^2$ diameter of 10 μm with a focused cone angle of 80 mrad (NA = 0.04).

NCF-240314-G

The laser beam with an average power of 13.9 W and a pulse energy of 35 μJ (5.8 MW peak power) was coupled without damage into a 1 m straight and 9.5 m coiled (15 cm coil diameter) NCF-230414-G with a coupling efficiency of 86%. As with the 1030 nm wavelength, the decrease in launch efficiency in comparison with the ns laser resulted from a slight mismatch between the focused cone angle and the fibre NA. Nevertheless, it allowed delivery of 6 ps pulses with energies of 28 μJ and a peak power of 4.7 MW (11.2 W average power) through the 1 m length, which correspond to energy and peak power densities of 45 Jcm^{-2} and 7.4 $TWcm^{-2}$ respectively. The 9.5 m NCF provided a fibre delivered beam with a pulse energy reduced to 18 μJ and a peak power of 3 MW (7.3 W average power). To determine the LIDT of the fibre the coupled pulse energy was slowly increased until fibre failure was observed. Damage to the fibre input end-facet occurred at a pulse energy of 50 μJ with a peak power of 8.3 MW [18]. Hence, the LIDT of the NCF-240314-G at 515 nm in the ps pulse regime is 64 Jcm^{-2} (10.6 $TWcm^{-2}$ peak power density), which significantly exceeds the performance of fused silica (LIDT of ~2 Jcm^{-2} for 6 ps pulses at 526 nm) as shown in Fig. 2.31.

NCF-080414-G

The maximum power of the laser beam launched into a 1 m straight NCF-080414-G without damaging its end-facet was 12.4 W with a pulse energy of 31 μJ corresponding to a peak power of approximately 5.2 MW. The coupling efficiency obtained was 88% (comparable to the results in the ns pulse regime), which resulted in a fibre delivered beam with an average power of 8.5 W and a pulse energy of 21 μJ (3.5 MW peak power). In this case, energy and peak power densities at the fibre output reached 48 Jcm^{-2} and 7.9 $TWcm^{-2}$ accordingly, which are comparable to the results obtained with the NCF-240314-G. Furthermore, a longer length of 8.8 m of this fibre was tested (coiled with a 7.5 cm radius). It delivered a laser beam with a pulse energy of 11 μJ and a peak power at the level of 1.8 MW. The NCF-080414-G experienced damage to its launch end-facet when the energy of the incident laser beam was increased to 35 μJ with a peak power of 5.8 MW (13.9 W average power), which corresponds to the LIDT of 70 Jcm^{-2} (peak power density of 11.5 $TWcm^{-2}$). Failure of the fibre occurred at lower pulse energy in comparison with the previously discussed NCF as a result of greater energy density at the launching end due to smaller diameter

of the focused laser beam. Nevertheless, the LIDT value is 35 times higher than the LIDT of fused silica glass as presented in Fig. 2.31.

NCF-150414-G

The NCF-150414-G was tested using two lengths of fibre, a 1 m straight piece and 8.8 m coiled with a 15 cm coil diameter. As before, a slight mismatch between the chosen focused cone angle and the acceptance angle of the fibre meant that the maximum coupling efficiency that could be obtained was 90%. The maximum delivered pulse energy through the short length of NCF without damage was 30 μJ (35 μJ coupled) with an average power of 12 W (13.9 W coupled) and 5 MW peak power which gives energy and peak power densities of 68 Jcm^{-2} and 11.3 $TWcm^{-2}$ respectively. The delivered pulse energy at this wavelength is higher than at 1 μm, which is not surprising as the fibre is specifically designed for the green spectral region. Furthermore, the coiled length delivered pulses with energies of 21 μJ and peak powers of 3.6 MW. As summarised in Table 4.8, this fibre performs better than the other two NCFs, presumably as a result of a better-optimised structure, and hence improved guidance properties, providing better light confinement in the core (as discussed in section 3.1.2). However, fibre failure (to the launch end-facet) occurred when the input pulse energy was increased to 40 μJ (test were repeated several times), and therefore the light guidance was immediately stopped. The LIDT of the NCF-150414-G was established as 80 Jcm^{-2} (13.3 $TWcm^{-2}$ peak power density).

The investigated NCFs can efficiently transmit 6 ps pulses at 515 nm wavelength with energies and average powers of up to 30 μJ and 12 W respectively, sufficient for precision machining of metals and glass [11]. The maximum delivered average power is more than double that reported by others with a hypocycloid Kagome HC-PCF [19]. Furthermore, the LIDT of 80 Jcm^{-2} established for the optimised NCF-150414-G is 40 times greater than the LIDT of the silica glass as shown in Fig. 2.31. Table 4.8 summarises the results at 515 nm.

Table 4.8. Results of ultrashort pulse delivery with NCFs at 515 nm.

Fibre	Avg. power [W]	Pulse energy [µJ]	Peak power [MW]	Energy density [Jcm^{-2}]	Peak power density [$TWcm^{-2}$]	LIDT [Jcm^{-2}]
NCF-240314-G	11.2	28	4.7	44	7.4	64
NCF-080414-G	8.5	21	3.5	48	7.9	70
NCF-150414-G	12.0	30	5.0	68	11.3	80

4.3.1.3 Characterisation of fibre delivered pulse

When an ultrashort pulse propagates through an optical fibre its temporal properties could be affected by dispersion effects (i.e. chromatic and intermodal). The refractive index of the fibre strongly depends on the optical frequency (wavelength) of propagating light. A laser pulse typically consists of multiple frequency components (as it has a certain bandwidth), which travel along the fibre with different velocities, and therefore the velocity difference results in temporal pulse broadening (as these components do not reach the fibre output at the same time). The fibres exhibiting a few-moded guidance suffer from intermodal dispersion resulting from the difference in the path lengths covered by the supported modes (as a part of them propagate in the vicinity of the core and the others near the core/cladding boundary), which also leads to pulse broadening [20]. Furthermore, due to a mismatch with the acceptance angle of the fibre, light could be unintentionally coupled into the silica cladding causing generation of additional wavelengths due to nonlinear effects (i.e. upconversion) in the glass which significantly alters the spectrum of the delivered pulse as shown in Fig. 4.7.

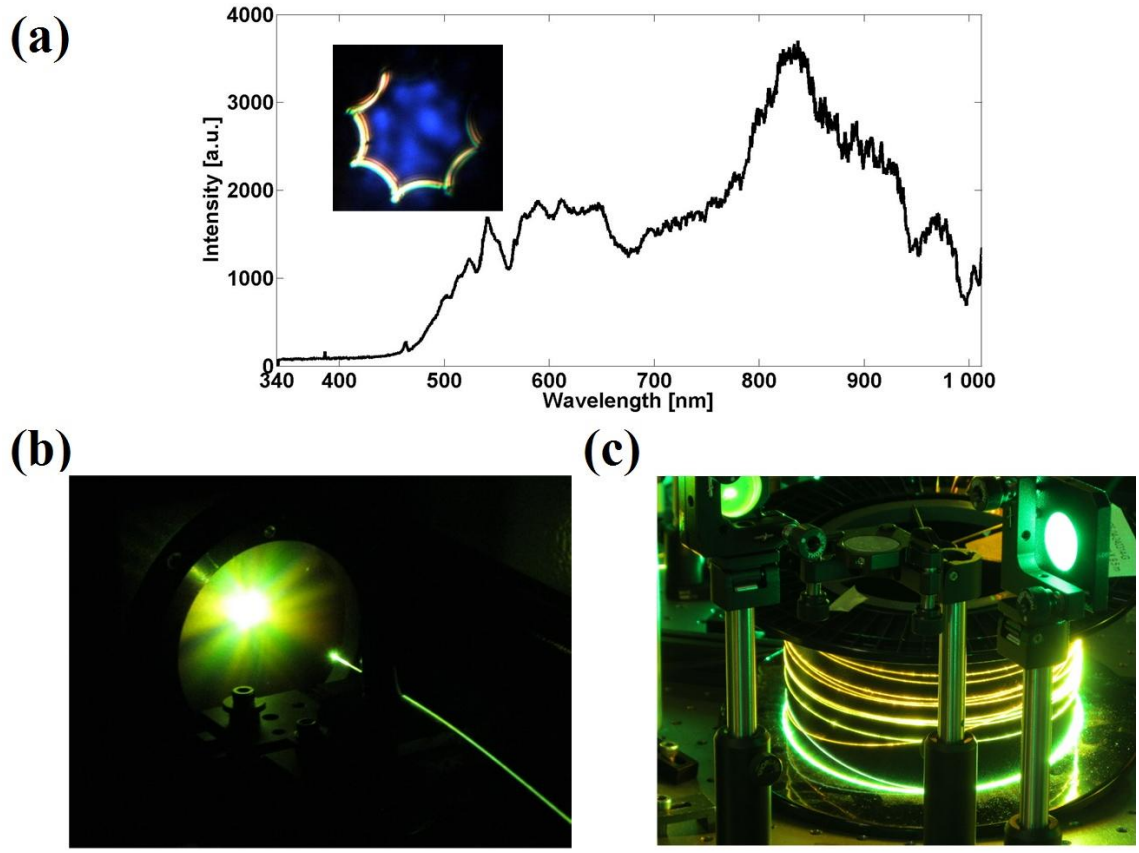

Fig. 4.7. (a) Spectrum of the delivered beam through the NCF-01(recorded with an Ocean Optics S2000 spectrometer) as a result of coupling 6 ps pulses at 1030 nm into the cladding. Imaged output end-facet of the fibre indicates generation of the additional wavelengths in the glass part of the NCF-01. (b) NCF-01 transmitting a broadband light generated in its cladding. (c) Similar phenomena observed with the NCFs when partially launching ps pulses at 515 nm onto the cladding.

NIR NCFs

To investigate the impact of the fibre on the spectral and temporal properties of the delivered laser pulses at 1030 nm an Advantest Q8384 Optical Spectrum Analyser (OSA, spectral resolution of 0.01 nm FWHM, 600 nm to 1700 nm wavelength range) and Femtochrome FR-103XL (used only with the NCF-01) and APE PulseCheck autocorrelators were used. Measurements (spectral and temporal) were conducted for the maximum delivered pulse energy through each NCF operating at this particular wavelength (for more details please see subsection 4.3.1.1).

The intensity autocorrelation of the delivered pulse through the 1 m NCF-01 presented in Fig. 4.8(a) shows no pulse dispersion in comparison with original laser pulse (see Fig. 4.8(b)). However, after propagation along 8 m of fibre the transmitted pulse was stretched to 8.7 ps FWHM as plotted in Fig. 4.8(c), likely to be associated

with intermodal dispersion rather than nonlinear effects [8]. No significant distortion of the pulse shape was observed.

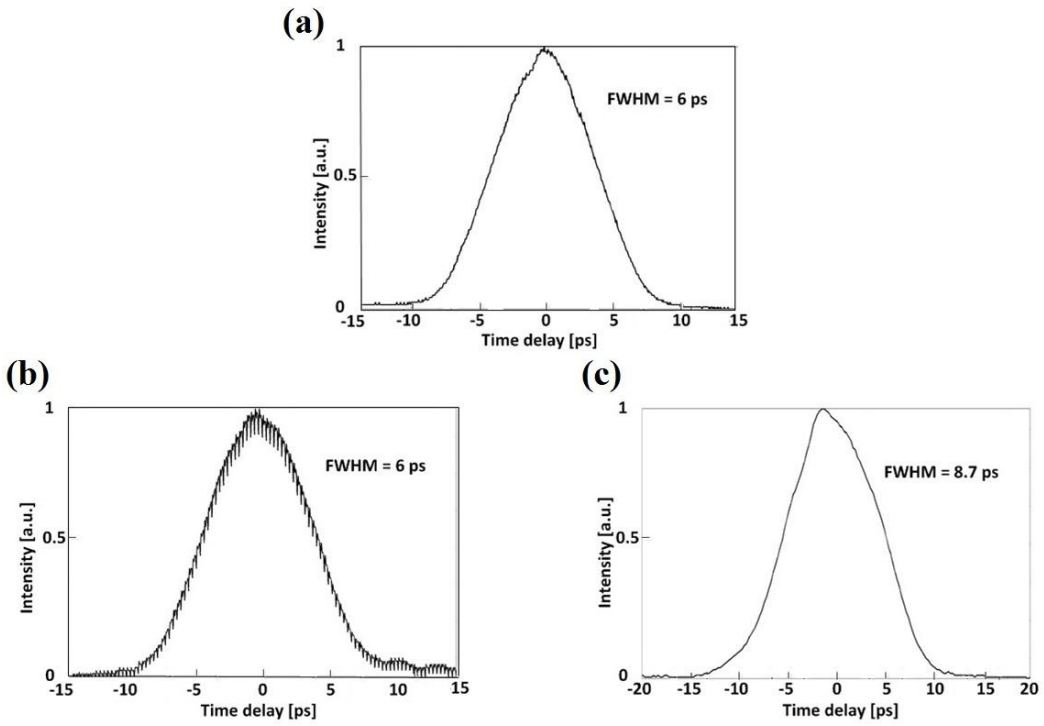

Fig. 4.8. Intensity autocorrelation of: (a) ps laser pulse; (b) pulse delivered through 1 m of NCF-01; (c) pulse transmitted through 8 m coiled (Ø 23 cm) NCF-01 (different scale on time delay axis).

Similar autocorrelation measurements were made using the APE PulseCheck autocorrelator with the other two fibres, NCF-140414 and NCF-150414-G (for maximum delivered pulse energy). In both cases, the duration of the laser pulse of 6 ps FWHM (Fig. 4.9) and its shape were perfectly maintained after propagation through 1 m (straight) and 7 m (coiled with 15 cm coil dia.) lengths of both fibres, demonstrating the strong singlemode operation. The autocorrelation traces recorded for both NCFs at 1030 nm were plotted in Fig. 4.9.

The spectrum analyser results (Fig. 4.10) demonstrate that the spectral properties of the original laser pulse are well preserved after propagation through all three NCFs (both lengths of each fibre) at 1030 nm. The additional features (multiple peaks) visible on the plots were induced by a singlemode fibre embedded inside the OSA with a cut-off wavelength of 1550 nm, which means that for the shorter wavelengths it supports higher order modes, which can alter the measured spectrum as an effect of the modal interference. Therefore, the included results are not a precise representation of the optical spectra of the laser and fibre delivered pulses and should be considered as an approximation. Nevertheless, the captured data clearly indicates no difference between

the laser and NCF delivered pulses as mentioned before. Due to the lack of suitable measurement device it was impossible to obtain more reliable and accurate results at 1030 nm.

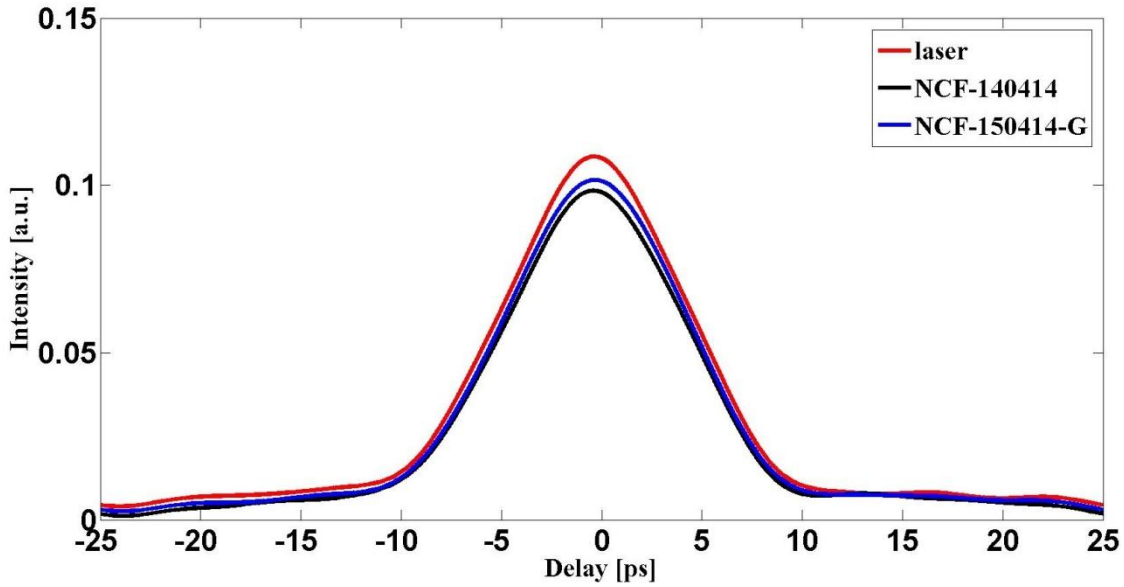

Fig. 4.9. Intensity autocorrelation traces of: ps laser pulse at 1030 nm (red line); pulse delivered through 7 m (coiled) NCF-140414 (black line); pulse after propagation via 7 m (coiled) NCF-150414-G (blue line).

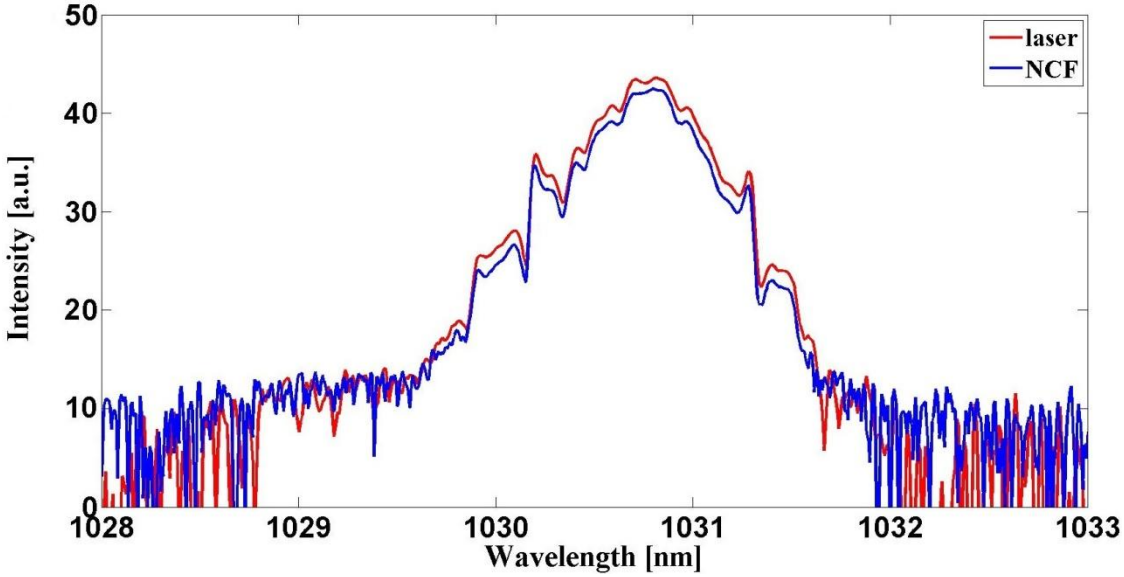

Fig. 4.10. Examples of optical spectra of: ps laser pulse (solid red line); pulse delivered through each investigated NIR NCF (solid blue line).

'Green' NCFs

Spectral and temporal properties of the picosecond pulses delivered through NCF-240314-G, NCF-080414-G and NCF-150414-G at 515 nm were characterised with an Ocean Optics S2000 spectrometer (0.05 nm FWHM spectral resolution, 332 nm

to 1012 nm wavelength range) and the APE PulseCheck autocorrelator. Measurements were conducted for maximum delivered power through the fibres (see subsection 4.3.1.2 for the relevant data). Two lengths of either green NCF, 1 m (straight) and 8.8 m (coiled with 15 cm coil dia.) were tested. The recorded spectra of the beam direct from the ps laser and after propagation through the NCFs (both lengths of the fibres) are shown in Fig. 4.11. The results demonstrate a lack of nonlinear effects with these lengths of these fibres. Furthermore, the captured data present the real shape of the laser and fibre delivered spectra due to a different spectrometer used (Ocean Optics analyser is without an optical fibre in its structure). The temporal properties of the original laser pulse were perfectly maintained on delivery through a 1 m length of the considered NCFs. The intensity autocorrelation traces (see Fig. 4.12) of the laser pulse delivered through all three 8.8 m long NCFs show that the NCF-150414-G preserved both the duration of the laser pulse and its shape, which indicates low dispersion of the fibre and an absence of nonlinear processes, while two other NCFs introduced a slight pulse broadening. In the case of these fibres, the ps pulse was stretched to 6.3 ps FWHM and 6.2 ps FWHM for NCF-240314-G and NCF-080414-G respectively. As these fibres exhibit few-moded behavior and maintain the spectral properties of the laser beam, the observed broadening most likely resulted from intermodal dispersion rather than from nonlinear effects (similarly to the phenomena noticed with the NCF-01). Furthermore, the 8.8 m NCF-240314-G did not significantly alter the pulse shape in comparison with the two other NCFs.

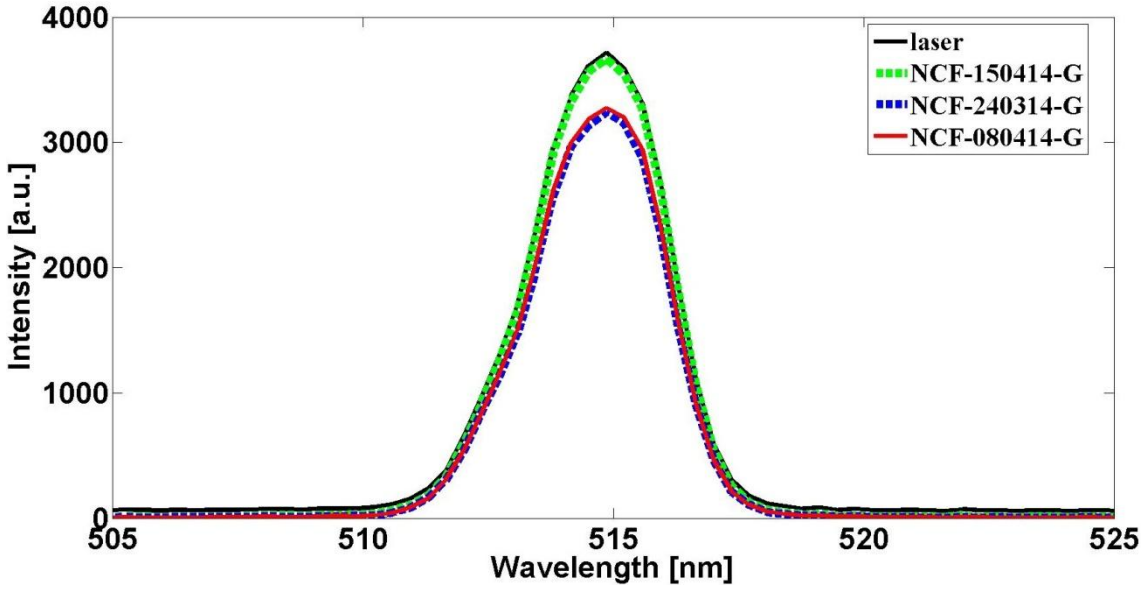

Fig. 4.11. Optical spectra of: laser pulse (solid black); delivered through 8.8 m lengths of NCF-240314-G (dashed blue), NCF-080414-G (solid red) and NCF-150414-G (dashed green) at 515 nm respectively.

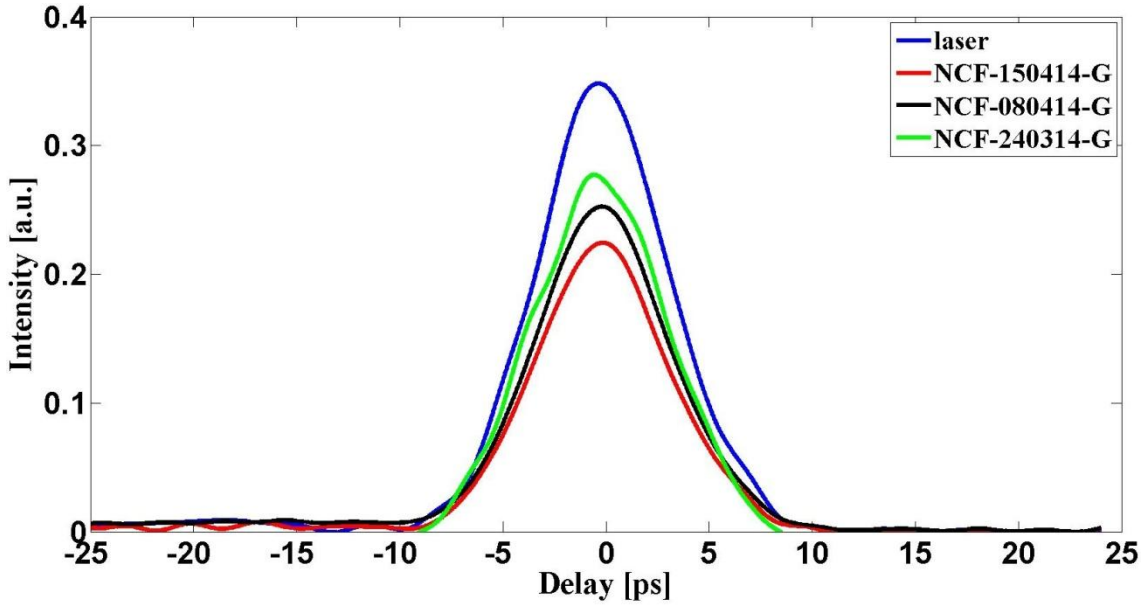

Fig. 4.12. Intensity autocorrelation traces of: ps laser pulse (blue); pulse delivered through 8.8 m NCF-240314-G (green), NCF-080414-G (black) and NCF-150414-G (red) at 515 nm.

The negative curvature hollow core fibre designed for guidance in the NIR and green spectral regions can deliver high energy ultrashort (ps) pulsed laser light without introducing any distortions to its spectral properties resulting from i.e. SRS or SPM. This is not possible with conventional solid core silica fibres as the critical pulse energy (for pulse duration of 35 ps) for generation of SRS and SPM is ~ 0.5 μJ [21]. Furthermore, short lengths (~1 m) of NCF do not change the pulse duration, however a pulse broadening can occur for a longer length (a few meters) when a fibre supports higher order modes as a result of intermodal dispersion. The optimised NCF-140414 (1030 nm) and NCF-150414-G (1030 nm and 515 nm) maintain the spectral and temporal properties (due to singlemode guidance and absence of nonlinear processes) of the transmitted pulse when either short or long lengths of these fibres are used, which confirms their excellent suitability for the efficient delivery of picosecond pulses. A comparison of the autocorrelation measurement results at 1030 nm and 515 nm with the NCFs is shown in Table 4.9.

Table 4.9. Picosecond pulse duration delivered through the NCFs at 1030 nm and 515 nm.

1030 nm	
Fibre	**Pulse duration (FWHM) [ps]**
NCF-01	6.0 (1 m) 8.7 (8 m)
NCF-140414	6.0 (1 m, 7 m)
NCF-150414-G	6.0 (1 m, 7 m)
515 nm	
NCF-240314-G	6.0 (1 m) 6.3 (8.8 m)
NCF-080414-G	6.0 (1 m) 6.2 (8.8 m)
NCF-150414-G	6.0 (1 m, 8.8 m)

4.3.2 Free Boundary Anti-Resonant Fibres

The free boundary fibres were tested in a similar way to the NCFs, to determine their LIDT, dispersion and nonlinearities, all with ps pulses from the Trumpf TruMicro ps laser.

4.3.2.1 Double-layer FBARF at 1030 nm

Two lengths of the double-layer FBARF were tested, a 1 m straight and a 7 m coiled with a diameter of 15 cm. The coupling parameters were optimised to deliver the highest possible power and avoid fibre failure at relatively low pulse energies. A plano-convex singlet focusing lens used provided a focused spot with a $1/e^2$ diameter of 36 µm with a focus cone angle of 60 mrad (NA = 0.03), which enabled a launch efficiency of 73% to be achieved. Similar to the results with the ns laser, a low coupling efficiency resulted from the mismatch between the focused cone angle and the fibre NA and the few-moded behaviour of the FBARF. As before, the adjusted coupling conditions did not provide any improvement and it was impossible to excite only the fundamental mode and obtain singlemode guidance. The maximum pulse energy delivered without damage through the 1 m fibre was 59 µJ (90 µJ coupled) with an average power of 23.5 W (36 W incident) and a peak power of 9.8 MW, which corresponds to energy and peak

power densities of 5 Jcm^{-2} and 0.7 $TWcm^{-2}$ respectively. After propagation through the 7 m double-layer FBARF the pulse energy significantly dropped to 20 μJ (8 W average power) as a result of the high intrinsic attenuation of the fibre and additional bend-induced loss. Furthermore, the fibre failed at pulse energies of 100 μJ, which corresponds to an LIDT of 10 Jcm^{-2}. This is two and six times lower than for the NCF-140414 and NCF-150414-G respectively. Nevertheless, the LIDT of this fibre structure is approximately 3 times greater than the LIDT of fused silica as presented in Fig. 2.31. Furthermore, it is reasonable to expect that further optimisation of this fibre focused on a reduction of loss and few-moded behaviour should enable the delivery of larger pulse energies (as a result of increased launch efficiency and LIDT).

4.3.2.2 Single-layer FBARF at 515 nm

A train of picosecond pulses was coupled into the fibre core with an efficiency of 84.4% via a focusing lens providing a focused spot diameter of 15 μm ($1/e^2$) and a focus cone angle of 60 mrad (NA = 0.03). However, it is likely that a high launch efficiency mostly resulted from the few-moded guidance of the fibre. The excitation of the fundamental mode only was not possible. The maximum laser power coupled into the single-layer FBARF without damage was 15.4 W with pulse energy of 38 μJ (6.4 MW peak power). The high sensitivity to bending and limited working space meant that the maximum length of fibre that could be used to deliver a laser beam with an energy at the level comparable with the other discussed fibres was 0.5 m (straight). This length allowed 6 ps pulses with energies of approximately 29 μJ (11.5 W average power) and a peak power of 4.8 MW to be delivered, which correspond to energy and peak power densities of 6 Jcm^{-2} and 0.9 $TWcm^{-2}$ respectively. The delivered power and pulse energy are at the same level as obtained with the green NCFs, however peak and energy densities are significantly lower due to larger MFD of the free boundary fibre. Furthermore, the fibre failed when the energy density at its launching end-facet reached 21 Jcm^{-2}, which is approximately 4 times lower than the LIDT of the NCF-150414-G at the same wavelength but an order of magnitude greater than the critical value for fused silica as shown in Fig. 2.31. Fibre failure caused a sudden decrease in transmitted power, however the light guidance was still maintained, even when the incident power was increased to the maximum value (23 W) available from the ps laser, which indicates a robustness of this particular structure. In addition, a longer length ~5.5 m (coiled with a 15 cm coil dia.) was tested in this pulse regime, although the maximum delivered power

was in the milliwatts range (equivalently to the results in the ns pulse regime) as a result of high loss (intrinsic and bend-induced) of the fibre.

4.3.2.3 Characterisation of fibre delivered pulse

The spectral and temporal properties of the picosecond pulses delivered through single- and double-layer FBARFs were characterised using the same approach and measurement equipment as discussed in subsection 4.3.1.3. The measurements were performed with two lengths of each fibre (the same as described earlier). The autocorrelation traces and optical spectra were captured for the maximum delivered pulse energy through each FBARF (see section 4.3.2 for further details).

The autocorrelation traces recorded for 1 m and 7 m lengths of double-layer FBARF at 1030 nm shown in Fig. 4.13 confirm that the shape of the laser pulse was well maintained. However, the pulse was broadened to 6.8 ps (FWHM) after propagation through the longer length. Since no light was observed in the fibre cladding and no measurable difference between the laser and fibre delivered spectra could be seen, it is assumed that the pulse broadening resulted from the intermodal dispersion only. The observed broadening was not as significant as that introduced by the NCF-01,which indicates lower dispersion of this fibre.

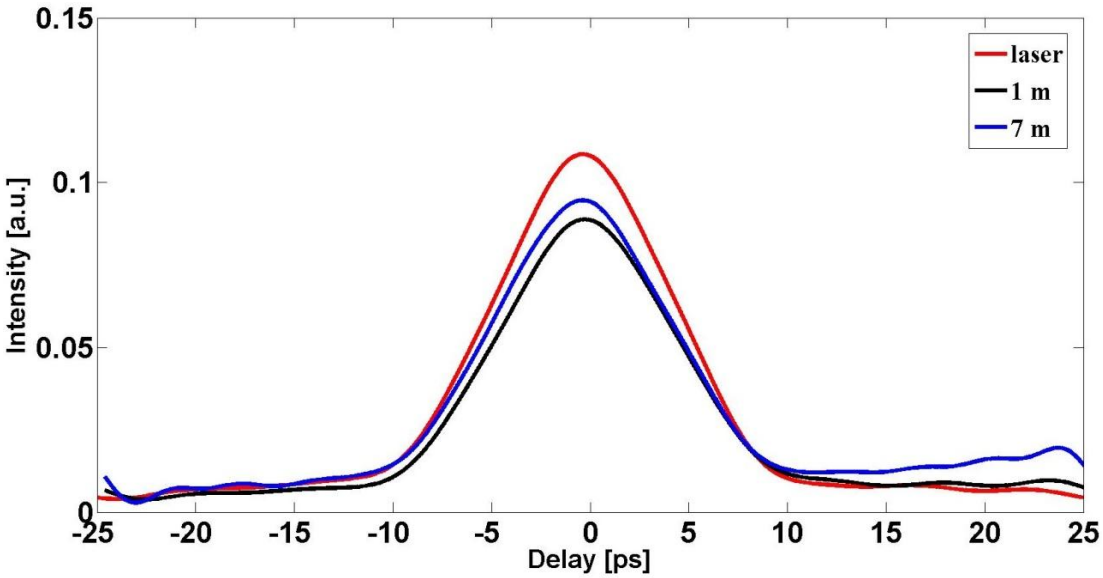

Fig. 4.13. Intensity autocorrelation traces of: laser pulse (red); the delivered pulse through 1 m (black) and 7 m (blue) double-layer FBARF at 1030 nm.

The characterisation of the pulses delivered through 0.5 m (straight) and 5.5 m (coiled) single-layer FBARFs has shown similar trends to green NCFs. A short length

of fibre did not introduce any changes to the transmitted pulse length and shape as shown in Fig. 4.14. However, the longer fibre stretched the laser pulse to 6.4 ps FWHM due to the few-moded guidance resulting in intermodal dispersion, comparable with the phenomena observed with NCF-240314-G and NCF-080414-G also supporting higher order modes. Furthermore, no spectral broadening was observed with either length as shown in Fig. 4.15.

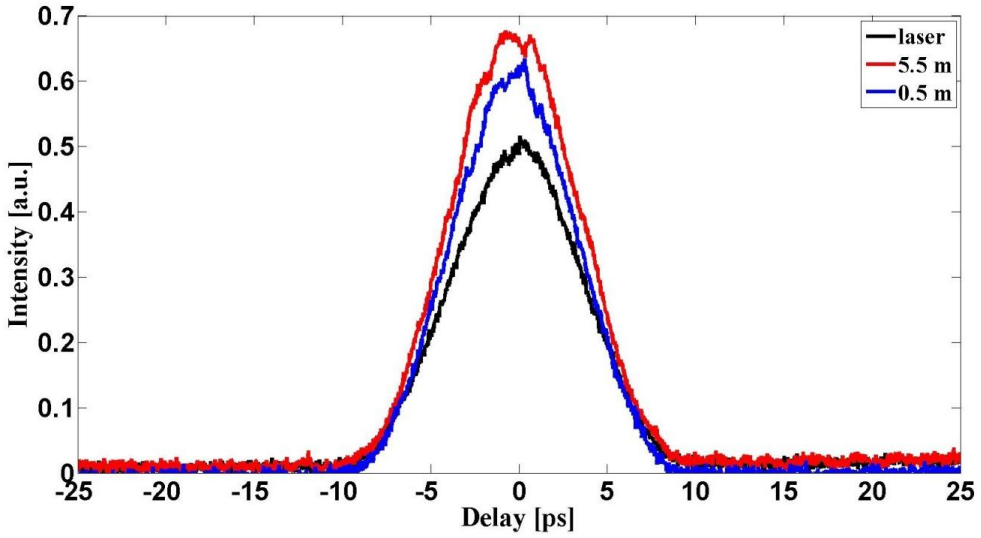

Fig. 4.14. Intensity autocorrelation traces of: laser pulse (black); the delivered pulse through 0.5 m straight (blue) and 5.5 m coiled (red) single-layer FBARF at 515 nm.

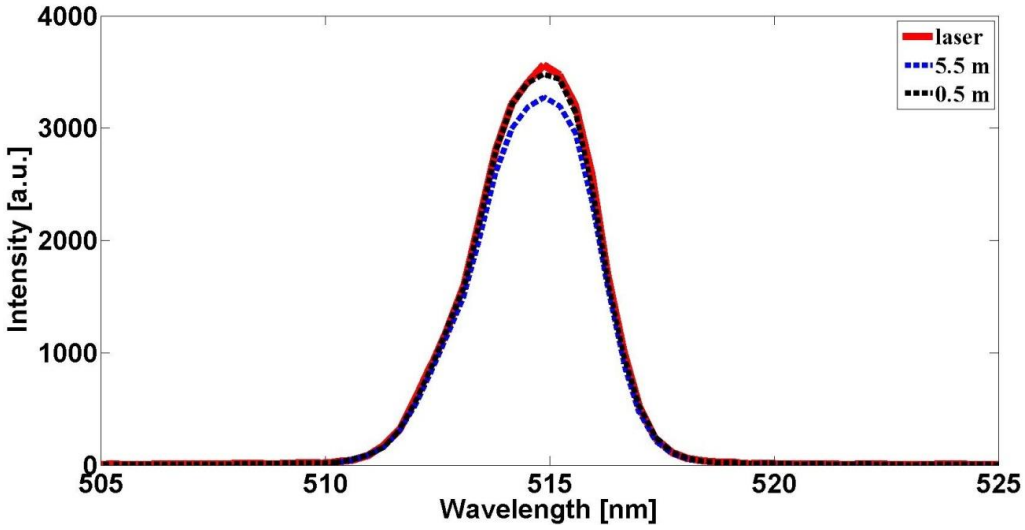

Fig. 4.15. Optical spectra of : laser pulse (solid red); delivered through 0.5 m straight (dashed black) and 5.5 m coiled (dashed blue) single-layer FBARF at 515 nm.

A comparison of the delivered picosecond pulse duration through single- and double-layer FBARFs (both investigated lengths of each fibre) at 515 nm and 1030 nm are included in Table 4.10.

Table 4.10. Picosecond pulse duration delivered through the FBARFs at 1030 nm and 515 nm.

Fibre	Pulse duration [ps]
Double-layer FBARF 1030 nm	6.0 (1 m) 6.8 (7 m)
Single-layer FBARF 515 nm	6.0 (0.5 m) 6.4 (5.5 m)

4.3.3 Summary

The experiments performed within this part of work were focused on the transmission of ultrashort, high energy picosecond laser pulses in the NIR and visible (green) spectral bandwidths through negative curvature and free boundary anti-resonant hollow core microstructured fibres.

The NCFs designed to operate in the vicinity of 1 μm and green wavelengths have shown excellent energy handling capacity in the 6 ps pulse regime. The optimised NCFs provide singlemode and high quality output with pulse energy at a level not achievable with the conventional solid core silica fibres and HC-PCFs and significantly exceed the performance of hypocycloid Kagome HC-PCFs (in the green). The delivered average powers in both spectral regimes are the highest reported values transmitted with an optical fibre. Furthermore, the NCFs exhibiting singlemode guidance well maintain spectral and temporal properties of the original laser pulse (after propagation through 7 m - 8.8 m lengths), which indicates their low dispersion and lack of nonlinear processes e.g. SRS and SPM dominant in this pulse regime, which cannot be overcome in the solid core fibres. However, when a NCF supports multiple modes the transmitted ultrashort laser pulse (after a few meters of fibre) experiences temporal broadening as a result of intermodal dispersion (as spectral properties are well preserved).

Both NIR and green guiding NCFs provide fibre delivered beams with a quality and energy at the level required for precision micro-machining applications (see chapter 5). Furthermore, the NCF-150414-G due to its dual-wavelength nature could find an application e.g. in systems for Raman wavelength conversion [22] or dual-wavelength processing of stainless steel [23].

The FBARFs guiding in both investigated spectral regimes are the preliminary versions of this kind of fibre structure, and therefore it was impossible to establish real power handling capability of these fibres in the ps pulse regime. The few-moded guidance, high intrinsic loss and sensitivity to bending of both fibres resulted in low transmission efficiency and unstable output (in comparison with the NCFs). However, based on the results obtained it is expected that further optimisation of the free boundary design should enable delivery of the ultrashort pulse with energies comparable (or even higher due to larger core size, hence lower energy density in the fibre) with that for the NCFs. In order to achieve this it is necessary to improve the uniformity of the fibre structure (discussed in more detail in previous chapter), which could lead to better light confinement, and therefore lower loss (both intrinsic and bend induced) and guidance within the fundamental mode only (hence higher coupling efficiency without excitation of higher order modes).

A comparison of picosecond pulse delivery results in the NIR and green spectral region with NCFs and FBARFs (highest obtained values with short lengths of each fibre) is presented in Table 4.11.

Table 4.11. Comparison of ps pulse delivery results at 1030 nm and 515 nm with NCFs and FBARFs.

1030 nm, 6 ps						
Fibre	**Avg. power [W]**	**Pulse energy [µJ]**	**Peak power [MW]**	**Energy density [Jcm^{-2}]**	**Peak power density [$TWcm^{-2}$]**	**LIDT [Jcm^{-2}]**
NCF-01	36.7	92.0	15.3	9.0	1.50	-
NCF-140414	29.8	74.5	12.4	17.2	2.90	21.0
NCF-150414-G	10.0	25.0	4.2	39.0	6.60	59.0
Double-layer FBARF	23.5	59.0	9.8	4.5	0.74	9.8
515 nm, 6 ps						
NCF-150414-G	12.0	30.0	5.0	68.0	11.30	80.0
Single-layer FBARF	11.5	29.0	4.8	5.5	0.90	21.0

4.4 Femtosecond pulse delivery at 1064 nm with NCF-01

The femtosecond pulse delivery tests described in this part of thesis was joint work carried out in collaboration with David G. Maclachlan (PhD student) on fibre aided waveguide writing in borosilicate glass (see [24] and chapter 5 for further details). The femtosecond source used was a Fianium Ytterbium-doped fibre laser providing 420 fs (FWHM) with pulse energies of 0.9 µJ (full specification of the laser is included in Table 4.12), which is ideal for the investigated application.

Table 4.12. Specification of the Fianium fs fibre laser.

Wavelength [nm]	Pulse duration [fs]	Repetition rate [MHz]	Pulse energy [µJ]	Average power [W]	Peak power [MW]	M^2
1064	420	1	0.9	0.9	2.0	<1.3 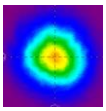

The tests were conducted with a 3 m length (bent through 180º with 6 cm bend dia. due to limited working space) NCF-01 (the only available NCF at the time that the measurements were taken) in the optical setup shown in Fig. 4.16. The laser power was set at the maximum available level and was not changed during the entire experiment. The laser beam was expanded with a Kaplerian telescope formed by two plano-convex lenses giving ~ 3 times magnification. The expanded beam was coupled directly into the NCF-01 core with a launch efficiency of 90% (calculated excluding fibre attenuation and bend-induced loss) using a NBK-7 lens giving a focused spot diameter of 36 µm ($1/e^2$) and a focus cone angle of 58 mrad (equivalent to NA = 0.029). The maximum delivered pulse energy was 0.6 µJ with average and peak powers of 0.6 W and ~ 1 MW respectively. A fibre failure did not occur.

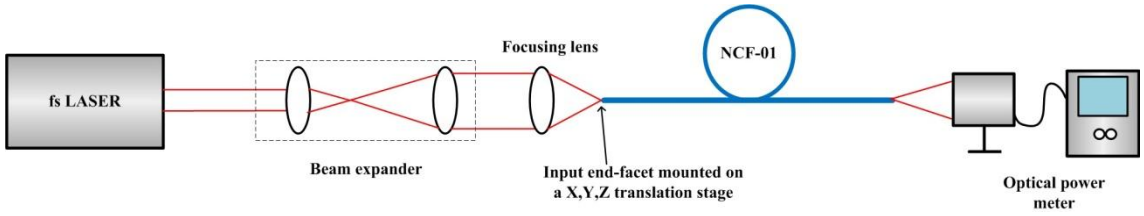

Fig. 4.16. Experimental setup for femtosecond pulse delivery tests.

The temporal and spectral properties of the NCF delivered femtosecond pulse were characterised with the Femtochrome FR-103XL autocorrelator (used in the ps pulse delivery tests) and an Anritsu MS9710A Optical Spectrum Analyser (600 nm - 1750 nm spectral range, 0.05 nm resolution FWHM). The data was captured for maximum delivered pulse energy through the NCF-01. The duration of original laser pulse (see Fig. 4.17(a)) was increased to 647 fs (FHWM) after propagation through 3 m NCF-01 as plotted in Fig. 4.17(b) as a result of intermodal dispersion along the fibre (previously discussed in subsection 4.3.1.3) and chromatic dispersion. Two peaks visible on the fibre delivered autocorrelation trace indicate a presence of higher order modes supported by the NCF-01. The optical spectrum of the laser pulse was not altered after transmission through the fibre as shown in Fig. 4.18. No spectral broadening nor generation of different wavelengths was observed, which indicates low nonlinearity of the fibre and an absence of light in the silica cladding. The difference between the laser and fibre delivered spectra (different number of peaks and their position) resulted from the issue with the spectrum analyser used (discussed previously in subsection 4.3.1.3) and was not related with nonlinear effects.

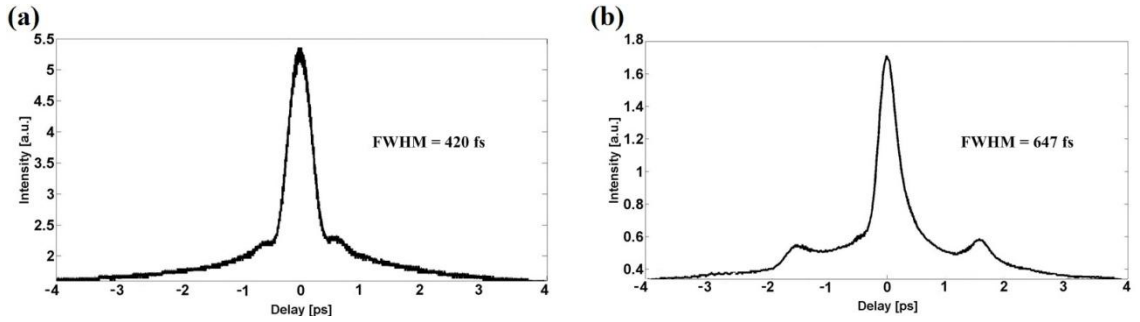

Fig. 4.17. Intensity autocorrelation traces of: (a) fs laser pulse; (b) pulse delivered through 3 m NCF-01 at 1064 nm.

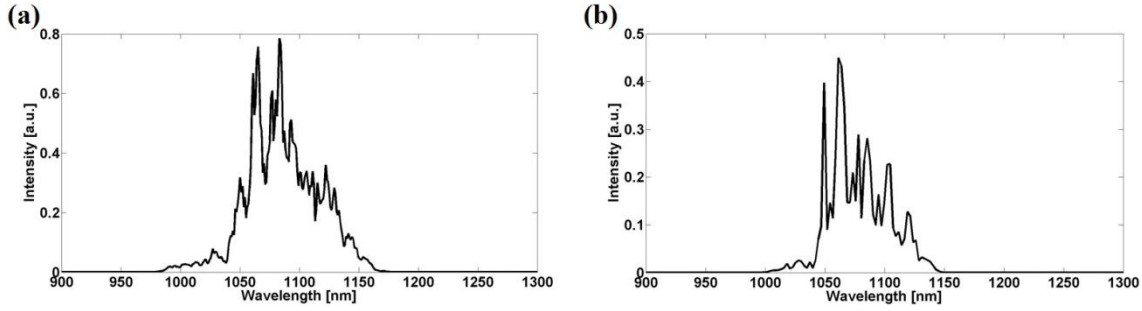

Fig. 4.18. Examples of optical spectra of: (a) fs laser pulse; (b) pulse delivered through 3 m NCF-01 at 1064 nm.

The experiments performed with the NCF-01 confirms its suitability for the delivery of femtosecond pulses. Although, its few-moded nature results in temporal broadening of the transmitted laser pulse, but the low overlap of the guided light with the glass means that nonlinear effect (e.g. SPM) are not observed at the energies available (0.9 μJ, 420 fs). Since the average and peak powers available were limited, the results cannot be accurately compared to the energy handling capabilities of the hypocycloid Kagome HC-PCFs. However, based on the similar performance of both types of anti-resonant fibres (hypocycloid Kagome and NCF) it is assumed that NCF should deliver femtosecond pulses with energies similar to that achievable with the hypocycloid fibres [25].

4.5 Conclusions

This chapter presented investigations of high peak power nanosecond, picosecond and femtosecond pulse delivery in the visible and NIR spectral regions through the NCFs and FBARFs discussed within this thesis. The results of performed experiments have proven high robustness of these fibres and their capacity to deliver pulsed laser light with peak powers significantly exceeding the nonlinear and damage thresholds of conventional solid core silica fibres and HC-PCFs. Flexible beam delivery with the use of NCFs can open a new application window (especially from the manufacturing point of view) for high peak power pulsed laser sources.

References

1. www.thorlabs.com
2. www.nufern.com
3. A. Urich, R. R. J. Maier, Fei Yu, J. C. Knight, D. P. Hand, and J. D. Shephard, "Flexible delivery of Er:YAG radiation at 2.94 μm with negative curvature silica glass fibers: a new solution for minimally invasive surgical procedures," Biomed. Opt. Express **4**, 193-205 (2013).
4. B. Debord, M. Alharbi, L. Vincetti, A. Husakou, C. Fourcade-Dutin, C. Hoenninger, E. Mottay, F. Gérôme, and F. Benabid, "Multi-meter fiber-delivery and pulse self-compression of milli-Joule femtosecond laser and fiber-aided laser-micromachining," Opt. Express **22**, 10735-10746 (2014).
5. G. Mann, J. Vogel, R. Preuss, P. Vaziri, M. Zoheidi, M. Eberstein, J. Kruger, "Nanosecond laser-induced surface damage of optical multimode fibers and their preforms," Appl. Opt. A **92**, 853-857 (2008).
6. B. C. Stuart, M. D. Feit, S. Herman, A. M. Rubenchik, B. W. Shore, and M. D. Perry, "Optical ablation by high-power short-pulse lasers," J. Opt. Soc. Am. B **13**, 459-468 (1996).
7. P. Jaworski, F. Yu, R. R. J. Maier, W. J. Wadsworth, J. C. Knight, J. D. Shephard, and D. P. Hand, "Picosecond and nanosecond pulse delivery through a hollow-core Negative Curvature Fiber for micro-machining applications," Opt. Express **21**, 22742-22753 (2013).
8. J. D. Shephard, J. D. C. Jones, D. P. Hand, G. Bouwmans, J. C. Knight, P. St. J. Russell, and B. J. Mangan, "High energy nanosecond laser pulses delivered single-mode through hollow-core PBG fibers," Opt. Express **12**, 717-723 (2004).
9. J. D. Shephard, F. Couny, P. St. J. Russell, J. D. C. Jones, J. C. Knight, and D. P. Hand, "Improved hollow-core photonic crystal fiber design for delivery of nanosecond pulses in laser micromachining applications," Appl. Opt **44**, 4582-4588 (2005).
10. B. Beaudou, F. Gerôme, Y. Y. Wang, M. Alharbi, T. D. Bradley, G. Humbert, J.-L. Auguste, J.-M. Blondy, and F. Benabid, "Millijoule laser pulse delivery for spark ignition through kagome hollow-core fiber," Opt. Lett. **37**, 1430-1432 (2012).
11. P. Jaworski, F. Yu, R. M. Carter, J. C. Knight, J. D. Shephard, and D. P. Hand, "High energy green nanosecond and picosecond pulse delivery through a Negative

Curvature Fibre for precision micro-machining," Opt. Express **23**, 8498-8506 (2015).

12. J. D. Shephard, J. D. C. Jones, D. P. Hand, J. C. Knight, "Delivery of nanosecond pulses through hollow core photonic crystal fibres and the associated damage limitations", *Proc. SPIE* 5991, Laser-Induced Damage in Optical Materials: 2005, 59911Y (February 07, 2006).
13. C. Dumitrache, J. Rath, and A. P. Yalin, "High Power Spark Delivery System Using Hollow Core Kagome Lattice Fibres," Materials **7**, 5700-5710 (2014).
14. T.J. Stephens, "Fibre-optic Delivery of High Peak Power Laser Pulses for Flow Measurement," PhD Thesis, HeriotWatt University, UK (2003).
15. F. Emaury, C. F. Dutin, C. J. Saraceno, M. Trant, O. H. Heckl, Y. Y. Wang, C. Schriber, F. Gerome, T. Südmeyer, F. Benabid, and U. Keller, "Beam delivery and pulse compression to sub-50 fs of a modelocked thin-disk laser in a gas-filled Kagome-type HC-PCF fiber," Opt. Express **21**, 4986-4994 (2013).
16. A. V. Smith and B. T. Do, "Bulk and surface laser damage of silica by picosecond and nanosecond pulses at 1064 nm," Appl. Opt. **47**, 4812–4832 (2008).
17. S. O. Konorov, A. B. Fedotov, O. A. Kolevatova, V. I. Beloglazov, N. B. Skibina, A. V. Shcherbakov, E. Wintner, and A. M. Zheltikov, "Laser breakdown with millijoule trains of picosecond pulses transmitted through a hollow-core photonic-crystal fibre," J. Phys. D: Appl. Phys. **36**, 1-7 (2003).
18. P. Jaworski, F. Yu, R. M. Carter, W. J. Wadsworth, T. A. Birks, J. C. Knight, J. D. Shephard, and D. P. Hand, "High peak power nanosecond and picosecond pulse delivery through a hollow-core Negative Curvature Fiber in the green spectral region for micro-machining," in *Advanced Photonics*, OSA Technical Digest (online) (Optical Society of America, 2014), paper SoM3B.5.
19. B. Debord, M. Alharbi, A. Benoit, D. Ghosh, M. Dontabactouny, L. Vincetti, J. -M. Blondy, F. Gerome, and F. Benabid, "Ultra low-loss hypocycloid-core Kagome hollow-core photonic crystal fiber for green spectral-range applications," Opt. Lett. **39**, 6245-6248 (2014).
20. N. Ravi Teja, M. Aneesh Babu, T. R. S. Prasad, T. Ravi, "Different Types of Dispersions in an Optical Fiber," IJSRP **2**, 2012.
21. P. Weidner, A. Penzkofer, "Spectral broadening of picosecond laser pulses in optical fibers," Optical and Quantum electronics **25**, 1-25 (1993).

22. L. Ben Yehud, and A. A. Ishaaya, "Efficient wavelength conversion in CF_4-filled photonic bandgap fibers," in *Advanced Photonics*, OSA Technical Digest (online) (Optical Society of America, 2014), paper SoTh2B.5.
23. W. Zhao, W. Wang, X. Mei, G. Jiang, B. Liu, "Investigations of morphological features of picosecond dual-wavelength laser ablation of stainless steel," Optics % Laser Technology, Vol. **58**, 94-99 (2014).
24. P. Jaworski, F. Yu, D. G. MacLachlan, R. R. Maier, R. R. Thomson, W. J. Wadsworth, J. C. Knight, J. D. Shephard, and D. P. Hand, "A hollow-core Negative Curvature Fibre for efficient delivery of NIR picosecond and femtosecond pulses for precision micro-machining, " in *Workshop on Specialty Optical Fibers and their Applications*, (Optical Society of America, 2013), paper F3.3.
25. F. Emaury, C. J. Saraceno, B. Debord, D. Ghosh, A. Diebold, F. Gèrôme, T. Südmeyer, F. Benabid, and U. Keller, "Efficient spectral broadening in the 100-W average power regime using gas-filled kagome HC-PCF and pulse compression," Opt. Lett. **39**, 6843-6846 (2014).

Chapter 5

Practical implementation and demonstration of fibre beam delivery

This chapter presents application of NCF delivered pulses to precision micro-machining processes; cutting and marking of metals and processing of transparent materials, which includes femtosecond waveguide writing. Furthermore, a potential solution for the compensation of bend-induced loss (fibre delivered power fluctuations) is demonstrated with a dynamic power stabilisation system based on an active element.

5.1 Demonstration of micro-machining with fibre delivered beam

The following subsections cover investigations into the suitability of NCF delivered short (ns) and ultrashort (ps and fs) laser pulses in the NIR and green spectral regions for cutting and marking of aluminium and titanium, micro-milling of fused silica and waveguide writing in borosilicate glass.

The experiments conducted in the nanosecond and picosecond pulse regimes were carried out with the experimental setup shown in Fig. 5.1. The lasers used were the Spectral Physics ns system and Trumpf TruMicro ps laser operating at their fundamental and second harmonic wavelengths (see chapter 4 for the specification of the lasers). A half-wave plate and a polarising beam splitter cube were used to provide precise power control (by rotation of the waveplate) without affecting the laser-fibre coupling efficiency. The coupling optics used were the same as previously discussed in chapter 4. The output of the fibre was collimated with a singlet NBK-7 plano-convex lens and expanded with a telescope (Keplerian) to match the entrance aperture of the galvanometer scan head. The galvo scan heads used in the machining arrangement were fitted with f-theta lenses with focal lengths of 125 mm and 163 mm for the ns and ps lasers respectively. The workpiece was fixed to a motorised translation stage providing precision alignment under the scan head. An optical power meter monitored the power of the delivered beam.

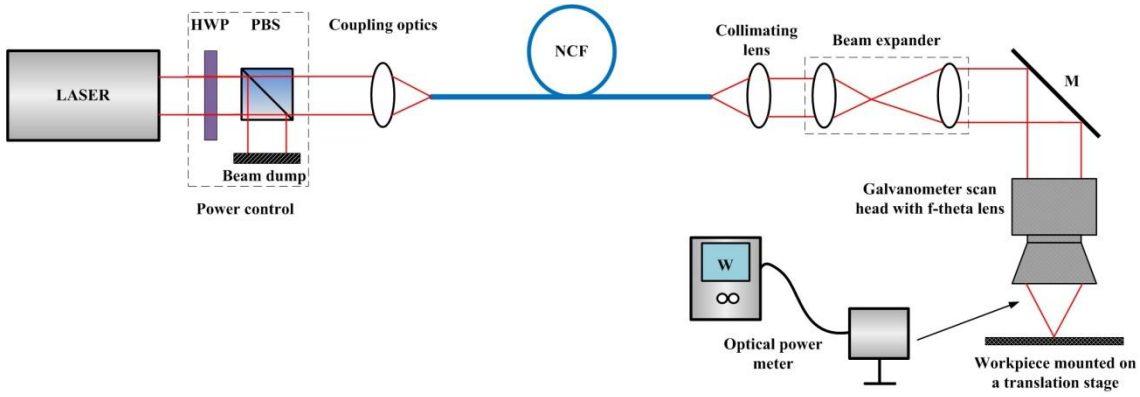

Fig. 5.1. Experimental setup for NCF-based nanosecond and picosecond laser micro-machining. HWP - half wave plate; PBS - polarising beam splitter cube; M - mirror.

5.1.1 Nanosecond cutting and marking

NCF-based nanosecond laser machining was demonstrated by through cutting and marking of aluminium and marking in titanium at 1064 nm and 532 nm. The fibres used were a 10.5 m long NCF-01 and an 8 m long NCF-150414-G in the NIR and green respectively. Both fibres were arbitrarily bent in order to fit into the available space on the optical bench. The patterns cut and marked in the metals with fibre delivered beam were designed in the SCAPS SAMLight laser machining software. The focused spot diameters ($1/e^2$) on the workpiece were approximately 36 μm and 25 μm at 1064 nm and 532 nm.

The 1064 nm, 60 ns laser parameters used for through cutting of the 0.3 mm thick aluminium sheet were 0.8 mJ pulses (with ~12 W average power) at a repetition rate of 15 kHz, which corresponds to an energy density on the sample of 79 Jcm^{-2}. The delivered pulse energy was sufficient to perform precise cutting of relatively small shapes, less than 1 mm by 1 mm, with a cutting speed of 1 mm/s as shown in Fig. 5.2(a). The parameters for the NCF-01 delivered beam used for marking of the aluminium sample were the same but with a marking speed of 50 mm/s and provided results as presented in Fig. 5.2(b). Despite the few-moded nature of the fibre high quality features were fabricated and no significant thermal damage to the surrounding material was noticed. An observed spatter around the marked and cut shapes most likely resulted from a high intensity of the beam causing some vaporisation, which leads to accumulation of melted material around the machined area [1,2].

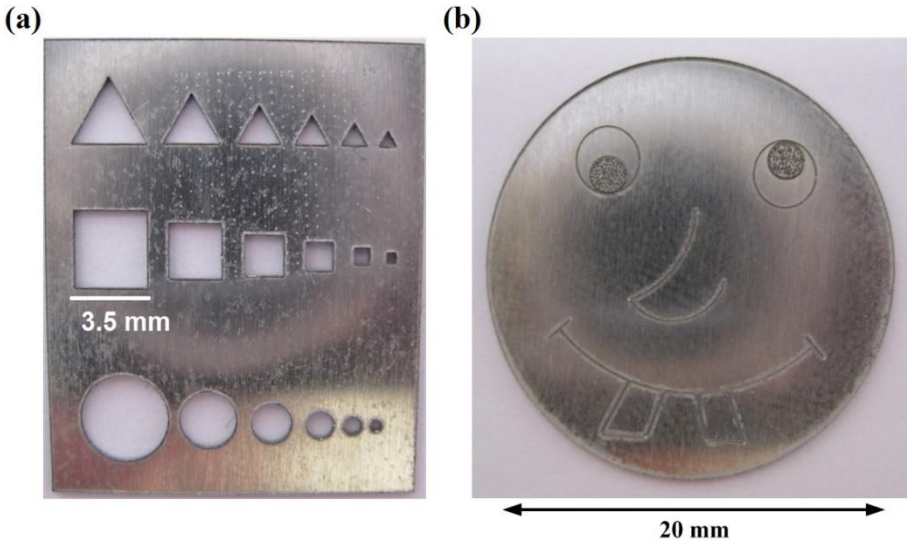

Fig. 5.2. Examples of machining of the 0.3 mm thick aluminium sheet with the NCF delivered ns pulses at 1064 nm: (a) through cutting; (b) through cutting and marking.

Marking in titanium at 1064 nm was performed using identical parameters, although with a significantly higher surface speed of 100 mm/s. To fabricate the desired features gray-scale bitmaps were uploaded to the SAMLight software and a raster scanning method with a 50 μm line separation was applied. Excellent results were achieved as shown in Fig. 5.3. The material surrounding the machined area was not affected by laser-induced thermal damage.

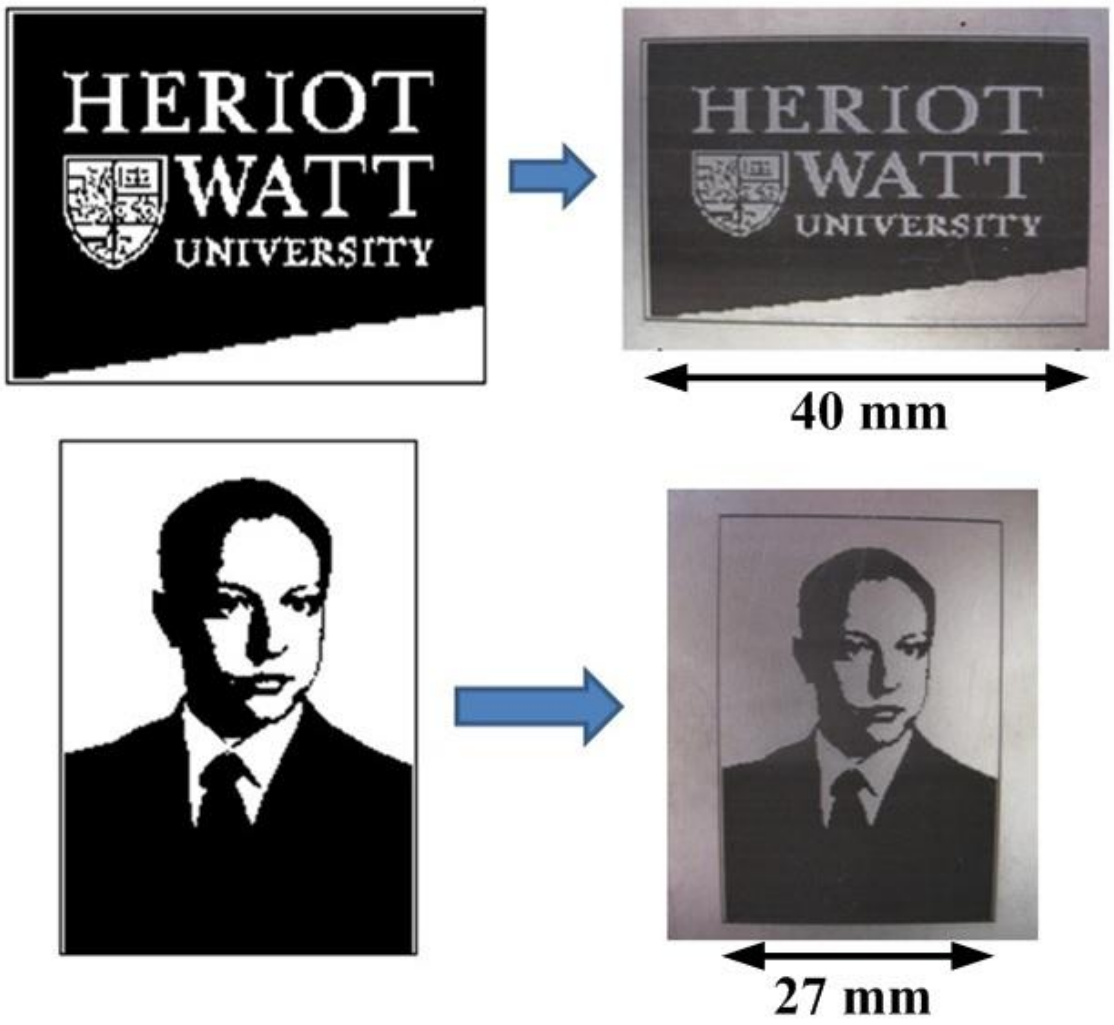

Fig. 5.3. Examples of NCF-based ns marking in titanium at 1064 nm: source bitmaps (left) and machined patterns (right).

As it was discussed in chapter 3, the NCF-01 exhibits a few-moded behaviour, which can have a significant impact on the quality of the processed features especially when the fibre is being dynamically bent (which is likely to be present in manufacturing applications e.g. in robotic devices). Fibre bending leads to coupling between the guided modes, and therefore random intermodal interference patterns are typically observed at the fibre output (discussed previously in subsection 3.1.1.2). This results in significant fluctuations of the fibre delivered power (as transmitted light is decoupled into the

higher order (lossy) modes) and the quality of the fibre delivered beam (M^2 can vary from 1.5 to 3.2, see subsection 3.1.1.1 for more details).

The impact of the dynamic bending of the NCF-01 on the quality of the machined features was tested by marking single lines in aluminium with ns pulses delivered through dynamically bent (arbitrarily) and stationary fibre (both ends of the fibre were fixed on micro-blocks during the experiment). The pulse energy used was the same as discussed earlier in this subsection, although the marking speed was decreased to 1 mm/s. The results shown in Fig. 5.4 clearly indicate strong influence from intermodal interference (induced by bending) on the machined area resulting in significant non uniformity in the marked line due to the aforementioned power fluctuations and changes in the delivered beam profile. However, when the fibre is stationary it maintains transmitted power level and delivered beam profile, hence the quality of machined objects is not affected.

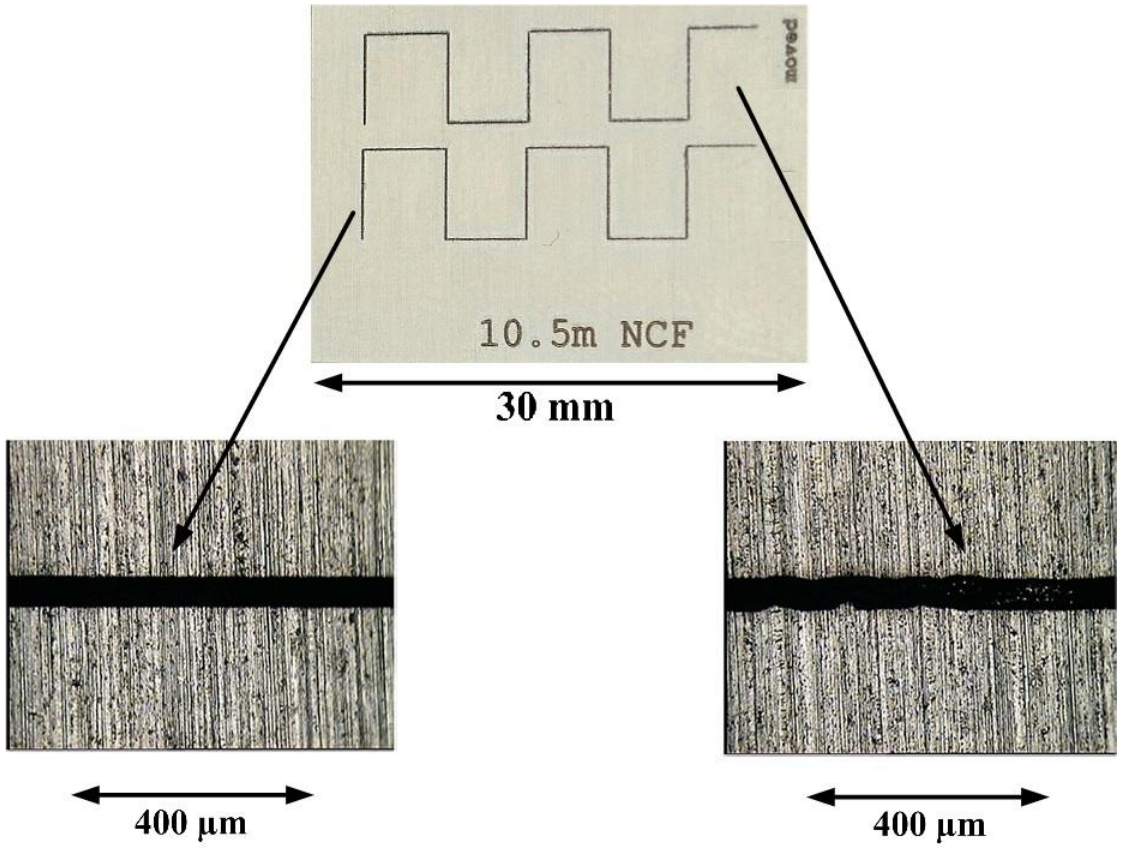

Fig. 5.4. Lines marked in aluminium (top) with ns pulses delivered through continuously bent (bottom right) and not moved NCF-01 (bottom left).

Similar experiments were performed with NCF delivered green 55 ns pulses. To perform both through cutting of 0.3 mm thick aluminium sheet and marking in titanium

and aluminium, identical ns pulse energies and repetition rates were used; 0.35 mJ (~5.3 W average power) and 15 kHz. For these parameters, the energy density on the sample exceeded 71 Jcm^{-2}. The scan speeds, however, were different and optimised to 0.1 mm/s and 100 mm/s for cutting and marking respectively. The pattern marked in titanium was machined using the same methods as discussed earlier in this subsection. In both cases the parameters allowed high quality features to be fabricated without introducing any damage to the surrounding material, as shown in Fig. 5.5.

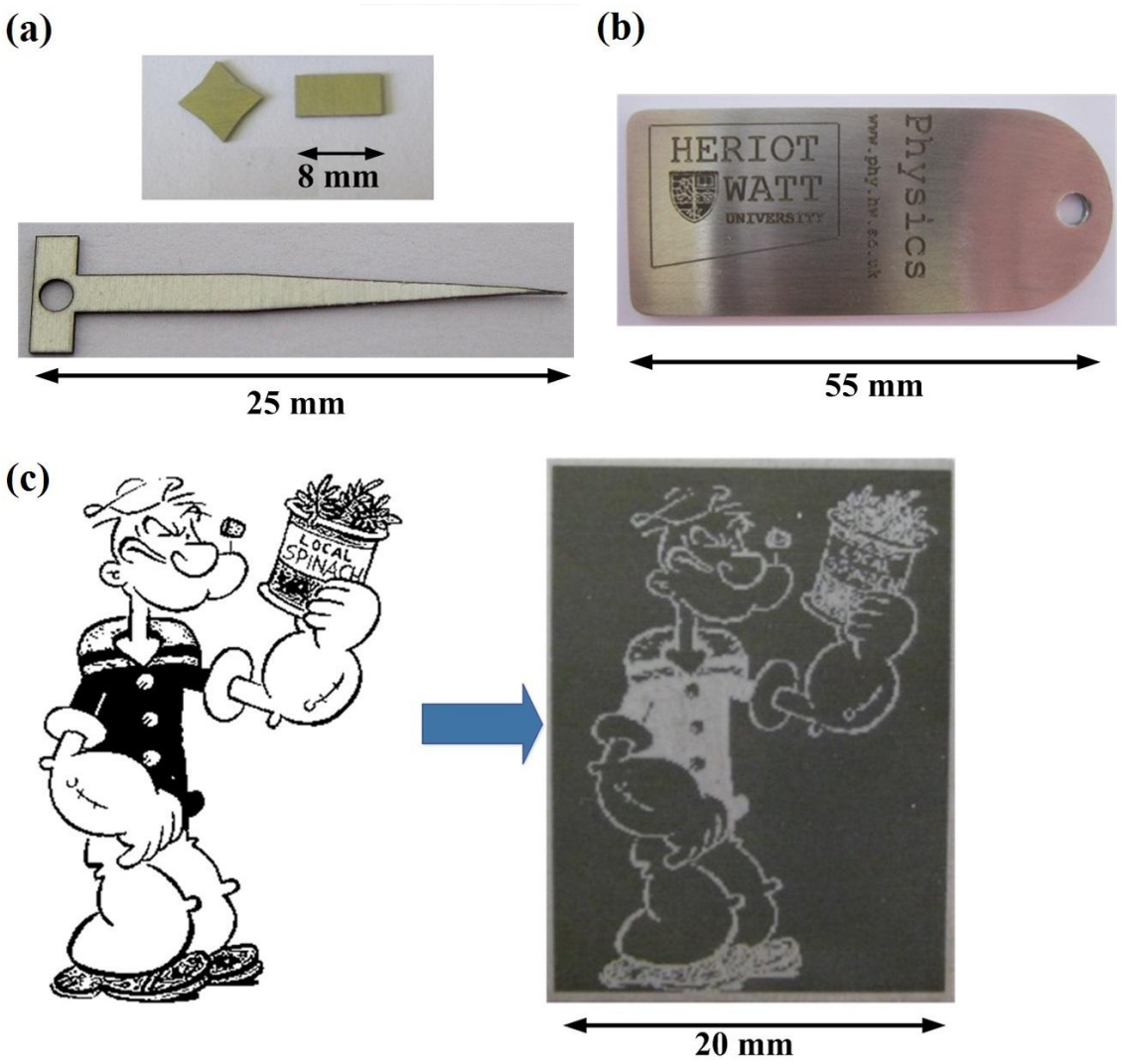

Fig. 5.5. Results of ns machining with NCF delivered pulses at 532 nm: (a) through cutting of 0.3 mm thick aluminium sheet; (b) marking of aluminium key ring; (c) marking in titanium: source bitmap (left) and marked pattern (right).

5.1.2 Picosecond cutting and marking

The suitability of NCF delivered beam for processing metals in the 6 ps pulse regime at 1030 nm and 515 nm was investigated with the same fibres as discussed in the previous subsection. However, a length of each fibre was reduced to 1 m (bent to a 15 cm dia.)

due to limited working space. The f-theta lenses embedded inside the galvo scan heads focused the fibre delivered beam to approximately 36 μm and 28 μm diameter spots ($1/e^2$) onto a machined sample in the NIR and green respectively. The shapes of fabricated features were designed in the Trumpf TruTops software which controls the machining parameters.

The parameters of the NCF delivered beam at 1030 nm used for cutting through 0.3 mm aluminium sheet were 38 μJ pulse energy (15 W average power) at 400 kHz repetition rate. This corresponds to an energy density on the surface of the sample of approximately 3.7 Jcm^{-2}. These parameters were at the level required to cut high quality shapes with dimensions down to less than 1 mm by 1 mm as shown in Fig. 5.6(a). The fabricated components are characterised by sharper and cleaner edges in comparison with the ns results (see Fig. 5.7). Marking in titanium was conducted with the same pulse energy and repetition rate using a raster scanning method, although the scan speed was increased to 100 mm/s. The separation between the consecutive lines was 40 μm. An example of marked object on a titanium plate is shown in Fig. 5.6(b). Again, no thermal damage to the surrounding material was observed and the result is comparable with the ns marking at 1064 nm.

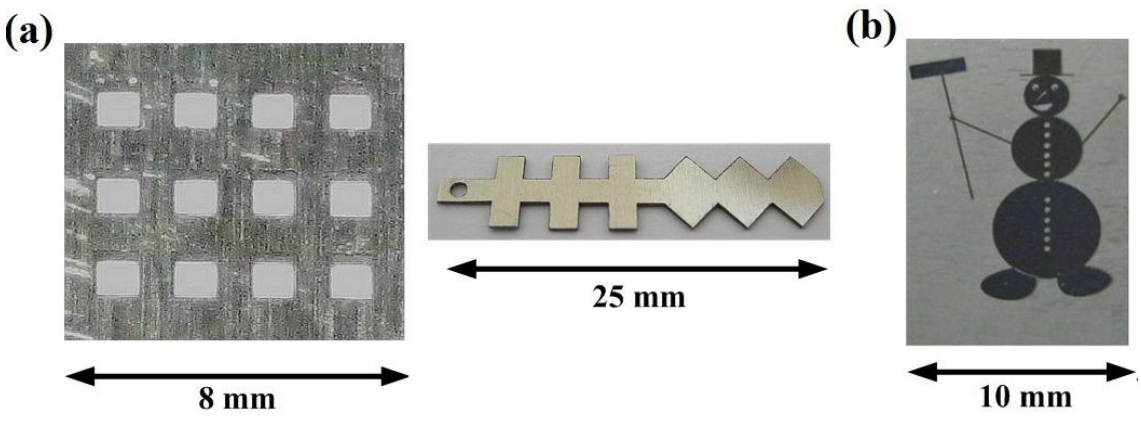

Fig. 5.6. Examples of picosecond micro-machining with NCF delivered laser beam at 1030 nm: (a) cutting of 0.3 mm thick aluminium sheet; (b) marking in titanium.

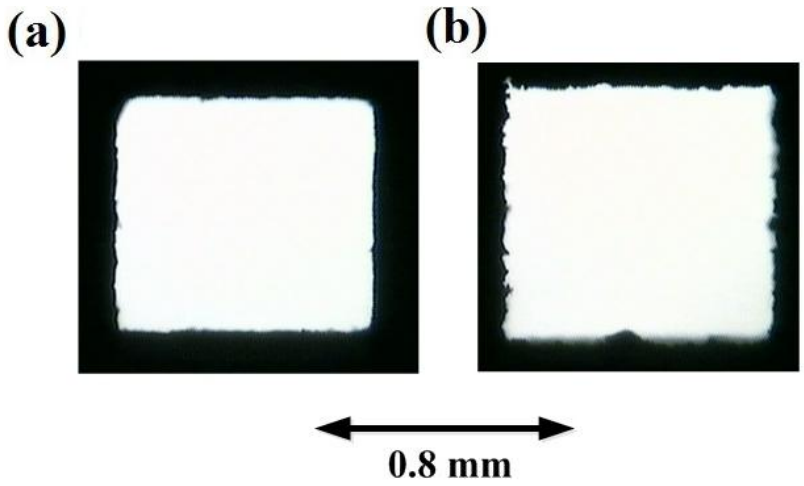

Fig. 5.7. Comparison of cutting of 0.3 mm thick aluminium sheet with NCF delivered beam (microscope images of cut squares): (a) picosecond at 1030 nm; (b) nanosecond at 1064 nm.

The suitability of green picosecond laser pulses (515 nm) delivered through the NCF for precision micro-machining was demonstrated with titanium marking. Here, the pulse energy used was 20 μJ (~8 W average power) at a 400 kHz repetition rate, which corresponds to an energy density of 3.2 Jcm^{-2}. Similarly to the experiments performed at 1030 nm a raster scanning method with the same line separation was used to mark a desired shape. A high quality fibre delivered beam and sufficient pulse energy enabled excellent results to be obtained as shown in Fig. 5.8. The quality of the machined component is at level comparable with the results at 1030 nm and in the green ns pulse regime. Unfortunately, cutting of aluminium with the fibre delivered green ps pulses was impossible due to insufficient energy delivery through the fibre.

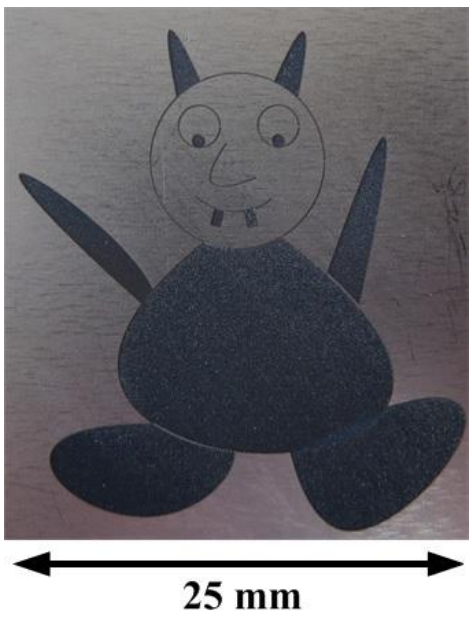

Fig. 5.8. Example of marking in titanium with NCF delivered picosecond pulses at 515 nm.

5.1.3 Picosecond micro-milling of fused silica

Precision and crack-free laser processing of fused silica is not possible with nanosecond pulsed light due to thermal effects in the glass and the significant size of the HAZ. Hence is only feasible with ultrashort laser pulses. Furthermore, a high energy laser beam is required for this particular application (due to properties of fused silica i.e. high transparency for 1 μm light) completely eliminating photonic bandgap hollow-core PCFs and solid core LMA fibres from being used as a flexible beam delivery tool in this application due to their limitations.

The ability to process glass with fibre delivered picosecond pulses at 1030 nm and 515 nm was demonstrated by micro-milling a 1.5 mm thick fused silica wafer. The laser beam was delivered to the galvo scan head through 1 m lengths (bent with 15 cm dia.) of NCF-01 and NCF-150414-G at 1030 nm and 515 nm respectively. The focused spot diameters and machining methods used were the same as discussed in subsection 5.1.2.

With the 1030 nm 6 ps pulses, the pulse energy used for machining was approximately 52 μJ at a 400 kHz repetition rate corresponding to an energy density on the sample of 5.1 Jcm^{-2}. The marking speed was set at 100 mm/s. This allowed fabrication of small objects with dimensions less than 1 mm by 1 mm with depth of 30 μm. Examples of micro-milled fused silica at 1030 nm are shown in Fig. 5.9. No cracks on the glass structure were observed. Experiments performed with lower pulse energies resulted in machining the bottom surface of the sample. A similar issue was observed during machining of Borofloat®33 glass at the same wavelength with 6 ps laser pulses as reported in [3], and can be assumed to result from self-focusing within the glass.

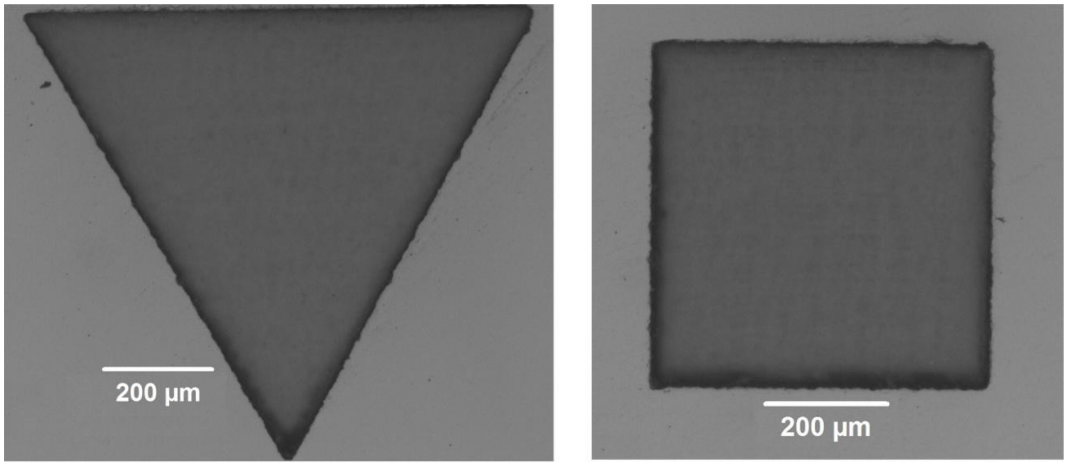

Fig. 5.9. Micro-milled patterns in fused silica with NCF delivered picosecond pulses at 1030 nm.

Machining the glass with shorter wavelength laser light (green, UV) is more desirable due to its optical properties and more readily accessed nonlinear absorption in comparison with the NIR wavelengths. Here, the energy density of the NCF delivered beam required for fabricating high quality features was 2.3 Jcm^{-2} (14 μJ pulse energy at 400 kHz repetition rate), which is more than 2 times lower than needed at 1030 nm. The machining speed, however was changed to 1 mm/s. These parameters enabled fabrication of objects with dimensions down to 400 μm by 400 μm without creating any cracks on either the machined or surrounding area of the glass sample as shown in Fig. 5.10.

Fig. 5.10. Examples of crack-free micro-milling of fused silica with picosecond pulses delivered through NCF at 515 nm.

5.1.4 Femtosecond waveguide writing

The waveguide writing process is based on a modification of the refractive index of the glass [4] via the nonlinear absorption principle. This requires a high intensity laser beam with a high repetition rate; which is easily accessible with femtosecond laser systems. Application of femtosecond pulsed laser light to optical waveguide writing in various types of glass (i.e. borosilicate, fused silica) has been extensively investigated over the last decade [5-7].

This part of work was focused on determining the suitability of femtosecond NCF delivered pulses for waveguide writing in borosilicate glass. The experiments were carried out in collaboration with PhD student David G. MacLachlan.

The waveguide writing process was carried out in the experimental setup shown in Fig. 5.11. Femtosecond pulses with repetition rate of 1 MHz at 1064 nm from a

Fianium system (the same as discussed in section 4.4) were coupled into a 1m straight NCF-01 (that was the only available negative curvature fibre when this experiment was carried out) via a set of plano-convex lenses (see section 4.4 for more details). The fibre output was collimated using a singlet lens to match the clear aperture of the writing lens. The writing optics used was an aspheric lens with an NA = 0.55 and a focal length of 4.51 mm providing a focused spot diameter of ~ 1.5 μm (calculated $1/e^2$ value). The intensity of the laser beam was controlled via a combination of a half wave plate (HWP1) and a polarising beam splitter (PBS). The connection of a quarter wave plate (QWP) and another half wave plate (HWP2) enabled precise polarisation control of the delivered beam required to obtain the desired modification of the refractive index in the borosilicate sample. The sample was mounted on a motorised X,Y,Z translation stage driven by computer software which allowed control of the sample position and writing (translation) speed. The laser beam was focused approximately 150 μm below the top surface of the substrate. The intensity of the incident beam and the inscription process were monitored using an optical power meter and a CCD camera (uEye UI-1120SE) respectively.

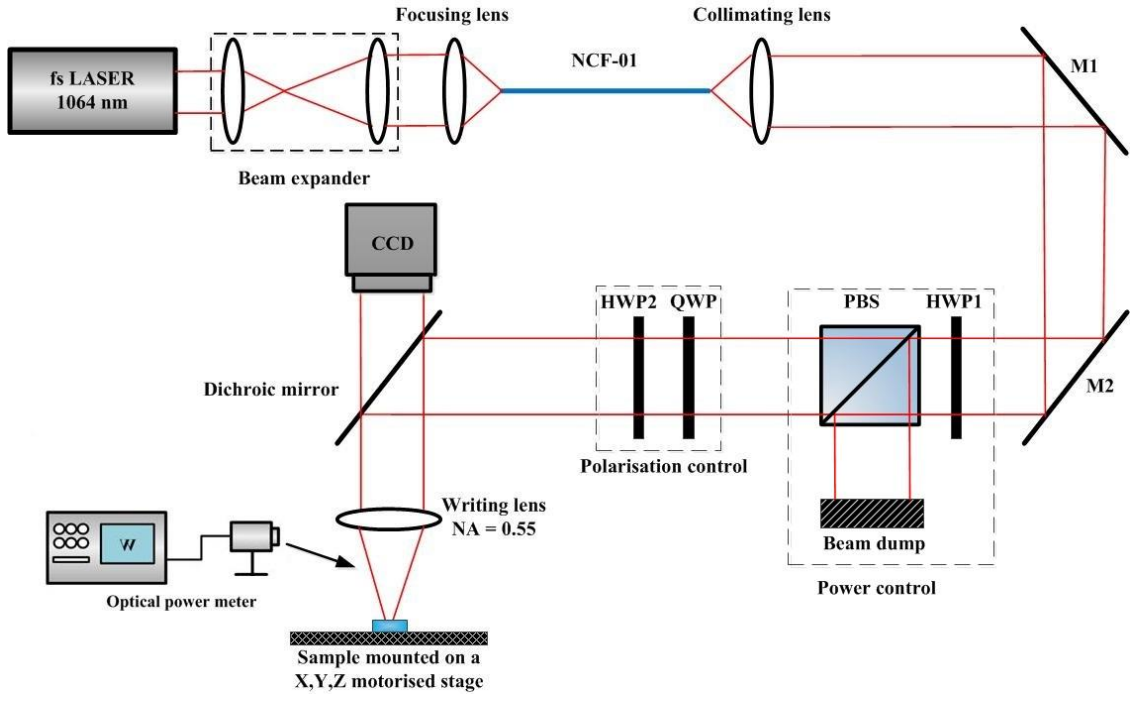

Fig. 5.11. Experimental setup for waveguide writing with NCF delivered femtosecond pulses. M1,M2 - silver mirrors, HWP1,HWP2 - half wave plates, PBS - polarising beam splitter, QWP - quarter wave plate.

The sample used was a borosilicate glass with dimensions of 2 mm (height) x 5 mm (width) x 10 mm (length). The waveguides were written by translating the sample

(35 consecutive scans for a waveguide) perpendicular to the incident laser beam at a translation speed of 0.8 mm/s. Fabricated waveguides have dimensions of ~4 µm x 4 µm x 10 mm. Separate work carried out by David MacLachlan (as a part of his PhD project) showed that a right-circular polarisation of the laser beam allows improvement in the quality of the obtained written waveguides (lower insertion loss). Different pulse energies, ranging from 60 nJ to 125 nJ (1 MHz rep. rate) were applied to determine the most suitable parameters for obtaining singlemode and low loss waveguides. The properties of written waveguides such as insertion loss and delivered beam profiles were characterised with a fibre-coupled laser source emitting coherent radiation at 980 nm using the experimental setup shown in Fig. 5.12. The laser beam delivered through a singlemode fibre (SMF) was butt-coupled into a written waveguide and a near-field beam profile was captured by directly imaging the waveguide output end-facet (with a 20x microscope objective) onto a CCD camera (uEye UI-1120SE). The insertion losses were calculated as a ratio of transmitted optical power through a waveguide to the power measured directly at the output of the SMF from the laser source. Fresnel reflection presented in the interface between the end-facets of the single mode fibre and a waveguide was minimised with a refractive index matching liquid. The sample and the SMF were fixed to X,Y,Z translation stages which allowed accurate positioning. The results are shown in Table 5.1.

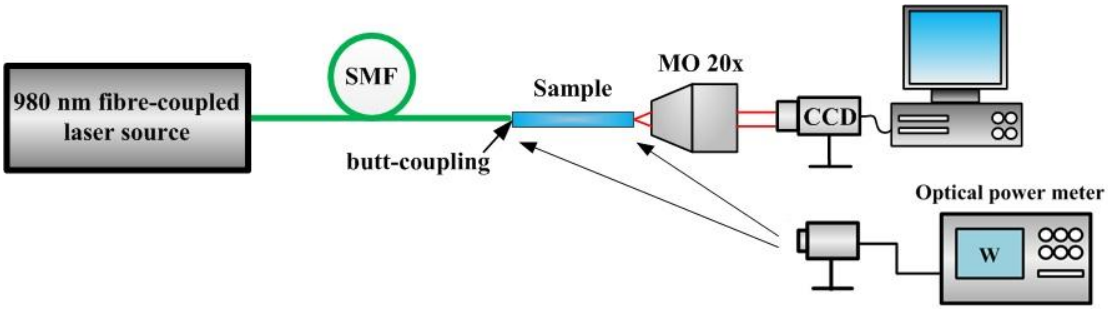

Fig. 5.12. Waveguide characterisation setup. SMF - singlemode fibre, MO - microscope objective.

Table 5.1. Results of waveguide writing in borosilicate glass with femtosecond NCF delivered pulses.

Pulse energy [nJ]	**Near-field delivered beam profile**	**Guidance**	**Insertion loss [dB]**
60 - 100	No results. Too low pulse energy.		
103		singlemode	2.4 ± 0.1
107	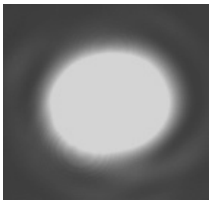	singlemode	1.8 ± 0.1
113		singlemode	2.3 ± 0.1
119		few-moded	2.7 ± 0.1
125	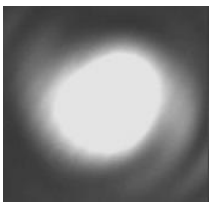	few-moded	3.4 ± 0.1

Femtosecond pulses with energies from 60 nJ to 100 nJ were not sufficient to modify the sample and write a waveguide. Waveguides characterised by singlemode guidance were obtained with pulse energies ranging from 103 nJ to 113 nJ. All waveguides machined with higher pulse energies exhibited a few-moded nature with greater insertion losses. The lowest insertion loss of 1.8 ± 0.1 dB was obtained in a waveguide inscribed with a pulse energy of 107 nJ.

In order to determine the impact of fibre delivery on the waveguide writing process the experiment was repeated without the NCF in the setup. The pulse energy used was in the same range as with the fibre. Characterisation of the guidance properties of the waveguide written with the beam directly from the fs laser was conducted using the same methods as discussed earlier. Similar to the results with the NCF pulse energies < 94 nJ were insufficient to write a waveguide. The optimum pulse energy required for obtaining a singlemode waveguide was in the range of 97 nJ to 113 nJ as shown in Table 5.2. The waveguide with the lowest insertion loss was written with an energy of 107 nJ (the same as with the fibre delivered pulses). The insertion loss in this case was 1.8 ± 0.1 dB, which is exactly the same as obtained with the fibre-written waveguide. Furthermore, the delivered beam profiles through both waveguides have a Gaussian-like shape, which indicates singlemode transmission as shown in Fig. 5.13. The difference between the delivered beam diameters (greater in the case of fibre-written waveguide) most likely resulted from the high M^2 value (NCF's $M^2 = 3.2 \pm 0.1$, M^2 of the fs laser = 1.3) of the fibre delivered beam, hence a different spot size was used during writing. Nevertheless, NCF delivered femtosecond pulses were confirmed to be highly suitabe for waveguide writing.

Table 5.2. Results of waveguide writing in borosilicate glass with femtosecond pulses delivered directly from the laser.

Pulse energy [nJ]	**Near-field delivered beam profile**	**Guidance**	**Insertion loss [dB]**
60 - 94	No results. Too low pulse energy.		
94	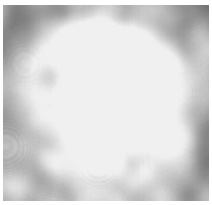	few-moded	2.9 ± 0.1
97	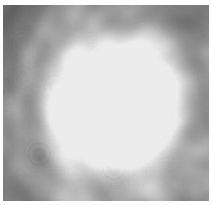	singlemode	2.5 ± 0.1
103	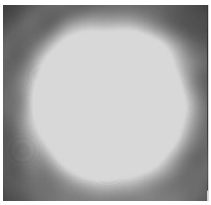	singlemode	2.3 ± 0.1
107	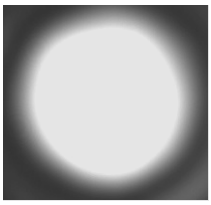	singlemode	1.8 ± 0.1
113	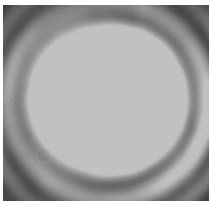	singlemode	2.0 ± 0.1
125		few-moded	3.2 ± 0.1

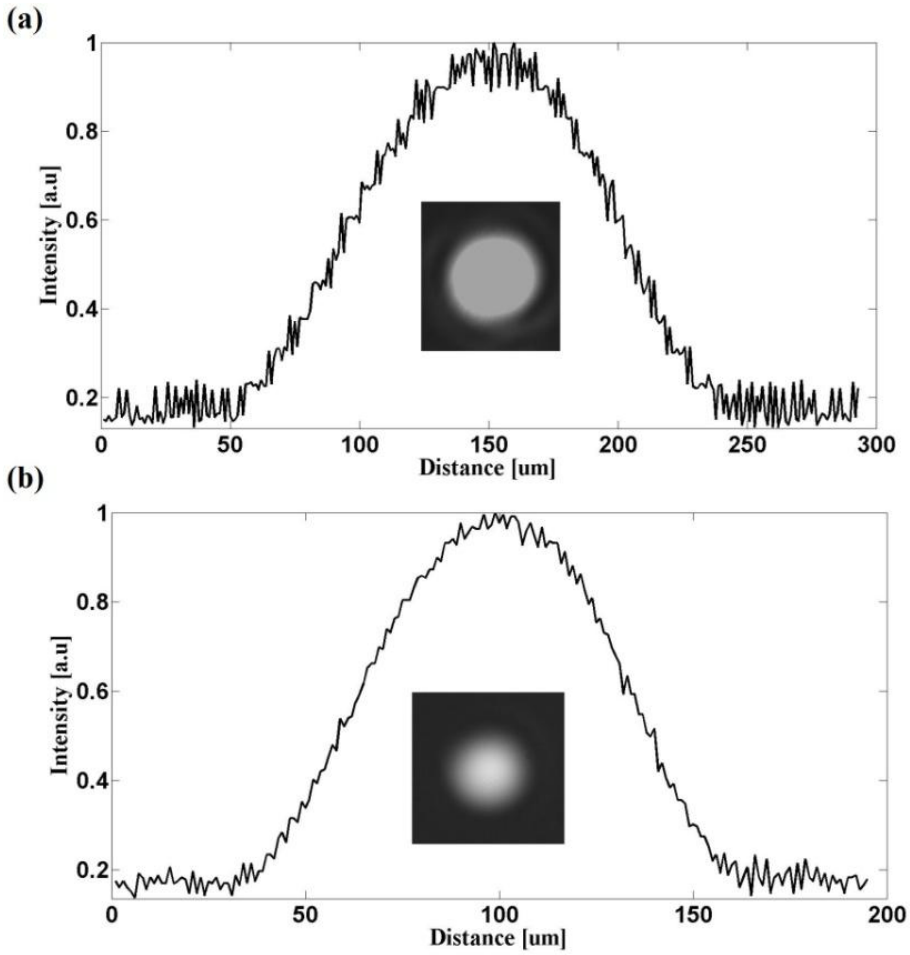

Fig. 5.13. Near-field beam profiles with intensity cross-sections delivered through waveguides written with: (a) NCF delivered pulses; (b) pulses directly from the fs laser.

5.1.5 Conclusions

The NCF delivered beam (in both NIR and green) is highly suitable for high quality cutting and marking of metals and machining of fused silica. Furthermore, the performed micro-milling of glass was the first demonstration of crack-free processing of fused silica with fibre delivered ultrashort (ps) pulses in the NIR and green spectral bandwidths [8,9].

The work carried out on femtosecond waveguide writing in borosilicate glass has shown the versatility of the NCF delivered laser radiation. The waveguide inscribed with the aid of fibre transmitted pulses is characterised by singlemode guidance with an insertion loss of 1.8 dB ± 0.1, which shows no degradation in comparison with the parameters of a waveguide written with the beam directly from the laser source. Hence

there is no negative impact from using the fibre on the waveguide writing process and it is perfectly suitable for this particular application.

The anti-resonant hollow-core photonic crystal fibre is an excellent candidate for the flexible beam delivery for high peak power laser sources, and hence can successfully extend the application range of these lasers, especially in micro-machining to process not only simple and planar components but more complex 3D structures.

5.2 Dynamic stabilisation of NCF delivered power

Laser sources often exhibit some instability in the power level of the emitted radiation resulting from pumping system, overheating issues etc., which is not desired in real applications. Therefore, the laser is provided with an additional system which monitors the intensity of the beam and compensates for fluctuations in order to maintain a constant, desired, output power level. Laser power stabilisation is realised with the use of an active element, e.g. electro- and acousto-optics modulators or a pockels cell as a power actuator [10-12]. These elements provide fast switching time and precise power adjustment, which allow overcoming the aforementioned issue.

Additional fluctuations of the delivered power were also observed with the fibres discussed within this thesis due to bending or an applied point force. These changes are especially significant in the case of the fibres exhibiting few-moded behaviour which leads to much higher power loss due to the different bend sensitivities of different fibre modes and have a strong impact on the quality of machined features with fibre delivered beam as shown in Fig. 5.4 and discussed earlier in this chapter and chapter 3. Hence, this part of work was focused on a development of a system with dynamic stabilisation of the fibre transmitted power. Furthermore such a system is also useful for singlemode fibres as these exhibit high bend-induced loss for very tight bending diameters (< 5 cm).

5.2.1 Liquid Crystal Polarisation Rotator (LCPR)

Dynamic compensation of delivered power fluctuations in the experiments was driven with an aid of a Liquid Crystal Polarisation Rotator (LCPR) from Meadowlark Optics used as an active element as shown in Fig. 5.14(a). The device consists of a variable retarder based on a nematic liquid crystal element (LCVR) and a quarter-wave retarder (QWR) as presented in Fig. 5.14(b). The LCVR provides a retardation of polarisation of the incident laser beam (linearly polarised) with regards to applied voltage which

through changes in the birefringence of the liquid crystal. In this case, the LCVR converts linear polarisation of the incident beam to elliptical polarisation. The QWR alters the polarisation back to linear, although rotated by a specific angle in comparison to the input state, which is equal to one-half the retardance change from the LCVR [13].

The LCPR provides the fast switching time < 150 µs and high laser damage threshold which are required in a power stabilisation system (see Table 5.3 for the specification). The device is controlled via LabView based computer software (see subsection 5.2.3). Furthermore, the LCPR requires an additional temperature stabilisation system to obtain optimum operation conditions. The temperature of the rotator is controlled by a Meadowlark D5020 liquid crystal driver connected with CellDRIVE 5000 computer software as shown in Fig. 5.15. The temperature of the LCPR was set to 25ºC during the entire experiment, as suggested by the manufacturer. The LCPR operates in the wavelength range spanning 480 nm to 1800 nm, however its parameters were optimised for 1030 nm to match the fundamental wavelength of the Trumpf TruMicro ps system used as a coherent light source in the experiments.

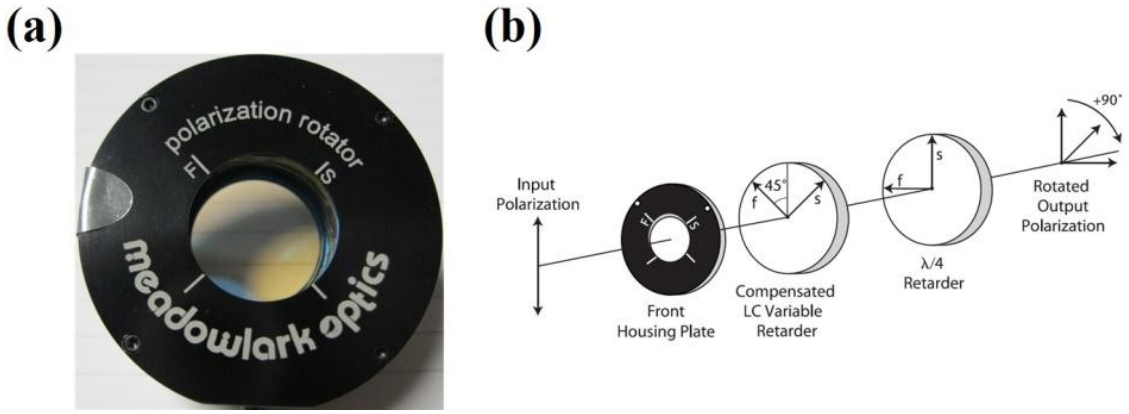

Fig. 5.14. (a) LCPR used in the experiments; (b) Operation of LCPR [13].

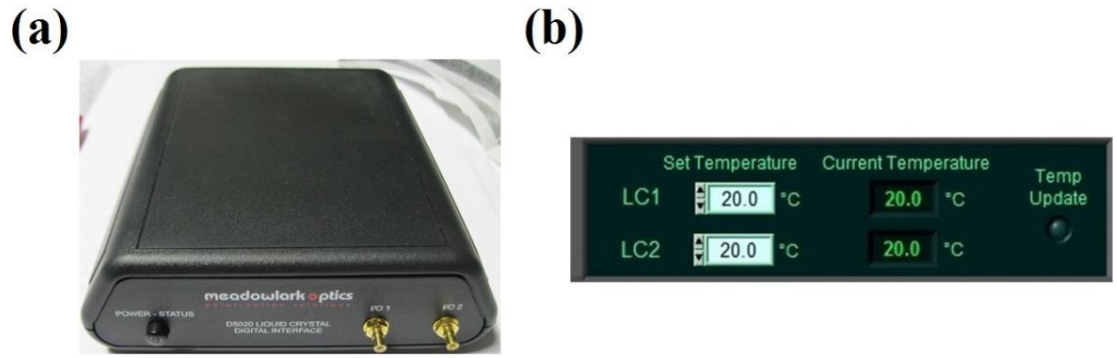

Fig. 5.15. (a) Meadowlark D5020 LCPR driver; (b) CellDRIVE 5000 software - temp. adjustment.

Table 5.3. LPCR specification [13].

Retarder material	Nematic liquid crystal with birefringent polymer
Substrate material	Optical quality synthetic fused silica
Diameter	1 inch
Switching time	< 150 µs
Wavelength	450 nm - 1800 nm (1030 nm central)
Polarisation rotation	180º or more
Polarisation purity	150:1 average
Transmittance	> 92% with polarised input
Operating temperature	0ºC to +50ºC
Laser damage threshold	500 W/cm^2, CW 300 mJ/cm^2, 10 ns, visible

5.2.2 NCF delivered power stabilisation system

The NCF power delivery stabilisation system designed during the experiments is shown in Fig. 5.16. The linearly polarised beam from the Trumpf TruMicro ps laser is directed onto the LCPR via a set of silver mirrors and a half-wave plate (HWP) designed for 1030 nm. The HWP is used to define the orientation of the laser polarisation, which must be precisely aligned with respect to the orientation of the LCPR. This is essential to obtain accurate polarisation rotation and best performance. The power actuator itself is formed of the rotator and a linear polariser (Thorlabs LPNIR050-MP2) set at a fixed angle. The maximum power is transmitted through the actuator when the orientation of the polarised beam leaving the LCPR corresponds to the angle of the polariser. The laser beam is focused directly into the fibre core via a plano-convex lens. The fibre output is collimated with a singlet lens and the delivered power is continuously monitored with a Thorlabs PDA520 silicon photodetector (PD). A non-polarising beam splitter cube (BS) placed before the PD splits the fibre delivered light into two beams with 10% (directed onto the PD) and 90% (attenuated with a beam dump) of the total

transmitted power to prevent the detector from being damaged. An ND filter is used to additionally attenuate the beam intensity and eliminate the possibility of over-saturating the PD. The signal from the photodector is acquired by a National Instruments NI USB-6009 data acquisition device, which transfers the data to a PC with a LabView power stability control software (see subsection below for further details). The data acquisition device is equipped with analog outputs which provide DC voltage in the range of 0 V to 5 V. One of the outputs supplies a control voltage to the LCPR. The applied voltage value is dynamically adjusted (via LabView software) in order to change (increase or decrease) the laser power coupled into the fibre (via the power actuator with ± 20 mW accuracy) and compensate for fluctuations in the fibre delivered power (measured with the PD) induced by fibre bending or a applied point force and, therefore, maintain its intensity at a constant, desired level.

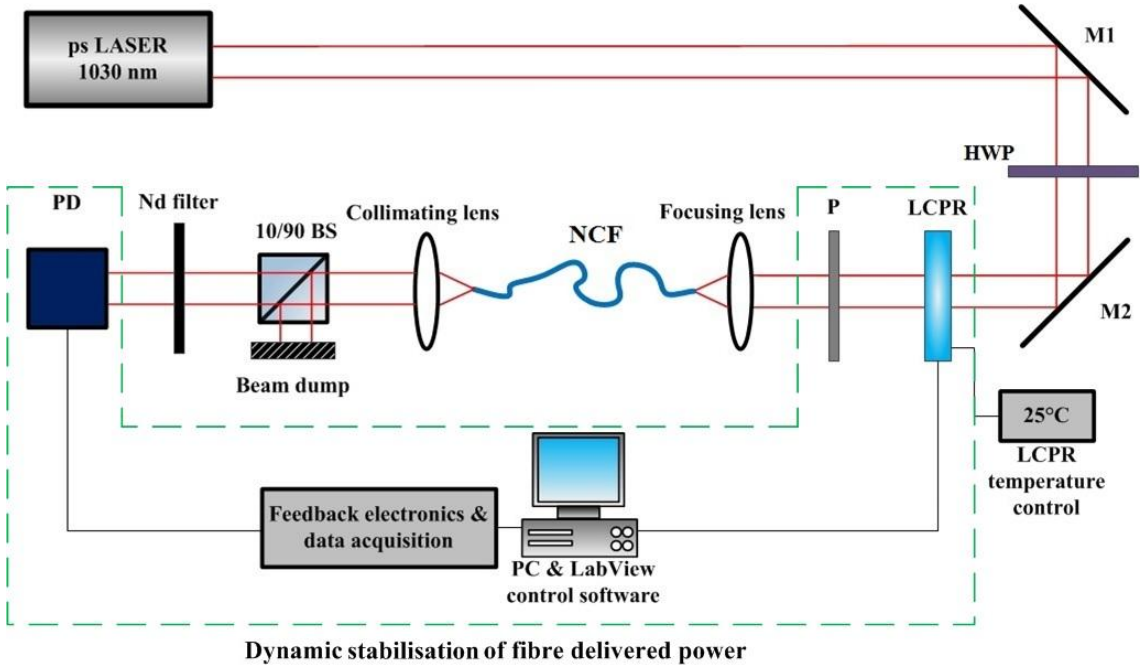

Fig. 5.16. Experimental setup for the NCF delivered power stabilisation. M1 and M2 are silver mirrors, LCPR is Liquid Crystal Polarisation Rotator, P is Polariser, BS is beam splitter cube, PD is photodetector.

5.2.3 LabView control software

The dynamic stabilisation of the NCF delivered beam is controlled via LabView based computer software designed during this part of work as shown in Fig. 5.17. The main software consists of two subprograms - "1 PD Voltage measurement - value to maintain" and "2 Parameters to set before start".

The first subprogram is used to define the intensity level of NCF delivered beam that is desired. The signal from the photodetector (voltage level which corresponds to fibre delivered power) is continuously measured for various voltage values applied to the LCPR. This is essential to establish the LCPR voltage for which the polarisation orientation of the laser beam is rotated such that the power actuator transmits sufficient power (which is then coupled into the NCF), and therefore obtain the desired intensity at the fibre output. The data acquisition parameters are defined by the number of samples (PD voltages) which are acquired and the frequency (rate) at which the samples are collected. Furthermore, the PD Voltage readout corresponds to the average voltage taken from 10 measured samples.

The second subprogram controls fibre delivered power level. Before the program is executed the earlier defined "LPCR voltage" and "PD voltage value to maintain" parameters have to be set together with a "Frequency of LCPR voltage change". This frequency is defined as

$$\text{Freq. of LCPR volt. change} = \frac{1}{\frac{\text{Sample}}{\text{Rate}} \times \text{Number of measured PD voltage values to average}} \quad (5\text{-}1)$$

The minimum frequency which enables sufficient dynamic compensation of the fibre delivered power fluctuations was in the range of 20 Hz to 30 Hz (dependant on the fibre bending or movement rate). The subprogram is continuously measuring the PD voltage and adjusting the LCPR voltage in order to maintain the desired output from the NCF. The measured data (PD voltage) is automatically saved in a ".txt" file while the program is operating.

Additional plots below the subprogram's windows show current and average voltage values read from the photodetector and changes of the LCPR voltage while power stabilisation is being carried out.

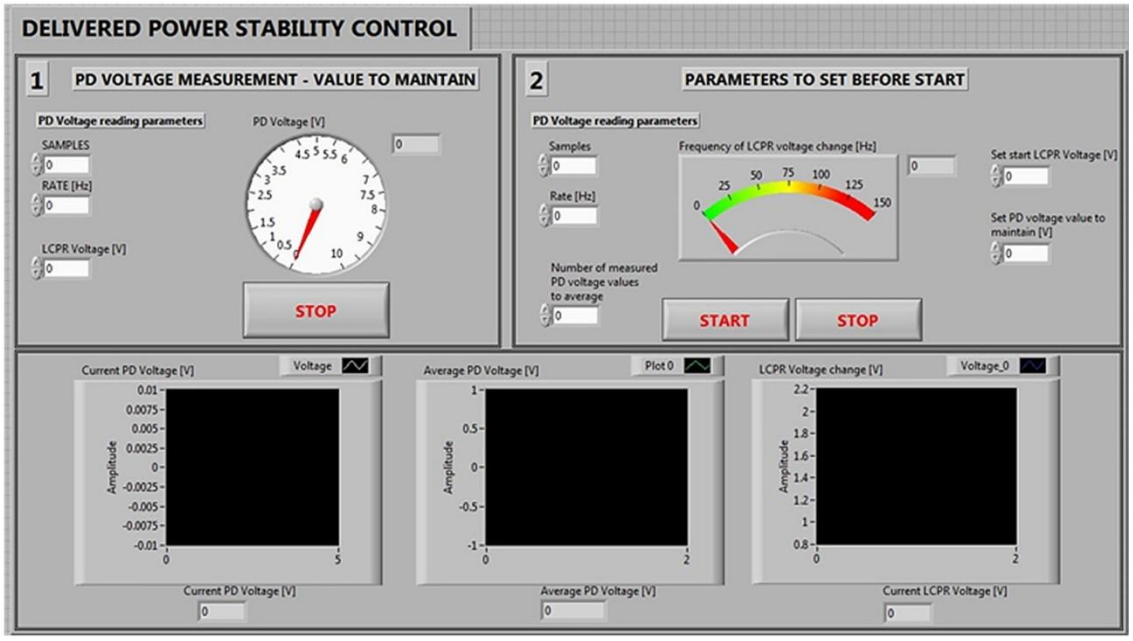

Fig. 5.17. LabView control software for stabilisation of fibre delivered power.

5.2.4 Results

The tests of the fibre delivered power stabilisation system were conducted with approximately 1 m long NCF-01 and the Trumpf TruMicro ps laser at 1030 nm. The NCF delivered power was measured over a period of time (~5-7 min.) during which the fibre was randomly bent in the setup with the dynamic power stabilisation switched either on or off. The measurements carried out without the power stabilisation have shown that fibre bending results in a highly unstable NCF output with significant fluctuations in the delivered power as marked with red-dashed lines in Fig. 5.18(a). When the dynamic power stabilisation system was switched on the bend-induced fluctuations of the delivered signal were efficiently compensated as shown in Fig. 5.18(b). It is assumed that the remaining changes in fibre delivered power (also visible in Fig. 5.18(a) during the time when the fibre was not bent) most likely resulted from insufficient measurement accuracy provided by the photodetector and the data acquisition device used. However further investigation into this issue should be carried out to determine the exact cause of the remaining power fluctuations i.e. measurements of the noise level.

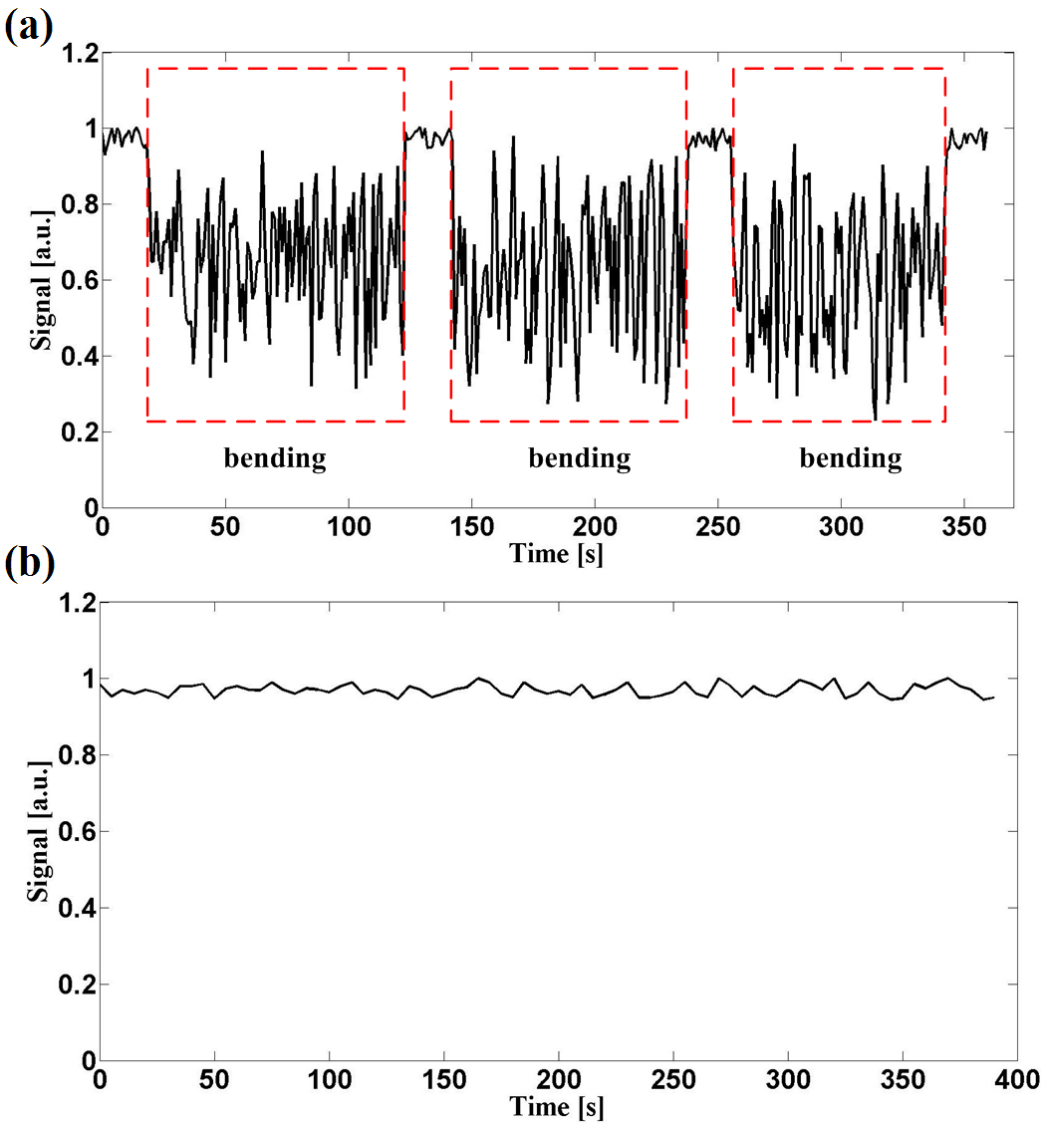

Fig. 5.18. Results of NCF delivered power stability tests: (a) fluctuations of the fibre delivered power due to bending measured without power stabilisation; (b) NCF delivered power changes due to bending recorded with power stabilisation system switched on.

5.2.5 Conclusions

The designed system for dynamic stabilisation of fibre delivered power provides efficient, effective, compensation for the power loss induced by fibre bending, which is especially important in the case of laser micro-machining setups consisting of robotic devices, which require flexible and stable beam delivery.

The active power actuator based on the LCPR provides fast response time and power adjustment which allows stable fibre output to be obtained.

Further optimisation of the system, especially focused on the data acquisition and signal measurements should provide better precision in its operation.

References

1. R. Beck, "Adaptive Optics for Laser Processing," PhD Thesis, Heriot-Watt University, UK (2011).
2. L. Lucas and J. Zhang, "Femtosecond laser micromachining: A back-to-basics primer," Industrial Lasers Solutions for Manufacturing (2012).
3. K. L. Wlodarczyk and D. P. Hand, "Picosecond laser machining of Borofloat®33 glass," ILAS 2013, Nottingham 12-13 March 2013.
4. S. Nolte, M. Will, J. Burghoff, and A. Tuennermann, "Femtosecond waveguide writing: a new avenue to three-dimensional integrated optics," Appl. Phys. A **77**, 109–111 (2003).
5. T. Toney Fernandez, G. Della Valle, R. Osellame, G. Jose, N. Chiodo, A. Jha, and P. Laporta, "Active waveguides written by femtosecond laser irradiation in an erbium-doped phospho-tellurite glass," Opt. Express **16**, 15198-15205 (2008).
6. S. M. Eaton, M. L. Ng, J. Bonse, A. Mermillod-Blondin, H. Zhang, A. Rosenfeld, and P. R. Herman, "Low-loss waveguides fabricated in BK7 glass by high repetition rate femtosecond fiber laser," Appl. Opt. **47**, 2098-2102 (2008).
7. X. Liu, W. Zhang, W. Zhao, R. Stoian, and G. Cheng, "Expanded-core waveguides written by femtosecond laser irradiation in bulk optical glasses," Opt. Express **22**, 28771-28782 (2014).
8. P. Jaworski, F. Yu, R. M. Carter, J. C. Knight, J. D. Shephard, and D. P. Hand, "High energy green nanosecond and picosecond pulse delivery through a Negative Curvature Fiber for precision micro-machining," Opt. Express **23**, 8498-8506 (2015).
9. P. Jaworski, F. Yu, R. R. J. Maier, W. J. Wadsworth, J. C. Knight, J. D. Shephard, and D. P. Hand, "Picosecond and nanosecond pulse delivery through a hollow-core Negative Curvature Fiber for micro-machining applications," Opt. Express **21**, 22742-22753 (2013).
10. P. Kwee, B. Willke, and K. Danzmann, "New concepts and results in laser power stabilization," Appl. Phys. B **102**, 515 (2011).
11. P. Kwee, C. Bogan, K. Danzmann, M. Frede, H. Kim, P. King, J. Pöld, O. Puncken, R. L. Savage, F. Seifert, P. Wessels, L. Winkelmann, and B. Willke, "Stabilized high-power laser system for the gravitational wave detector advanced LIGO," Opt. Express **20**, 10617-10634 (2012).
12. Z. Chang, "Fundamental of Attosecond Optics," publ. by Taylor and Francis Group, ISBN: 978-1-4200-8938-7.

13. www.meadowlark.com

Chapter 6

Summary and future work

Chapter 6 summarises the results of high peak power pulse delivery in the NIR and green spectral regions using NCFs and FBARFs as well as the versatility of the fibre delivered beam for various manufacturing applications.

Negative Curvature Fibre

The NCFs discussed within this thesis were fabricated from silica glass and exhibit light guidance via the ARROW principle. They have been optimised to provide low-loss, singlemode and low bend-sensitive transmission of high peak power short and ultrashort laser pulses in the NIR and green spectral regions.

Optimisation of the fibre parameters, including the position and shape of the low-loss transmission windows, has enabled a significant reduction of fibre loss (both attenuation and bend-induced) in comparison with the preliminary NCFs. The latest fibres are characterised by an attenuation of 0.04 dB/m and 0.15 dB/m in the NIR and green, which significantly exceeds the performance of photonic bandgap HC-PCFs currently offered on the market. This resulted in the efficient delivery of nanosecond, picosecond and femtosecond pulses with peak powers at a level not obtainable with conventional fibres and HC-PCFs. These fibres have the capacity to deliver 6 ps pulses with peak powers of 15 MW (92 μJ pulse energy) and 5 MW (30 μJ pulse energy) at 1030 nm and 515 nm without fibre damage. In the ns and fs pulse regimes the NCFs provide fibre delivered peak power at the kilowatt and megawatt levels respectively. The NCFs deliver a singlemode output whilst perfectly maintaining the spectral and temporal properties of the original 6 ps laser pulses even after propagation through several meters (~ 9 m) of fibre. This indicates low dispersion and a lack of nonlinear processes, unlike solid core fibres. Furthermore, the performance of the NCFs is at the level comparable with the more complex hypocycloid Kagome HC-PCFs. Future work in the area of ultrashort pulse delivery through the NCFs should focus on the transmission of femtosecond pulses with energies of tens of microjoules.

The results of fibre bending tests have shown that the optimised NCFs exhibit relatively low bend-induced loss for bend diameters above 5 cm, which is perfectly sufficient for the applications discussed within this work. In the case of fibres providing a singlemode output, bending results only in delivered power fluctuations and has no impact on the delivered beam profile. On the other hand, the few-moded NIR and green NCFs are characterised by higher bend losses, as expected, due to strong coupling between the fundamental mode and higher order lossy modes. In order to further reduce the negative influence of fibre bending on the delivered power a stabilisation system has been developed. The system enables dynamic compensation of the power fluctuation via a Liquid Crystal Polarisation Rotator (LCPR) used as a power adjustment element and

LabView computer software. The system at this stage allows efficient compensation of bend-induced delivered power fluctuations to be achieved, however further optimisation is still required. The system could be improved by reducing noise in the signal detection and data acquisition system as it is assumed that the remaining fluctuations are due to the lack of sufficient accuracy in these parts of the system. However further measurements (i.e. noise level) have to be performed in order to establish the root of this issue.

Suitability of NCF delivered laser pulses for manufacturing applications has been demonstrated by micro-machining metals and glass. These fibres deliver a high quality beam with energies at the level required for precision nanosecond cutting and marking of aluminum and titanium without introducing any significant thermal damage to the surrounding material. Fibre delivered picosecond and femtosecond pulses have been shown (for the first time) to be highly suitable for crack-free processing of fused silica and waveguide writing in borosilicate glass. This is impossible with the solid core fibres or photonic bandgap HC-PCFs as these applications required high energy pulses in both NIR and green, which cannot be delivered through these fibres. Future work in this area should focus on the development of an all-fibre micro-machining system without the need of a glavo scan head. Furthermore, NCFs could be implemented into the already existing robotic systems used in industry for ultrashort laser processing.

Further development and optimisation of the NCF design for guidance in the NIR and green spectral regions is not planned for the future. However, it can be assumed that improvements in uniformity of the fibre structure (as some asymmetry of the structure was noticed) should result in an improvement of the light confinement in the core, hence a reduction in bending loss for low diameter fibre bending. The negative curvature design should be developed to obtain low-loss guidance and efficient pulse delivery in the UV spectral range. Delivery of high energy pulsed light in the UV is essential to open a completely new application window of the optical fibres and laser sources including e.g. processing of silicon microelectronic devices.

Free Boundary Anti-Resonant Fibre

The Free Boundary Anti-Resonant Fibre is a modified design of the NCF structure in which the cladding nodes no longer exist. The main design principle of this structure is to reduce fibre loss caused by the presence of higher order lossy modes supported by the

waveguides formed by these nodes. Two fibres with single- and double-layer cladding have been initially proposed.

The experiments described in this thesis that focus on the characterisation of the properties of these fibres have shown that both fibres exhibit few-moded guidance, high intrinsic and bend-induced losses and provide low quality output. This is expected as both structures tested were preliminary designs and require further optimisation of their parameters, including the position of the low-loss transmission window and reduction of imperfections of the structure. The lack of structure symmetry is especially significant in the case of the double-layer fibre. The misalignment between each pair of nested capillaries forming the second cladding layer has a strong impact on the leakage loss as these strictly depend on the angle between the two diagonal inner tubes. It is assumed that the elimination of these issues should result in stronger light confinement, hence lower intrinsic loss, reduced sensitivity to bending and hence more efficient transmission.

The energy handling capability tests performed in the ns and ps pulse regimes have shown that despite high loss both free boundary fibres can withstand pulse energies close to the NCFs. However, due to the lack of optimised free boundary fibres it was impossible to establish the full potential of this design. Nevertheless, it is assumed that these fibres, due to the larger core size in comparison with the NCFs (hence lower energy density in the core), should deliver laser pulses with higher energies than presented in this thesis.